INTEGRATED SINGLE-MOLECULE BASED SINGLE-PHOTON SOURCES FOR PHOTONIC QUANTUM TECHNOLOGIES

International Doctorate in Atomic and Molecular Photonics
2016-2019

European Laboratory for Non-Linear Spectroscopy
University of Florence
Coordinator: Dr. Francesco Cataliotti

Candidate
Maja Colautti

Supervisor
Dr. Costanza Toninelli

UNIVERSITÀ
DEGLI STUDI
FIRENZE

Contents

Introduction

Differently from any classical theory, which speaks about *what happens*, quantum mechanics treats *what is measured*, or observed. This subtle difference implies the division of the world into two parts, the observed system and the observer, with an utterly arbitrary boundary [1]. In order to explain such a division, i.e. the measurement process, the Projection Postulate was introduced [2, 3]. However, being in contradiction with Schrödinger equation of motion [4, 5], this gave rise to several alternative interpretations of the equations [1, 6, 7]. In the many-worlds approach for example, the observed system and the observer both evolve according to the Schrödinger function, with no necessity of an arbitrary division and with all possible output states being realized and coexisting in orthogonal universes [8]. This solution was refused by the community being intrinsically untestable [9], nevertheless the doubts that it arises are still non-trivial and under current investigation, as e.g. in the exploration of the boundary between quantum and classical systems pursued by Prof. Arndt and collaborators [10]. Indeed, despite the theory of quantum mechanics has been thoroughly corroborated, it is still unclear to which size-domain quantum properties prevail on classical behavior and to which extent they are exploited. Only recently, quantum coherences were demonstrated to play a crucial role in some organic mesoscopic systems able to perform photosynthesis with 99% efficiency and room-temperature conditions [11, 12], something that is classically inexplicable.
While on one side there is interest in understanding to which limit quantum phenomena still survive in macroscopic systems, on the other side, efforts are focused to push the control and manipulation down to the single particle level, in order to exploit quantum properties on the macroscopic scale.

Our society strongly relies on high-tech facilities and powerful computers, and future technological progress is projected on moving to ever smaller structures of improved efficiency, targeting operations at the single-particle level. In this context, quantum properties can be leveraged on. A full and functional control on single quanta might enable e.g. fully secure communication protocols [13], exponentially faster computers [14], simulations of quantum chemical and physical systems [15], along with un-

precedented sensing abilities [16] e.g. for bio-medical applications. Very recently, for example, a Google research team has demonstrated the superiority of a superconductive quantum processor over the biggest IBM classical supercomputer, by solving a computation of high complexity in 200 seconds [17] (compared to the 2.5 days-time of the classical IBM counterpart [18]).
In particular, in the field of quantum photonics, which is based on the use of single quanta of light, i.e. single photons, the benefit of operative quantum schemes over classical machines is not far from reach, and has already been demonstrated for specific tasks. In *boson sampling*, the use of tens of single photons in many optical modes enables the computation of classically hard and costly tasks [19, 20], such as the calculation of the permanent of a matrix. Moreover, truly *random number generators* [21], based on quantum-based random processes, already offer a commercial alternative to the pseudorandom sequences used in Monte Carlo simulations. Finally, quantum key distribution protocols allow for information-theoretic secure communication with a spatially distant party, thus assuring total privacy on the forwarded message. In particular, the BB84 protocol has been extensively demonstrated with 'emulated' single photons from attenuated laser sources [22, 23], and recently also with realistic single-photon emitters [24]. Such pioneering investigation and testing of quantum science was possible because photons are excellent and low-noise carriers of quantum information. Weakly interacting with the environment, photons do not suffer from decoherence as matter-based qubits systems, and consequently do not require cryogenic operation and high vacuum conditions. Information is easily stored and encoded e.g. in the photon polarization state, in the spatial path or in the arrival time, and in general in any available degree of freedom. Nevertheless, for a large-scale processing of quantum information, which depends on the realization of robust and scalable photonic architectures, integrated quantum photonics (IQP) is essential.
IQP, by leveraging the commercially available tools from the metal-semiconductor industry, enables state generation, quantum state manipulation and single-photon detection at increasing scale and level of complexity [25]. However, the standard single-photon generation approaches primarily rely on parametric effects that are intrinsically non-deterministic with typically few percents production probability [26]. By contrast, harnessing quantum effects on large-scale devices requires on-chip generation of a big number of identical photons on demand. Moreover, epitaxially grown hybrid-semiconductor chips bear limitations in terms of geometries and materials. As a consequence, shifting to quantum phenomena in increasing size systems, as quantum interference of more than two photons in the same mode, is still challenging to achieve within conventional planar schemes [27]. A common approach consists in de-multiplexing a single-photon source into several spatial modes [20], and typically involves serious losses due to optical switchers ($\sim 20\%$ losses are reported

in Ref. [20] for de-multiplexing into 20 modes).
All considered, new requirements to traditional photonic platforms are needed, such as the integration of ideally identical quantum emitters and the extension to three-dimensional geometries.

Single-photon emitters convey a single photon after each excitation-emission cycle. They hold promise as on-demand sources of non-classical light [28, 29], once provided their transition linewidth is broadened only by spontaneous emission processes, and not by any interaction with the environment (e.g. by decoherence, spectral diffusion, blinking). Among them, atom-like emitters in the solid state, such as fluorescent atomic centers in diamond [30, 31], quantum dots (QD) [32] and single molecules [33], are emerging due to the possibility of integrating them in photonic circuits. In particular, QD technology has demonstrated fundamental results both in quantum computation [20] and communication [24], as well as for the integration in nanophotonic devices [34, 35, 36]. However, structuring the environment around quantum emitters in the wavelength scale affects the emission properties, typically degrading its quantum coherence and photostability [37, 38], thus limiting on-chip operation. In this sense, nanofabrication of semiconductor hybrid devices results demanding and hardly scalable, while the final performances are very sensitive to imperfections [39, 40]. Despite some recent progress, deterministic integration of quantum emitters into optical systems remains a major challenge towards future progress on on-chip measurements beyond the classical limit. Seminal results reported in Refs. [41, 42, 43] point at the key advantages of single-emitter integration in polymeric microstructures, such as one-step 3D patterning and a-priori positioning of the emitter in high-intensity regions of the electro-magnetic field. Nevertheless, the colloidal diamond systems employed in Refs. [41, 42] are not suitable for most quantum applications due to decoherence and spectral diffusion [37, 44], whereas the epitaxially grown quantum dots in [43] are not favourable for a full 3D integration.

Single organic molecules of polyaromatic hydrocarbons (PAHs) in suitable host crystals have shown remarkable quantum optical properties both at liquid-helium temperatures and at room temperature [33], and are potentially compatible with polymer chemistry. In general, single PAHs have been demonstrated to be excellent candidates as non-classical light sources [45, 46, 47, 48], non-linear elements at the few photon level [49, 50, 51] and nano-scale sensors for electric fields, pressure and strain [52, 53, 54, 55]. Recently they have been successfully integrated in open optical cavities [51, 56] and antennas [57] and evanescently coupled to nanoguides [58, 59] and waveguides [60, 61, 62]. In particular, the realization of Anthracene nanocrystals doped with Dibenzoterrylene molecules (DBT:Ac NCXs) exhibiting photostable single-

photon emission and Fourier-limited line-widths at 3 K [63], has opened the pathway to their full embedding in polymeric devices [52, 64]. Besides the already mentioned advantages of single-emitter integration and 3D designs, polymers can provide free-standing structures, hybrid integration [65] and interchip connection [66]. Another major benefit is the possibility of tailoring their physical, electronic and optical properties by means of chemistry engineering [67], thus enabling full customization of the photonic structures. The employment of photo-reactive or electro-optical features [68, 69] allows conceiving an alternative approach to tunable components and programmable processors [70].

In this thesis, I present the development and realization of an all-organic platform which combines on a chip the freedom of three-dimensional polymeric architectures with the optimal properties of single photon emission from fluorescent molecules [71]. I demonstrate the potentials of the developed fabrication technique and the unique solutions that it offers for photonic integrated quantum technologies.
In particular, in Chapter 1 the theoretical framework of single-photon emission and coupling to nanophotonic structures is outlined. In Chapter 2, the nanostructured single-photon source employed in this thesis, developed by our group [63] and especially suitable for integration in photonic architectures, is introduced and characterized. In Chapter 3, owing to the remarkable photonic properties, the molecule-based single-photon source is demonstrated to find practical application as a low-photon-flux standard for the calibration of single-photon detectors [72]. In Chapter 4, the 3D polymeric platform for the integration of the molecular single-photon source is presented. The numerical modelling of the photonic structures designs and the fabrication methods are explained, and the final experimental results are analyzed. In Chapter 5, preliminary measurements on the employment of polymers for deterministic positioning of our single-photon emitters on hybrid semiconductor photonic circuits are finally discussed [64].

1

Single Photon Sources

This chapter provides a short introduction to single photon sources and their properties and sets the theoretical framework for the following experiments. Examples of state-of-the-art quantum emitters for single-photon emission are presented and briefly compared. The last part focuses on the essential concepts of light-matter interaction and on the working principles of photon-collection strategies, some of which are then explored in this thesis work.

In 1951 Einstein wrote - "All these fifty years of pondering have not brought me any closer to answering the question, What are light quanta?" [73].
Nowadays the definition of a single photon remains non trivial, and much discussion can be found in the literature on this point [74]. The most common definition is that a photon is an elementary excitation of a single mode of the quantized electromagnetic field [75]. However, it does not help much our intuition: a single monochromatic photon is considered as a particle of light, but is 'everywhere' in space, and can not be localized in time without being destroyed.
In practice, one often deals with propagating "single photon wave packets" that are localized to some degree in time and space and are mathematically described as superpositions of monochromatic electromagnetic modes [75]. Such multi-mode single photons can be strictly associated to the state of the electromagnetic field following a spontaneous emission event [75]. As it will be explained further on in this chapter, in the field of quantum nano-photonics it is convenient to rather couple the emission to one specific mode of the electromagnetic field, in order to collect it and manipulate it in an efficient way.
It is hence useful to introduce a further type of photons which follows from the quantization of the electromagnetic field. In general, a *number state* $|n\rangle$, or *Fock state*, is a quantum state of a well-defined number $n \in Z$ of photons in a given mode. Hence, a single photon in a defined mode is a Fock state with $n = 1$. In practice, while the vacuum state $|n\rangle = |0\rangle$ is trivial to obtain (no light) and superpositions of many Fock states $|\alpha\rangle \propto \sum_{n=0}^{\infty} \frac{\alpha^n}{\sqrt{n!}} |n\rangle$ are promptly conveyed by laser field, number-states of light are very hard to handle. Up to recent years single-photon generation has primarily relied on processes of probabilistic nature (parametric down conversion, four-wave mixing), which indeed brought to fundamental achievements [76, 77, 78]. Benefiting from the advanced technology of integrated optical circuits, high-quality multi-photon sources have been realized on single chips, enabling e.g. the generation of high-dimensional entangled states [25], the on-chip implementation of algorithmic processing of quantum states of light with up to eight photons [79], as well as the demonstration of chip-to-chip quantum teleportation [80]. These schemes are however intrinsically limited to low generation rates, thus restricting the possibilities of scaling up the resources to increasingly large devices and complex quantum systems.
An ideal single-photon source (SPS), able to convey single photons *on demand* with specific properties, is indeed still lacking. In this context, much effort has been put in developing a reliable SPS, and the currently most promising systems in terms of practical operation and photophysical features are quantum emitters in the solid states, which will be briefly analyzed in Sec. 1.1.3.
In the following, we briefly outline the mathematical framework used to the describe a quantum-emitting system, and introduce the optical properties characterizing a SPS [81, 82, 83, 74].

1.1 Photophysics of SPS

New generations of SPSs have originated from recent progress in the fabrication, optical detection, characterization and manipulation of single quantum objects. Such single quantum emitters hold promise as SPSs. Indeed, approximately described as two-level systems, once efficiently prepared in the excited state, they convey one and only one photon per excitation cycle via spontaneous emission. However, in order to satisfy the definition of *on demand* SPS, more conditions must be fulfilled, e.g. unitary quantum yield, that is the probability of radiative decay, certainty of the excited state preparation, as well as control over the emission mode.
Here, we describe the interaction processes from which the emission properties yielding a reliable SPS can be deduced.

1.1.1 Light-Matter Interaction

We here define a quantum emitter (QE) as a two-level system (TLS) with ground state $|g\rangle$ and excited state $|e\rangle$ characterized by a radiative electromagnetic transition with energy $\hbar\omega_A$. In practice, solid state QEs, which are at the focus of this thesis, exhibit a more complex scheme of energy levels, including triplet states and vibrational modes. However, if we consider the typical experimental configurations, the TLS approximation is licit. Indeed, in a resonant excitation scheme a monochromatic laser is used to excite the main transition and coupling to other energy levels is negligible, while in an off-resonant excitation scheme, relaxation processes are so fast that the population of the vibrational levels can be neglected.
In order to describe the dynamics of a TLS, we introduce the Hamiltonian relative to the interaction with a single mode of the electromagnetic field (e.g. in a resonant cavity), considering a reference frame rotating at the angular frequency of the light field ω_P. This can be described as follows [81, 82]

$$\hat{\mathcal{H}} = -\hbar\Delta\omega\hat{\sigma}_{eg}\hat{\sigma}_{ge} + \hbar\omega_P\hat{\mathbf{f}}^{\dagger}(\mathbf{r})\hat{\mathbf{f}}(\mathbf{r}) - \hat{\mathbf{d}}\cdot\hat{\mathbf{E}}(\mathbf{r})\,. \tag{1.1}$$

Here, the first term of Eq. 1.1 corresponds to the Hamiltonian of the TLS, where the presence of $\Delta\omega = \omega_P - \omega_A$ follows from the rotating reference frame. $\hat{\sigma}_{ij} = |i\rangle\langle j|$ are the coherences between the levels *i* and *j*, and the product $\hat{\sigma}_{eg}\hat{\sigma}_{ge}$ reduces to the population of the excited state once we consider $|g\rangle\langle g| = 1$. The second term identifies the excitation of the light field, with energy $\hbar\omega_P$ and described by the bosonic operators $\hat{\mathbf{f}}^{\dagger}$ and $\hat{\mathbf{f}}$, for the creation and annihilation of a photon. Finally, the last term of Eq. 1.1 relates to the light-matter interaction, which is mediated by the emitter transition dipole operator $\hat{\mathbf{d}} = \mathbf{d}^{*}\hat{\sigma}_{eg} + \mathbf{d}\hat{\sigma}_{ge}$, with matrix elements $\mathbf{d} = \langle g|\,\hat{\mathbf{d}}\,|e\rangle$.
Having described the system energy operator $\hat{\mathcal{H}}$, we introduce the TLS dynamics by

first giving some brief notions of an *open quantum system*. The TLS is indeed treated as and open quantum system, *i.e.* a quantum system S which is coupled to another system B, called the *environment*, and which is hence a subsystem of the total system S+B. This interaction with the surroundings gives rise to system-environment correlations which affect the dynamics of the state of S, which is no longer represented by a unitary Hamiltonian dynamics. Hence, the time evolution of the TLS induced by the dynamics of the total system is referred as *reduced dynamics* and is deduced by considering the reduced density matrix for the TLS $\hat{\rho}$, which describes solely the state of the emitter. This evolves according to the following master equation [84]

$$\frac{d\hat{\rho}}{dt} = -\frac{i}{\hbar}[\hat{\mathcal{H}}, \hat{\rho}] + \mathcal{L}(\hat{\rho}) \tag{1.2}$$

where $[\cdot,\cdot]$ is the commutation operator, and

$$\mathcal{L}(\hat{\rho}) = \sum_{ij} \frac{\Gamma_{ij}}{2}(2\hat{\sigma}_{ji}\hat{\rho}\hat{\sigma}_{ij} - \hat{\sigma}_{ii}\hat{\rho} - \hat{\rho}\hat{\sigma}_{ii}) \tag{1.3}$$

is the Lindblad operator [85, 86], with $\hat{\sigma}_{ii}$ denoting the occupation probability of state $|i\rangle$. The Lindblad operator describes the excited state decay rate and the decoherence of the TLS owing to the interaction with the reservoir, *i.e.* an environment with an infinite number of degrees of freedom. Specifically, the operator has three non-zero elements $\Gamma_{eg} \equiv \Gamma_{21} \equiv 1/\tau$ and $\Gamma_{ee} = \Gamma_{gg} \equiv \Gamma_{deph} \equiv 1/T_2'$, which are, respectively, the spontaneous emission rate associated with the transition $|e\rangle \rightarrow |g\rangle$, and the pure dephasing rate through which the TLS incoherently interacts with the environment, without undergoing a transition.
By assuming Markovian dephasing processes and using the rotating wave approximation, the steady-state elements of the density matrix can be inferred from Eq. 1.2, yielding the following solutions (solutions of the optical Bloch equations [87]):

$$\rho_{ee} = \frac{2\Gamma_2\Omega^2}{\Gamma_{21}(\Gamma_2^2 + (\Delta\omega)^2 + 4(\Gamma_2/\Gamma_{21})\Omega^2)}\,, \tag{1.4}$$

$$\rho_{ge} = -\frac{\Omega(i\Gamma_2 + \Delta\omega)}{\Gamma_2^2 + (\Delta\omega)^2 + 4(\Gamma_2/\Gamma_{21})\Omega^2)}\,, \tag{1.5}$$

$$\rho_{gg} = 1 - \rho_{ee}\,, \tag{1.6}$$

$$\rho_{eg} = \rho_{eg}^*\,. \tag{1.7}$$

We have here introduced $\Omega = \mathbf{d}\cdot\mathbf{E}/\hbar$, which denotes the Rabi frequency for the driving field amplitude at the emitter position ($\mathbf{E} =< \hat{\mathbf{E}} >$), which is the frequency of oscillations in the populations of the two levels $|g\rangle$ and $|e\rangle$ (as e.g. sketched in Fig. 1.1,

where coherent excitation of the TLS is assumed).
From Eq. 1.4 we can also define:

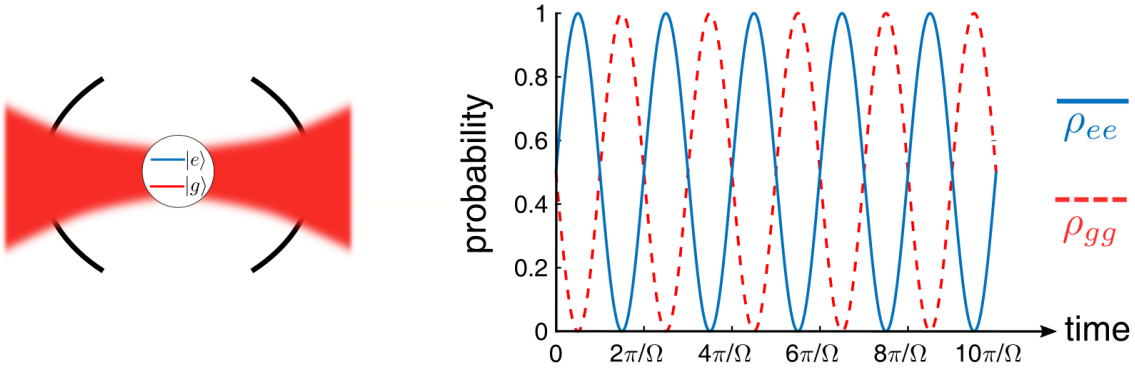

Figure 1.1: **Rabi Oscillation**. When a TLS is coherently coupled to the electromagnetic field (as e.g. in the strong coupling regime for an emitter coupled to a cavity mode - **left**) it will cyclically absorb photons and re-emit them. The resulting oscillations of the excited state and ground state populations (ρ_{ee} and ρ_{gg}, respectively) are known as Rabi oscillation - **right**.

- **the coherence damping rate** of the emitter (from Eq. 1.3), with

$$\Gamma_2 = \Gamma_{21}/2 + \Gamma_{deph}\,, \tag{1.8}$$

  which can be otherwise written as $1/T_2 = 1/(2\tau) + 1/T_2'$, with τ the excited state lifetime.

- **the transition linewidth broadening** (full width half maximum: FWHM)

$$\Delta\omega_{hom} = 2\Gamma_2 = \frac{1}{\tau} + \frac{2}{T_2'}\,, \tag{1.9}$$

  which for zero dephasing reduces to the so-called *life-time limited linewidth* $\Delta\omega_{nat} \equiv 1/\tau$.

- **the amplitude saturation** of the TLS-emission, when a continuous wave (CW) resonant laser is switched on at time $t = 0$, with the emitter initially in its ground state. In this situation, the system is driven to a steady-state $\frac{d\rho_{ee}}{dt} = 0$ in which spontaneous emission exactly compensates excitation, as follows from [88]:

$$\rho_{ee}(t) = \rho_{ee}(t \to \infty)[1 - e^{-(\Gamma_{12}+\Gamma_{21})t}]\,. \tag{1.10}$$

  In the expression, $\Gamma_{12} \equiv \Gamma_{12}(I,\Omega)$ is the absorption rate and is a linear function of the intensity I of the excitation laser, and $\rho_{ee}(t \to \infty) = \frac{\Gamma_{12}}{\Gamma_{12}+\Gamma_{21}}$ is the excited

steady-state occupation. For small excitation intensities, the population ρ_{ee} increases linearly with I. For increasing intensities, the slope decreases falling to zero in the limit of large intensities, at which the largest possible excitation is reached and yields $\rho_{ee} = \rho_{gg} = 1/2$.

- **the exponential decay and fluorescence intensity** of the TLS excited state, when the laser is suddenly turned off. The system decays exponentially into the ground state through spontaneous emission:

$$\rho_{ee}(t) = \frac{\Gamma_{12}}{\Gamma_{12} + \Gamma_{21}} e^{-t/\tau} . \tag{1.11}$$

Correspondingly, we can define the fluorescence intensity $R(t) = R(0)e^{-t/\tau}$. Here, R is the experimental observable, corresponding to the emitted photon rate. This can be defined as $\frac{dn}{dt} = \frac{d\rho_{ee}(t)}{dt} = \Gamma_{21}\rho_{ee}(t)$, and is hence proportional to $\rho_{ee}(t)$. Such a dynamics follows from the random nature of fluorescence emission. Statistically, only few times the emitter conveys its photons at precisely $t = \tau$, whereas 63% of them decay at shorter times and 37% decay at $t > \tau$ [89][1].

In this thesis work we will speak about single-photon streams obtained from CW-excitation, which we remark being different from Fock states. A method to trigger single-photon emission on demand can be based on off-resonant pulsed optical excitation, exploiting e.g. a vibrational level of the excited state to achieve population inversion. Once prepared in the excited state, the emitter decays generating a single photon on the time scale of the fluorescence lifetime, upon optimization of the laser source repetition rate and pulse duration [90, 91].

1.1.2 Key Features of Single-Photon Emission

In practice, the performance of a SPS can be evaluated by accounting for several parameters. The fundamental ones are described hereafter relying on the previously presented concepts, and the experimental methods to quantify them are briefly outlined.

Purity - Photon Statistics

The essential requirement for a reliable SPS is a negligible multi-photon probability within the excited state decay time τ. In this context, the statistics of the emitted

[1] Experimentally, these curves can be obtained from measurements of the time resolved photon arrival probability, by means of time-correlated single-photon counting (TCSPC) technique, described in Sec. 2.2.2.

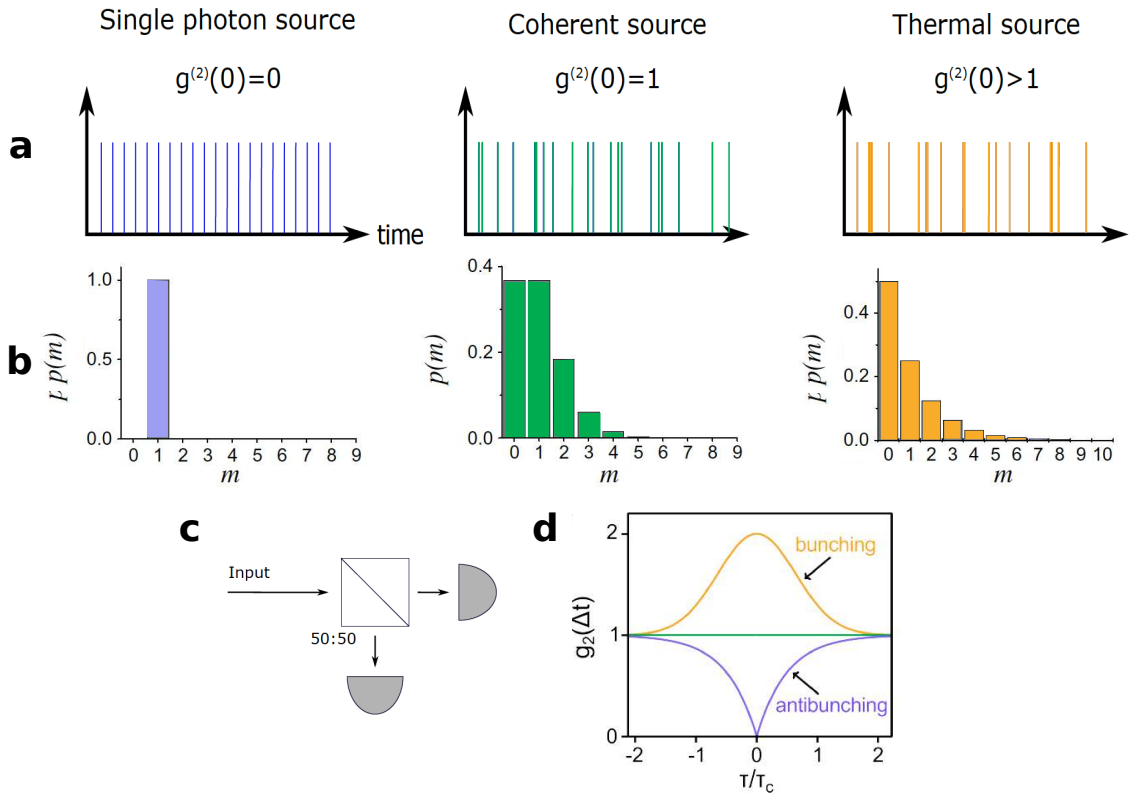

Figure 1.2: **Photon statistics**. Photon arrival time (**a**) and statistical distribution of photon numbers (**b**) for a deterministic single photon source (violet), a coherent source (green) and a thermal source (yellow), respectively. E.g. under pulsed excitation, an ideal single-photon source emits exactly one photon at a time with certainty. The emission from a coherent source follows a Poissonian statistics, as well as the distribution of photon number. Finally, a thermal source emission exhibits large intensity fluctuations at short time scales, leading to a so-called super-Poissonian distribution of photon numbers. **c** - A sketch of he Hanbury-Brown and Twiss setup. The imput photon stream is divided in two, and the histogram of coincidences between the two detectors at the outputs gives the distribution of pairs of consecutive photons. **d** - g^2-function for the three sources, showing antibunching, Poissonian flat correlations and bunching, respectively. The time scale is here normalized to the coherence time T_c.

light in a given state can be characterized by means of the second-order correlation function of the electric field. This can be expressed in terms of the number of clicks n in the detector as

$$g^{(2)}(\tau) = \frac{< n^*(t)n^*(t+\tau)n(t+\tau)n(t) >}{< n^*(t)n(t) >^2}, \tag{1.12}$$

which corresponds in the quantized picture to the probability of detecting a second photon at time $t+\tau$ after a first one is detected at t. Before introducing the emission

statistics of SPS, it is instructive to compare the solutions of Eq. 1.12 for more standard light sources (see Fig. 1.2).

A macroscopic source of light, e.g. a lamp, can be modeled as a an ensemble of many independent emitters (**thermal source**), and the emitted field is consequently a superposition of incoherent waves. Assuming the same time-dependence for each wave, and random phase and delay, the overall emission field is given by

$$\mathbf{n} = \sum_i e^{i\phi_i} \mathbf{n}_0(t - t_i)\,. \tag{1.13}$$

By feeding Eq. 1.13 in Eq. 1.12, the latter reduces to two series of terms, and the following relation holds

$$g^{(2)}(\tau) = 1 + [g^{(1)}(\tau)]^2\,,\ g^{(1)} = \frac{< n^*(t+\tau)n(t) >}{< n^*(t)n(t) >}\,, \tag{1.14}$$

where $g^{(1)}(\tau)$ is the first-order correlation function of the field. Since $g^{(1)}(0) = 1$, one obtains $g^{(2)}(0) = 2$, which accounts for the large intensity fluctuations deriving from the Bose–Einstein statistics of black-body radiation.

Differently, a **coherent source** of light, e.g. a laser source, is classically modeled as a wave with constant amplitude and phase. Consequently, $g^{(2)}(0) = 1$, which indicates no amplitude fluctuations. The quantum representation, written in the Fock states basis, yields

$$|\alpha\rangle = e^{-|\alpha|^2/2} \sum_n \frac{\alpha^n}{\sqrt{n!}} |n\rangle\ , \tag{1.15}$$

and corresponds to a Poissonian probability of finding a certain number of photons in a given time interval.

In contrast to a strongly attenuated laser beam where two photons can be separated by any delay owing to Poissonian statistics, in a TLS one photon is emitted for each excitation-relaxation cycle, requiring a certain delay. This phenomenon corresponds to a dip in the correlation function for zero time delay $g^{(2)}(0) = 0$ (called **anti-bunched**). Anti-bunching would be simple to detect by using an ideal detector with a dead-time smaller than the fluorescence life-time. Nevertheless, real photon-counting detectors have dead-time periods of blindness and also spurious counts can derive from the after-pulses owing to stray charges released upon the detecting avalanche. The practical way to eliminate these events is to split the photon-stream and use two detectors, in a Hanbury Brown and Twiss configuration (Fig. 1.2c, as

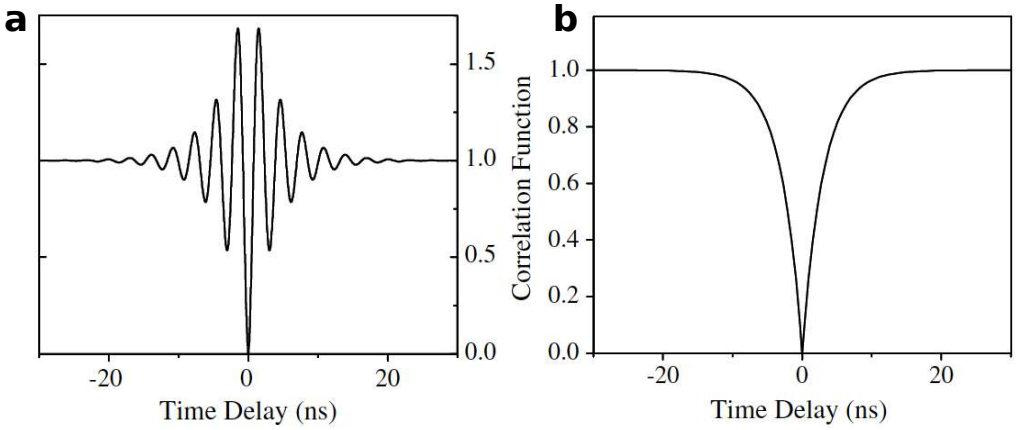

Figure 1.3: **Anti-bunched light**. Comparison of the anti-bunching dips in CW-excitation. **a** - Rabi oscillations appear for single-photon emitters at cryogenic temperatures, for long coherence times and strong resonant excitation intensities. **b** - For short coherence times, or off-resonant excitation, the correlation function tends to the unity at large Δt.

described in Sec. 2.2.2), respectively on the transmitted and on the reflected beam. Hence, a histogram of coincidences between the two detectors gives the distribution of pairs of consecutive photons. The $g^{(2)}(\tau)$ function gives instead the distribution of intervals for all pairs of photons, but the two are nearly equal for short time delays [92, 93, 28]. In Fig. 1.3, there are two examples of the output results for anti-bunched light of an emitter excited by a CW laser. For emitters at cryogenic conditions, for long coherence times and strong resonant excitation intensities, Rabi oscillations appear. Fig. 1.3b shows instead the anti-bunching dip for short coherence times, or off-resonant excitation, when the correlation function tends to the unity at large Δt. In general, while an ideal TLS emits by definition one and only one photon at a time, in practice, several experimental factors can lower the single-photon purity of the detected source's emission (i.e. an inefficient detection resolution, causing collection of the emission from two or more nearby sources, dark counts of the detectors [94], background photons [95], multi-photon processes in the emission). Therefore, not correcting for the spurious events affecting the measurement, it is commonly agreed that a $g^{(2)}(0) < 0.5$ is evidence for single-photon emission. This follows from the theoretical value of the second-order correlation function for $< n >= 2$ emitting single-photon sources, which yields $\mathrm{g}^{(2)}(0) = 1 - \frac{1}{<\mathrm{n}>} = 0.5$ [96].

Quantum efficiency

Another requirement for reliable SPSs is a quantum yield (or quantum efficiency) QY close to unity. This is the probability of radiative emission per excitation-cycle [97],

defined as:

$$QY = \frac{\Gamma_{rad}}{\Gamma_{21}}\,, \tag{1.16}$$

where $\Gamma_{21} = \Gamma_{rad} + \Gamma_{non-rad}$ here sums up to all possible decay channels, which for a complex emitter can be both radiative and non-radiative. Indeed, while an ideal TLS has $QY = 1$, in practice solid-state QEs might undergo a transition to an intermediate state from which decay to the ground state occurs non-radiatively or via emission of a "non-usable" photon. Consequently, the detection of fluorescence emission exhibits a temporary intermittence, which is named *blinking* (Fig. 1.4a). Moreover, in the case of fluorescent molecules, a permanent interruption of fluorescence can occur, due to quencher agents such as oxygen [98], a phenomenon called *photobleaching*. However, as discussed in the next chapter, for molecules embedded in a suitable matrix and at low temperature conditions, photobleaching can be excluded [99].

Experimentally, evaluation of the QY is not straightforward, but can be achieved by

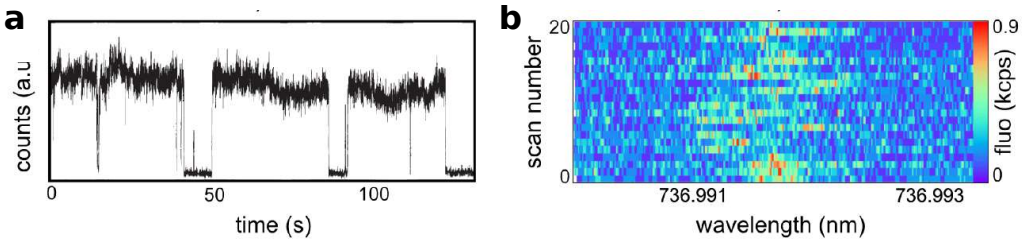

Figure 1.4: **a** - Blinking behaviour arises from the time trace of the emission intensity of a single CdSe quantum dot coated with a seven-monolayer-thick ZnS shell, in CW-excitation (Figure adapted from Ref. [100]). **b** - Resonant frequency scans around the excitation-line of an individual SiV-centre showing spectral diffusion (Figure adapted from Ref. [37]).

estimating all possible decay rates. While Γ_{21} is obtained with a lifetime measurement, by means of the time-correlated single-photon counting (TCSPC) technique for time-resolved photon arrival probability (see Sec. 2.2.2), information about the complete dynamics can be inferred by the study of the $g^{(2)}(\Delta t)$ at long time delays [101].

Maximum Fluorescence Intensity

The maximum rate R at which single photons can be emitted depends on the following parameters

$$R(I) = \frac{1}{\tau}\rho_{ee}(I)QY\,, \tag{1.17}$$

with ρ_{ee} being the expected occupation probability of the excited state and I the excitation intensity. At saturation conditions the emitted photon rate reaches the half of

its maximum value R_∞, according the following expression [102]:

$$R(I) = R_\infty(\frac{1}{1+I_s/I}), \tag{1.18}$$

with the saturation intensity I_s being indeed defined as $R(I_s) = 1/2R_\infty$. For resonant excitation, the maximum emitted rate is $R_\infty = 1/2\tau$, whereas $R_\infty = 1/\tau$ for off-resonant excitation, which enables a complete population inversion, e.g. via the excitation of a vibrational level of the electronic excited state. We remark that these assertions are valid for a CW excitation scheme, which is the one employed in the experiments of this thesis work. However, it is worth mentioning that pulsed resonant excitation is a crucial tool in quantum information technologies, used extensively for the initialization of quantum bits in various physical systems as e.g. trapped ions [103], quantum dots [104] , and superconducting quantum circuits [105]. Indeed, coherent manipulation between two energy levels can be achieved by applying optical excitations with so-called π-pulses, which result in an inversion of the two-level system with respect to its initial state, thus enabling full population of the excited state. In practice, this is typically accomplished with a pulsed-laser, by tuning it in resonance with the optical transition, and adjusting the pulse duration to $t = \pi/\Omega$, such to coherently drive the Rabi oscillation for half a cycle. Owing to the spectral overlap with the emitted single photons, polarization rather than spectral (see Sec. 2.2.2) filtering is used to suppress the laser background [106, 107], with a main drawback of reducing the single-photon collection efficiency of 50%. Recently, an alternative background-free method for coherent excitation was proposed and demonstrated using a phase-locked dichromatic electromagnetic field with no spectral overlap with the optical transition [108], suggesting promising perspectives for a future implementation of a resonant excitation scheme.

Indistinguishability - the Wave-Nature of Photons

This last characterization complements the particle-view of the single-photon stream of a QE by giving an evaluation of its wave-nature. This can be characterized by the absolute value of the first-order coherence $|g^{(1)}(\Delta t)|$, which can be usually experimentally quantified by the visibility in a single-photon interference measurement [96]. In particular, the parameter $|g^{(1)}(0)|^2$ is called *indistinguishability* of the single-photon stream, and is a number within zero and unity which characterizes the interference ability of the photons.
Indeed, many quantum-optics algorithms, e.g. in quantum computation and telecommunication, require effective photon–photon interactions to implement two-photon entangling quantum gates, where the state of one photon is determined by the state of a second one. This effective interaction can be implemented using the

quantum interference of two indistinguishable single-photon wavepackets, i.e. that cannot be distinguished from one another by any measurement. If we decompose the photon wavepackets as an ensemble of plane wave modes

$$|\psi\rangle = \sum_{k,p,n} c_{k,p} \, |n\rangle_{k,p} \ , \tag{1.19}$$

where each mode is associated to a defined polarization p and spatial frequency $k = \omega/c$ (with c the speed of light), and $|n\rangle_{k,p} = |1\rangle_{k,p}$ for single photon states, indistinguishability is achieved when each wavepacket is a pure quantum state with defined complex coefficients $c_{k,p,n}$. Experimentally, this can be measured in a Hong-Ou-Mandel (HOM) experiment [109], where single-photon wavepackets successively generated by the same emitter are temporally overlapped on a $50/50$ beamsplitter. If they are in the same pure quantum state they exit together at either one of the two output ports, a phenomenon named *quantum coalescence*. This effect is a consequence of the Bose-Einstein statistics of the single-photons and essentially of a destructive interference effect which deletes the two possibilities of separate outputs. In practice, assuring that the photon wavepackets share the same spatial mode can be achieved by coupling the photons to an optical fibre or by placing the emitter at the focus of a parabolic mirror. We consider for simplicity the latter case, since allows a decomposition into co-linear plane-waves and the single-photon state can be written as

$$|\psi\rangle = \sum_{\omega} c_{\omega} \, |1\rangle_{\omega,p} \ , \tag{1.20}$$

with the coefficients depending only on the frequency ω, the wavevectors $|\psi\rangle$ being collinear, and

$$\mathbf{k} = \frac{\omega}{c}\mathbf{u} \, , \quad \sum_{\omega} |c_{\omega}|^2 = 1 \, , \tag{1.21}$$

being $\mathbf{u}$ a unitary vector. Quantum interference occurs when all the c_{ω} are equal for all photon wavepackets [110]. While for an ideal TLS this is always true, the coupling of the exciton to the solid-state environment can lead to pure dephasing, resulting in a partial mixture of the state [111]. In this sense, indistinguishability is characterized by the mean photon wavepacket overlap in the HOM experiment, which is equivalent to [112, 113]

$$M = \frac{T_2}{2\tau} \, , \tag{1.22}$$

and corresponds to perfect indistinguishability for $M = 1$. Hence, an essential requirement, and indirect measurement, for single-photon indistinguishability is a Fourier-limited spectrum (with $\Delta\omega_{hom} = 1/\tau$, as follows from Eq. 1.9).
In practice, in the HOM experiment the two-photon interference visibility is normal-

ized by the case of maximal distinguishability, obtained by varying a degree of freedom of one of the photons, commonly the polarization, and cancelling the quantum interference effect. The mean photon wavepacket overlap M, which corresponds to the joint first order coherence $|g^{(1)}(0)|^2$, can hence be determined by

$$M = \frac{g_{\parallel}^{(2)}(0) - g_{\perp}^{(2)}(0)}{g_{\parallel}^{(2)}(0) + g_{\perp}^{(2)}(0)}, \tag{1.23}$$

where $g_{\parallel}^{(2)}(0)$ stands for the second-order coincidence counts at zero time delay for indistinguishable photon states (e.g. parallel polarizations), while the $\perp$ subscript indicates distinguishable photon states (e.g. orthogonal polarizations).

Experimentally, an efficient route to indistinguishability is working at cryogenic temperature, where coupling to vibrational levels is reduced and the purely electronic main transition between the ground and excited state (the zero-phonon line ZPL) can achieve its natural-linewidth. Additionally, coupling the ZPL to a cavity would enable to suppress the higher phononic modes, which contain incoherent not-indistinguishable photons. However, for indistinguishability, the ZPL stability is also crucial. Indeed local changes of the electrostatic environment of the emitter can cause spectral-diffusion, i.e. slow fluctuations of the emission frequency which exhibits drifts or jumps and compromise the possibility of interference. This damaging contribution can be evaluated at cryogenic temperature by recording the excitation spectrum repeatedly in time, and by comparison with the Fourier-limited expression (see Eq. 1.9).

In summary, a reliable single-photon emitter must convey pure and indistinguishable single-photons on demand, with high rates in a useful photonic mode. Up to date, unifying all this properties within a single quantum emitter is still a challenge. Therefore, the most suitable SPS is to be chosen accordingly to the foreseen application.

1.1.3 State-of-the-Art Single Photon Sources (SPS)

In this section we briefly discuss the principle of operation and main properties of solid-state SPS in the quantum-optics field. For more details, and for a description of further existent SPS, Ref. [29, 114] can be consulted.

here we argue that QEs are the most promising, etc..., through a comparison with other leading SPS technologies, SPDC and trapped atom/ions

Here we argue that solid-state QEs are the most promising systems for operative applications, through a comparison with other leading SPS technologies, macroscopic sources and atom/ions in the gas-phase. Macroscopic SPSs comprehend faint laser pulses and parametric sources of entangled pairs. The former are obtained by using a standard pulsed laser and calibrated attenuators. The latter by e.g. spontaneous parametric down-conversion (SPDC) in non-centrosymmetric crystals such as KDP, BBO, LBO or $LiNbO_3$. In SPDC, non-linear interaction of a pump laser pulse with the crystal occasionally splits one high frequency pump photon into two lower-frequency signal and idler photons [115]. The frequencies and wavevectors of the three photons satisfy the energy conservation and phase-matching conditions, and in general, the two output photons exit in non-collinear direction. This allows heralding the single-photon generation by measuring one of the two, which gives the trigger signal for the single-photon experiment. However, parametric sources, as well as faint laser light, deliver Poissonian-distributed photons (or photon-pairs), from which multi-photon events can never be completely suppressed. In the case of SPDC, the photon-pair creation process is extremely inefficient ($\sim 10^{-4}$), and the output signal is inevitably a trade-off between high emission rates and low multi-photon probability. Nevertheless, compared to quantum emitters, SPDC is much easier to operate and this is the reason why it is currently widely used in advanced quantum technology experiments [116, 117, 118]. Indeed, key advantages comprehend room temperature operation and straightforward optical setups, based on common laser sources and non-linear optical media, both commercially available products. Nevertheless, for applications in e.g. quantum cryptography or all-optical quantum computing, where high multi-photon states rates are required to scale up to large quantum optical systems, the probabilistic nature of SPDC becomes a crucial limiting factor. On the contrary QE SPSs, even if require technically demanding fabrication processes, they can in principle convey single photons with high purity and with rates that are limited only by the radiative lifetime (provided one can prepare the TLS with 100% probability into the excited state each time it gets excited).

On the other side, the big advantage of atoms, over all solid-state emitters, is that their states are perfectly reproducible and well-known, they are very stable under laser-illumination and do not present long-lived dark states [119, 120, 121]. They convey single-photons with high QY and life-time limited. However, their main drawback is in isolation of the individual atom, manipulation and trapping, which require expensive setups, long preparation times and ultra-high vacuum conditions. Furthermore, the operation time is limited to few seconds for a cold atom in a trap, owing to the dwell time in the cavity mode.

All considered, the great potential of QEs in the solid-state is the optimal compromise

between the reliability of single-photon emission, as following the definitions in Sec. 1.1.2, and the ease of manipulation, which is necessary to any operative application. In the following, some of the more promising solid-state QE SPS will be introduced and compared, highlighting the fundamental advantages and drawbacks of each system.

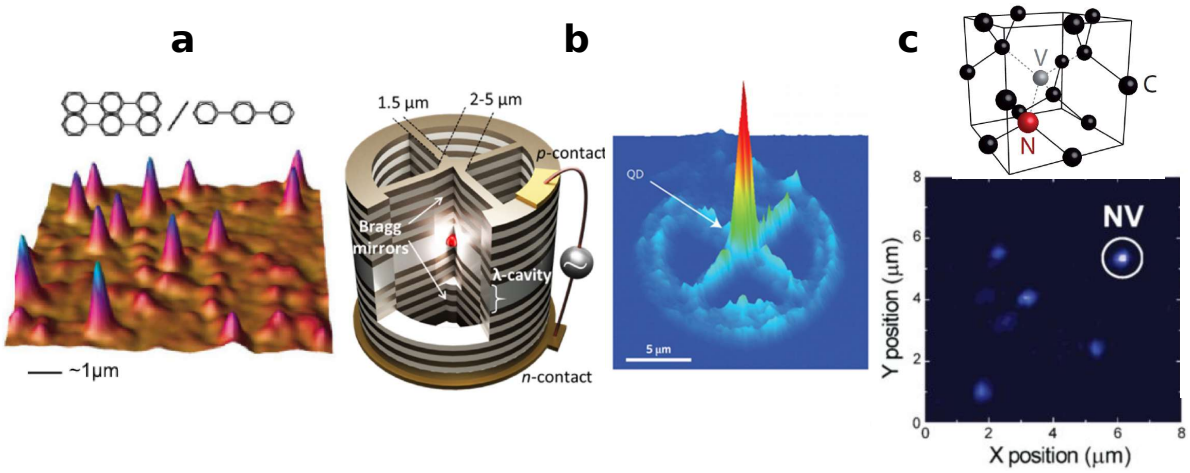

Figure 1.5: **Examples of SPSs**. **a** - Fluorescence microscopy image of single terrylene molecules in a p-terphenyl crystal at room temperature (Figure adapted from Ref. [28]). **b** - Concept of the micropillar cavity embedding an InGaAs QD layer and surrounded by GaAs/AlGaAs distributed Bragg reflectors (left). Photoluminescence map showing the bright emission from the coupled QD at the centre of the device. (Figures adapted from Ref. [106]). **c** - Atomic structure of an NV center in diamond (top). Fluorescence map of NV centers in a diamond sample (bottom; Figure adapted from Ref. [122]).

Individual Organic Molecules

Single-fluorescent molecules have the evident advantage, compared to the other solid-state emitters, of being nominally all identical (with differences only due to local environment effects), truly nanometric systems, and very easy to fabricate, relying on well-established chemical methods. The main drawback, is their lack of stability when embedded in aqueous solutions or in polymer, or when simply dispersed on a substrate, where blinking and photobleaching strongly compromise their brightness. However, when embedded in crystalline matrices, which protect from quencher agents (as oxygen), organic molecules can exhibit excellent photostability, both at room and cryogenic temperatures. It is worth-noting that organic molecules were the first condensed matter system for which antibunching was demonstrated [123].
Differently from atoms, the eigenstates of molecules in condensed matter involve vibarations and phonons, besides the purely electronic states. Therefore at room temperature the transition is very broad. However, when cooled down to cryogenic

temperatures, dephasing of the transition due to interactions with the phonons of the matrix vanishes and the ZPL becomes extremely narrow [124], approaching lifetime-limited values of the order of 10 MHz.
In order to obtain the best performance in terms of single-photon emission, a suitable choice of both the guest emitter and the host matrix is essential. The most stable guest impurity molecules have been selected exclusively from the class of rigid conjugated polycyclic aromatic hydrocarbons (PAHs) (e.g. terrylene molecules in a p-terphenyl crystal [28] are shown in Fig. 1.5a). Common hosts are organic crystals, such as naphtalene and anthracene, in which the guest molecules are primarily embedded at well-defined insertion sites. The molecular emission is here particularly stable with narrow 00- ZPLs, limited only by the excited state lifetime. A complete review of the most used dyes, hosts and their properties can be found in Ref. [125]. Since organic molecules are the designated SPS for this work, a deeper analysis is to be found in Chapter 2.

Self-Assembled Quantum Dots

A self-assembled quantum dot (QD) consists of nanoscale islands of a lower band gap semiconductor embedded in higher band gap semiconductor (e.g. gallium arsenide (GaAs) in aluminium gallium arsenide (AlGaAs)), grown epitaxially on single-crystalline substrates from molecular beams and/or reactive gases, by chemical vapour deposition. The band offset gives rise to a 3D-confinement of electrons and holes, initially present in the valence band and in the conduction band, respectively. By optical or electrical excitation, electron-hole pairs are formed which quickly non-radiatively decay into the QD excited state, forming an exciton bound state. Consequently, a single-photon is emitted following the radiative recombination channel. A typical drawback, is that the high refraction index of the embedding semiconductor strongly limits the photon extraction efficiency via total internal reflection events, requiring a variety of possible developed solutions. Among them, up to date, self-assembled InAs/GaAs QDs in pillar cavities exhibits the highest performance as SPSs, in terms of purity and indistinguishability [106, 107] (Fig. 1.5b). In general, the fabrication process, which is standard in the semiconductor industry, facilitates the integration of QDs in embedding structures, but is intrinsically limited to 2D designs. In terms of photophysical properties, spectral diffusion due to charge noise has been effectively reduced via electrical bias and other mitigation techniques [126, 127, 128, 129, 107], and blinking, which is particularly pronounced in single nanocrystal QDs [130, 131, 132], in epitaxial QDs is mostly reported in poor quality samples [133] and for QDs in proximity to defects and etched surfaces [134]. Furthermore, the possible presence of multiple excitation lines in QDots has been exploited in the last years to realize triggered sources of entangled photon-pairs through biexci-

ton–exciton cascaded radiative processes [135, 136, 137], recently achieving remarkable results in terms of purity and brightness [138]. Instead, a bigger disadvantage of QDs over e.g. molecules, which on the contrary are nominally all identical, is the lack of control over the emission spectral properties. Indeed, the ensemble inhomegeneous broadening is huge (typically tens of meV compared to the homogeneous linewidth of μeV [139]), and typically the identification of the many different transitions of even a single quantum dot is a challenging task. For the former issue, big effort is consequently required for the efficient implementation of wide spectral tuning of QDs emitters [139].
More in general, non-classical emission of light form QDs has been demonstrated [140], even at room temperature [141]. At cryogenic temperatures, the emission line is close to the natural width. For more information on QDs as SPSs refer to [32, 20, 142].

Colour Centers in Diamond

Point defects and vacancies in wide band-gap inorganic semiconductor crystals often give rise to color centres with very strong absorption and fluorescence bands. A great advantage brought by the inorganic matrix is high photostability and mechanical rigidity, especially in the case of diamond. Nitrogen-vacancy (NV) centres in diamonds (Fig. 1.5c) were the first single colour centre ever detected [143] and proved to exhibit single-photon emission by means of antibunching measurements [144, 95]. The ZPL around 637 nm is visible even at room temperature, however the lifetime-limited emission is strongly affected by spectral diffusion because of the influence of the matrix [145]. The main drawback, is the poor branching ratio into the ZPL even at low temperatures (~ 0.04). Owing to the diamond high refractive index, extraction of fluorescence light is rather difficult, however nano-structuring of the matrix [145] can improve collection efficiency. The great advantage for quantum communication and computing schemes, is rather the presence of a spin in the ground state [146]. Indeed, recent experimental spin-photon entanglement demonstrations have highlighted the potential of NV centres as key candidates for quantum registers in quantum network realizations [147].
Recently, among the many explored colour centers, Silicon (SiV) and Tin (SnV) vacancies defects have emerged as promising SPS. The ZPL of SiV centres in diamonds is narrow and very intense (Debye-Waller factor 0.8; see Sec. 2.1.2) and, being at 738 nm, it falls in a region where background fluorescence from diamond is low. Single-photon emission and Hong-Ou-Mandel interference has also been demonstrated [148, 149], nevertheless the typically low brightness is the main drawback for SiV centers. A higher fluorescence intensity has been shown from SnV centers (besides still lower than quantum dots and organic molecules), which also exhibit a narrow and intense

ZPL, and for which a good single-photon purity has been demonstrated [150, 151]. One general shortcoming of point-defects in diamond for photonic quantum technologies regards the nano-structuring of the bulk matrix, which brings essential advantages of nano-positioning and enhanced coupling to photonic structures, but typically leads to spectral instability of the exciton line and intermittence of the emission [37, 152, 153].

1.2 Photon Collection Strategies

In the last decades, much experimental effort has been put into optimizing and identifying potential SPSs with near-ideal performances. However, for practical application, and especially in the perspective of a compact and operational quantum-photonic device, a further fundamental parameter to take into account is the coupling efficiency between the quantum emitter and a useful mode of the electromagnetic field. Indeed, besides the intrinsic QY and brightness of the SPS, efficient excitation, collection and manipulation are essential for an effective deployment of the single-photon stream in quantum algorithms. The coupling between a laser-excitation photon and an emitter approximately depends on the overlap between the radiation and the emitter cross section, which in a homogeneous medium is in general rather poor, owing to their significant size mismatch. In particular, collection efficiency is typically bound to few percent due to the approximately isotropic source emission and the limited collection. This is why in general it is convenient to generate a single photon into a precise single optical mode (e.g. that of an optical fiber) rather than a multimode single photon. The strategy to manipulate the modes into which emission may take place, as well as its directionality and rate, consists in modifying and engineering the local photonic nano-environment.

1.2.1 Waveguides

Coupling the emitter to waveguides is a fundamental step towards on-chip generation, routing and detection, as well as off-chip connection [154, 155], by enabling to directly channel the emission into confined propagating modes, and consequently increasing the single-photon coupling efficiency to a useful mode. In general, in a dielectric waveguide (WG) the electromagnetic radiation can be confined in two dimensions (xy) and guided along the third dimension (z). Owing to the WG xy-dimensions of the order of λ and to the high refractive index contrast between the structure (higher n) and the surroundings (cladding), this can be classically explained in terms of total internal reflection (see e.g. the simplest case of a ridge WG in Fig.

1.6b). Different examples of guiding structures, here not discussed, are slot WGs and photonic crystal WGs [156, 157]. In the following we briefly present the key concepts of propagation into a guiding structure and the two figures of merit to quantify the coupling between a QE and the WG.

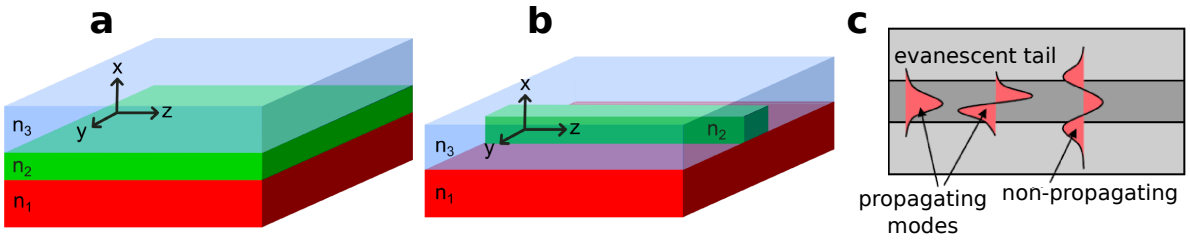

Figure 1.6: **a** - Planar dielectric slab ($n_2 > n_1; n_3$, with n refractive index) leading to light-confinement in the x-direction. **b** - Ridge waveguide; light is confined in both the x- and y-direction. **c** - Sketch of electromagnetic field modes in the core-cladding WG structure. For propagating modes the field intensity peak is within the WG core, whereas evanescent tails extend to the cladding material.

The solution of guided modes into a rectangular WG are achieved in this thesis work through numerical methods. As a preliminary analysis for the study of propagation into a rectangular WG (Fig. 1.6b), we first consider three semi-infinite layers (as displayed in Fig. 1.6a) with refractive indexes $n_2 > n_1; n_3$ to ensure guiding in the intermediate layer by total internal reflection [158], i.e. a slab. We will introduce confinement in the y-direction later. Accounting for continuity conditions on the electric and magnetic fields at the dielectric interfaces, and for the wave conditions at infinity, propagating light waves with frequency ω are found by simply solving Maxwell's equations, in absence of any source. Assuming homogeneous layers, the solutions for the electric and magnetic optical modes are hence $\mathbf{E}(\mathbf{r},t) = \mathbf{E}(x)e^{i(\beta z-\omega t)}$ and $\mathbf{B}(\mathbf{r},t) = \mathbf{B}(x)e^{i(\beta z-\omega t)}$. Here β, is a complex constant accounting for possible absorption and scattering losses, and the solely x-dependence in the expressions is consequent to the infinite y- and z-direction (see Fig. 1.6a). For a given refractive index profile there are in general infinite eigenvalues β, and corresponding infinite eigenvector modes. However, only a discrete number, which is limited in the range $n_3\omega/c \leq \beta_m \leq n_2\omega/c$ with $m\,(=0,1,2,3,...)$, are guided [158]. Each guided mode m is then characterized by an effective refractive index $n_{eff} = \beta_m/k_0$ and a consequent effective phase velocity of the guided light $v_f = c/n_{eff}$. In a wave-optics view, the vector fields $\mathbf{E}_m(x)$ and $\mathbf{B}_m(x)$, with m number of nodes, describe the distributions of the electromagnetic field in the transverse x-direction, which is sinusoidal inside the WG and decay exponentially in the cladding layers (Fig. 1.6c). Guided modes can show different directions of polarization and are generally grouped into TE (Transverse Electric) and TM (Transverse Magnetic). For the fundamental TE mode ($m = 0$), for small ω, the wavelength is larger than the core size and the mode spreads into the

cladding material.
At a fixed frequency ω, the number of modes supported by the structure is related to the thickness t of the waveguiding layer and on the refractive indices of the materials [159].

In order to quantify the coupling of a QE to the WG structure the fundamental figures of merit to be considered are emission enhancement and couling efficiency. The emission enhancement α is defined as

$$\alpha = \frac{\Gamma_{WG}}{\Gamma_{hom}}, \tag{1.24}$$

with Γ_{WG} the emission rate into a waveguide mode and Γ_{hom} as defined in Eq. 1.32. This parameter accounts for the modification of the emitter decay rate owing to the photonic structure (see Purcell factor - Eq. 1.33), which is however very small in the case of ridge WGs but can be important for other structures (e.g. for cavities). On the other side, the ratio of photons coupled into the waveguide is quantified by the waveguide-to-dipole coupling efficiency, namely the β-factor:

$$\beta = \frac{\Gamma_{WG}}{\Gamma_{tot}} \tag{1.25}$$

representing the probability of a photon being emitted into a guided mode, with $\Gamma_{tot} = \Gamma_{rad} + \Gamma_{WG}$.

We consider now the rectangular WG as in Fig. 1.6b, defined by a refractive index distribution $n(x,y)$ which confines light in two dimensions (x and y). For sake of simplicity, the WG is assumed to be single-mode, i.e. only one guided field distribution $\mathbf{E}(x,y)$ exists. Γ_{WG} can be calculated from the Fermi's golden rule (Eq. 1.31), and the quantization volume V for the considered guided mode is given by the product of a quantization length L and the effective mode area, which is defined as [160]:

$$A_{eff}(\mathbf{r}_0) = \frac{\int\int n^2(x,y|\mathbf{E}(x,y)|^2 dxdy)}{n^2(\mathbf{r}_0)|\mathbf{E}_{\parallel}(\mathbf{r}_0)|^2}. \tag{1.26}$$

Here, $\mathbf{E}_{\parallel}(\mathbf{r}_0)$ is the electric field component parallel to the dipole at the position of the emitter $\mathbf{r}_0$. The effective mode area represents a measure of the mode field concentration at the dipole position, or in other words the overlap between the guided mode and the dipole emission pattern. In particular, from the resulting expressions for the

LDOS and guided emission rate, which yield respectively [161]

$$D(\omega) = \frac{L}{2\pi v_g(\omega)}\,, \quad \Gamma_{WG} = \frac{\omega}{2\hbar n^2 \epsilon_0 A_{eff} v_g} |\mathbf{d}|^2 < \hat{\mathbf{d}} \cdot \hat{\mathbf{p}} >^2\,, \tag{1.27}$$

(with v_g the group velocity of the guided mode), we can derive the possible strategies to maximize the emission rate into the guided mode. These include shrinking the effective mode area A_{eff} and reducing the group velocity (i.e. increasing the interaction time between the emitter and photon).
In particular, using dielectric WGs, rather than the excited lifetime of the QE, which is not relevantly affected by the presence of the structure, the optimization primarly regards the maximization of the β-factor. This can be achieved by means of 3D numerical simulations, according to the equivalence [162, 160] $\Gamma_{WG}/\Gamma_{tot} = P_{WG}/P_{tot}$, where P stands for the classical dipole radiated power.

In this context of rectangular dielectric WGs, the practical experimental approach to maximize the QE-WG coupling efficiency, consists in placing the emitter in the vicinity of the WG-cladding interface (that is usually between the dielectric material and air) and by exploiting the evanescent tail of the guided mode which extends at the outside of the WG-core (as in Fig. 1.6c). Consequently, the waveguide geometrical parameters are optimized for the best compromise between intensity of the evanescent field at the emitter position (Eq. 1.27), and guiding efficiency. However, despite the level of optimization achievable via nano-fabrication, this operational scheme based on evanescent coupling has an intrinsic limit. Indeed, the guided field intensity at the emitter position $|\mathbf{E}_{\parallel}(\mathbf{r}_0)|^2$ will always be much lower than the maximum of the field mode intensity, as it is in the core of the WG structure. Hence, following from Eq. 1.27, the theoretical value for the β-factor can not go much further than $\sim 50\%$ (in this merit see the related paper of the group at Ref. [60], on the coupling between a molecular SPS and a WG in silicon nitride).
Therefore, in this thesis work we opt for a second possible approach, which is based on the direct coupling of the SPS to the maximum intensity of the guided field. The difficulty in this case, is that the emitter must be embedded right within the WG photonic structure. This is a challenge both in terms of materials and fabrication technique, as well as for the consequences that the overall fabrication process might have on the emitter photophysical properties (as discussed in Sec. 1.1.2). Our solution to the problem is presented in detail in Chapter 4, whereas information on the numerical simulations used for the geometry optimization are found also in Appendix A.

1.2.2 Solid Immersion Lenses

A different strategy to enhance collection efficiency is to compensate for the limited numerical aperture of the collection optics by using a solid immersion lens (SIL). The general principle consists in reducing the index contrast between the emitter matrix, or the substrate on which is deposited, and the proximate surroundings, usually air, by applying a high refractive index dielectric material. Hence, by structuring the external interface into a highly curved profile (the lens), the emission can be refracted towards smaller collection angles. Differently from cavity quantum electrodynamics approaches, the collection enhancement is here a simple consequence to geometrical optics principles, and typical dimensions span the μm-mm scale. In practice, a standard SIL consists of a truncated sphere of high refractive index forming a plano-convex lens of short focal length, and can be typically bought commercially or manufactured by polishing a small glass sphere.
Solid immersion microscopy was invented by Mansfield and Kino in 1990 [163] and since then its simple and effective approach brought to an increasing interest, especially in quantum nanophotonics. SILs can be an effective solution to extract light from emitters naturally embedded in high-index bulk materials (e.g. QDots, colour centers in diamond), thus avoiding losses due to total internal reflection. In this case, the SIL geometry is directly carved into the native material of the emitter host matrix. More in general, SILs can efficiently funnel the dipole-emission into narrow angles compatible also with low numerical aperture (NA) objectives, where $\mathrm{NA} = \mathrm{n}\sin(\theta_{\mathrm{NA}})$, with n the refractive index between the sample and the objective, and θ_{NA} half the planar angle of the maximum acceptance cone of the objective.
Let's consider an emitter modeled as a small dipole inside the substrate matrix and

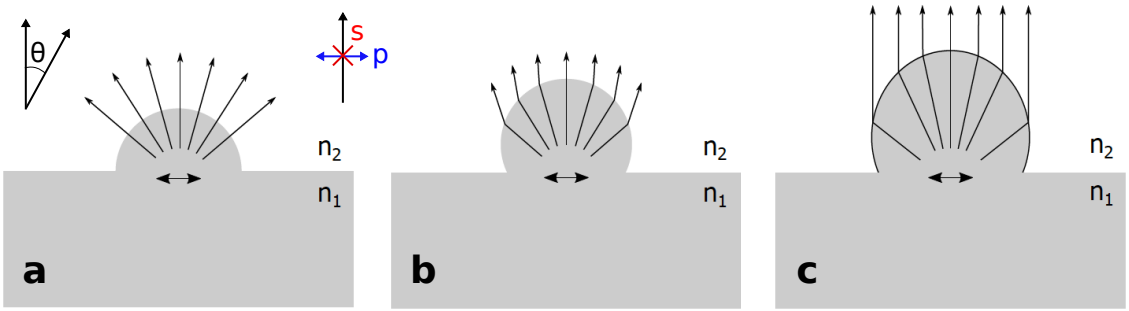

Figure 1.7: **Solid immersion lenses**. Concepts of a standard hemispherical SIL (**a**), a Weierstrass SIL (**b**), and an elliptical e-SIL (**c**). The parallel/orthogonal (p/s) polarization of the emitted light, the azimuth angle θ of its propagation direction, and the refractive indexes of the SILs material and of the surrounding are respectively indicated.

oriented parallel to the substrate surface in the x-direction (Fig. 1.7), in absence of a SIL. By assuming that the distance between the emitter and the surface interface

is large enough to neglect evanescent components, the total collection efficiency η is given by the proportion of light transmitted through the interface into air and collected by the objective [164]:

$$\eta^{s,p} = \int_0^{2\pi} \int_0^{\theta_{NA}} I^{s,p}(\theta,\phi)T(\theta,\phi)sin(\theta)d\theta d\phi\,, \tag{1.28}$$

where θ and ϕ are the emission angle and the azimuthal angle measured from the x-axis (as in Fig. 1.7), respectively, and s/p stand for the normal/parallel polarizations. $T(\theta,\phi)$ is the transmittivity through the interface (which can be considerably lower than 1 in the case of emitters buried in a bulk material, due to total internal reflection), and $I(\theta,\phi)$ is the normalised emission intensity, that for a single dipole in a bulk material can be expressed as [165]:

$$I^s(\theta,\phi) \propto \frac{3}{8\pi}[1 - sin^2(\theta)cos^2(\phi)]sin^2(\phi)\,, \tag{1.29}$$

$$I^p(\theta,\phi) \propto \frac{3}{8\pi}[1 - sin^2(\theta)cos^2(\phi)]cos^2(\phi)\,. \tag{1.30}$$

Considering the example of an emitter buried in a bulk material with $n_1 = 3.5$, and $n_2 = 1$, under an ordinary microscope objective with e.g. $NA = 0.8$, collection efficiency would be limited to few percents [166]. The situation is improved if a hemispherical SIL (Fig. 1.7a) is centered directly over the emitter, which translates in a modification of the term $I(\theta,\phi)T(\theta,\phi)$ in Eq. 1.29. With this scheme, total internal reflection is avoided because of the emitted light impinging perpendicularly to the interface and collection has been predicted to improve of about 6-times [166]. In the different case of a stand-alone SIL placed at the top of the emitter, the enhancement in the collection efficiency primarily depends on the refractive index difference between the SIL material and the substrate. In practice, the potential of a SIL can be further improved by simply employing a reflective substrate, thus avoiding radiation in the lower hemisphere.
Besides the hemispherical SIL design, other geometries are possible. In Fig. 1.7b and 1.7c the Weierstrass SIL and the elliptical SIL (eSIL) are shown, respectively [165, 166, 167]. The Weierstrass geometry has a height of $(1 + 1/n_2)r$, with n_2 the refractive index of the SIL and r its radius of curvature. With an overall subtended angle $> 2\pi$, hence larger than the hemisphere, the light emitted by a source in the focus of the SIL is now incident obliquely upon the curved interface (Fig. 1.7b). Therefore, transmission takes place at smaller angles owing to refraction, and for a fixed objective NA, the collection efficiency is higher compared to the hemispherical SIL. A 12-times increase in the collection compared with a planar surface has been predicted for a $n = 1.88$ Weierstrass SIL in combination with a low numerical aperture lens [166].

With an eSIL, collection efficiency can be further improved, owing to the collimating effect at the interface, compared to the resulting divergent transmission of the previous examples (Fig. 1.7a,b). In the work by Schell et. al. [167], a comparison based on numerical methods was made among all the three SIL cases, yielding an expected collection efficiency as high as 65% with an eSIL and an objective NA of 0.3 . However, as it will be discussed in Chapter 2, the drawback of this geometry is a higher sensitivity to fabrication imperfections.
In general, there have been successful attempts to use SILs in combination with NV centres in diamond [164, 168, 169], to increase photon extraction from the high refractive index of the matrix ($n = 2.4$).
By placing commercially available ZrO_2 SILs directly on the top of the emitter [163], efficient excitation and detection of single dye molecules have been demonstrated [91, 170]. Moreover, enhanced count rates were reported from small diamond nanocrystals containing individual NV centres [168].

1.2.3 Cavities

A useful method to achieve high collection and enhanced emission rate in a well-defined mode is by coupling the emitter to a cavity. The working principle is better understood by recalling *Fermi's Golden rule*, a fundamental result of light-matter interaction in first order time-dependent perturbation theory (valid for weak light-matter interaction). This expression describes the transition rate between an initial and final state of a quantum system, which is given by[2] [171]:

$$\Gamma_{i\to f} = 2\pi|g(\mathbf{r},\omega)|^2 D(\omega) = \frac{\pi\omega}{\epsilon\hbar}(\hat{\mathbf{d}}\cdot\hat{\mathbf{p}})|\mathbf{d}|^2\frac{D(\omega)}{V}\,,\quad g(\mathbf{r},\omega) = \sqrt{\frac{\omega}{2\epsilon\hbar V}}|\mathbf{d}|(\hat{\mathbf{d}}\cdot\hat{\mathbf{p}})| \tag{1.31}$$

Here, $g(\mathbf{r},\omega)$ is the TLS-field coupling strength, depending on the dielectric permittivity of the surrounding material ϵ, on the quantization volume of the electromagnetic field V, on the angle between the transition dipole and the electric field polarization $\mathbf{p}$, and assuming zero detuning $\Delta\omega = \omega_P - \omega_A = 0$ (Sec. 1.1.1). Then, $D(\omega) = \frac{1}{\hbar}\frac{dN}{d\omega}$ is the photonic density of the final states, namely the number of photonic states N with energy $\hbar\omega$, which owes to the specific nano-environment of the emitter and is known as local density of states (LDOS). Fermi's golden rule enables to calculate the spontaneous emission rate of an atom-like emitter when embedded both in an homogeneous medium with refractive index n and in a non-uniform environment, e.g. in a photonic structure. Hence, in a homogeneous medium, for the spontaneous

[2] It can be interpreted as a statement of energy conservation.

emission rate Eq. 1.31 yields [172]

$$\Gamma_{12}^{hom} = \frac{n\omega^3}{3\pi\hbar\epsilon c^3}|\mathbf{d}|^2\,, \tag{1.32}$$

which is solely dependent by the intrinsic initial and final states of the emitter (and by the medium refractive index), and describes a dipole-like electromagnetic field pattern. If instead the emitter is placed nearby interfaces, the field pattern and decay rate consequently modify. Purcell was the first to point out the possibility of engineering the LDOS, and calculated the difference between the rate in vacuum Γ_0 and in a resonant circuit, i.e. a cavity, as follows:

$$F_P = \frac{\Gamma_{cav}}{\Gamma_0} = \frac{3}{4\pi^2}(\frac{\lambda}{n})^3\frac{Q}{V}\,, \tag{1.33}$$

which is known as *Purcell factor*, with λ the emission wavelength, and Q and V the quality factor and the mode volume of the cavity, respectively. In particular, here we assume perfect alignment between the emitter transition dipole and the electric field polarization. This result triggered the development of micro-fabrication techniques to enhance or suppress spontaneous emission of emitters and to tailor their emission pattern in a well-defined mode, by coupling to photonic structures such as single mirrors [173], planar or spherical cavities [174, 175, 176], optical and plasmonic antennas [177].

The spacial confinement provided by the cavity structure alters the local electromagnetic boundary conditions and consequently modifies the density of available states in the close vicinity of the emitter. Hence, following from Eq. 1.33, its spontaneous emission rate can be conveniently enhanced (or suppressed).

A simple cavity consists in two highly reflective surfaces, which can be metallic or distributed Bragg reflectors (DBR), or a hybrid combination of the two (see Fig. 1.8a). A photon in the cavity is reflected on the two mirrors several times before being dispersed, and the number of reflections are related to a fundamental figure of merit, namely the quality factor Q of the cavity. This can be defined as the ratio between the cavity resonance frequency f_r and its FWHM Δf, i.e. the frequency bandwith:

$$Q = \frac{f_r}{\Delta f}\,. \tag{1.34}$$

In particular, cavity resonance occurs when the reflected fields are respectively in phase, so that they constructively interfere. By placing an emitter inside a resonant cavity the generated photon will be reflected back and drive a successive excitation, in a continuous cycle. The coupling parameter g of this interaction can be expressed

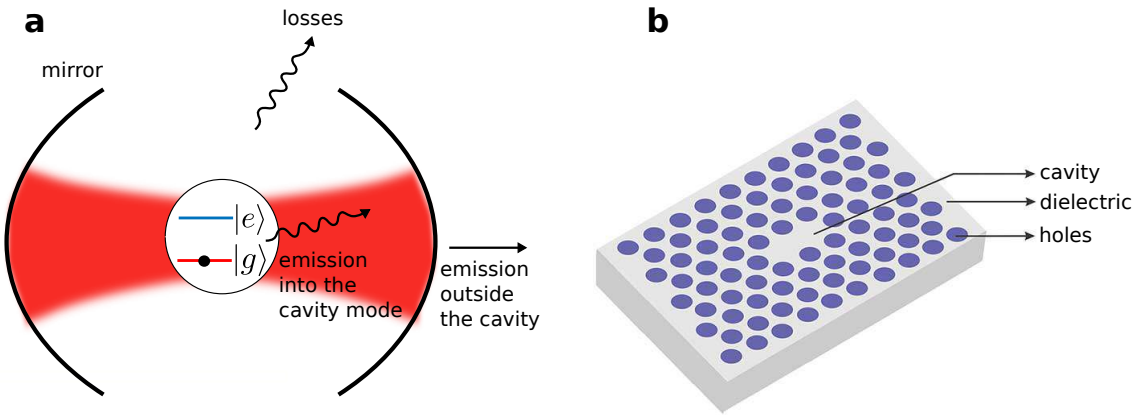

Figure 1.8: **Examples of cavities**. Example sketches of a quantum emitter coupled to a two-mirror Fabry-Pérot cavity (**a**) and a photonic crystal cavity (**b**), respectively.

as [178]:

$$g = \frac{d}{\hbar}\sqrt{\frac{\hbar\omega_r}{2\epsilon_M V}}, \tag{1.35}$$

with d the transition dipole (assuming alignment with the electric field), ϵ_M the dielectric constant in the cavity, $\omega_r = 2\pi f_r$, and V the cavity mode volume. Depending on the ratio between the g parameter and the decay rates of the system, i.e. the cavity-field decay rate Γ_{cav} and the free space decay rate Γ_0, two regimes of coupling can be defined: weak coupling, for $g < \Gamma_{cav}, \Gamma_0$, and strong coupling, for $g > \Gamma_{cav}, \Gamma_0$. In the strong coupling case, the emitter is coherently coupled to the cavity field and spontaneous emission is reversible. The presence of an exciton gives rise to vacuum Rabi oscillation between the two coupled states 'excited emitter with empty cavity' and 'ground-state emitter with one photon in the cavity' [179].
On the other hand, in the weak-coupling case, the spontaneous emission is irreversible, and, if the source is resonant to the cavity its emission will be enhanced, and *vice versa*. This increase in the spontaneous emission rate is defined by the Purcell factor, which we remind being $F_P \propto (\frac{\lambda}{n})^3 \frac{Q}{V}$, with λ the emission wavelength and n the refractive index of the cavity. The emission enhancement is hence maximized through high Q, i.e. narrow Δf, and/or by shrinking the cavity volume V. It is worth mentioning that for single-photon sources with narrow-band emission, coupling to a high Q cavity relies on the accurate matching to its resonance. This can be achieved by either the tuning of the source emission through e.g. Stark shift, or the tuning of the cavity resonance. However, in some cases a more practical solution might be a reduction of the Q factor, and therefore a broader bandwidth to couple to.
The fraction of the source emission that is coupled into one particular cavity mode is the spontaneous emission coupling factor β_{cav}, which is related to the Purcell factor

via the following expression [180]:

$$\beta_{cav} = \frac{F_P}{F_P + 1}\,, \tag{1.36}$$

which hence improves when the Purcell factor is bigger. Therefore, if the emission rate is strongly enhanced by its interaction with a cavity mode, the fraction of spontaneous emission going into all other modes $1 - \beta_{cav}$ is reduced. In this way, the collected fluorescence from the quantum emitter can be effectively enhanced and channeled into a convenient mode, e.g. benefiting the ZPL branching-ratio.

Efficient cavity-coupled single-photon sources were demonstrated with single quantum dots embedded in microcavities [181, 182]. The cavities consist of a high-refractive-index spacer containing the emitter sandwiched between two dielectric Bragg mirrors. The confinement of light results from the combined action of the DBR in the longitudinal direction, and total internal reflection in the transverse direction. $\beta_{cav}\eta_{lens} \sim 0.9$ (where η_{lens} is the collection efficiency at the first lens) has been achieved with planar microcavity samples consisting of Bragg mirror GaAs/AlGaAs layers surrounding an adiabatic cavity embedding an InGaAs QD [183, 184]. An enhancement of the emission rate from single InAs/GaAs quantum dots with a Purcell factor of $F_P \sim 7.6$ and $Q \sim 6400$ has been recently reported for micropillars of $2\,\mu$m-diameter [20, 107, 126]. Despite this promising results, β_{cav} is however limited by loss mechanisms typically owing to the micropillar sidewall roughness. Other emitters which have also been embedded in a microcavity are, e.g. NV centres in diamond and organic molecules [56, 185, 186]. Recently, a Purcell factor of ~ 38 and $\beta_{cav} \sim 93\%$ have been demonstrated for a single organic molecule coupled to a high Q microcavity.
Compared to micropillar cavities, photonic-crystal cavities (see Fig. 1.8b) provide strong optical confinement with $V \sim 0.1 - 0.3\,\lambda^3$ as well as near unity β_{cav} [142]. Photonic crystals refer to structures with periodic dielectric constants. Most research efforts have been focused on planar photonic crystals [187, 188], where the light confinement results from the combined action of DBR in the 2D photonic crystal and internal reflection in the remaining dimension. By standard microfabrication methods, 2D cavities can be realized e.g. by making periodic holes in a slab material, and by leaving a region without holes, where a photonic bandgap is formed and propagation of light is inhibited [32]. The optical properties of the cavity can be tuned by changing the spacing and the size of the holes. High-Q 3D photonic crystal cavities with coupled QDs have also been demonstrated [189]. 3D photonic crystals are especially interesting because they offer the opportunity for light manipulation in all three dimensions in space, but their fabrication is very difficult.

1.2.4 Surface Plasmons

Another method to confine light to small volumes is by using metallic resonators which exploit plasmonic effects. Surface plasmons are electromagnetic waves that are guided by the interface between a metal and a dielectric and are coupled to the coherent oscillations of free electrons on the metallic surface. They have electromagnetic fields that peak at the interface and decay exponentially in the dielectric. Plasmonic devices can enable light confinement on thin metallic films or metal particles into significantly smaller volumes than their dielectric counterparts [190, 191]. Nevertheless, Q factors are typically significantly lower due to the high absorption of metals.
Recently, plasmonic structures have been investigated as alternative method to enhance the spontaneous emission rate of emitters [192, 193, 194]. Plasmonic enhancement between a silver nanowire and a silver metallic surface was reported for dye molecules, with $F_P = 1000$ [195].
However, owing to the losses in the metals, which lead to high rates of non-radiative recombination, plasmonic approaches are not the most convenient for an overall improvement in the collection efficiency.

In this thesis work, we will focus on the coupling of molecule-based quantum emitters to photonic waveguides and micro-lens devices. Cavity-based architectures are certainly included within the future projects of the group, however we rather explore here the possibilities of efficient integration of organic single-photon sources via cost-effective and scalable approaches. We hence study, fabricate and analyze the basic elements of a photonic circuit for the implementation of enhanced coupling and collection efficiency.

2

Single Molecules 2.0: Organic Nanocrystals

In this chapter, we propose and present anthracene (Ac) nanocrystals doped with dibenzoterrylene (DBT) molecules, as reliable quantum emitters. This particular combination of guest chromophore and host matrix (DBT:Ac) exhibits excellent optical properties, as photostability both at room and cryogenic temperature and Fourier-limited linewidths at $3\,K$*, which are remarkably preserved also in a nanostructured environment. The combination of such properties in a nanocrystalline emitter is unique, and opens the pathway to the full integration of organic nanocrystals in photonic structures and to their use in quantum technologies.*

In the last years a plethora of promising quantum emitters have been developed using e.g. individual cold atoms [120], quantum dots [129, 106] and colour defects in diamond [148, 150, 151]. All presenting key advantages and drawbacks, choosing among them is strongly related to the specific application they are envisioned for. Here, we identify organic molecules as especially promising quantum systems. Single fluorescent molecules of polyaromatic hydrocarbons are intrinsically identical, with an optical coherence lifetime longer by one order of magnitude with respect to quantum dots, and with forbidden multi-photon emission [123, 90]. For properly chosen fluorophore-matrix matches and at cryogenic temperatures ($\leq$3 K) they behave like a two-level system [125] and with a fluorescence quantum yield close to unity, therefore exhibiting optical properties similar to trapped atoms. In comparison to atoms, they require a much simpler preparation, consisting in a fast and easy fabrication step and in the cooling down to liquid helium temperatures. Furthermore, the photostability of molecules embedded in matrices is excellent, allowing continuous optical measurements over days [46].
However, despite some interesting recent progress [61, 62, 196, 197, 60, 57], only proof-of-principle experiments were possible because deterministic coupling of molecules into optical systems remains a challenge. Besides the issue of keeping light-matter interactions coherent, a major difficulty is realizing a high coupling efficiency, which for a successive effective quantum processing of the single-photons is convenient to exceed 80%. An effective coupling to a photonic structure demands nanometer accuracy in positioning the emitter at the optimal location, which is hard to achieve in the case of molecules embedded in a mesoscopic matrix. Current methods mainly rely on statistics, by e.g. identifying the best configuration after repeated depositions of the emitter, or among several fabricated devices, as well as by controlling the fluorophore concentration within the guest-host system. In this sense they are far from being deterministic.
In this thesis work, we plan to go a step further towards deterministic coupling and attain better position-control by nano-structuring the emitter matrix. Sub-micrometric size crystals, compared to bulky emitters, are naturally amenable to integration in hybrid devices and to accurate positioning on photonic structures. Indeed, the material separation between the photonic architecture medium and the nanostructured emitter enables independent selection and optimization of both sytems. Various approaches to deterministic integration and positioning were developed for diamond nanocrystal containing NV colour centers, as e.g. via a fiber taper waveguide for coupling to a disk resonator, achieving a position accuracy of $\sim$ 100 nm [198], as well as through pick-and-place manipulation with AFM [199] or tungsten [200] tips for precise alignment onto a photonic crystal cavity, obtaining enhanced Purcell factors. Alternatively, a tungsten tip was also employed to position a polymer photonic crystal cavity membrane onto a the pre-selected diamond nanocrystal itself [201]. Further-

more, lithographic patterning was exploited e.g. to define hole-windows on a sacrificial resist layer in order to favor selective placement of nanocrystal QDots during the deposition of the colloidal solution, by playing with the QDot size and with the surface functionalization [202].

In this chapter, we report on our recent fabrication protocol to obtain anthracene (Ac) nanocrystals doped with a controlled amount of dibenzoterrylene (DBT) molecules. We demonstrate that the optimal features of the bulk system, belonging to the family of polycyclic aromatic hydrocarbons (PAH), are remarkably preserved also in the sub-micrometric environment, and that typical surface effects as spectral instability [37, 152, 153] do not arise.
Experiments on single molecules are carried through fluorescence excitation spectroscopy, which is briefly introduced. The experimental setup used to perform all the measurements on single-molecule emission in this manuscript is described in detail. Finally, a full characterization of the optical properties of DBT:Ac nanocrystals (NCX) is given.

The fundamental results in this chapter are reported in *Self-assembled nanocrystals of polycyclic aromatic hydrocarbons show photostable single-photon emission* by S. Pazzagli, et al., *ACS Nano* **12**, (2018).

2.1 The DBT:Ac System

The identification of a suitable fluorophore-matrix match is determinant for the reliability of a molecule-based single-photon source. Three major classes of host matrices have been typically used for single molecules [203]: polymers, mixed molecular crystals and Shpol'skii matrices[1]. While in polymer matrices molecules are usually subject to spectral diffusion [205] and photo-induced jumps [206], in Shpol'skii matrices the stability is higher, with narrow ZPL, but molecules still undergo spontaneous and light-induced spectral jumps. On the other hand, mixed molecular crystals usually provide well-defined and stable insertion sites for the guest molecules, with consequent good optical properties. The system of Dibenzoterrylene molecules embedded in Anthracene crystal (DBT:Ac) is especially attractive, with excellent photophysical features, owing to the specific structure of its energy levels. Compared to other standard single-molecule chromophores such as terrylene (Tr)[207] or dibenzanthanthrene (DBATT) [208] as a guest in Ac, DBT is well suited to high-resolution single-molecule studies. Indeed, owing to the energetic position of its first singlet ex-

[1] Shpolskii systems are rapidly frozen solutions of polycyclic aromatic hydrocarbons in n-alkanes, described for the first time in 1952 [204]

cited state, which is lower than the triplet state of the host, the intersystem crossing is strongly reduced (see Sec. 2.1.1), hence maximizing the fluorescence yield [209]. Compared to other crystal matrices Ac has many advantages [209, 48]. It does not undergo any phase transition upon cooling [210, 211] and is stable at room temperature. Furthermore it is cheap, it can be easily purified and handled, and the available fabrication processes are undemanding and fast, allowing e.g. to obtain high quality Ac crystals of few tens of nanometer thickness [46]. In particular, thin films are suitable for coupling to nanostructures, since the emitter is directly positioned in the near-field, and they can also be integrated into micro-cavities, either as part of a layered structure in a linear configuration or via evanescent coupling to a whispering-gallery resonator or a photonic crystal cavity. On the other side, organic systems are not compatible with some fabrication steps typically employed for the manipulation of inorganic materials, as e.g. chemical etching or cleansing in solvents in lithographic protocols, as well as unfavorable vacuum or temperature conditions. Nevertheless, the use of suitable polymers as protective layers can prevent any damaging of the host-guest system. More in general, alternative fabrication approaches can be implemented by exploiting the extreme versatility of polymer materials to realize all-organic photonic architectures or hybrid polymer-semiconductor platforms, as shown in Chapters 4 and 5.

2.1.1 Energy Levels

DBT and Ac are both polyaromatic hydrocarbons, consisting of 8 and 3 benzene rings, respectively (Fig. 2.2a). Owing to their similar chemical structure, DBT molecules are located within stable and well-defined positions of the Ac matrix, and mostly in the main insertion site centered at 785 nm [48]. There is also a small probability (few percents) that DBT molecules occupy the secondary insertion site, known as the red site, which is rotated by $\sim 7^\circ$ with respect to the main orientation and is centered at ~ 794 nm [48, 209]. The in-plane component of the DBT transition dipole moment, for both sites, is predominantly along the "b" axis (see Fig. 2.1a for a representation of the Ac crystallographic axes) of the Ac crystal (within a few degrees; see Fig. 2.1b) [48]. The DBT:AC system is especially attractive because the ZPL lays within the maximal sensitivity of silicon avalanche photodiodes (APDs) (the efficiency peak is at ~ 750 nm) and is suited for propagation in telecommunication fibers, upon frequency conversion. Furthermore, this near-IR emission is proximal to the atomic lines of rubidium and potassium, offering the possibility of an optical interaction between Fourier-limited photons and atomic alkali vapours, which can constitute an efficient hybrid quantum memory[213].

The multi-level energy structure of DBT in the main insertion site is described in the

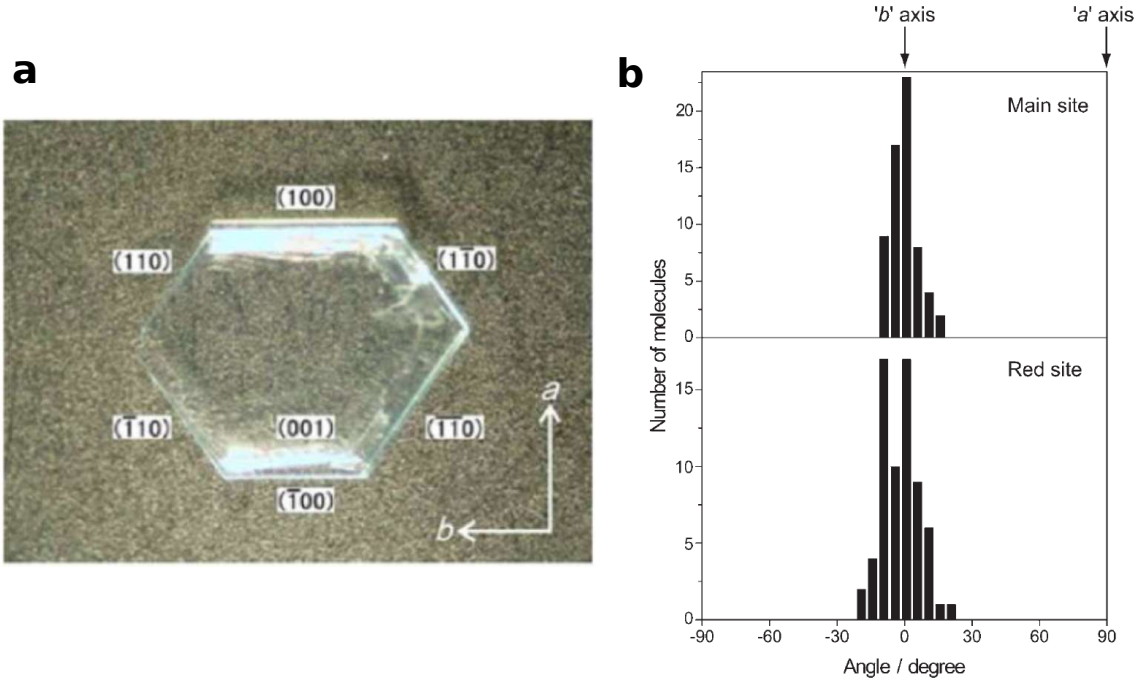

Figure 2.1: **Orientation of the transition dipole moments with respect to the crystallographic axes**. **a** - Figure adapted from Ref. [212], showing a 10 mm-sized Ac single crystal obtained by physical vapor growth and highlighting the crystallographic axes. **b** - Histograms of the orientations of the transition dipole moments of ensembles of DBT molecules of the main site (top) and of the red site (bottom), taken from Ref. [48].

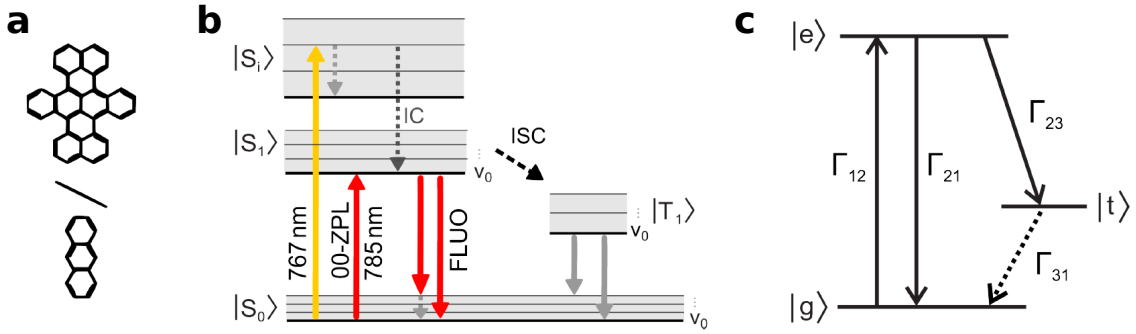

Figure 2.2: **The DBT:Ac system**. **a** - Chemical structures of DBT and Ac. **b** - Jablonski diagram of the DBT:Ac system. S and T label the singlet and triplet electronic states respectively, and V_i stand for the vibrational levels. Radiative transitions are represented by solid arrows while dashed arrows indicate non-radiative transitions. **c** - Simplified energy-level diagram of the DBT:Ac system.

Jablonski diagram in Fig. 2.2b, where energy increases along the vertical axis. The main electronic transition of the DBT molecules is between the highest occupied molecular orbital (HOMO), the singlet ground state, $|S_0\rangle$, and the lowest unoccupied

molecular orbital (LUMO), the singlet excited state $|S_1\rangle$. While for singlet states all electrons in the molecule are paired, the spin of an excited electron can also be reversed, usually leaving the molecule in the first excited triplet state, $|S_1\rangle$. The singlet transition is the ZPL, which for DBT in Ac has a wavelength of ~ 785 nm. This wavelength is slightly different for DBT in different host matrices [214, 215, 216, 217], owing to the different spatial configurations of the embedded molecule. Each electronic level has also higher vibrational states. Therefore, besides the direct decay into the electronic ground state, an excited molecule can also emit a red-shifted photon and decay into a vibrational state of the electronic ground state.
Associated to the excitation and detection scheme employed in this work, all the photo-induced radiative (solid arrows) and non-radiative processes (dashed arrows) are drawn. Single-molecule experiments are performed by pumping a resonant (coherent) excitation with a 785 nm laser, or a non-resonant (incoherent) excitation with a 767 nm laser. In the first case, a purely electronic transition takes place bringing an electron to the first excited state $|\mathrm{S}_1\rangle$ from the vibrational ground state $|\mathrm{S}_0\rangle$. This scheme is typically used at cryogenic temperatures to probe the excitation spectrum of the ZPL-transition. For room-temperature experiments, incoherent pumping is used, promoting the electron to a vibrational level of a higher excited electronic state $|\mathrm{S}_{\mathrm{i,v}}\rangle$. While absorption always occurs in the femptosecond time scale, decay from the excited states entails a more complex dynamics. The molecule first decays from a general excited state $|\mathrm{S}_{\mathrm{i,v}}\rangle$ to $|\mathrm{S}_{1,\mathrm{v}=0}\rangle$ through non-radiative processes:

Vibrational relaxation & internal conversion - the two processes denote decay between vibrational levels within the same electronic state or of different electronic states, respectively. The second, typically dominates at high electronic states, where it is facilitated by the strong energy overlap between electronic states and the manifold of vibrational levels. In both cases, dissipation arises from transfer to thermal energy through collisions with the surrounding environment.

Then, from $|\mathrm{S}_{\mathrm{i,v}=0}\rangle$, two mechanisms compete in the relaxation to the ground state:

Fluorescence - radiative relaxation to the electronic ground state via the emission of a photon. Differently from the coherent pumping scheme, fluorescence is here red-shifted (Stokes-shifted) in the energy spectrum compared to the excitation wavelength.

Intersystem Crossing (ISC) - radiation-less process due to spin-orbit coupling and involving the transition between the two almost iso-energetic vibrational levels of $|\mathrm{S}_1\rangle$ and $|\mathrm{T}_1\rangle$. This transition is spin-forbidden and is hence weakly allowed. For the same reason, the radiative de-excitation from $|\mathrm{T}_1\rangle$ to $|\mathrm{S}_0\rangle$ (**phosphorescence**) is very slow, happening in the microsecond time scale.

A simplified energy diagram can therefore be derived by neglecting the fast vibronic

transitions and by treating DBT:Ac as a three-level system (Fig. 2.2c), consisting in the ground ($|\mathrm{g}\rangle$), excited ($|\mathrm{e}\rangle$) and triplet ($|\mathrm{t}\rangle$) states. Accounting for all the possible radiative and non-radiative processes, the transition rates can be easily defined as follows:

$$\frac{d}{dt}\rho_{gg} = \Gamma_2 1\rho_{ee}(t) + \Gamma_{31}\rho_{tt}(t) - \Gamma_{12}\rho_{gg}(t) \tag{2.1}$$

$$\frac{d}{dt}\rho_{ee} = \Gamma_{12}\rho_{gg}(t) - (\Gamma_{21} + \Gamma_{23})\rho_{ee}(t) \tag{2.2}$$

$$\frac{d}{dt}\rho_{tt} = \Gamma_{23}\rho_{ee}(t) - \Gamma_{13}\rho_{tt}(t) \tag{2.3}$$

with Γ_{ij} the rate of the transition $\mathrm{i} \rightarrow \mathrm{j}$ and σ_{ii} referring to state occupation probability, as introduced in Sec. 1.1.1. It is straightforward that, in order to achieve a high fluorescence rate, ISC should be weak, namely the triplet yield should be low and the state life-time short (big Γ_{31} and small Γ_{23}). Otherwise, a long-lived and highly probable triplet dark state would consequently cause blinking, to the extent of making the single-molecule spectroscopy impossible for the case of highly facilitated ISC transition [209]. Γ_{31} and Γ_{23} depend both on the guest molecule and host matrix, and in the case of DBT in Ac the combination is very well-suited for high resolution single molecule studies. The Ac host matrix, with its triplet state at $680\,\mathrm{nm}$, energetically higher than the first guest's singlet excited state, makes possible only virtual transitions from the guest-singlet to the guest-triplet via the host-triplet, therefore lowering the ISC.
The quantum yield parameter is very hard to measure at low temperature conditions. The ISC can be instead extracted by the analysis of the second order correlation function for long times, and in DBT:Ac this is indeed very low (10^{-7}), with short triplet state life-time ($1.5\,\mu$s [46]). Therefore, neglecting the triplet contribution, DBT:Ac can be considered as a two-level system with quantum yield approximating 1. With an excited state life-time of $\sim 4.2\,\mathrm{ns}$ [55], the fluorescence intensity is very high, reaching $\sim 10^6$ photons per second at saturation. Thank to the shielding action of Ac from quencher agents as oxygen, also photostability is remarkable, allowing more than 10 hours of strong illumination without bleaching at room temperature (to compare with the typical few-second timescale for a dye molecule in solution) [46]. Finally, also the well-defined orientation of the transition dipole of the DBT molecules in Ac, parallel to the crystal plane [46] (parallel to substrate e.g. for spin-coated Ac layers), is especially suitable for efficient coupling to photonic structures [60].

2.1.2 Physical Principles and Spectroscopy

Single-Molecule Excitation Lineshape

In general, for all molecules embedded in a solid matrix, single-molecule fluorescence lineshape is composed of two parts, the ZPL, associated to the purely electronic transition, and the phonon sideband (PSB). The latter, originates from the possible generation or absorption of a phonon of the anthracene crystal, during the absorption or emission of a photon. While at room temperature the PSB is a continuous and broad envelop of all phonon excitations of different frequencies, the ZPL feature clearly appears at cryogenic temperatures, when thermal phonons are frozen. This narrow transition, can be described by the the following Lorentian function, obtained from the transition dipole moment for an electric dipole oscillator [218]:

$$I(\omega_p - \omega_A) = \frac{1}{4\pi} \frac{\Delta\omega_{hom}}{(\omega_p - \omega_A)^2 + (\Delta\omega_{hom}/2)^2} \tag{2.4}$$

where $(\omega_{\mathrm{P}} - \omega_{\mathrm{A}})$ is the detuning of the laser frequency from the transition frequency of the chromophore, and $\Delta\omega_{\mathrm{hom}}$ is the full width at half maximum (FWHM) of the homogeneously broadened Lorentzian lineshape. In particular, the homogeneous optical linewidth is governed by the two time constants T_2' and τ (pure dephasing and lifetime of electronic excited state) according to equation 1.8. In crystalline matrices at low temperatures ($\leq 2\,\mathrm{K}$), T_2' approaches infinity as host phonons and local modes are essentially quenched and the linewidth is solely determined by the lifetime contribution as $\Delta\omega_{\mathrm{nat}} \sim 1/(2\pi\tau)$. For DBT:Ac this value is $\sim 40\,\mathrm{MHz}$ ($\tau \sim 4.2\,\mathrm{ns}$). However, any increase in temperature activates low frequency modes of the matrix (phonons) which lead to a broadening of the homogeneous line (see Fig. 2.3a), as described by Arrhenius law [219]:

$$\Delta\omega_{hom}(T) = \omega_{hom}(0) + A \exp\left(\frac{-E_a}{K_b T}\right), \tag{2.5}$$

where $\omega_{hom}(0)$ is the line width at zero temperature, K_b is the Boltzmann constant, E_a is the activation energy (equal to the energy $\hbar\omega_{LP}$ of the local phonon) [220], and A is a constant depending on the electron–phonon coupling. Furthermore, from manipulations of Eq.s 1.4 in steady state, one can derive the dependence of the excitation linewidth to the excitation intensity [221]:

$$\Delta\omega(I) = \Delta\omega_{hom}\sqrt{1 + I/I_s}\,. \tag{2.6}$$

which describes an increase in the FWHM, also called power broadening. A fundamental parameter strongly dependent on temperature [222, 223], is the Debye-Waller

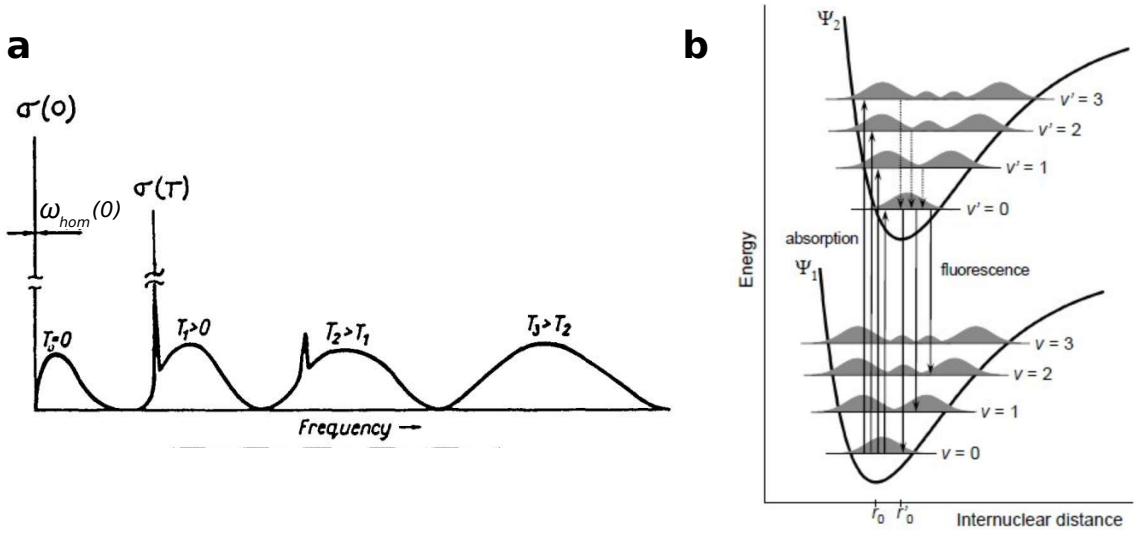

Figure 2.3: **a** - Illustration of the emission spectrum of a single molecule embedded in a solid matrix at room temperature. At cyogenic temperature ($T_0 = 0$) the ZPL and the phonon wings are resolved, and the ZPL linewidth is life-time limited (ω_{hom}). As the temperature increases, the ZPL is broadened and the phonon wings grow, until at room temperature a uniform broad spectrum arises. **b** - Diagram of the vibrational levels of a single molecule as a function of the nuclear displacement. Transitions are drawn as vertical arrows since, following from the Frank-Condon principle.

factor, which defines the proportions of fluorescence intensity emitted in the ZPL ($\mathrm{I_{ZPL}}$) and in the PSB ($\mathrm{I_{PBS}}$):

$$\alpha_{DW} = \frac{I_{ZPL}}{I_{ZPL} + I_{PSB}} \quad . \tag{2.7}$$

In order to have a high narrowband signal of indistinguishable photons, α_{DW} should be as high as possible. The intensity of the 00-ZPL is also defined by the branching ratio between the decay rate into the ground state $|\mathrm{S}_{0,\nu=0}\rangle$ and into all other vibrational sublevels. According to the classical approximation, the Franck–Condon principle states that an electronic transition is most likely to occur without changes in the positions of the nuclei in the surroundings, due to the infinitesimal electron mass compared to the nuclei's. From a quantum mechanical point of view, the intensity of a vibronic transition is proportional to the square of the overlap integral between the vibrational wavefunctions of the two states that are involved in the transition (given by the Frank-Condon factor α_{FC}). A representation of this principle is given in Fig. 2.3b, where transitions are drawn as vertical arrows since they do not affect the atomic coordinates. A typical value for α_{FC} is 0.4 [224], while for the DBT:Ac system the combination $\alpha_{\mathrm{FC}}\alpha_{\mathrm{DW}} > 0.3$ has been measured [91, 62]. This value is much higher than the 0.04 measured for NV-centers in diamonds [225, 226] but still

below the 0.8 measured for the silicon-vacancy centers [148, 226]. However, it can be enhanced via coupling the DBT:Ac system to an optical cavity tuned to be resonant with the 00-ZPL, so that emission to higher phonon modes is suppressed [227].

Inhomogeneous Broadening

Inhomogeneous broadening is a fundamental photo-physical phenomenon which facilitates the detection and measurements of the single-molecules emission in solids and at low temperatures. In an ideal perfect crystalline sample with identical local environments, the optical absorption of each molecule would be a single narrow Lorentian line at same exact frequency, uniquely defined by the guest-host match. However, in real samples, each molecules happens to have a different absorption frequency [228, 229], within an overall envelop profile, termed inhomogeneous broadening, which can extent from less than 1 GHz to 10 THz, depending on the conditions of the host material. Indeed, such a distribution of resonance frequencies is caused by dislocations, point defects, or random internal electric and strain fields in the matrix, which are generally always present [230], but are more relevant in e.g. amorphous materials. The overall profile is the result of an approximately Gaussian distribution of center frequencies for the absorbers (Fig. 2.4).
This effect highlights molecules as powerful probes of the nano-environment, owing

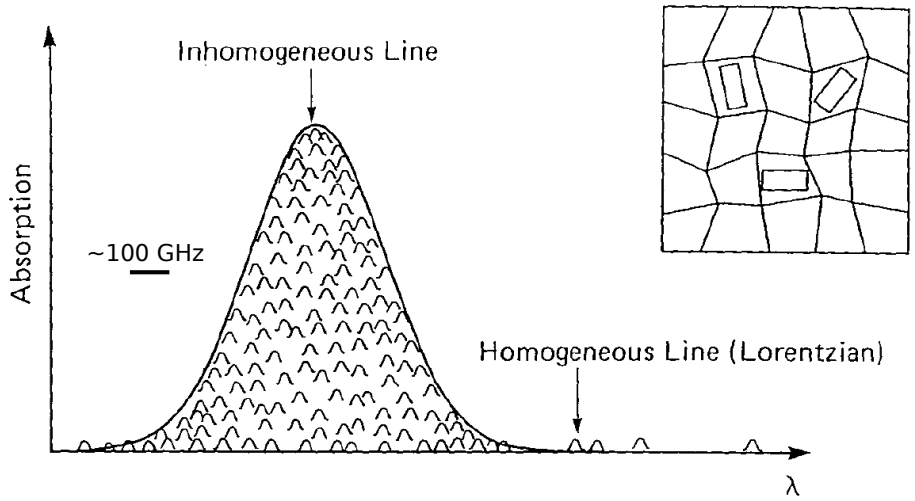

Figure 2.4: **Inhomogeneous broadening**. In a real crystal imperfections like strain fields or defects are present. The embedded fluorescent molecules are hence subject to different nano-environments (inset). Consequently, their lorentian ZPL transitions, which in an ideal crystal would be equal, are inhomogeneously distributed in frequency.

to the very stable and narrow linewidth and to the sensitivity of the absorption frequency to the surroundings. Especially, inhomogeneous broadening facilitates spec-

tral selection of individual molecules for single-molecule spectroscopy. Indeed, by employing a sample with a low enough doping level and using a narrowband tunable laser, single molecules can be easily pumped selectively, one at a time.

Frequency Tuning

Despite its advantages in single-molecule spectroscopy, inhomogenous broadening can rather be a complication for applications in quantum nano-photonics. For an effective interference between independent single photons, i.e. emitted from different sources, indistinguishability is indeed necessary, and the emission wavelengths are required to be identical. This interaction is a basic operation in the realization of photonic networks [20, 231], therefore, to shift from proof-of-concept experiments to an effective deployment in quantum photonic schemes, matching the emission frequency of different organic molecules is essential. This is also useful when using a cavity to collect the single-photons, for which the detuning between the quantum emitter and the cavity resonance must be properly adjusted.
An effective method to tune the emission frequency of an organic molecule (or of an emitter in general), is by applying an electric field. The spectral position of the narrow optical transition is consequently modified, and the shift is known as *Stark shift*. This response is due to the difference between the ground state and excited state dipole moments. Many dyes, and DBT among them, however, are centrosymmetric and hence present no intrinsic dipole moment. By embedding these molecules in a solid matrix, their symmetry is though broken and they can obtain a permanent dipole moment. The transition shift $\Delta(\hbar\omega)$ has usually a linear and quadratic term, as described by the following expression [222, 232]:

$$\Delta(\hbar\omega) = -\Delta\vec{\mu}\cdot\vec{E} - \vec{E}\cdot(\Delta\vec{\alpha}/2)\cdot\vec{E}\,, \tag{2.8}$$

and depends on the dipole moment difference $\Delta\vec{\mu}$ between the transition levels and on the polarizability tensor $\Delta\alpha$.
Several host-guest systems with different contributions of the linear and quadratic Stark effects have been reported in the literature [233, 234, 210, 235], and quadratic Stark shift up to hundreds of GHz has been recently demonstrated for DBT:Ac, while preserving the narrow emission linewidth [52]. In practice, electric potential is typically applied by using matal or 2D functional material electrodes (as e.g. graphene), the latter having the advantage of being transparent.

2.2 Optical Setup and Experimental Methods

2.2.1 Detection at the Single Molecule Level

The challenge of single-molecule spectroscopy is to detect the faint signal of a single molecule above environmental background in a reasonable period of time. The key parameter in this context is the peak absorption cross-section σ_{A} of the guest molecules. Considering the focal spot cross-sectional area A, greater or equal to the diffraction limit $\sim \lambda^2$ (with λ the optical wavelength), the pumping rate of the resonant optical transition is defined by the product of the incident photon flux and σ_{A}. Otherwise stated, $\sigma_{\mathrm{A}}/\mathrm{A}$ gives the probability that the molecule absorbs the incident photon from the laser beam.
The maximal achievable absorption cross-section for a single two-level system in vacuum under a plane wave illumination is given by $\sigma(\omega) = 3\lambda^2/(2\pi)$. This relation implies perfectly parallel orientation of the transition dipole to the incident pump light polarization. In reality, the broadening of the transition linewidth ($\Gamma_{\mathrm{hom}}/\Gamma_{\mathrm{nat}}$), the Frank-Condon and the Debye-Waller factors (see Sec. 2.1.2), and the angle θ of dis-alignment between the laser beam polarization and the transition dipole, all contribute to the reduction of σ_{A}. Therefore, for a single molecule in a solid matrix the complete expression of the absorption cross-section is the following:

$$\sigma(\omega) = \alpha_{FC}\alpha_{DW}\frac{3\lambda^2}{2\pi}\frac{\Gamma_{nat}}{\Gamma_{hom}}cos^2(\theta). \tag{2.9}$$

Summarizing, in order to achieve a high signal to noise ratio for single-molecule spectroscopy, it is fundamental to maximize σ_{A}, or/and to minimize A. Working at low temperatures is essential since σ_{A} considerably increases and indeed extinction from a single molecule is observable routinely [236, 237, 197]. Considering then fluorescence detection, which is a fundamental tool first demonstrated in Ref. [238], the quantum yield for photon emission per absorption event should be high. Additionally, scattering background from both the sample and the substrate should be minimized, and the ISC (see Sec. 2.1.1) should be low. In particular, the fundamental technical requirements for enabling single-molecule detection are the following:

- **highly efficient detectors** such as avalanche photodiodes, electron-amplifying CCDs or superconducting detectors, which exhibit low dark-counts.
- **efficient collection and high spatial resolution** by using a high NA objective. Following the Abbe priciple $\mathrm{D} = 0.5\lambda_{\mathrm{ex}}/\mathrm{NA}$, where λ_{ex} is the excitation wavelength, the resolution limit D can be stretched by maximizing the objective (optics) NA. Therefore, efficient isolation and excitation of the individual molecule is achieved. Also, in order to be diffraction limited, NA should be maximized.

- **low BG scattering** via spatial isolation (low molecule concentration sample, and small excitation volume) and via spectral isolation from the pump (efficient optical filters).

2.2.2 Setup Configuration

The experimental set-up used in this thesis is a home-built, versatile epifluorescence scanning confocal microscope. In such a configuration, excitation of the molecule and detection of the fluorescence are done through the same microscope objective, with the advantage that the beam of collected light results automatically collimated once the excitation beam is. In Fig. 2.5 a schematics of the set-up is shown.

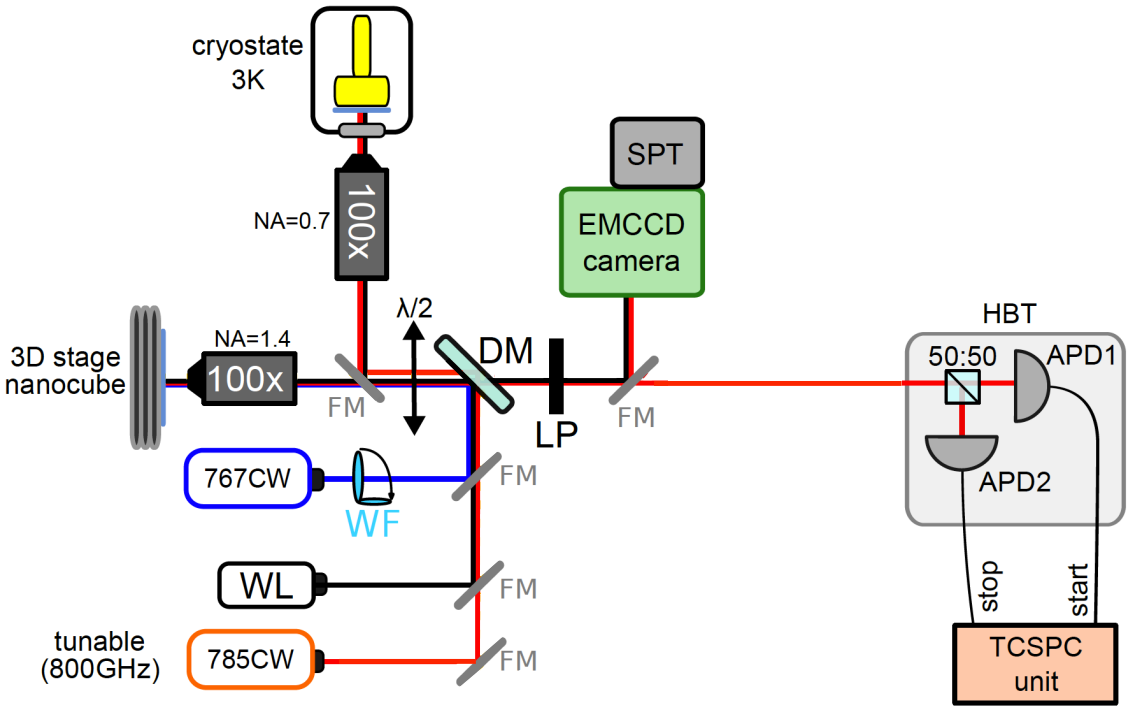

Figure 2.5: **Setup**. Simplified diagram of the experimental set-up. Flippable Mirrors (FM) allow to switch between two fiber-coupled lasers and white light illumination (WL). Excitation can be performed both in confocal and wide-field configurations, the latter by inserting a wide-field lens (WF). High NA objectives are used to efficiently collect the fluorescence signal. Samples can be mounted either on a piezo stage for room temperature measurements or inside a cryostat for measurements at 3 K. In the latter case, the laser spot is scanned on the sample by using a galvo mirror and a telecentric lens system (not shown in the scheme). Fluorescence is efficiently separated from the excitation light through a dichroic mirror (DM) and a longpass filter (LP) in detection. Two avalanche photodiodes (APDs) - arranged in Hanbury Brown-Twiss configuration (HBT) and supplied with a TSPC unit - and an EM-gain CCD camera equipped with a grating spectrometer enable signal detection.

Excitation Line

Depending on the molecular transition to excite, different lasers can be coupled to the fluorescence microscope through flippable mirrors, polarizing beam splitter cubes and half-wave plates. Additionally, a white light (WL) lamp is used for sample imaging. For non-resonant excitation, a 767 nm continuous-wave (CW) single mode laser (Toptica DL110-DFB) is employed. Resonant pumping is performed with a tunable narrowband DFB (Toptica, LD-0785-0080-DFB-1) laser, with central frequency 784.6 nm, and a mode-hop-free scanning range of 800 GHz. The laser is spatially filtered by coupling to a polarization-maintaining single-mode optical fiber, allowing for well-defined excitation in confocal mode. The laser spectral tails are filtered out via a narrow band-pass filter (BP1, Semrock Brightline FF01- 769/41), and the frequency stability is monitored by directing a fraction of the beam into a scanning Fabry-Perot cavity (FP) ($\mathrm{FSR} = 5$ GHz) and by observing the transmission onto an oscilloscope (Tektronix DPO2024B, 200 MHz). The laser intensity is adjusted by means of neutral density filters. A system of flippable telescopes is used to control the beam size and to switch from confocal to wide-field (WF) excitation. Finally, a non-polarizing dichroic mirror (DM, Semrock FF776-Di01) is employed to send the collimated excitation light to the microscope objective. Before the dichroic mirror, a half-wave plate is used to optimize the linear polarization of the light onto the transition dipole moment of the target molecule.
The last part of the excitation path is divided into two independent lines for cryogenic cooling or for room temperature measurements, respectively. For low temperature (LT) experiments, the sample is placed inside the vacuum chamber of a closed cycle helium cryostat (Cryostation by Montana Instruments), and glued for thermal coupling on the cold finger at 2.7 K. A low working distance window ensures optical access. In this configuration, the excitation light is focused onto the sample by a glass-thickness-compensation air objective (OptoSigma 50x, $NA = 0.65$, $WD = 10.48$ mm). Through a telecentric lens system (for mode-matching with the objective lens back entrance) and a dual-axis galvo-mirror, the laser spot can be spatially scanned over the sample by small deviations of the beam from the orthogonal incidence.
For room temperature (RT) measurements, the sample is assembled onto a piezoelectric nanopositioner (NanoCube by Physik Instrumente), mounted on a manual translation stage for coarse positioning. In this case a high NA oil-immersion objective (Zeiss Plan Apochromat, 100X, NA=1.4) or an air objective with NA = 0.7 (Mitutoyo 100X Plan Apochromat) are commonly used.

Detection & Data Acquisition

The emitted Stokes-shifted fluorescence, collected by the objective, is separated by the laser light before the detection box through the double action of the DM and a long-pass (LP) filter (Semrock RazorRedge-785RS-25). Inside the detection box, which shields the detectors from the external environmental light, the beam can be focused on a multi-elements electron multiplying CCD (EM-CCD) camera (Andor iXon 885, 1004×1002 pixels, pixel size $8\mu\mathrm{m} \times 8\mu\mathrm{m}$) for fluorescence or white-light imaging. Spectral analysis is performed on a grating Czerny-Turner spectrometer with 0.1 nm resolution, directly connected to the EM-CCD camera. Alternatively, single-element (pixel) APDs (τ-Spad-50 Single Photon Counting Modules by PicoQuant) with low dark count rates (< 50 cps), short dead time (< 70 ns) and detection efficiency up to 50% at 785 nm, are used for single molecule measurements in confocal configuration.
The electronic devices of the setup are interfaced and possibly operated together with a dedicated acquisition software [239]. By controlling the DFB laser driver via a digital ramp, excitation spectra of the 00-ZPL of individual molecules can be measured, and by repeating such a measurement in time the spectral stability map can be recovered.

Dipole Orientation and Emission Pattern

Knowledge of the molecular emission pattern is crucial for assessing and enhancing the excitation and collection efficiency of the single-photon source. The emission pattern can be accessed by performing back-focal-plane (BFP) imaging. The spatial distribution of the emitted light is directly encoded in the intensity profile collected on the back-focal plane of the objective (i.e the back-aperture plane) [240]. Fig. 2.6 gives a simple illustration to explain the geometry of the optical collection: photons emerging from the source dipole with different orientations of the wave vector k, namely with different q-angles with respect to the optical axis, are projected to different points on the objective BFP, whereas parallel wave vectors correspond to the same point on the BFP. The intensity profile observed on the BFP can be therefore directly mapped to the angular distribution of the emitted light. In terms of Fourier optics, the objective projects the Fourier transform of the collected field onto the BFP. An image of the BFP can be obtained by placing the imaging lens of the camera off focus, so that the BFP - rather than the source - is imaged onto the CCD. Alternatively, in order not to remove the imaging lens, an additional lens can be inserted before the camera, such that the two-lenses system approximately fulfils the required focal length[2]. The position of such second lens can be optimized by placing a reference image at the entrance of the objective, and by adjusting its WL imaging on the camera.

[2]Additionally, a spatial filter made of a telescope and a pinhole can be used to increase resolution and contrast

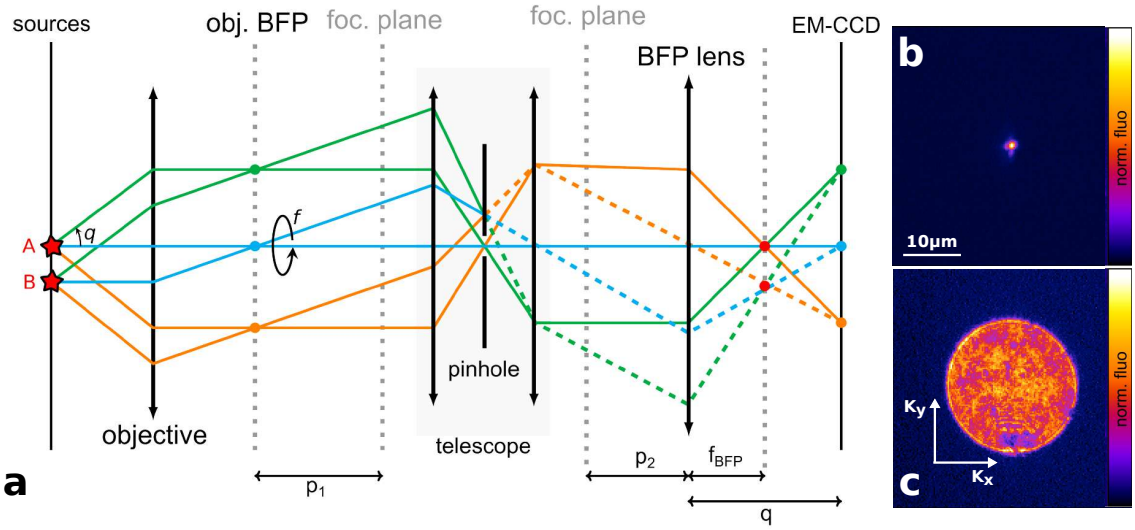

Figure 2.6: **BFP measurement**. **a** - Illustration of the optical collection scheme. **b** - Example of fluorescence map of an individual DBT molecule in an Ac nanocrystal under confocal excitation (fluorescence is collected from above the substrate, through air). **c** - Correspondent BFP image in the K-vector space, measured in the same conditions. The homogeneously illuminated circular area is the angular distribution of the collected emission intensity, with the center of the circle denoting the optical axis and the external conference defining the angular collection limit of the experimental numerical aperture.

Hanbury Brown-Twiss set-up

By using two APDs arranged in the Hanbury Brown-Twiss (HBT) configuration, the entire $g^{(2)}$-function can be reconstructed.
The HBT set-up consists of two highly efficient photodetectors monitoring the outputs of a 50:50 beamsplitter (BS, Fig. 2.7). At the BS, the incoming photon stream is equally splitted, forming the single-mode entangled state $(1/\sqrt{2})(|1_a 0_b\rangle + |0_a 1_b\rangle)$. By changing the APDs respective distance from the BS, or alternatively the delay time Δt via a time-correlated single photon counting (TCSPC) modulus [3], the hystogram of coincidences between the two APDs can be recovered, and the $g^2(\Delta t)$-function at short times can be retrieved. The distribution of coincidences normalized by the average photon count rate gives the normalized autocorrelation function, which can be fitted by:

$$g^{(2)}(\Delta t) = 1 - be^{-|\Delta t|/\Gamma} \tag{2.10}$$

[3]The resulting output pulses of photons impinging on the detector are fed into the start and stop inputs of a TCSCP module (PicoHarp300 by PicoQuant), which records the time delay Δt between the pulses from the two detectors (D1 and D2 in Fig. 2.7), while simultaneously counting the number of pulses at each input. Registration of arrival times with high accuracy is enabled by the fast TCSPC electronics and the high quantum efficiency APD-detectors (timeing-jitter$\sim$ 100 ps).

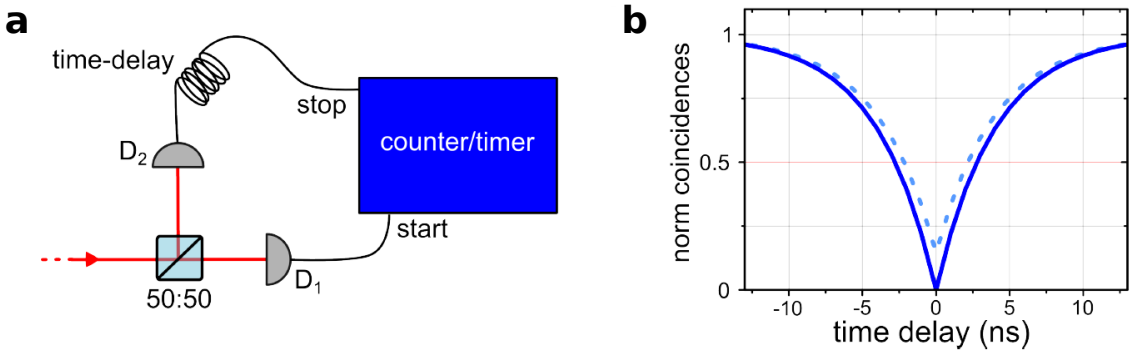

Figure 2.7: **a** - Sketch of the HBT set-up. Coincidences between counts on the two detectors, D1 and D2, are processed through the TCSPC unit and give access to the $g^{(2)}$ correlation function. **b** - Comparison between the expected $g^{(2)}$-function for and ideal quantum emitter (dark blue line), and the lower dip at zero delay time resulting from the false coincidences which arise in presence of background photons (light blue dashed line).

where Γ accounts for the excitation and spontaneous emission rates [91] and $\mathrm{b} = 1 - \mathrm{g}^{(2)}(0)$ is the dip depth.

Hong-Ou-Mandel Configuration

The absolute degree of first order coherence $|\mathrm{g}^{(1)}(\Delta\mathrm{t})|$ can be here characterized by measuring the interference visibility between two single-photon streams. In this configuration, two photons in the same mode impinging onto the opposite inputs of a 50:50 BS form the two-mode entangled state $(1/\sqrt{2})(|2_\mathrm{a}0_\mathrm{b}\rangle + |0_\mathrm{a}2_\mathrm{b}\rangle)$. Performing the same measurement for the evaluation of the $\mathrm{g}^{(2)}(\Delta\mathrm{t})$ with the TCSCP unit, the coincidence probability as a function of delay time between the streams can be obtained. In terms of shape, the recording is described by the same temporal behaviour as the single-photon antibunching. Interference visibility is hence defined as follows:

$$|g^{(1)}(0)|^2 = \frac{g_{\perp}^{(2)}(0) - g_{\parallel}^{(2)}(0)}{g_{\perp}^{(2)}(0) + g_{\parallel}^{(2)}(0)}\,, \tag{2.11}$$

as it was already introduced in Eq. 1.23.

We employ the setup sketched in Fig. 2.8a,b to realize the HOM configuration. The stream of indistinguishable photons from the ZPL transition of an individual molecule is selected through a narrowband filter of 2 nm-bandwidth (see Sec. 3.1). The fiber-coupled fluorescence is hence split into two identical copies at a free space PBS, upon optimization of the input polarization via fiber-polarization controllers (PC). The two streams are then outcoupled into two other fibers and relatively delayed against each other by several coherence lengths to make them independent

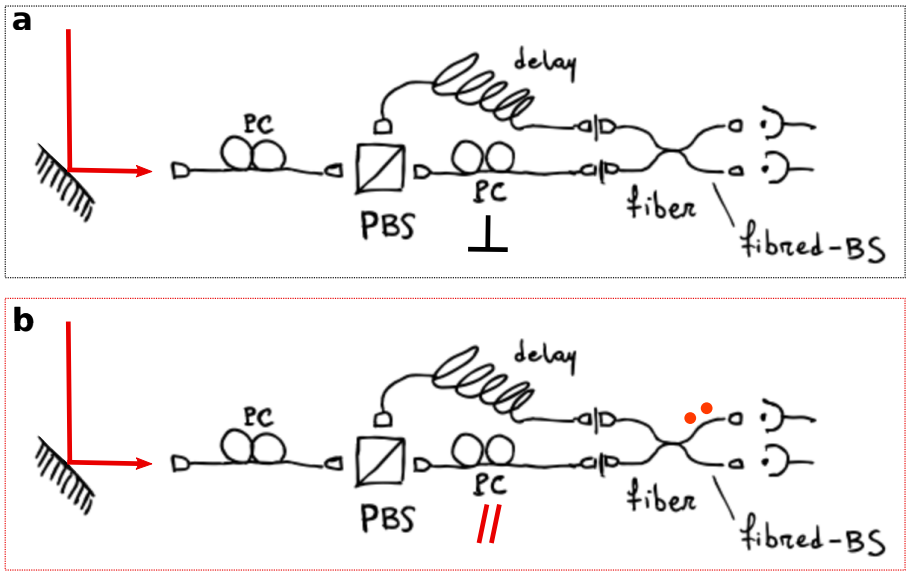

Figure 2.8: **HOM configuration**. Sketches of the experimental setup for a HOM measurement. The indistinguishable photon stream is split in two at a polarizing BS and through fiber-polarization controls (PC). The two streams are coupled two other two fibers, properly delayed to make them correlation-independent, and finally incoupled into a fiber non-polarizing BS. Trough the second fiber-PC, the polarizations can be set orthogonal (**a**) or parallel (**b**)), in order to extract the normalized interference visibility.

(mimicking streams from two separate molecules). Finally, the fibers are incoupled into the fiber non-polarizing BS in HBT configuration for the interference measurement. The second PC in the figure, is used to set orthogonal/parallel polarizations (Fig. 2.8a/b) at the BS inputs.

2.3 Optical Characterization of DBT-doped Ac Nanocrystals

In this section the experimental optical characterization of DBT:Ac nanocrystals (NCX) is presented. The measurements here discussed assess the performances of DBT:Ac NCX as reliable single-photon sources despite their sub-micrometric size. This characterization also represents a reference for the expected observables in the experiments discussed in the following chapters.
Our protocol to grow DBT-doped Ac NCX was adapted by Dr. Sofia Pazzagli from the reprecipitation method developed by Kang [241]. Such a reproducible and cost-effective technique, allows to obtain in half-an-our time an aqueous suspension of NCX of high crystallinity and mostly monodisperse in size, with an average thickness

of about 65 nm and diameter of about 110 nm. Samples are then obtained by drying in a desiccator a few-μL droplet of suspension. More details about the fabrication protocol and the morphological characterization can be found in Appendix B and in the reference paper [63].

2.3.1 Microscopy at Room Temperature

Microscopy at room temperature is studied on NCX doped with single-molecule concentration (see Appendix B), with the oil-immersion objective (therefore observing the sample through the glass) under off-resonant excitation.
In Fig. 2.9a, a representative example of white-light imaging and corresponding flu-

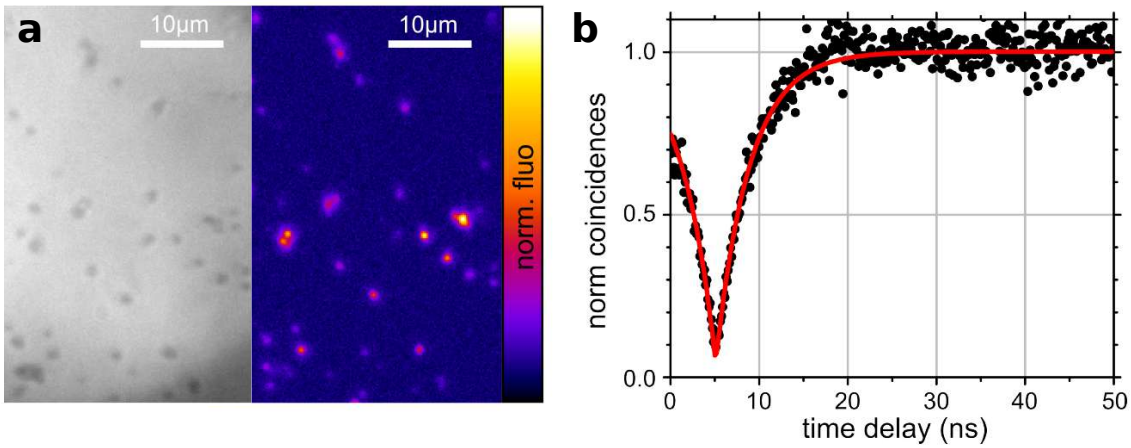

Figure 2.9: **a** - White light and fluorescence wide-field images of the same region of a sample of DBT:Ac NCX doped with single molecule concentration. **b** - Measurement of photon anti-bunching from an individual DBT:Ac NCX without any background correction (black dots). By correcting for the background noise (Eq. 2.12) we obtain a single-photon purity $g^{(2)}(0) \sim 0.0025$.

orescence map is shown, demonstrating more than 90 % success in doping Ac NCX with DBT molecules. In order to test the success in doping each single nanocrystal with an individual DBT molecule, a HBT measurement is performed in confocal mode with an excitation intensity below saturation (see Sec. 1.1.1) and with optimized polarization. The analysis performed on 40 fluorescing NCX shows that 73% of them display an antibunching dip larger than 50%, demonstrating that the protocol for single-molecule DBT-doped Ac NCX is reliable. The remaining $\sim$ 25% typically exhibit $g^{(2)(0)} \sim 0.50$, suggesting the presence of two molecules. A representative example of $g(2)$ measurement performed on a single-molecule DBT:Ac nanocrystal is shown in Fig. 2.9b, featuring a strong antibunching dip which is fitted with Eq. 2.10 and yields a dip depth of 95%, namely a single-photon emission purity $g^{(2)(0)} = 0.05$.

However, in order to correctly interpret a $g^{(2)}$ measurement it is customary to correct the experimental value with an independent measurement of the background counts and of the time response of the HBT set-up. Given a signal-to-background ratio (S/B), one can estimate the actual value of $g^{(2)}(0)$ from the measured value $g^{(2)}_{exp}(0)$ as:

$$g^{(2)}(0) = 1 + \frac{g^{(2)}_{exp}(0) - 1}{P}, \quad P = \frac{S}{S+B}\,. \tag{2.12}$$

If we consider a typical count rate of 400 Kcps for the fluorescence signal and 20 Kcps for the background noise, we obtain a background-corrected purity as low as $\mathrm{g}^{(2)} = 0.0025$. The brightness of the fluorescence emission is evaluated by measuring the saturation curve of the system, detecting the Stokes-shifted fluorescence with an APD at different excitation intensities (Fig. 2.10a). Data are fitted with

$$R(P) = (a + bP) + R_\infty P/(P + P_s)\,, \tag{2.13}$$

which derives from Eq. 1.17 with P the laser power, Ps the saturation power and $(a + bP)$ accounting for the residual laser scattering as a linear contribution. A saturation intensity $\mathrm{I_s} = (80 \pm 6)\,\mathrm{KW/cm^2}$ and a maximum detected rate $\mathrm{R}_\infty = (1.5 \pm 0.02)$ Mcps are obtained. Accounting for the quantum efficiency of the APD ($\eta_{\mathrm{det}} \sim 50\%$), the measured value for R_∞ corresponds to a collected photon rate of 3 MHz at the detector, consistent with what was reported for the bulk system [46].

Finally, in Fig. 2.10b a typical BFP image of a single NCX is shown. While in free space the radiation pattern of a molecule is given by the $\sin^2(\theta)$ distribution [242], with θ being the angle between the dipole and the optical axis, for a molecule close to dielectric interfaces the emission pattern is altered due to refraction and reflection events. Indeed, the emission pattern in Fig. 2.10b, features two side lobes beyond the critical angle ($\mathrm{q_c} = \arcsin(\mathrm{n_{air}}/\mathrm{n_{glass}}) \sim 34°$), corresponding to the coupling between the evanescent wave in air and the propagating wave in the coverglass [243]. This distribution, similar for different molecules, allows to infer that the transition dipole of the DBT molecule inside the Ac NCX is parallel to the crystal plane [240], in agreement with previous studies on the bulk system [46]. The behaviour is also confirmed by the theoretical prediction [57] of the far field intensity from a single DBT molecule embedded in a 60 nm-thick Ac layer, oriented with the molecular dipole parallel to the layer (Fig. 2.10c).

Regarding photostability at room temperature of the DBT:Ac NCX, after several hours of illumination blinking phenomena can be observed, typically before they stop to fluoresce. Photobleaching, most probably due to chemical reactions of the dye molecule with ambient oxygen [244], is more likely to occur in conjunction with the sublimation of Ac at room temperature. For our sub-micrometric crystals we observe that sublimation takes place on a time-scale of about one day but it is completely

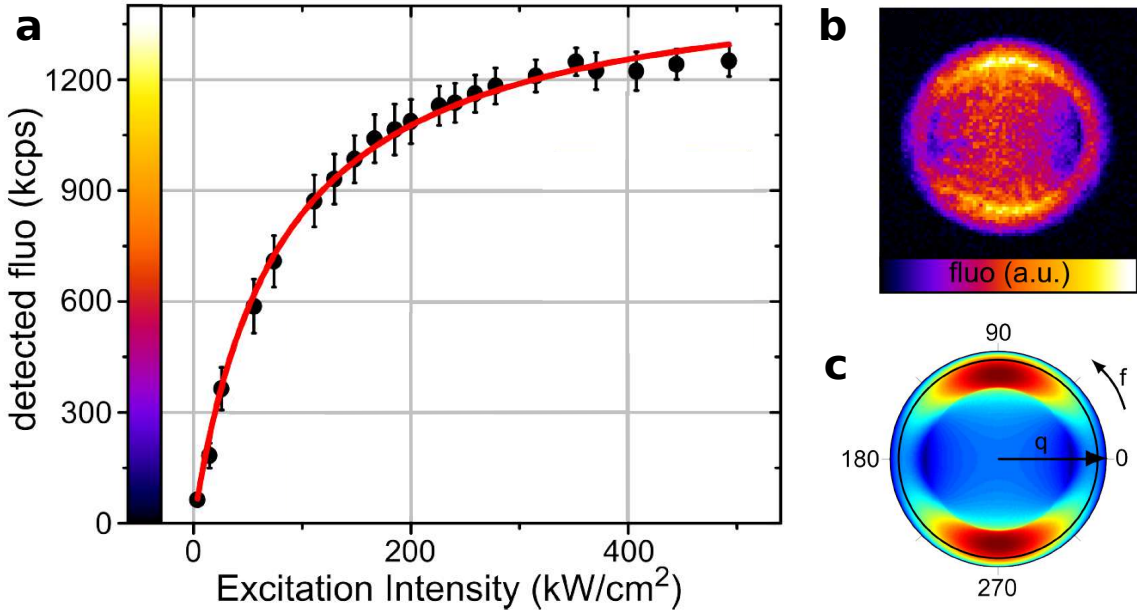

Figure 2.10: **a** - Saturation measurement performed on a DBT:Ac NCX (black dots). The fitted red curve yields a saturation intensity of $I_s = (80 \pm 6)$ kW cm^{-2} and a maximum detected rate $R_\infty = (1.50 \pm 0.02)$ Mcps. **b** - BFP image of a single DBT molecule in confocal illumination. **c** - Theoretical prediction for the BFP measurement. It displays the normalized intensity emitted from an on-plane oriented dipole embedded in a 60 nm-thick Ac layer, and collected on a plane in the far field. The black circle indicates the maximum collection angle of the immersion-oil objective (NA = 1.4), and f the azimuth angle on the BFP.

suppressed when covering the sample with a thin layer of polyvinyl alcohol (PVA). Sublimation is also completely avoided once nanocrystals are cooled down to low temperatures.

2.3.2 Spectroscopy at Cryogenic Temperature

For single-molecule spectroscopy at 2.9 K, we use densely doped DBT:Ac NCX (see Appendix B), which are suitable for being spectrally selected within the experimental range of our tunable narrowband laser (800 GHz around 784.6 nm).

An example of collection of excitation spectra of an individual nanocrystal in the 800 GHz spectral range is shown in Fig. 2.11a, where more than 80 peaks can be distinguished, corresponding to different embedded molecules. Peak intensities appear different consequently to the fixed linear polarization of the pump laser, and therefore to unequal molecules excitation efficiencies. In the histogram of Fig. 2.11b a statistics on 20 NCX, collected in wide-field illumination and at two orthogonal polarizations to excite all the embedded molecules, gives an estimation of the inho-

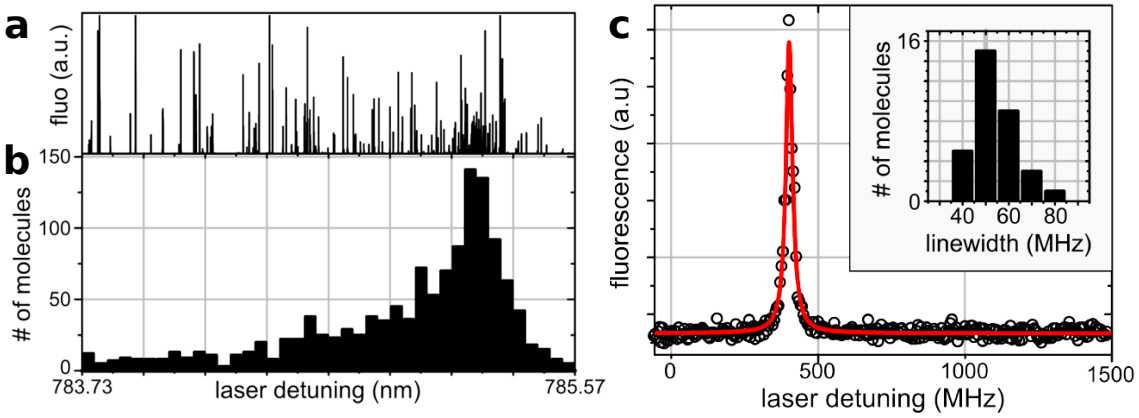

Figure 2.11: **a** - Example of excitation spectra collected from a NCX at 3 K, within a frequency range of 800 GHz around 784.6 nm. Each peak corresponds to a single molecule. **b** - Estimation of the inhomogeneous distribution of the ZPLs obtained from the collection of the excitation spectra from 20 NCX. The distribution yields a standard deviation of of 0.4 nm around a mean value of 785.1 nm. **c** - Resonant excitation spectrum of a single DBT molecule in one Ac NCX measured at 2.9 K. The Lorentian fit (red curve) to the data yields a FWHM of (51 ± 10) MHz. The linewidth distribution in the inset is obtained from the collection of linewidth measuremnts on 35 molecules in different NCX.

mogeneous distribution of the ZPLs of DBT in Ac NCX. We deduce a mean value of the transition frequency equal to 785.1 nm with a standard deviation of 180 GHz. The excitation spectrum of a single DBT molecule, collected with an APD in confocal excitation mode and below saturation, is displayed in detail in Fig. 2.11c. The Lorentian fit yields a FWHM of (51 ± 10) MHz. Repeating this procedure on 35 molecules in different NCX, the linewidth distribution displayed in the inset is obtained, with a low-width cut-off consistent with the lifetime-limited value of 40 MHz. The presence of molecules with broader linewidth can be accounted to the sub-micron size of the NCX and to the consequent interface effects on fluorescence stability. However, the narrow linewidth distribution confirms the high crystallinity of the Ac NCX grown via reprecipitation. In Fig. 2.12a a typical saturation profile and the line broadening of a single molecule in logarithmic scale are evaluated by measuring the maximum fluorescence count rate (blue circles) and FWHM (red circles) of the excitation spectrum for several pump powers. Detected counts yield a saturation intensity $I_S = (0.73 \pm 0.03)\,W/cm^2$ and a maximum number of detected photons $R_\infty = (16.8 \pm 0.04)$ Kcps ($R_\infty = 34$ Kcps if corrected for η_{det}). The power broadening of the homogeneous spectral line $\Delta\omega(I)$ fits perfectly to the expected saturation law (blue line in figure) given by Eq. 2.4, suggesting negligible spectral diffusion.

Then, the absorption frequency stability in time of the single molecules is directly analysed. In Fig. 2.12b, the color map is obtained by repeatedly measuring the excitation spectrum of two DBT molecules in an Ac nanocrystal within the same spec-

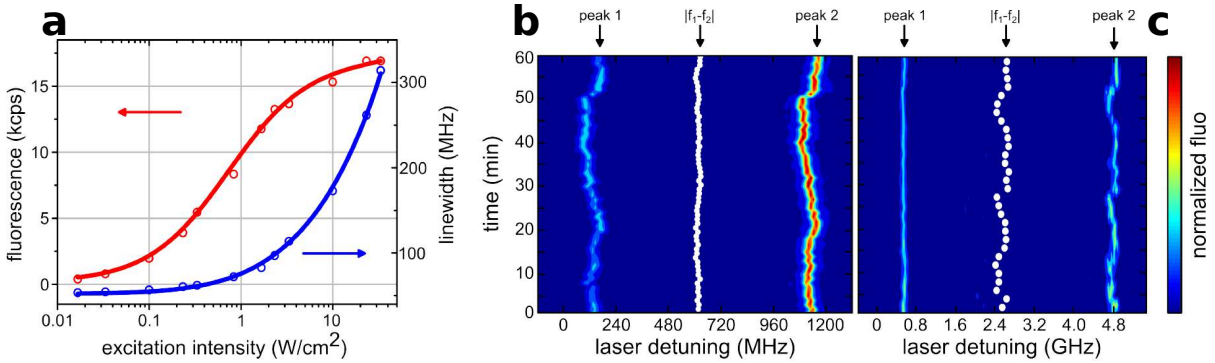

Figure 2.12: **a** - Saturation curve (red) and power broadening (blue) of the homogeneous 00-ZPL collected as a function of the resonant excitation intensity. The saturation curve yields a maximum number of detected photons $R_\infty = (16.8 \pm 0.04)$ kcps. **a,b** - Time traces of the spectral lines of single molecules. In the explored frequency ranges two molecules are present each time. In order to subtract the laser instability contributio, nhe analysis of spectral diffusion is done on the difference of the two peak central frequencies, plotted as white circles. In **a**, the resulting maximum variation is 17 MHz, which is well within the molecule linewidth and suggests absence of spectral wondering. In **b** the only observed case of a molecule undergoing spectral diffusion is displayed, yielding a maximum variation in the difference between the two peak centers of 54 MHz.

tral range, for 1 h. Their comparison is fundamental to infer the pump laser residual instability (the laser diode is thermally stabilized but not referred to any absolute frequency standard). Analyzing the difference of the two peak central frequencies (white circles), we can get rid of the laser contribution, and evaluate a maximum variation within 17 MHz, which is well within the molecule linewidth and suggests absence of spectral diffusion for DBT:Ac NCX at 3 K. In general, in this system spectral diffusion is ascribed to rearrangements of local charges under the influence of the applied electric field. It is worth mentioning that spectral instability, if present, is not necessarily common to all the emitters within an individual nanocrystal, and is rather an independent feature of the single chromophore, originated by its local nano-environment. Performing the same analysis described in Fig. 2.12b on couples of molecules in 8 different NCX, we observe only one molecule undergoing spectral diffusion, shown in Fig. 2.12c. Here, we calculate a $\mathrm{FWHM} = (64 \pm 7)$ MHz for peak 1 and a $\mathrm{FWHM} = (86 \pm 30)$ MHz for peak 2. The maximum variation of their difference is 54 MHz, which gives an estimation of the spectral diffusion observable in DBT:Ac NCX.

In Fig. 2.13a, the effect of temperature on the overall emission spectrum is shown, which is obtained by pumping an individual nanocrystal with the off-resonant laser centered at 767 nm, and by collecting the Stokes-shifted fluorescence. The PSB clearly grows at increasing temperatures, until when the ZPL is no more visible at room temperature conditions (Fig. 2.13b).

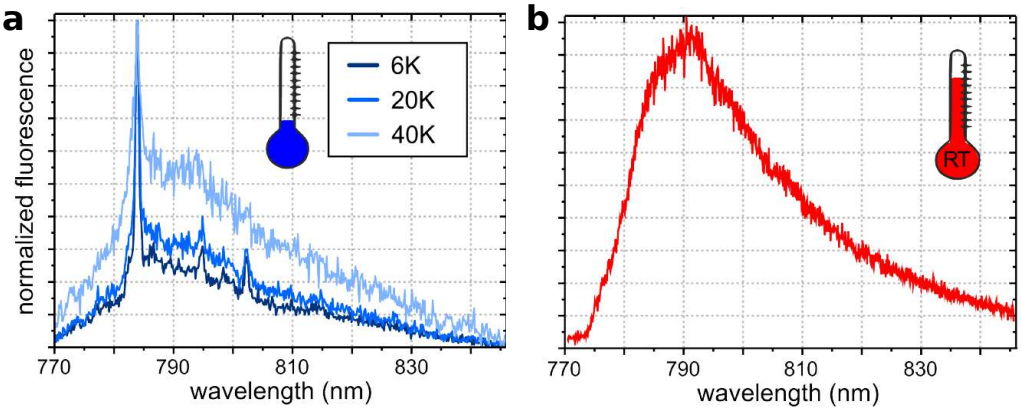

Figure 2.13: **a** - Non-resonant emission spectra at cryogenic temperatures. Below $40\,\mathrm{K}$, the ZPL and the PSB start being resolved. **b** - Non-resonant emission spectrum of DBT molecules in Ac recorded at room temperature.

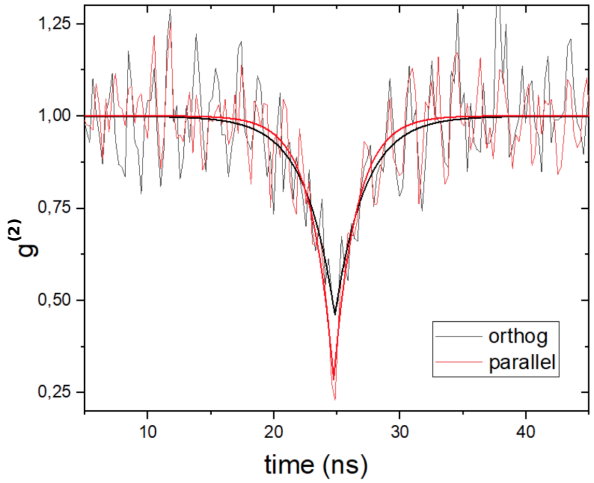

Figure 2.14: **HOM measurement**. The histogram of coincidences in a HOM experiment is reported for parallel (red) and orthogonal (black) polarizations of the two single-photon streams, respectively, together with the corresponding fits. Following from Eq. 2.11, the resulting single-photon interference yields $\sim 50\%$.

Finally, in Fig. 2.14 we report a preliminary measurement of HOM interference. By fitting the anti-bunching dips respectively obtained for parallel and orthogonal polarizations of the single-photon streams, we obtain from Eq. 2.11 an interference ability $|g^{(1)}(0)|^2 \sim 50\%$. Such a precursory result is to be considered a good starting point for quantum coalescence experiments with DBT:Ac NCX. Indeed, optimal interference fringes can be foreseen upon substitution of our $2\,\mathrm{nm}$-bandpass filter, employed to select the ZPL-photons, with a narrower one (notch filter - bandwidth

0.2 nm) able to substantially reduce PSB-photons.

Observation of spatially controlled all-optical frequency tuning of DBT emission

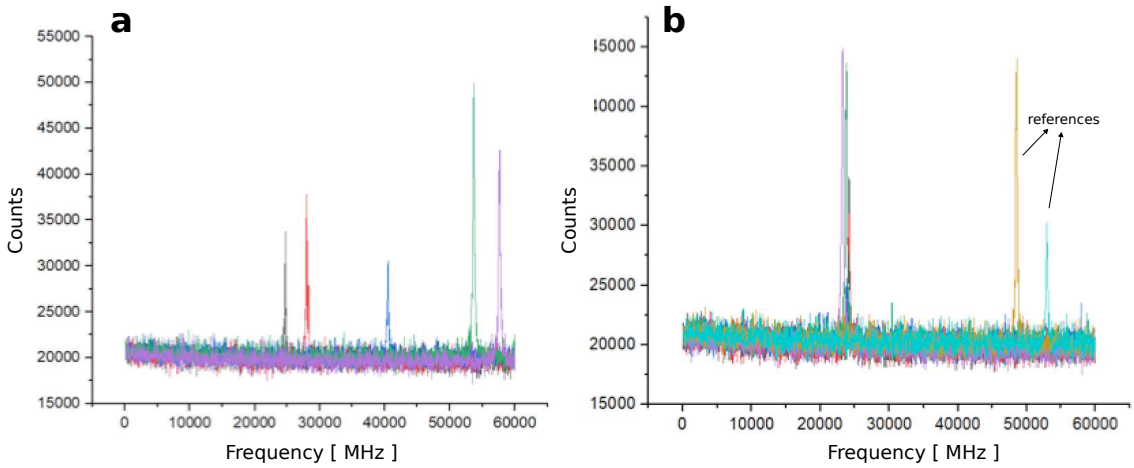

Figure 2.15: **Emission frequency tuning based on laser illumination**. Excitation spectra (at cryogenic temperature) of five molecules (red,black,blue,green,violet) before (**a**) and after (**b**) frequency tuning. In **b**, where other two molecules are shown as references, frequency matching is achieved within few linewidth range.

We conclude the chapter with preliminary results on the observation of the ZPL shift in DBT:Ac NCX consequent to laser illumination, without any externally applied electric potential. We have investigated the phenomenon and found that the shift amount is linear with excitation power and exposure time. In particular, the shift is induced by exciting the nanocrystal in confocal mode, and is detected by measuring the excitation spectrum, with the resonant laser. The full analysis of the physical mechanism is still in progress, but the current most reasonable explanation is that laser excitation induces a migration of charges in the Ac matrix, which is responsible of a local Stark shift effect. The phenomenon is especially interesting because the modification of the transition frequency is permanent. Furthermore, compared to the application of an external voltage for Stark shift effects, this approach enables high precision manipulation to the level of single-molecule addressing. A limitation in using electrodes is that a relatively large area of the sample is involved, with several molecules undergoing a shift all together. In this other case instead, each single ZPL can be independently modified and tuned to a specific frequency. Following this method, in Fig. 2.15a,b preliminary results demonstrate successful matching of the transition linewiths of several molecules (the excitation spectra of the molecules is compared before (**a**) and after (**b**) detuning).

3

Single Molecules Applied in Quantum radiometry

In this chapter we show that our molecule-based SPS can find direct application for quantum radiometry. We use here Ac nanocrystals doped with single DBT-molecule concentration integrated in a basic planar antenna configuration. We demonstrate at cryogenic temperatures narrow-band emission and high purity of the single-photon stream along all the range of photon fluxes explored ($(10^5 - 10^6)$ photons/sec). With such a combination of properties, the molecular SPS is deployed as low-photon-flux reference for the calibration of a silicon Single-Photon Avalanche Detector (SPAD) against a low-noise analog silicon photodiode.
At first we present a metrological characterization of the source which encompasses the evaluation of the intensity, purity and bandwidth of the singe-photon emission. In the second part of the chapter we discuss the experimental results for the direct calibration of a SPAD, based on the developed SPS.

Sources of single photons, besides being key components for linear optical quantum computing (LOQC) and quantum communication [245], turn out to be ideal sources for quantum radiometry, where low photon fluxes (in the fW-range) have to be measured with low uncertainty. Indeed, current standards do not provide constant adjustable fluxes for calibrating single photon detectors and consequently all optical elements [246, 247]. Even in the intermediate step of bridging the radiant power from single photon streams to the regime accessible with standard silicon photodiodes (calibrated against the primary standards), the problem of fluctuations in the average photon number per unit time arises in the case of attenuated lasers [248, 249] and a sub-Poissonian photon stream would be desirable. Although in practice single-photon sources are never ideal due to the non-unitary collection and quantum efficiency, they may provide a reproducible photon flux once metrologically characterized. In fact, from the quantum theory of photodetection (see e.g. Ref. [83]), considering the photon count statistics measured in a time interval of Δt, the relationship between the variance in the measured photon flux $(\Delta N)^2$ and the corresponding variance in the emitted photon flux $(\Delta n)^2$ in the same time interval is given by $(\Delta N)^2 = \eta(\Delta n)^2 + \eta(1-\eta) < n > /\Delta t$, where η is the overall emission, collection and detection efficiency. In other words, the advantage of using photon Fock states with respect to weak coherent pulses, consists in a factor $(1-\eta)$ lower in the variance of the measured photon flux. In case of pulsed excitation and ideal photon source, n is exactly the pump repetition rate, whereas for continuous wave (CW) pumping, the maximum average photon flux is essentially determined by the inverse of the excited state lifetime $1/\tau$. In both cases a sub-Poissonian photon stream is obtained whose variance can be related to the time-dependent Mandel's parameter as discussed in Ref. [29].

In this respect, as discussed in the previous chapter, DBT molecules hosted in an Ac matrix show an unmatched combination of suitable properties in very simple experimental configurations: quantum yield close to unity, pronounced branching ratio in favor of the narrowband ZPL at cryogenic temperature and photostable emission [48, 46].

Since a high photon flux is relevant for applications in quantum radiometry, to maximize collection efficiency of single-molecule fluorescence we adapt the multilayer configuration discussed in Ref. [57]. In the work reported therein, a planar directional antenna is realized by embedding a DBT molecule within dielectric spacers and two metal reflectors. In particluar, the antenna optimal working region is defined for a dipole-to-gold distance of $\sim$ 130 nm, for which the single molecule ration is effectively funneled into narrow collection angles. A simple and cost-effective adaptation of this scheme consists in depositing our $\sim$ 200 nm-thick DBT:Ac NCX over a gold mirror (see Fig. 3.2b). In such a way, isolated single molecules satisfy, in average, a dipole-to-gold distance of $\sim$ 100 nm, which maximizes the emission directionality

within a small angle around the polar axis [250]. Furthermore, single-molecule doped DBT:Ac NCX enable single-emitter addressing in off-resonant excitation, therefore allowing the deployment of the entire 00-ZPL single-photon stream.
In the following sections, we briefly report on the characterization of the 00-ZPL single-photon stream, which is then effectively exploited for the calibration of a single-photon detector directly against a classical silicon photodiode. This, is in turn traced to the primary standard for optical radiant flux, i.e. the cryogenic radiometer. The next step from this radiometric experiment, is moving to a scheme based on the pulsed excitation of the molecule-based quantum emitter, which under this condition might realize a standard of low optical radiant fluxes.

The fundamental results in this chapter are reported in *A molecule-based single-photon source applied in quantum radiometry* by P. Lombardi, et al., *Advanced Quantum Technologies*, in press.

3.1 Setup and Methods

For the experiment reported in this chapter, we adapt the setup described in Section 2.2.2. In general, measurements are carried at cryogenic temperatures and under CW-laser excitation, in confocal mode. Preliminary selection of the optimal emitters, in terms of distance from the metallic layer, is achieved by choosing the brightest NCX in off-resonant wide-field illumination and imaging on the camera. Indeed, the spatial distribution of the molecule position inside the host matrix translates into a statistics of distances from the metallic layer, with consequent unequal collection efficiencies. Once a promising nanocrystal is selected, the optical characterization of the source is performed by switching to confocal illumination.
Ideally, application in quantum radiometry requires control over the photon flux of the SPS in a wide dynamic range. Therefore, here the dichroic mirror in the setup (see Section 2.2.2), used to reflect the light towards the objective lens and conversely transmit the incoming signal, is substituted with a more efficient beam sampler BS (Thorlabs BSF20-B) (see Fig. 3.1). Indeed, the BS exhibits $\sim 0.1/0.9$ reflection/transmission coefficients compared to the $\sim 0.05/0.6$ coefficients of the dichroic mirror. Then, a second bandpass filter (BP2, Semrock TBP01- 790/12), whose transmission window can be shifted to the blue by tilting, is added in the detection path, if selection of the 00-ZPL line is required. In fact, while in the previous chapter densely doped DBT:Ac NCX are employed for single-molecule spectroscopy at cryogenic temperature, here NCX with single-molecule doping (see Appendix B) assure spatial isolation. Therefore individual molecules can be excited in off-resonant illumination and the Stokes-shifted 00-ZPL transition can be filtered out. Hence, the photon flux is redi-

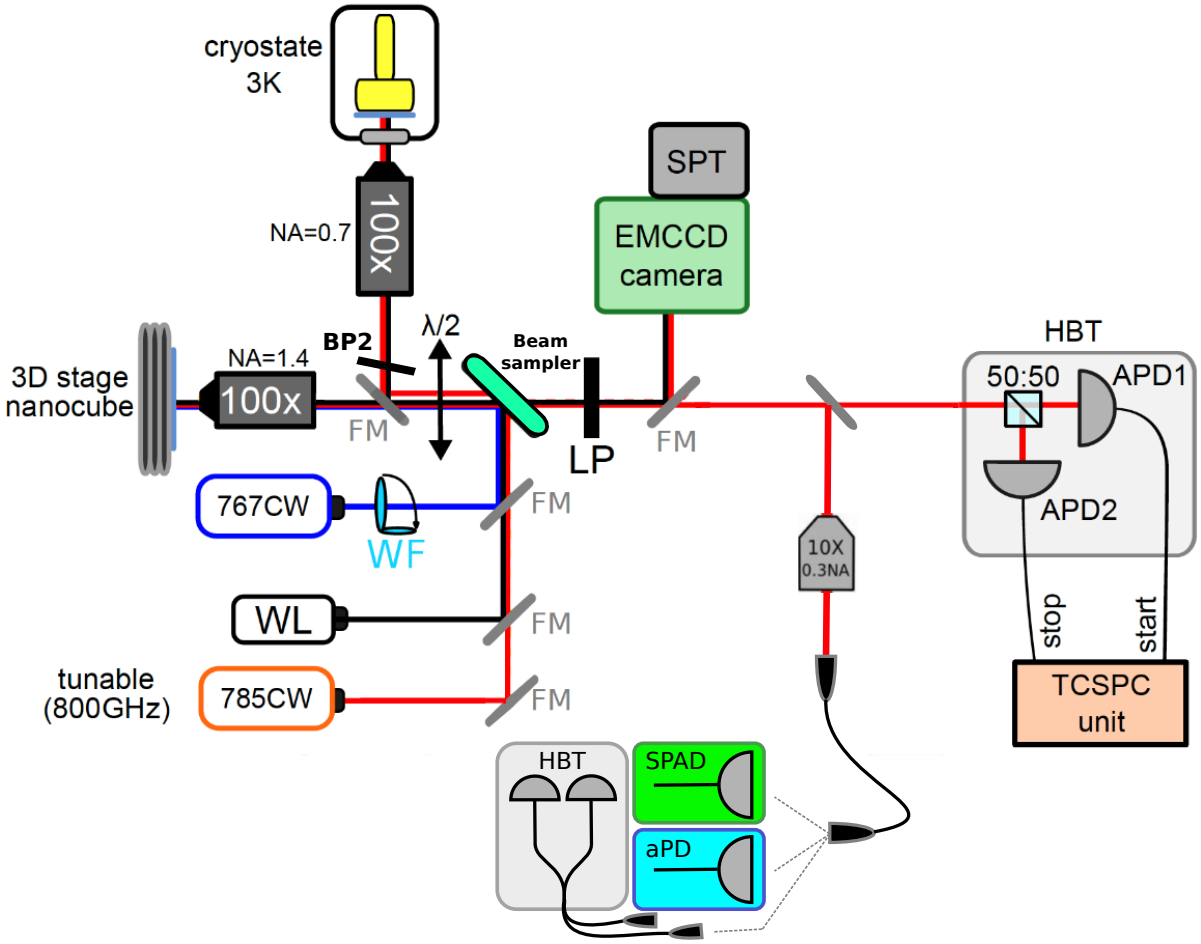

Figure 3.1: **Setup**. Scheme of the experimental setup. With respect to the one already presented in Chapter 2, in Fig. 2.5, here the dichroic mirror is substituted with a beam sampler, for improved collection of the emitted fluorescence. Furthermore, for the SPAD calibration measurements, a fiber delivers the single-photon stream to either a low noise analog Si detector (aPD) or to a calibrated Si SPAD. Alternatively, through a fibered-BS coupled to two fibered SPADs, $g^{(2)}$-measurements can be performed in a HBT configuration.

rected to a fiber coupling system (see Fig. 3.1) consisting in a low magnification objective lens (Olympus UPlanFL N, $10\times$, $N.A. = 0.30$, transmission at $785\,nm = 0.8$) focusing light into a cleaved multi-mode fiber (Thorlabs M42L02, core diameter $50\,\mu$m, $N.A. = 0.22$). For the calibration measurements, the fiber can deliver the photon stream to either a low noise analog Si detector (Femto FWPR-20-s), or to a calibrated Si SPAD (Perkin Elmer SPCM-AQR-13-FC). Alternatively, the fiber can covey the photons to a couple of fibered SPAD in Hambury- Brown and Twiss (HBT) configuration (Excelitas 800-14-FC) through a fiber-beamsplitter (Thorlabs FCMM625-50A-FC) (in

substitution of the free space BS used in the previous chapter), for the $g^{(2)}(\Delta t)$ analysis.

Traceability chain for the calibration of the reference Si-detector

The ultra-low noise Si-detector consists of a fibre coupled Si photodiode of $1.1 \times 1.1\,\mathrm{mm}^2$ active area and a trans-impedance amplifier with gain of 1×10^{12} V/A. The minimum noise equivalent power (NEP) of the detector is $0.7\,\mathrm{fW/Hz}^{1/2}$. Its spectral responsivity $S_{Si}(\lambda)$ is determined by calibrating it against a working standard traceable to PTB's primary standard for optical power, i.e. the cryogenic radiometer [5]. In a first step of the complete traceability chain (see Ref. [72] for a more detailed scheme) a Si trap detector is calibrated against the cryogenic radiometer at specific wavelengths and optical powers (μW). Then, a spectrally flat detector, i.e. a thermopile detector, is used to determine the responsivity of a Si photodiode, which acts as working standard at the specific wavelength of the photons emitted by the single photon source, i.e. $785.6\,\mathrm{nm}$. Finally, the spectral responsivity of the low-noise Si-detector used for the calibration of the Si-SPAD detector is obtained by means of the double attenuation calibration technique described in Ref.[8] and the Si photodiode working standard. The spectral responsivity obtained at $785.6\,\mathrm{nm}$ is,

$$S_{Si} = (57.52 \pm 0.58) \times 10^{-2}\, A/W\,. \tag{3.1}$$

The uncertainty of the spectral responsivity here reported corresponds to a standard uncertainty (k = 1).

Evaluation of Emitter Brightness

The brightness of the SPS can be evaluated by comparing the count rate R_{exp} read by the SPAD with the ideal maximal rate of the source R_∞ ($R_\infty = 1/\tau$ in case of CW excitation; see Sec. 1.1.2). The two rates are related through the expression

$$R_{exp}/R_\infty = \beta_{det}\beta_{opt}\beta_{col}\beta_{mol}P \tag{3.2}$$

where β_{det} is the quantum efficiency of the detector, β_{opt} is the overall optical setup efficiency, β_{col} the collection efficiency of the first lens (objective) considering all radiative and non-radiative losses, β_{mol} the probability for the molecule to emit a stored excitation as a photon in the ZPL, and P accounts for the efficacy of the pumping illumination. Consequently, the brightness at first lens is determined as

$$B = \beta_{col}\beta_{mol}P = R_{exp}/R_\infty/\beta_{det}/\beta_{opt} \tag{3.3}$$

We here anticipate that according to the photon flux characterization presented in the next section, the evaluation of the detector efficiency in Sec. 3.3, and the overall optical setup efficiency ($\beta_{opt} \sim 0.18$; see Appendix C for the table reporting the efficiency of each element in the setup), the brightness of the source at first lens (for $N.A. = 0.67$) amounts approximately to $B \sim 3.5\%$.

3.2 Metrological Characterization of the SPS

Overall, the developed source shows promising characteristics in order to operate as a secondary standard source for SPAD calibration. As a rule of thumb, a single-photon source delivering a photon stream with flux at detector > 1 Mphoton/s , $g(2)(0) < 0.1$, and spectrum FWHM< 2 nm, yields comparable results in the calibration process as an attenuated laser. These figures arise from the following considerations: a photon flux of 1×10^6 photons per second at a wavelength of ~ 785 nm corresponds to ~ 250 fW of optical power. As described in Ref. [251], this power level is reasonably measurable with Silicon photodiodes and is therefore set as a lower limit. The bandwidth limit of 2 nm reduces the measurement uncertainty associated with the spectral sensitivity of the Silicon detector itself. Finally, here we employ a CW-excitation scheme, but a method based on the pulsed excitation of such a quantum emitter (planned as one of the next steps of the project) would get beyond the break-even point and become advantageous with respect to the use of attenuated laser pulses. In particular, under the condition $g^{(2)}(0) = 0.1$, the influence of multi-photon events on the measured detector efficiency would be comparable to the one obtained in the Poissonian regime for an average number of photon per detector dead-time of 0.1 [249].

In Fig. 3.2a, a typical wide-field fluorescence map of the sample (Fig. 3.2b) is shown, from which the brightest individual NCX are chosen to be studied in confocal mode. The emission spectrum of the embedded single molecule, which is metrologically characterized and deployed in this chapter, is shown in Fig. 3.3a, where the peak around 767 nm is due to the residual laser light, whereas the most intense signal is associated to the molecule 00-ZPL transition For the characterization, the peak is then filtered in a bandwidth of about 2 nm by carefully setting the BP2 filter (see Sec. 3.1). In the inset of Fig. 3.3a, the resulting spectrum is reported. It appears limited by the spectrometer resolution (~ 0.2 nm), but it can be independently measured via excitation spectroscopy, finding a linewidth smaller than 100 MHz. In particular, we report a ZPL linewidth of (65 ± 20) MHz, quite close to the natural Fourier-limited value of (36 ± 3)MHz, corresponding to the average lifetime of the excited

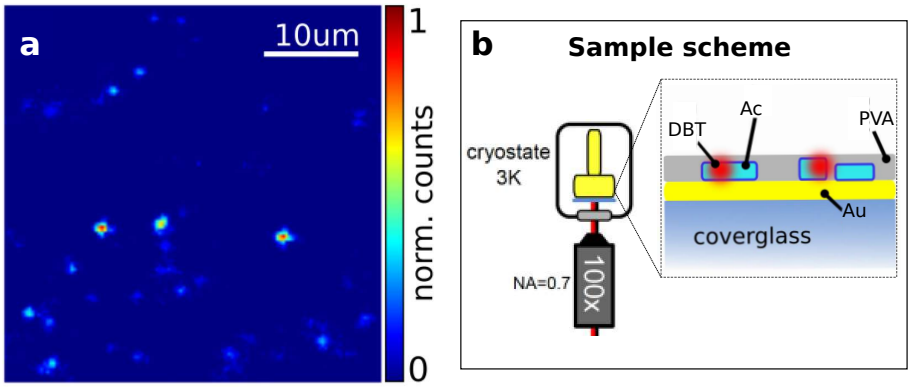

Figure 3.2: **a** - Wide-field fluorescence image on a region of the sample showing bright NCX. **b** - sketch of the device operated as single-photon source at cryogenic temperature: Au – gold, Ac – anthracene, DBT – dibenzoterrylene, PVA – polyvinyl alcohol.

state $\tau = (4.4 \pm 0.4)$ ns, which is in this case obtained from $g^{(2)}(\Delta t)$ measurements at low pumping rate. We attribute the residual dephasing contribution to the operating temperature (3 K), which is close to the activation temperature for DBT:Ac system [48, 46, 252]. On this merit, an ultimate improvement of the single-photon coherence requires an upgrade of the cryostation setup to enable lower target temperatures. As preliminary next step we will try to realize a better thermal contact between the sample and the cold finger of the cryostat, which at the moment is realized by application of a silver paste and can in some cases be reduced by the formation of air bubbles while gluing the sample. A possibility is to induce a mechanical pressure onto the sample substrate via e.g. designated screws, in order to avoid or reduce the presence of air in the conductive paste.

The employed CW-pumping scheme allows for the highest average photon rates at the detector for a given overall efficiency (see Sec. 1.1.2). On the other side, unlike the case of pulsed operation (for which the variance in the number of emitted photons is ideally null for all times), this implies a photon statistics becoming Poissonian for long integration times. This owes to the randomness of the excited state decay process, which was already mentioned in Sec. 1.1.1 (only few photons are precisely emitted after an excited-state lifetime τ; many are emitter at shorter or longer times). Using the fibered HBT configuration or the single fiber directly coupled to the APD, respectively, the photon flux (Fig. 3.3b) and the $g^{(2)}(\Delta t)$ function (Fig. 3.3c,d) are measured as a function of the excitation power. The molecular-based SPS delivers at the fiber-coupled detector up to 1.4×10^6 photons per second, keeping high purity of the single-photon emission for any set rate (in particular, $g^{(2)}(0) = 0.08 \pm 0.01$ at maximum photon rate, without deconvolving for the SPAD response function). These

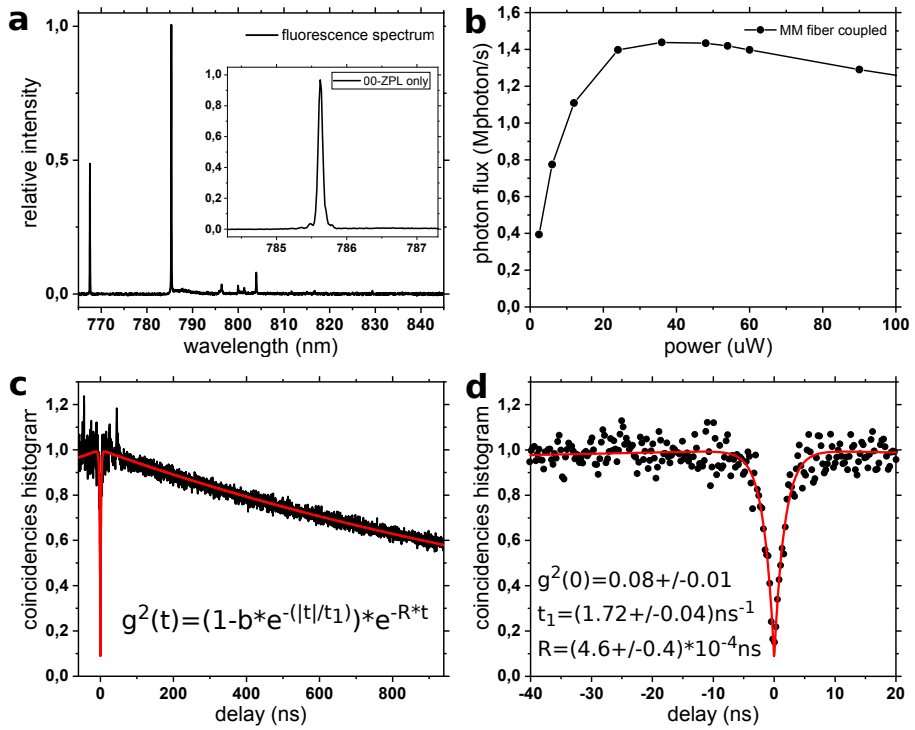

Figure 3.3: **Metrological characterization** of the molecule emission. **a** - Fluorescence spectrum; inset: fluorescence spectrum when filters are set to select a 2 nm-wide spectral window around the molecule 00-ZPL (785.6 nm in this case). **b** - Photon flux detected with the SPAD as a function of the laser pump power. **c** - Normalized histogram of the inter-photon arrival times for maximum photon flux operation (30 μW pump power). **d** - Zoom on the histogram in **c** around zero time delay, representing $g^{(2)}(\Delta t)$: the anti-bunching behaviour shows the high purity of the single-photon stream. The red lines are a fit to the data with the expression shown in **c**, while best estimation of the fit parameters is reported in **d**.

characteristics are outstanding considering quantum emitters operated in absence of optical cavities or local nano-structuring of the host material, especially in terms of the detected power in a given frequency interval. Indeed, according to the linewidth measurements reported in the previous chapter, around 2/3 of the collected photon flux, i.e. more than 0.9×10^6 photons/s, fall within a 50 MHz-wide spectral window. Regarding the $g^{(2)}(\Delta t)$ function, it is fitted with the expression

$$g^{(2)}(\Delta t) = 1 - be^{-|\Delta t|/\gamma}e^{-R\Delta t} \tag{3.4}$$

which differs from Eq. 2.10 for the last term $e^{-R\Delta t}$ accounting for the effect of the arrival time statistics, considering Poissonian distribution (R is the average count rate per SPAD). In first approximation a bunching contribution to the histogram profile given by the intermittency in fluorescence emission (blinking), occurring when the molecule falls in the meta-stable triplet state, can be excluded. Indeed, in DBT:Ac sys-

tem, as discussed in Section 2.1.1, this ISC yield is smaller than 10^{-5}, and the triplet life-time is limited to few microseconds. These characteristics lead to dark periods of few microseconds separated by millisecond-long bright periods, with a negligible bunching contribution to the $g^{(2)}(\Delta t)$ profile. This assumption is confirmed by the agreement between the value for R obtained by the fit and the count rate directly read by each detector. It should be also noted that the saturation curve reported in Fig. 3.3b decays for very high pump powers. To the best of our knowledge, this behavior has not been reported before for organic molecules and is currently under investigation [253]. Among different possible explanations, there could be a power-dependent heating of the host matrix induced by the pump light, with a corresponding reduction of both the molecule absorption cross-section and emission branching ratio in the spectrally selected transition (ZPL). An alternative hypothesis relies on a more complex non-linear dynamics occurring in the system, resulting in a power-dependent shelving effect. Despite the physical origin of such behaviour, which limits the ascessible photon flux, this is sufficient for the proposed radiometric applications.

In the framework of metrological applications, it is relevant to determine also the

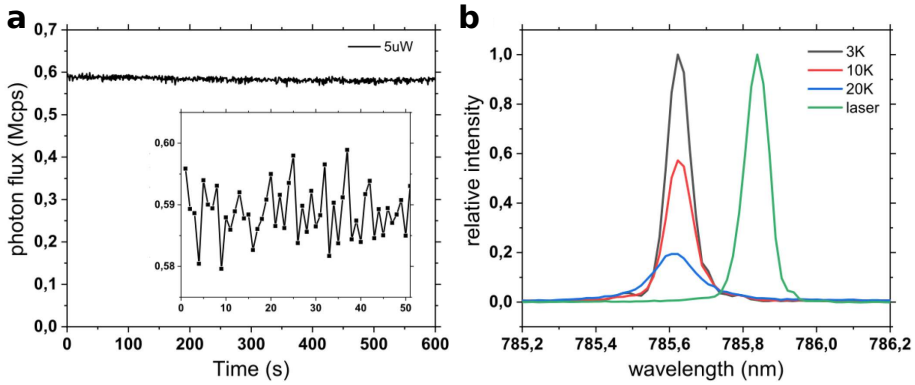

Figure 3.4: **a** - Temporal stability of the photon flux under CW excitation. We report a drift of around 2% due to the pump light alignment within a time interval of 10 minutes, and less than 1% fluctuations on a time-scale of few seconds (inset). **b** - Spectral response of the narrowband line as a function of temperature, for a fixed pump power equal to 30μW. A lower absorption cross-section is observable already at 10 K, while spectral broadening is evident at higher temperature only, due to the limited spectrometer resolution (~ 0.2 nm estimated from laser line (green curve)).

stability of the photon flux over time. We report less than 1% fluctuations on short time-scale (seconds), and a drift of around 2% due to the pump light alignment within a time interval of 10 minutes (see Fig. 3.4a). Another set of measurements has been devoted to the determination of the highest temperature at which the device is able to guarantee a photon stream with reasonable optical properties for metrological applications (see discussion in Section 3.3). Raising the temperature indeed, line-broadening is expected, together with a lowering of both the absorption cross section

and of the branching ratio into the 00-ZPL, as discussed in Section 2.1.2. In Fig. 3.4b, the emission spectrum for different temperatures is shown for a fixed pump power. Due to the limited resolution of the spectrometer, broadening of the line becomes evident only around 20 K. However, the combined effect of the other two aspects is effective already at 10 K and can be only partially mitigated by a stronger excitation. Table 3.5 gathers the results of this analysis, which fixes the maximal operating temperature of the device to approximatively 20 K.

Temperature [K]	Power [a)] [μW]	Max photon flux [Mphoton/s]	$g^{(2)}(0)$
3	30	1.36	0.08+/-0.01
5	42	1.27	
10	42	1.20	
15	42	1.09	0.06+/-0.02
15	72	1.19	
20	72	1.08	0.09+/-0.02

a) power measured at the entrance of the objective lens

Figure 3.5: **Table** - Attainable flux and purity of the single-photon stream for different temperatures

3.3 Calibration of a Single-Photon Detector

In this work, the detection efficiency of a Si-SPAD detector is determined by comparing the photon flux measurements of the SPS performed with the SPAD detector (device under test) and an analog reference Si-detector. The reference detector and the SPAD are equipped with a FC/PC fiber connector and their coupling efficiency is optimized for a multimode fiber. The photon flux measurements are performed sequentially. Thus, the SPAD detection efficiency η_{SPAD} is determined as $\eta_{SPAD} = \frac{<N_{SPAD}>}{<N_{ref}>}$, where N_{SPAD} is the count rate (counts/s) measured with the

SPAD detector, while N_{ref} is the photon flux rate derived from the source optical flux measurement ϕ_S and the photon energy E ($E = 2.53 \times 10^{-19}$ J for photon at 785.6 nm). ϕ_S is obtained as the ratio between the measured average photocurrent $\langle I_f \rangle$ and the reference detector responsivity $S_{ref} = (57.52 \pm 0.58) \times 10^{-2}$ A/W), and hence $< N_{ref} >= \frac{<\phi_S>}{E} = \frac{<I_s>/S_{ref}}{E}$. Fig. 3.6 shows the detection efficiency ob-

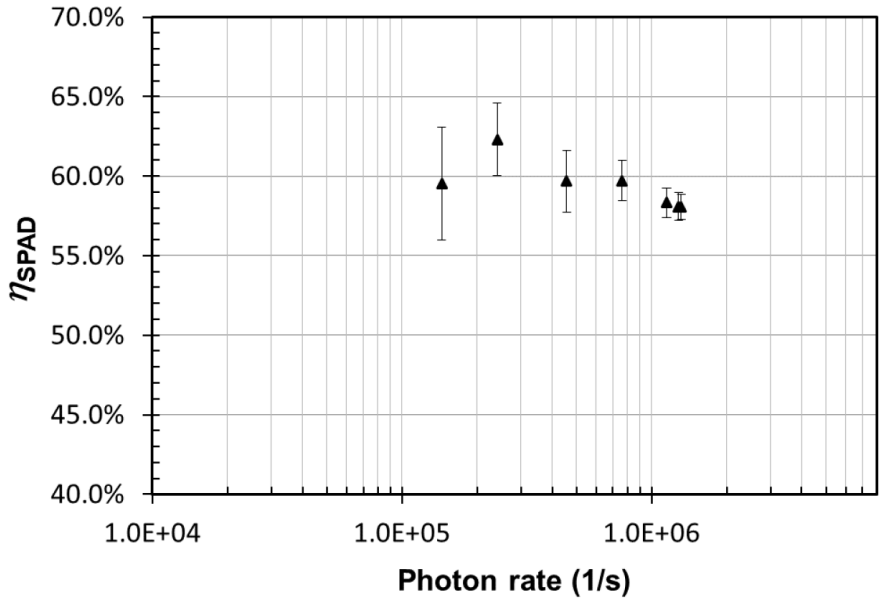

Figure 3.6: Calibration result for the SPAD detection efficiency (Perkin Elmer, SPCM-AQRH- 13-FC) using the molecule-based SPS and a low-noise reference analog detector.

tained for the SPAD detector (Perkin Elmer,SPCM-AQRH-13-FC) within the photon rate range from 0.144 Mphoton/s to 1.32 Mphoton/s, which corresponds to an optical power range between 36.5 fW to 334 fW. To the best of our knowledge, such broad flux interval was never explored so far with a SPS, in the framework of detectors calibration. Interestingly, the molecule emission rate approaches the regime in which the detector dead time (τ_{dead}) affects the measurement of the detection efficiency η_{SPAD} [249]. The standard uncertainty associated with each measurement value is indicated by an error bar (according to Ref. [5]). The achieved uncertainty varies within the range from 2% to 6%, depending on the photon rate, i.e. the lower the photon rate, the higher is the uncertainty. This can be ascribed to the reference detector random noise, which is the highest contribution to the total uncertainty at fW-levels. The final value obtained for the Si-SPAD quantum efficiency is $\eta_{SPAD} = (0.603 \pm 0.012)$.

In order to evaluate the potentiality of the device, we can consider the attainable brightness and photon flux in case of optimal operation of the device:

1. From semi-analytic simulations [57], we estimate the collection efficiency with our objective to be around $\beta_{col} \sim 0.35$, which leads to a source quantum efficiency $\beta_{mol}P \sim 10\%$. This value is much lower than the 40% expected from literature, and we attribute this mismatch to the anomalous behaviour presented in Sec. 3.2. Depending on the origin of the photon flux dimming at high power, different strategies can apply to mitigate the effect. In case we are facing the consequences of a local heating of the host matrix, a bath cryostat would help in terms of cooling power. Alternatively, off-resonance pulsed operation is expected to avoid completely the issue provided that the average impinging power is smaller than $20\,\mu$W. In case of multi-photon dynamics, resonant excitation combined with cross-polarized detection should allow efficient pumping for power well below the level of activation of the detrimental effect;

2. β_{col} can be increased exploiting higher N.A. objective lenses (e.g., we estimate $\beta_{col} \sim 0.45$ for $N.A. = 0.8$);

3. in a dedicated optical setup with optimized AR coatings, filters, and optical path length, the overall optical setup efficiency can easily be pushed to $\beta_{opt} = 0.6$;

4. finally, we have demonstrated in Ref.[57] that with the addition of a second metallic layer on top of the Ac nanocrystals, for the appropriate thickness and distance from the bottom mirror the emission of the molecule is further redirected towards the polar axis, resulting in $\beta_{col} \sim 0.55$ for the considered N.A.

According to these considerations, $B \sim 13\%$ and a photon flux at first lens (detector) of ~ 7 Mphoton/s (4 Mphoton/s) for 50 MHz pump repetition rate is expected with the present device. A factor 1.5 enhancement for both quantities is envisioned for the next generation of devices, based on the argument introduced above (point 4).

In conclusion, we demonstrate the realization of an absolute single-photon source based on the emission of an organic dye molecule operated at cryogenic temperature. This result is obtained by linking the single-photon stream generated by the molecule to a national radiometric standard for optical fluxes via an analog Si-detector, calibrated through an unbroken traceability chain and able to read optical radiant fluxes down to a few tens of fW. The source presented here shows significant advances with respect to previous demonstrations in the field of radiometry in terms of flux (1.32 Mphoton/s), linewidth (< 0.2 nm) and purity ($g^{(2)}(0) < 0.1$) of the emission. The traceably measured optical radiant flux adjustable between 37 fW and 334 fW at a wavelength of (785.6 ± 0.1) nm is unprecedented and allows the direct calibration of a single-photon detector (SPAD) through comparison with calibrated high-sensitivity analog Si detector for the first time. The reported single-photon source can in principle be operated in pulsed conditions, with an estimated photon flux of

around 5 Mphoton/s at first lens ($N.A. = 0.67$) for 50 MHz pump repetition rate. Under these conditions the device can work as a predictable true single-photon source whose photon flux is directly tuned by acting on the pump repetition rate, with high reliability and precision also at power levels below the detection limit of conventional photodetectors. Being thus pulsed operation the crucial setup upgrade to implement, the developed device may realize a standard source for quantum radiometry.

In the previous chapter we have characterized the photophysical properties of DBT:Ac nanocrystals. Here, we have demonstrated that such unique optical features are leveraged for an immediate application in quantum radiometry. We have also discussed how, under pulsed-excitation, and with minor setup improvements, we expect to outperform calibration techniques based on attenuated laser pulses.
The following chapters of this thesis work explore different approaches to the integration of such molecule-based single-photon source in hybrid photonic architectures by exploiting the flexibility of polymer materials.

4

3D Integration of NCX in Polymeric Photonic Structures

In this chapter we discuss a hybrid polymeric photonic platform based on the coupling of single molecules to 3D integrated optical elements, patterned via direct laser writing. The compatibility with molecules and the flexibility of the fabrication technique is shown by fully embedding Ac nanocrystals doped with DBT molecules in different architectures. The performances of the hybrid devices and the emitter photophysical properties are investigated. In particular, close-to Fourier limited emission is observed from embedded molecules at cryogenic temperatures, and record photon flux from organic molecules is reported within a micro-dome solid immersion lens design. These results offer unique solutions for the development of integrated devices for photonic quantum technologies.

The realization of a DBT:Ac NCX (Chapter 2) opens the pathway both to deterministic positioning and to the integration in photonic structures. Here, we show how on-chip integration is possible, while preserving the coherence properties of the single-photon emission. In particular, we realize a hybrid photonic platform where single molecules are directly coupled to 3D integrated optical elements. We report on how NCX are fully embedded in the 3D architectures via direct laser writing (DLW) on commercial photoresists. Thanks to the broad flexibility of this lithographic technique, different structures, on silica and on gold substrates and with NCX embedded at different heights, are fabricated. In the following sections, critical aspects like the performances of the hybrid photonic devices under cryogenic cooling, the effect of the whole fabrication process on the emitter quantum coherence, and the residual scattering losses due the emitter inclusion in the photonic structures are investigated.

The fundamental results in this chapter are reported in *A three-dimensional polymeric platform for photonic quantum technologies* by M. Colautti, et al., arXiv:1909.07334 *Under submission.*

4.1 3D direct laser writing

Direct laser writing is a lithographic technique which allows to write polymeric structures in three dimensions with sub-micron spatial resolution. It is based on a non-linear photo-polymerization process which requires high intensities, and is initiated by tightly focusing ultra short laser pulses into photosensitive liquid materials. Within the diffraction-limited focus volume, two-photon absorption is exploited to confine the effectively exposed region to the very central part of the laser spot, where the Gaussian intensity distribution overcomes the threshold for polymerization. In this way, non-linear laser-induced crosslinking transforms the liquid resist into solid polymer, within a resolution volume that breaks the diffraction limit. The precise dimensions of such a volume, of ellipsoidal shape and termed *voxel*, clearly depend on the power threshold for the two-photon absorbance in the photo-sensitive medium and on the objective optical power. In practice, any 3D structure can be fabricated voxel by voxel by scanning the laser focus along 3D trajectories within its target volume.

4.1.1 Two-photon polymerization

Photo-polymerization refers to the light-initiated chemical reaction where isolated monomer molecules in a liquid state form polymer chains and result in a solid state. Via cross-linking, the different polymer chains connect to each other in three-dimensio-

nal networks and the rigidity of the structure is further increased. In particular, monomer chain growth is promoted by the addition of molecules, called photo-initiators, which after photon absorption rapidly decay into free radicals activating a cascade reaction. Notably, by chemical engineering of the monomer structure, the photophysical, chemical and mechanical properties of the solidified resin can be readily tuned.
Highly resolved 3D lithography is achieved through the non-linear process of two-photon absorption polymerization (TPP) (Fig. 4.1: 2PP). In TPP, the transition of photo-initiators is resonant to the sum of two absorbed photons and the cross-section depends on the squared intensity of light. It is this non-linearity in the process threshold that confines the reaction within the laser focus, providing high spatial resolution and feature sizes down to $\sim 100\,\mathrm{nm}$[1] (as sketched in Fig. 4.1). Another advantage of TPP is that many polymers have next-to-none linear absorption in the near-infrared, allowing the laser to penetrate deeply into the material. These two aspects allow creating nano-structures that are otherwise not possible to produce. Conversely, linear absorption mechanisms (see Fig. 4.1: 1PP) are limited in resolution and have poor penetration ability, enabling polymerization just on the surface of the liquid resist.

4.1.2 Setup

In this work we employ the DLW commercial workstation Photonic Professional system (Nanoscribe GmbH), shown in Fig. 4.2. The source, is a femtosecond($120\,\mathrm{fs}$)-pulsed erbium-doped fiber laser (see optical scheme in Fig. 4.3), with central wavelength at $780\,\mathrm{nm}$, $100\,\mathrm{MHz}$ repetition rate and $60\,\mathrm{mW}$ maximum power. A drop, or a spin-coated layer, of photo-sensitive resist is previously deposited on a coverglass, and an immersion oil objective (100X, Zeiss Plan Apocromat, NA = 1.4) in contact with the medium (dip-in laser lithography mode), is used to focus the laser beam at the substrate-resist interface. After the writing process, the unexposed photoresist is eventually removed in a development bath.

Within the optics cabinet (see Fig. 4.3), an acusto-optic modulator (AOM) is combined with an electronic shutter to tune the laser power. The system comprises an inverted microscope both to focus the laser beam into the photoresist and for the observation of the printing process via a CCD camera. The sample is inserted through a holder in a three-axes motorized piezo, mounted on a stage (see Fig. 4.2). While the stage allows manual coarse translation on the whole sample ($\approx 2 \times 2 \times 2\,\mathrm{mm}^3$), writing is actuated via the piezo fine positioning along software-monitored 3D trajec-

[1] In TPP, the upper threshold of the dynamic range for controlled polymerization is laser-induced breakdown. When laser power is excessive, surface ablation and micro explosions in the bulk medium are detrimental to high-resolved patterning.

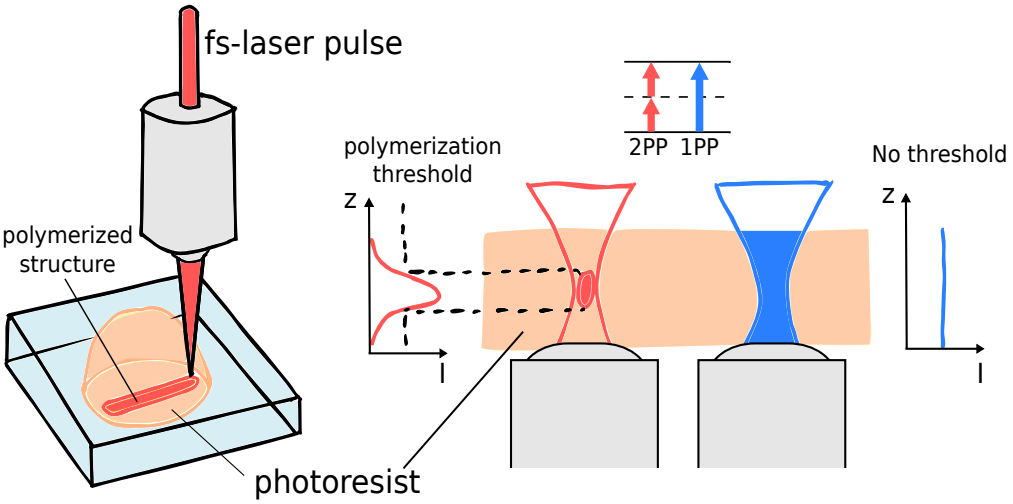

Figure 4.1: **DLW**. **a** - Illustration of the DLW process with a negative-tone photoresist. By moving the sample (or the laser focus), arbitrary 3D trajectories can be polymerized via two-photon absorption, and with spacial resolution below the diffraction limit. **b** - Comparison between one-photon (1PP) and two-photon (2PP) absorption processes within a thin layer of photoresist material. 1PP leads to uniform polarization over the entire penetration volume (which is limited to the surface of liquid resists). The non-linear 2PP process, depending on the field intensity, enables to confine the polymerization within a small volume at the laser focus.

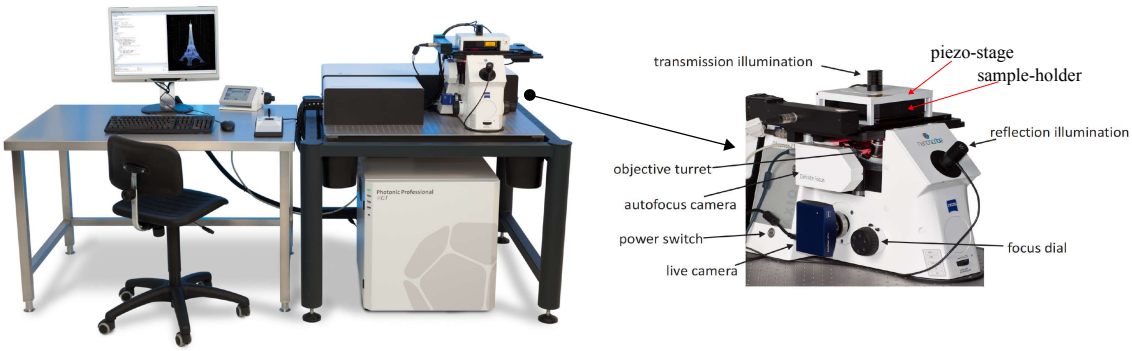

Figure 4.2: Overview of the Photonic Professional (GT) DLW workstation and details of the microscope with its major components.

tories with respect to the laser focus. In particular, the piezo works within the coordinate system of $300 \times 300 \times 300\,\mu\text{m}^3$, centered at the current stage position. The DLW process is fully-automated, and is driven by input files, in General Writing Language (GWL), which configure the system parameters and describe the trajectories which build up the target structure. The whole system is installed on an optical table for isolation from vibrations, which are detrimental to attain sub-micron scale features.

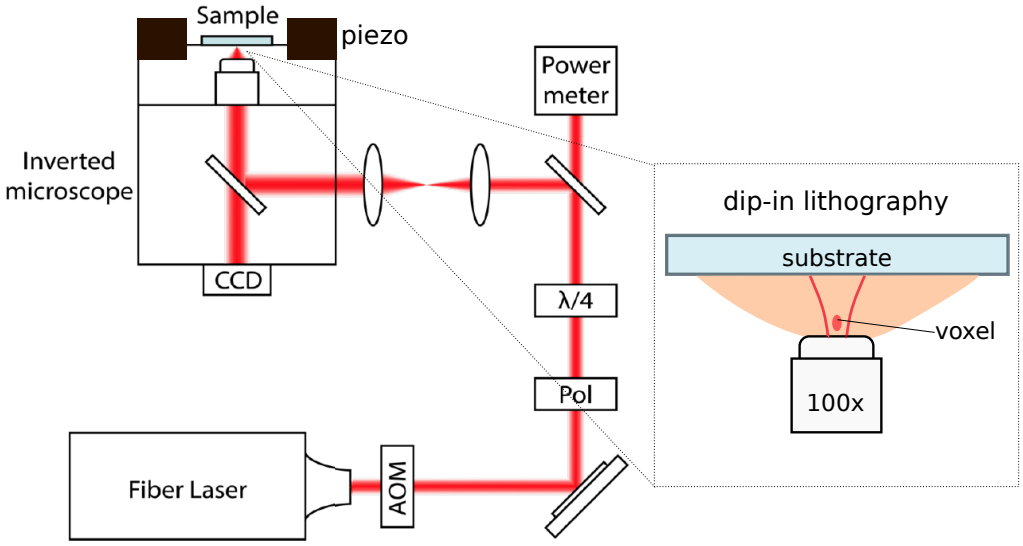

Figure 4.3: Illustration of the optical setup of the commercial workstation. It consists of a piezo-stage mounted on top of an inverted microscope and a pulsed laser with 120 fs pulse-width, 780 nm wavelength and 100 MHz repetition rate. The laser power is calibrated through an acousto-optic modulator (AOM) and a high numerical aperture (N.A. = 1.3) objective tightly focuses the light into a tiny volume (i.e. the voxel). A CCD camera allows for white-light imaging of the sample. In this thesis work we employ dip-in lithography, i.e. we fabricate the structures with the objective in direct contact with the resist, for index matching (inset).

Practically, the GWL-file must be customed for every set of structures, and the writing parameters, mainly laser power and writing velocity, are chosen upon characterization of the voxel, which defines the resolution of the polymerization process for each specific photoresist. Then, the planned 3D architectures must be translated in layers of optimized trajectories in order to obtain the desired surface smoothness, structure rigidity and dimensions.

4.2 Platform Concept

The broad flexibility of the photo-lithographic technique enables here to envision the DBT:Ac NCX embedded at variable heights in different 3D architectures, fabricated either on silica or on gold substrates (the detailed fabrication protocol is explained in the next section). This ability opens the pathway to future developing of suitable integrated devices for many applications, which could hardly be fabricated through planar technologies. These include the realization of quantum effects with increasing size systems, such as the interference among more than two particles, using on-demand single photons generated by individual molecules embedded e.g. in 3DL-

written polymeric tritters [254]. In general, the proposed approach allows conceiving e.g curved-surface optical elements [255], 3D photonic crystals [256], free-standing structures for tunable and optomechanical applications [257], and effective polarization controls [65], everything on-chip and by integrating molecule-based quantum emitters for single-photon generation.

The envisioned 3D platform is shown in the respective artistic views of Fig. 4.4a,b,c. The integrated emitter is represented by a dipole (black arrow) and red arrows highlight the promoted direction for the emitted fluorescence. Fig. 4.4a shows a microdome on a transparent dielectric substrate (silica, refractive index $\mathrm{n} = 1.45$). This is a modified Weierstrass SIL (see Sec. 1.2.2), consisting of a hemisphere and a cylindrical base built on top of one DBT:Ac nanocrystal.
NCX are previously deposited on the substrate (grey in the Figure and with a zoom on the DBT chemical structure) and selectively addressed upon preliminary characterization of the fluorescence intensity at room temperature. The structure is therefore centered on the emitter, so as to maximize upwards redirection and collection efficiency at narrow angles. In Fig. 4.4b a similar design is sketched, this time realized on a gold-coated layer (~ 200 nm thick) to avoid radiation in the lower hemisphere. With DLW, suspended architectures can also be fabricated, such as the arch WG outlined in Fig. 4.4c. In this case the nanocrystal is completely enveloped at the middle-point of the structure, which is conceived to efficiently route fluorescence throughout the silica substrate. Besides the improvement in terms of integrated coupling efficiency [41], the possibility of suspended integration is crucial to avoid losses through the substrate due to the usually low refractive index of polymer materials (following from Sec. 1.2.1). The correct emitter position in the vertical dimension is ensured by the use of two photoresist layers with different viscosity but equal refractive indices.

4.2.1 Materials

The choice of the photo-sensitive materials is made accordingly to the following general requirements for the fabrication of the hybrid platform:

- low DLW polymerization threshold, to minimize damaging of the embedded NCX during exposure to the high field intensity femto-laser pulses. The writing laser wavelength at 780 nm is indeed close to the DBT:Ac ZPL transition at 785 nm;
- low developing time, to minimize the risk of deterioration of the Ac-matrix in the organic chemical bath;

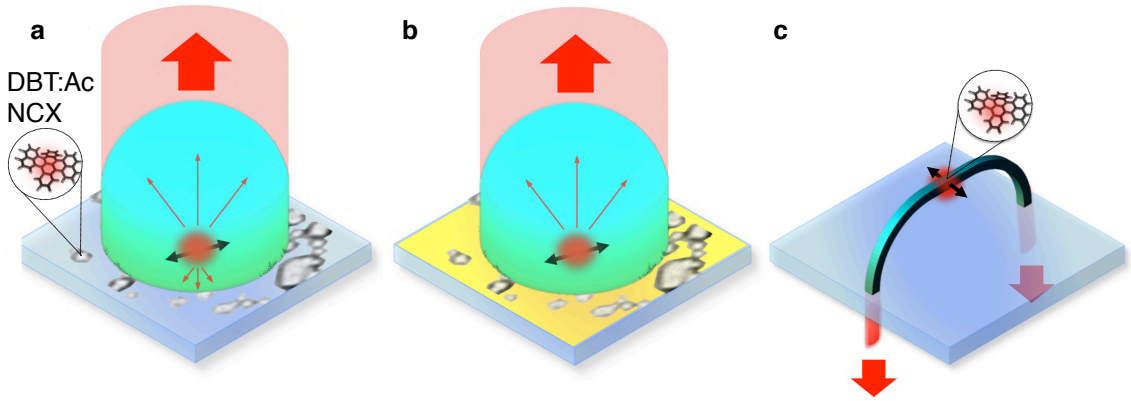

Figure 4.4: **3D-platform concept**. Artistic views of three light collecting devices realized with Direct Laser Writing and fully embedding a DBT:Ac NCX. The black double arrow represents the integrated emitter dipole and red arrows highlight the promoted direction for the emitted fluorescence. **a,b** - Micro-dome lens design for upwards redirection, respectively realized on a silica substrate, and on a gold-coated layer to avoid bottom radiation and maximize collection efficiency. **c** - Suspended arch waveguide, fully enveloping the nanocrystal at its middlepoint, for efficient routing of fluorescence throughout the silica substrate.

- negligible fluorescence in the near-IR, to minimize background noise during measurements on molecules single-photon emission;
- high refractive index, to maximize index contrast with the substrate/air and optimize coupling to the emitter;
- compatibility with cryogenic temperatures, which are necessary to perform the characterization of an integrated SPS for quantum technology applications;

finally, for the suspended WG design:

- compatibility with Ac to minimize deterioration of the NCX optical properties;
- high viscosity, to ensure suspended positioning of the NCX between the two resist layers until writing. Owing to the platelet-like shape of NCX [63] (see Appendix B), a highly viscous material can be alternative to a solid layer.

Indeed, as illustrated in Fig 4.5a, the suspended WG design is based on the deposition of the NCX on a first photoresist layer, which is subsequently covered with a second layer. This ensures vertical positioning of the emitter, which can therefore be addressed and integrated in the middle point of the suspended WG by selective DLW. While in this case NCX enter in direct contact with the resist material, in the micro-dome design (Fig 4.5b) NCX are previously deposited on the substrate, and successively covered with a few nanometer thick layer of polyvinyl alcohol (PVA) for

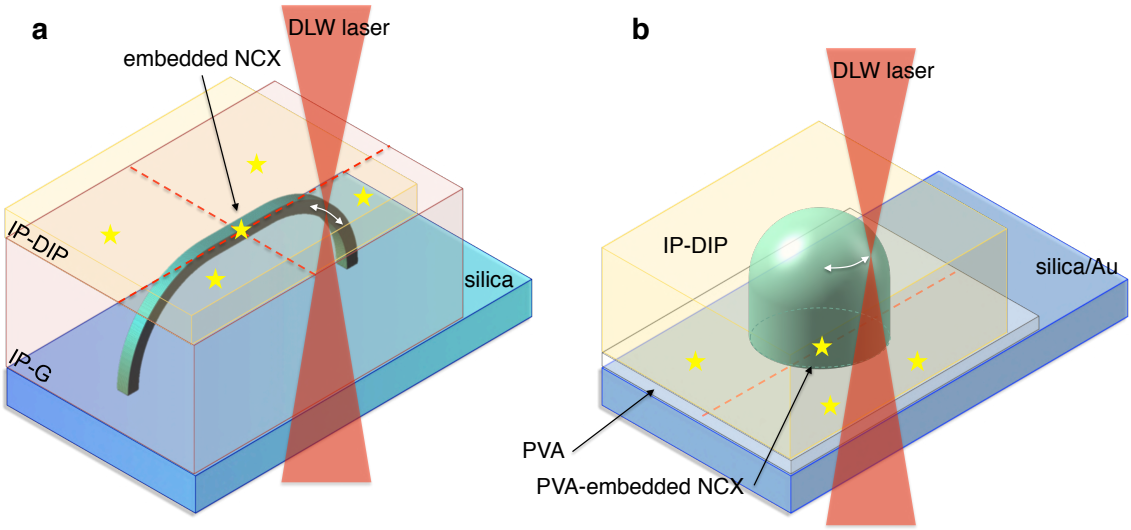

Figure 4.5: **a** - For the suspended WG design, DBT:Ac NCX are sandwiched between two photoresist layers with similar DLW-parametrs. In particular, the first layer of IP-G is spin-coated to a target film thickness of $5 - 10\,\mu$m, which defines the NCX height and hence the WG structure dimensions. The WG is written in one step, by embedding the NCX in the WG middlepoint. **b** - For the micro-dome design, the DBT:Ac NCX are deposited on the substrate (silica or Au) and covered with a PVA thin layer via spin-coating. The structure is then written on the top of the emitter.

preventive protection from matrix sublimation.
Accordingly to the presented requirements, we employ commercially available negative-tone IP-photoresists provided by Nanoscribe. Indeed, IPs provide high resolution and high mechanical stability for structures in the micro- and sub-micron range, typically exhibiting low stress, little shrinkage, low proximity effect and a high adherence to glass substrates. Moreover, we have verified chemical compatibility with the anthracene crystalline matrix and they require few-mW avarage laser power for the writing process and few minutes developing time [258, 259]. Finally, they do not show background fluorescence in the spectral range of the molecule emission, having the absorption peak in the UV-range. In the following table the main features of these photoresists are summarized:

photoresist	IP-G	IP-DIP
prebake 30' at $100°$	yes	no
cast process	drop-casting	drop-casting
exposure	2PP at 780 nm	2PP at 780 nm
refr. index	1.52	1.54

with the refractive index referring to the polymerized material (polymerization induces an increment of ~ 0.02 with respect to the photo-resist). In particular, IPs do not require curing at high temperatures, which would compromise the embedded emitters, nor special safety tools. Only IP-G is pre-baked to increase the viscosity, but previously to NCX deposition. As for the substrate, we use fused silica ($\mathrm{n} = 1.45$) for both the WG and micro-dome designs, in order to ensure a sufficient refractive index contrast with the polymer. For the micro-dome, we perform the fabrication also on a gold surface, obtained by sputter-coating.
In the following, we report the theoretical analysis for the optimization of the structures design, oriented to the efficient coupling of single molecules to the polymeric structures and to the enhanced collection efficiency of the emitted fluorescence.

4.3 Nanophotonic Structures Design

4.3.1 Suspended waveguide

The suspended WG is promising in terms of collection efficiency. Conventional schemes based on evanescent coupling of the emitter to the device [60] are intrinsically restricted by the limited portion of the guided field employed for the excitation/collection of/from the source. On the other hand, localizing the emitter at the maximum of the guided mode field would increase the emission rate into the structure. Following from the discussion in Sec. 1.2.1, our goal is to fabricate a WG with a tight mode confinement within its core, where an individual DBT:Ac NCX is integrated. The optimal case corresponds to a single-mode (SM) WG, which is ideal for collection efficiency and for coupling e.g. to a fiber mode. Here, the geometry is kept simple to ensure fabrication via easy and fast trajectories and minimize damage of the embedded emitter. A squared transverse section is chosen, constant along the whole structure and with $1\,\mu$m-side to guarantee the nanocrystal inclusion, and quarter of rings are envisioned

to outcouple the guided fluorescence throughout the transparent substrate. Outcouplers allow for adiabatic bending towards orthogonal incidence at the substrate surface, so that no further nano-structuring of the facets is needed. At the same time the overall shape gives mechanical self-support to the suspended structure.

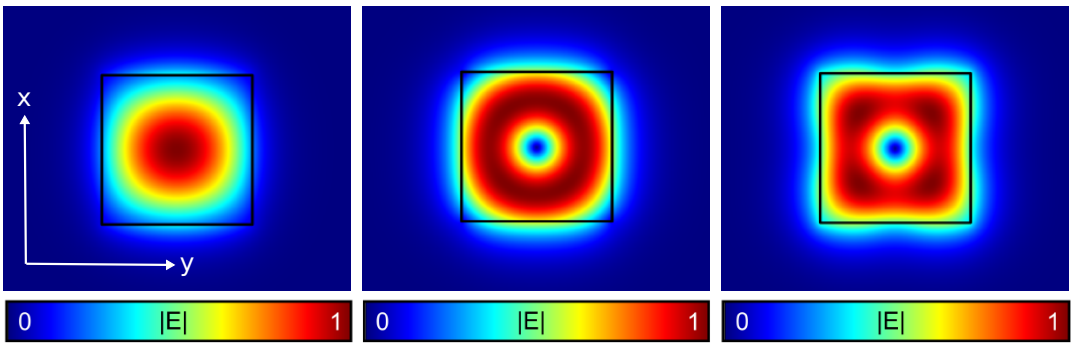

Figure 4.6: 2D plots of the normalized electric field intensity of the first three modes supported by the polymeric WG (lateral size of 1μm) at 785 nm.

Due to the $1\,\mu$m thickness, the WG supports multiple electromagnetic modes at our operation wavelength ($785\,$nm). These are however preliminary results and we plan to go to SM WGs through future optimizations of the fabrication method. These could include e.g. the integration of fluorescence imaging capability in the DLW workstation, as done e.g. in Ref. [41], which would enable the selection of smaller NCX and hence the reduction of the WG thickness.
Using the Mode Solver from Comsol, we calculate the field distribution of the modes supported by the $1\,\mu$m-thick WG, as shown in Fig 4.6 for the first three modes. As expected, the refractive index contrast between polymer and air allows for an efficient confinement of the fundamental mode inside the suspended structure. Higher order modes do exhibit an evanescent component, which reduces the overall coupling efficiency, but we expect a correspondingly low excitation probability because of the central position of the embedded emitter. The key figures of merit of the emitter-to-waveguide coupling, i.e. the β-factor and emission enhancement α, are estimated by excitation of the fundamental mode only. This entails an overestimation of the coupling efficiency, indeed higher order modes contribute to radiation and transition losses, owing to the bigger evanescent component, hence reducing coupling efficiency. However, this evaluation is still representative of the general photonic performance. In the 3D model in Fig. 4.7a, the dipolar source is modeled as a linear harmonic current along the y-axes (white double-arrow in figure) and placed at the center of the WG. The figures of merit α and β are calculated as explained in Appendix A and yield respectively $\alpha = 1.2\%$ and $\beta = 52\%$. The latter value can be ascribed to

the interference occurring among the propagating modes, as evident from Fig. 4.7b. Notably, coupling efficiencies up to 80% can be obtained upon optimization of the waveguide geometry [41], for example by reducing the structure thickness for single-mode propagation. In this work, the thickness choice is motivated by the lack of control on the NCX size during fabrication for this specific configuration, thus requiring a thicker WG to ensure full embedding. As previously mentioned, we envisage to improve these preliminary results through future optimization.

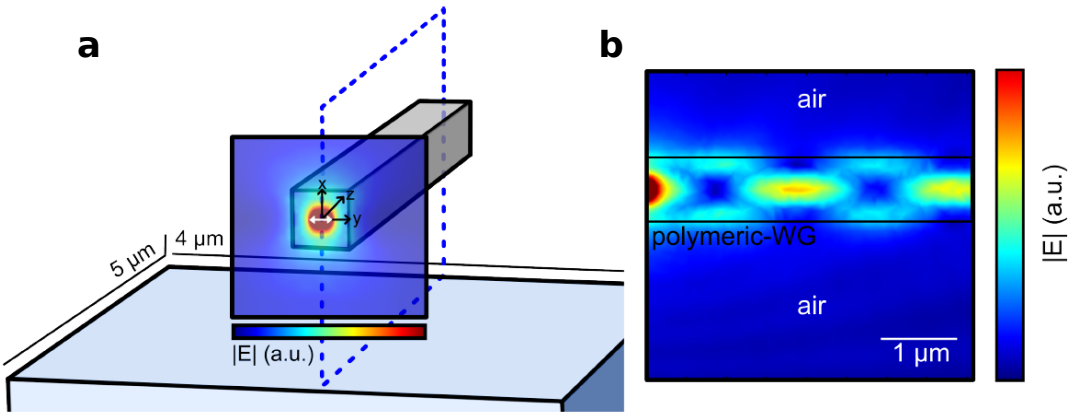

Figure 4.7: Layout of the 3D numerical simulations displaying half of the waveguide total length ($10\,\mu$m). **a** - 2D color map of the electric field norm on the transverse plane containing the dipolar emitter (white arrow). **b** - Longitudinal WG section showing the electric field norm. Interference among the guided modes supported by the polymeric structure is evident.

Finally, we estimate the bend losses due to the outcouplers in the whole suspended WG. These sum up to two different contributions: radiation losses, due to the phase front rotation and consequent shift of the guided mode from the center of the WG towards the radial direction; and transition losses, related to the change in the effective refractive index of the bent part with respect to the the straight top part of the WG. Both contributions are estimated by means of 2D numerical simulations, where half WG is modelled such to have a long enough straight part for the propagating modes selection and the emitter is represented by a current line at the right side. Since the WG height, and therefore the couplers radius, depend on the experimental NCX-to-substrate distance, in Fig. 4.8 we show the results for the smallest realized WG of $3\,\mu$m-height and for the highest WG allowed by mechanical stability ($13\,\mu$m, as discussed in the next chapter). The overall bend losses are calculated as the ratio of the power flux at detectors (3) normalized to the power flux detected at (1). They yield 6.5% for Fig 4.8a, and reduce below 1% for coupler radii $>10\,\mu m$.

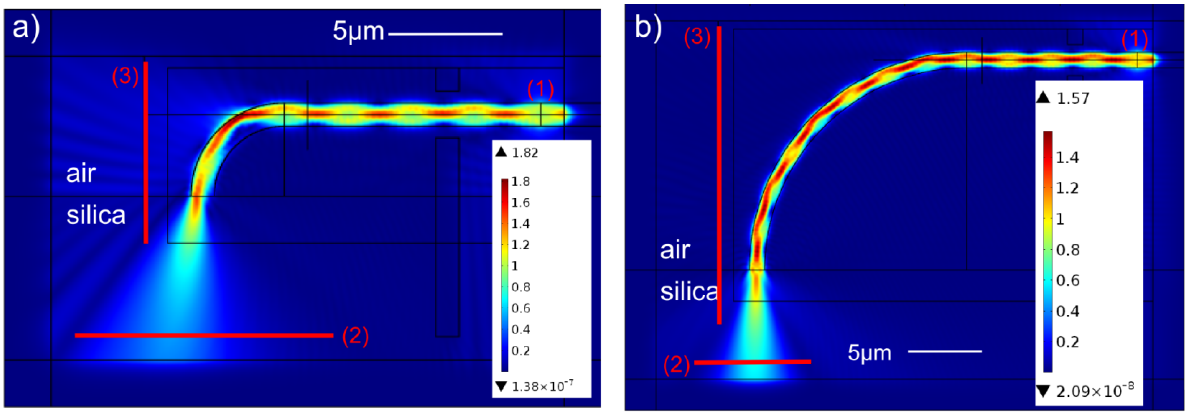

Figure 4.8: 2D simulation models to study the bend losses due to the quarter-ring outcouplers. The color plots (with calibration bars displayed in arbitrary units) show the norm of the electric field distribution along the WG longitudinal section, for the lowest and the highest fabricated WGs, respectively yielding $3\,\mu$m (**a**) and $13\,\mu$m (**b**). The guided mode is pumped by a line source (1), and the amount of bend losses is evaluated as the energy flux through the detector line (3) normalized to the energy fluxes through detector (1).

4.3.2 Micro-dome lenses

We choose the micro-dome design to investigate the performances of the hybrid polymeric platform in terms of light extraction from single molecules. As reminded in Fig4.9b, compared to a standard SIL, a Weierstrass SIL design provides redirection via refraction at all upwards angles and efficiently compresses emission into a small numerical aperture [2]. In particular, the micro-dome is the result of our modification to the Weierstrass SIL (see Sec. 1.2.2), where the lower truncated hemisphere is substituted with a cylindrical base, for simplicity of fabrication.

We use 2D numerical simulations to optimize the micro-dome dimensions in terms of the collected photon flux and we compare it to the standard and Weierstrass SIL geometries, in terms of fabrication advantages. As sketched in the detail in the concept scheme in Fig. 4.9a, the silica substrate is covered with a $180\,\mathrm{nm}$-thick layer of gold, the nanocrystal is modelled in each configuration as a $800\,\mathrm{nm} \times 400\,\mathrm{nm}$ platelet of anthracene ($\mathrm{n} = 1.7$), and a layer of $200\,\mathrm{nm}$ of PVA ($\mathrm{n} = 1.475$) covers the whole considered area, including the NCX. IP-Dip is chosen for its higher refractive index, and the structure's dimensions are optimized for a molecule dipole-to-gold distance $\mathrm{dipole_h} = 100\,\mathrm{nm}$, which promotes emission in the upper hemisphere, following Ref. [57]. The collected photon flux is evaluated by calculating the total emitted power flux within the polar angle defined by the experimental numerical aperture ($NA = 0.62$,

[2] In both configurations the emitter/source of light is at the center of the lens base.

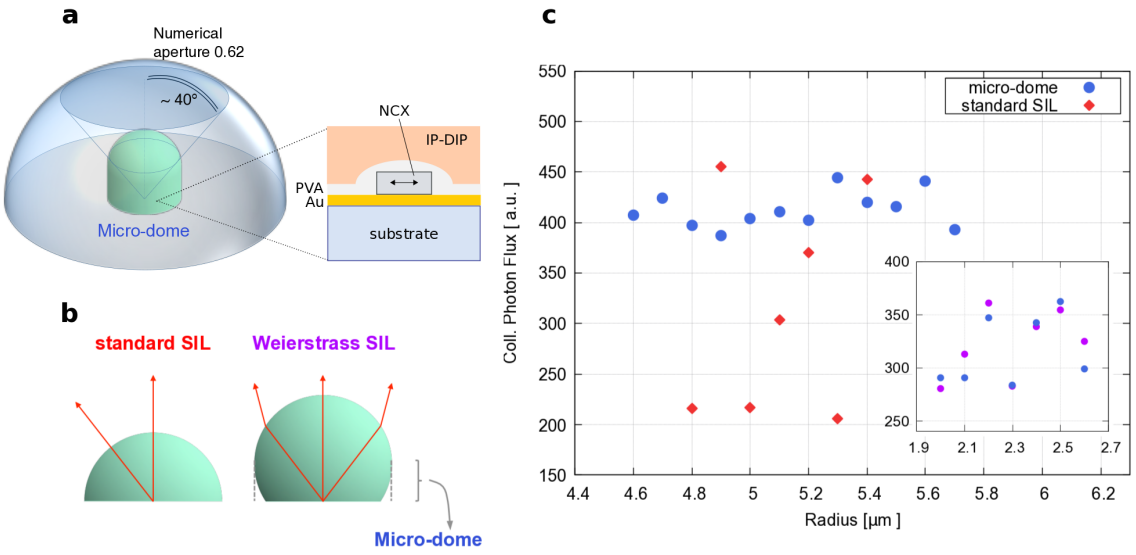

Figure 4.9: **a** - Concept of the simulation model used to evaluate the collection efficiency achieved with a SIL structure and with an objective $NA \sim 0.62$. **b** - Reminder of the design of the standard hemispherical SIL (red label) and the Weiestrass SIL (violet label). The micro-dome geometry is adapted from the Weistrass one by substituting the lower truncated hemisphere with a cylindrical base (blue label). **c** - Simulation results of the collected photon flux for varying SIL radius, by considering a micro-dome (blue dots) and a standard SIL (red dots) structure, respectively. Within $\sim 1\,\mu$m radius variation, the micro-dome structure is remarkably more stable, with a maximum of $\sim 10\%$ variation in the collected photon flux. In the inset, the results for the micro-dome and the Weierstrass (violet dots) design are directly compared, which highlight a slight difference in terms of collected photon flux. This convinced us to employ the micro-dome design for the experiment, since it involves a simpler fabrication.

as illustrated in Fig. 4.9a). As for the lenses dimensions, we finely explore a radius range of $\approx 5 \pm 0.5\,\mu$m, which represents a good compromise between DLW time and ease of distinguishing and addressing the structures on the sample during the characterization step. In Fig 4.9c, comparing the results for the different lenses geometries, it is evident that the micro-dome offers advantages of both collection efficiency and robustness against imperfections. While the maximum values of collection efficiency are comparable for the standard SIL and the micro-dome, the first shows a high instability with variations $> 50\%$ within $100\,$nm of radius shift, compared to an average instability of few percents for the micro-dome. In the inset, the same data for the micro-dome are compared to the Weierstrass-SIL case, highlighting that the modification leading to the dome geometry only entails few percents of difference in the output.

For its photonic performance and robustness to fabrication imperfections the micro-dome is especially suitable to our purposes. As a result from the previous set of simulations, the optimized dimensions for $\mathrm{dipole_h} = 100\,$nm yield a total height and ra-

dius $h_{th} = 8.7\,\mu m$ and $r_{th} = 5.3\,\mu m$. In terms of advantage in collected photons, with respect to a bare NCX on silica the optimized micro-dome on silica leads to an improvement of $\sim 2.5\times$, which is enhanced to a remarkable $\sim 12\times$ by coating the substrate with gold. Here, we can also exploit constructive interference patterns arisen during laser-lithography (see Sec. 4.4.1 and the outlook discussion in Chapter 6) for a further enhancement, leveraging a weak cavity effect.

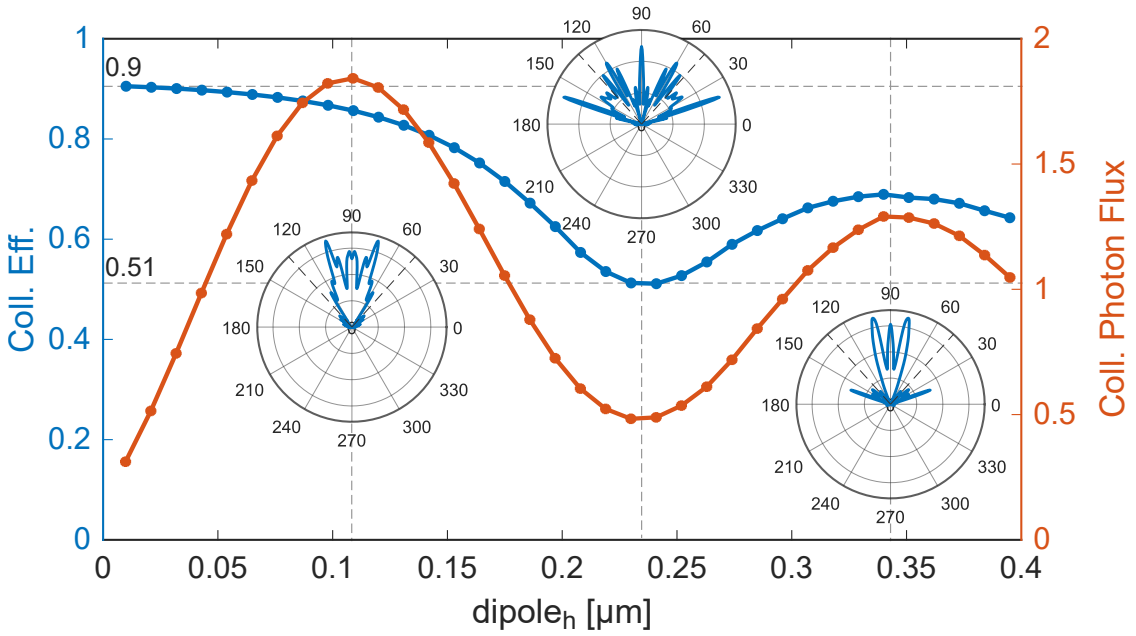

Figure 4.10: Collection efficiency and collected photon flux calculated as a function of the fluorophore vertical position within the nanocrystal volume ($dipole_h$), for the the micro-dome on gold. The collected photon flux is calculated as the radiated power within the numerical aperture acceptance $NA = 0.62$ and the total power emitted in a homogeneous medium. For $dipole_h = 110\,$nm the collection efficiency is maximum, above 85%, and the corresponding polar plot shows a highly directional pattern with $\sim 80\%$ of the total emission within a polar angle of $\sim 30°$. While the emission is quenched close to the metal layer, at bigger distances the overall collection efficiency is reduced due to emission lobes beyond the collection limits (grey dashed lines in the polar plots), as displayed in the corresponding emission patterns.

Since experimentally there is no control over the fluorophore vertical position within the nanocrystal volume [3], we perform calculations varying its value within a reasonably largest possible NCX thickness of $400\,$nm, in the micro-dome geometry on gold with optimized dimensions. In Fig. 4.3.2 the results of 2D numerical simulations for

[3]The DBT alignment within anthracene crystal is instead well known and lies horizontally on the plane of the substrate [46].

the collection efficiency and the collected photon flux are summarized. Here, the collection efficiency is evaluated by integrating the far fields within the experimental $\mathrm{NA} = 0.62$, and normalizing by the integrated far fields on the whole 2π angle. The collected photon flux is calculated as the ratio between the power radiated by a dipole in the far field within $\mathrm{NA} = 0.62$ and the power radiated by the same dipole in a homogeneous medium with the anthracene refractive index 1.7 . As a result, for $\mathrm{dipole_h} = 100\,\mathrm{nm}$, a remarkable collection efficiency above 85% is obtained, together with a small enhancement of the total emission rate. In the corresponding polar plot, the emission pattern appears highly directional, resulting in 80% of the total emission funnelled within a polar angle of about $30°$. The oscillatory behaviour in the detected photon flux is due to the interference nature of the photonic redirection effect, as already discussed for a similar case e.g. in Ref. [57]. Close to the metal layer, the dipolar emission is obviously quenched. As the dipole position is further displaced away from the gold surface, the onset of emission lobes beyond the critical angles is clearly visible in the second polar plot, reducing the overall collection efficiency, even when constructive interference in the forward direction is recovered for $\mathrm{dipole_h} = 350\,\mathrm{nm}$.

The efficient directivity conveyed by the structure is evident also from Fig. 4.3.2, where the collection efficiency is analyzed as a function of the maximum collection angle. In particular, the dashed grey line highlights our value $\mathrm{NA} = 0.62$, and the color bar refers to the dipole vertical position $\mathrm{dipole_h}$. For all the explored $\mathrm{dipole_h}$ range, more than 45% of the emitted fluorescence is collected within our NA. Notably, the presented micro-dome on gold configuration is not a resonant structure and consequently admits a broadband operation. Indeed, numerical simulations for the emitter position at the optimal distance $\mathrm{dipole_h} = 110\,\mathrm{nm}$ reveal an almost flat behavior for the Collection Efficiency and Collected Photon flux over a wide bandwidth $\Delta\mathrm{dipole_h} \sim 150\,\mathrm{nm}$ (see inset in Fig. 4.3.2).

4.4 Nanophotonic Structures: Fabrication

The fundamental concern with the fabrication procedure is the possible damaging of the DBT:Ac NCX, due e.g. to surface charge generation and heating of the anthracene crystalline matrix consequent to the DLW exposure. On the other hand, high quality polymeric structures are desirable, in terms of surface smoothness, homogeneity and mechanical stability, to obtain the photonic performances predicted by simulations. Therefore, it is necessary to find a suitable compromise, in terms of DLW parameters, such to realize optimized features through the shortest exposure and lowest laser power.

In the following, we report the voxel characterization, which gives the spatial resolution of the writing process, and we describe the optimization of the fabrication

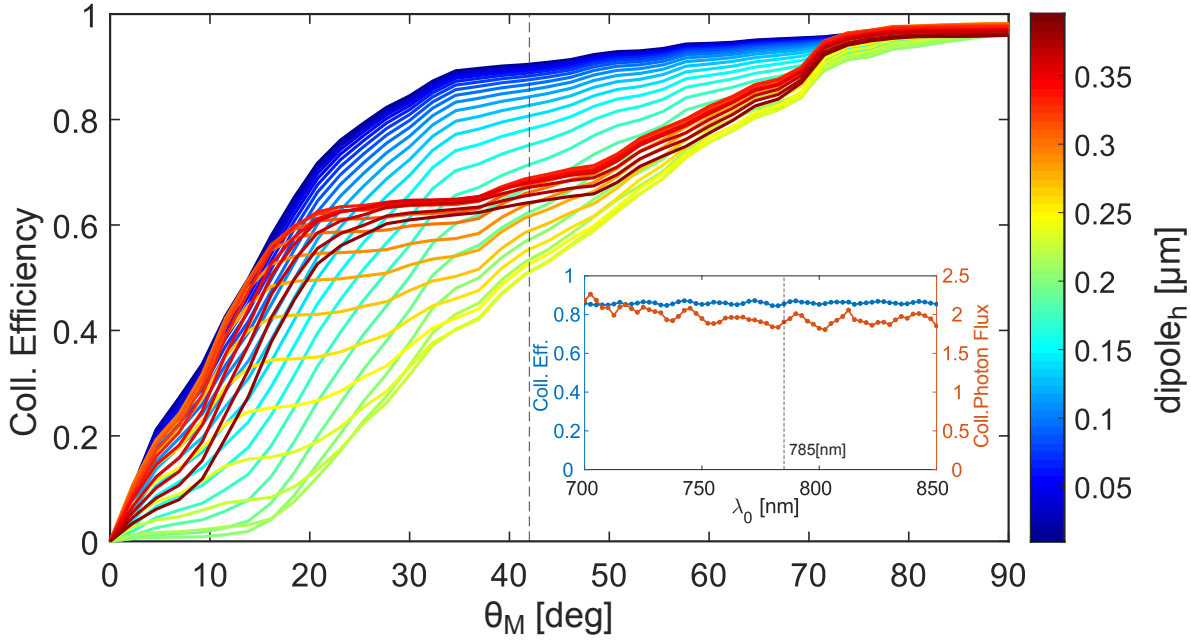

Figure 4.11: 2D numerical simulation of the collection efficiency for the micro-dome on gold, as a function of the maximum collection polar angle (the dashed grey line indicates the numerical aperture of our setup $\sim 42°$. Each line describes the behaviour for a specific vertical position of the emitter dipole ($dipole_h$) within the volume of the nanocrystal. Inset: 2D numerical simulation of the collection efficiency (left axis) and normalized collected photon flux (right axis) as a function of the emitter wavelength for a micro-dome on gold, with the emitter placed at $dipole_h = 110$ nm.

protocols for the the suspended WG and micro-dome, respectively.

4.4.1 Voxel characterization

Owing to its ellipsoidal shape, the voxel is defined by its minor radius $\mathrm{r_{xy}}$ (parallel to sample surface), by its longitudinal radius $\mathrm{r_z}$ (orthogonal to the sample, along the laser beam propagation), or alternatively by the aspect ratio $\mathrm{r_z/r_{xy}}$. A rough estimation of the voxel dimensions can be given by the following empirical rule [260]:

$$r_{xy} = \frac{0.325\lambda}{\sqrt{2}NA^{0.91}}; \qquad r_z = \frac{0.532\lambda}{\sqrt{2}}\left(\frac{1}{n-\sqrt{n^2-NA^2}}\right) \tag{4.1}$$

with $\lambda = 780\,\mathrm{nm}$ the laser wavelength, $\mathrm{n} = 1.52$ the IP-Dip refractive index (before polymerization) and $\mathrm{NA} = 1.4$ for the employed objective, for our workstation. The resulting voxel dimensions yield $\mathrm{d_z} = 2\mathrm{r_z} \approx 260\,\mathrm{nm}$ and $\mathrm{d_{xy}} = 2\mathrm{r_{xy}} \approx 780\,\mathrm{nm}$, with the aspect ratio being $\mathrm{r_z/r_{xy}} = 3$.
Equations 4.1, besides featuring some fundamental contributions to the writing res-

olution, they do not include writing parameters such as laser power and scan velocity, which critically affect the voxel aspect ratio. Indeed, as the laser power increases or the writing velocity decreases, the Gaussian power distribution at the laser focus grows along the propagation axis while saturating in the xy-plane. A proper combination of the writing parameters is therefore needed to exploit a suitable spatial resolution and avoid low degree of polymerization or micro-explosions caused by temperature increase. [261].

In the following, we employ two standard methods to characterize the voxel dimen-

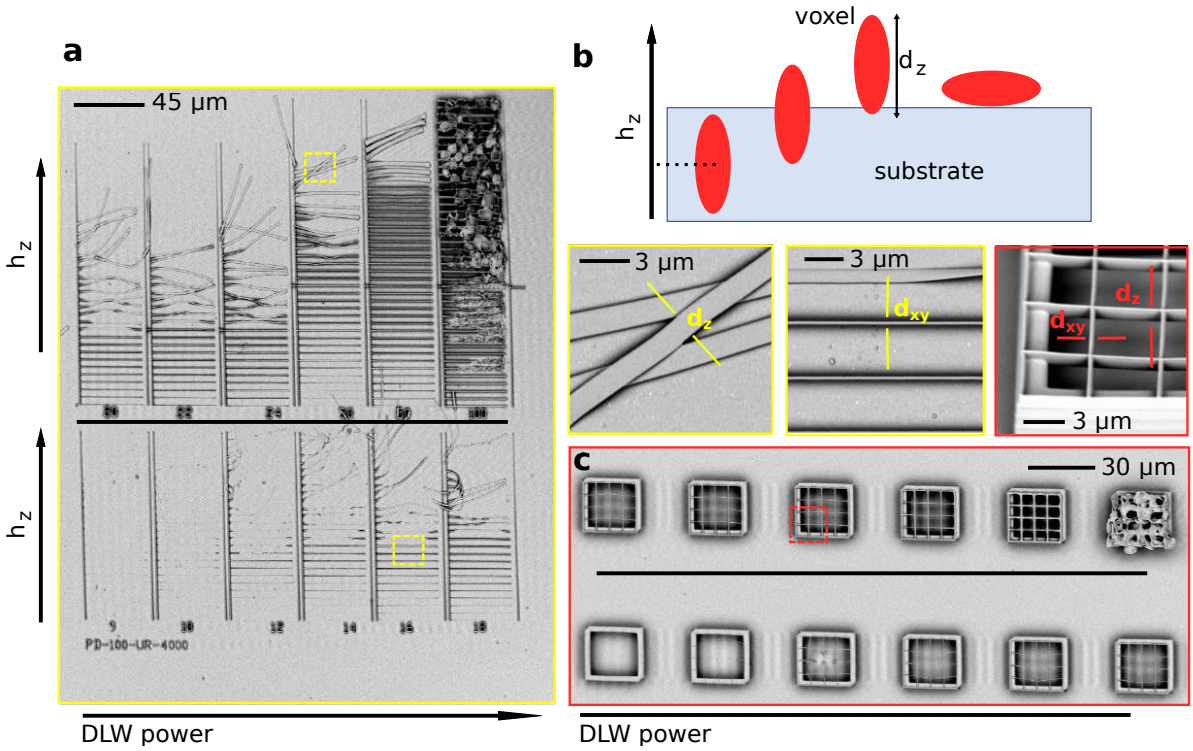

Figure 4.12: Methods for voxel characterization. **b** - Concept of the method in **a**: horizontal polymer lines are written from within the substrate at increasing z-offsets, until they first emerge from the substrate and then collapse. From the last non-collapsed standing line and from the collapsed line d_{xy} and d_z can be evaluated, respectively, through a SEM image (see **a** and corresponding yellow-framed details). **c** - Method to evaluate the voxel dimensions of suspended lines. Lines are suspended over a thick polymer frame, and both d_{xy} and d_z can be measured through a $45°$-SEM. In both methods, the characterization is shown for increasing powers. Both the polymerization threshold and the over-exposure stage can be clearly identified.

sions depending on the writing parameters (Fig. 4.12a,c). A first approach consists in fabricating sets of single lines, for each combination of parameters, at different z-positions (h_z) with respect to the substrate interface (Fig. 4.12a). By incrementally increasing h_z from microns within the substrate material to microns-distant from the

interface, the lines correspondingly emerge and eventually fall off when $h_z > d_z$ (Fig. 4.12b). The voxel dimensions can be evaluated e.g. with a scanning electron microscope (SEM) by measuring d_z from the fallen lines and d_{xy} as the maximum line thickness, which can be measured on the line written at greatest h_z but still stuck at the surface.
A second approach is employed to characterize the voxel dimensions and rigidity of suspended lines, as shown in Fig. 4.12c. Here, for each set of parameters several isolate lines are supported by thick frames. The longitudinal and transverse thickness (d_z and d_{xy}, respectively) can therefore be measured by setting a suitable SEM tilt angle ($45°$ in the figure).
For these procedures we explore the full laser power range of $0 - 50\,\mathrm{mW}$, with larger

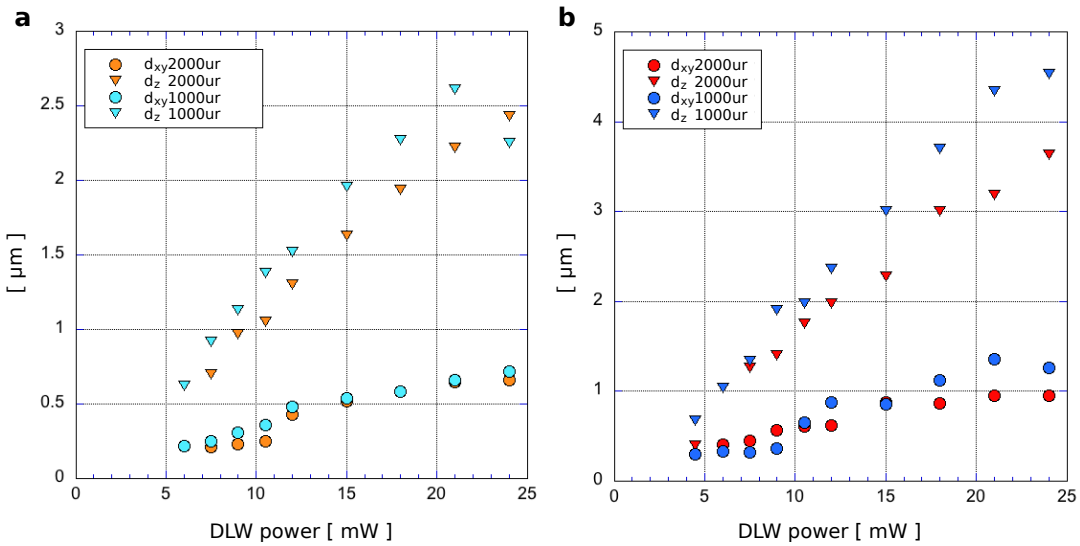

Figure 4.13: Results of voxel characterization on silica (**a**) and gold (**b**) substrate, respectively. The characterization is shown for two writing velocities: $100\,\mu$m/s (1000ur in the figure) and $200\,\mu$m/s (2000ur in the figure). Triangles and circles refer to d_z and d_{xy}, respectively.

increments for higher powers, and two writing speeds $100\,\mu\mathrm{m/s}$ and $200\,\mu\mathrm{m/s}$. In both methods used on a silica substrate and shown in the figure, the polymerization threshold and the onset of micro-explosions are clearly visible, as extremes of the useful range of parameters. The resulting voxel dimensions are compatible for IP-G and IP-DIP and within the two approaches, and are displayed in Fig. 4.13a, limited to the useful power range. In particular, the polymerization threshold occurs at $6\,\mathrm{mW}$ and at $7.5\,\mathrm{mW}$ for the $100\,\mu\mathrm{m/s}$ and $200\,\mu\mathrm{m/s}$ speed respectively, and the minimum voxel size yields $d_{xy} = 200\,\mathrm{nm}$ and $d_z = 600\,\mathrm{nm}$, with a voxel ratio of 3, compatible with the rough estimation of equation 4.1. Nevertheless, increasing the laser power and for the lowest speed, the voxel ratio scales up to ≈ 4, with a maximum

voxel volume defined by $d_{xy} = 700\,nm$ and $d_z = 2.6\,\mu m$.
According to the suspended waveguide design discussed in the previous section, for both the investigated writing speeds there is a range of low powers exhibiting voxel sizes within the waveguide dimensions, suitable for fabrication. Moreover, the compatibility between IP-G and IP-DIP in terms of resolution allows to write the whole structure around the NCX in a single step and with the same parameters.

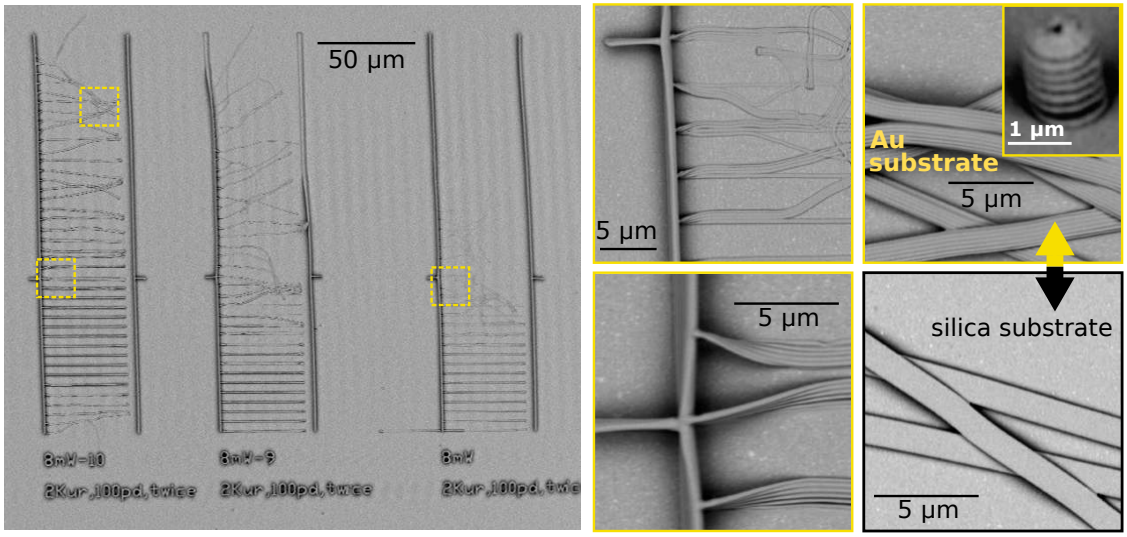

Figure 4.14: **DLW on gold**. SEM images of a sample area for voxel characterization: details are zoomed-in to show the interference patterns arising from DLW on a reflective surface. In contrast, in the black-framed square, corresponding features written on silica are displayed, exhibiting a smooth surface. In the top-right inset, an example of micropillar written through a single line on gold is also shown.

The issue of fitting the voxel volume to the target structure dimensions is a minor concern for the micro-dome design, being not suspended and of considerably bigger volume. However, it is worth noticing that DLW on a highly reflective surface, as planned for the micro-dome on gold configuration, is a non-standard procedure which needs special considerations. In Fig. 4.14, SEM images of single lines fabricated on a silica glass covered with gold[4] are displayed, and compared to the analogous fabrication on silica. Transverse modulations in single written lines are evident [262, 263], especially in the micro-pillar displayed in the inset, and are the result of the interference pattern originated by the direct laser beam impinging on the sample and its backwards reflection. This is confirmed by the measured interference period of $\approx 260\,nm$, compatible to $\lambda/2n = 780\,nm/(2 \times 1.52)$. At the nodes

[4]The silica substrate is sputter-coated with a $200\,nm$-thick layer of gold, as for the micro-dome on gold samples, for total reflection at $785\,nm$.

and anti-nodes of the standing wave, the photoresist is consequently less or more polymerized. The effect is especially visible when, for lower powers, the polymerization threshold is not achieved at the nodes positions, and what should be a single line breaks into multiple filaments. In Fig. 4.13b, we show the results on voxel dimensions, obtained by measuring the overall non-detached bulky structures, excluding the multi-filaments. The power-threshold at which the modulated line does not break is at $4.5\,\mathrm{mW}$, lower than on silica, while the minimum and maximum voxel dimensions are $(\mathrm{d_{xy}} = 300\,\mathrm{nm};\ \mathrm{d_z} = 400\,\mathrm{nm})$ and $(\mathrm{d_{xy}} = 1.3\,\mu\mathrm{m};\ \mathrm{d_z} = 45\,\mu\mathrm{m})$, with the voxel ratio going from 1.3 to 3.6, respectively. We verified through the second method for the characterization of suspended lines, that as soon as the laser focus is detached from the interface, the polymerization threshold is compatible to the results in Fig. 4.12 for the writing on silica. At the interface with gold instead, the onset of micro-explosions is hardly defined and reproducible, making it advisable to always start writing at $\sim 100\,\mathrm{nm}$-distance from the gold surface. However, despite any optimization on the DLW trajectories, writing structures on gold involves a weaker adhesion to the substrate and intrinsic interference patterns in proximity to the interface (as evident from the micro-pillar image in the inset of Fig. 4.14, where the first node in the interference pattern endangers the structure stability).

4.4.2 Waveguides optimization

The suspended WG design is defined by the nanocrystal position, which sets the structure total height. Therefore, the control on the first layer of IP-G photoresist, on which NCX are deposited, is crucial. In general, IP-photoresists are not suited for spin-coating, and especially IP-G, which is highly viscous. Hence the formation of a homogeneous and few-micron thin layer is not trivial. Furthermore, the technique of spin-coating, which we employed for this goal, is sensitive not only to air humidity and temperature in the working area, but also to the slight changes in the IP-G viscosity due to e.g. frequent use and exposure of the photoresist to air. However, by means of reflection-based thickness measurements with a spectrometer, we optimized the spin-coating recipe such to obtain a resulting thickness of $10 \pm 2\,\mu\mathrm{m}$ [5], with minimized thickness variability, and a surface roughness of $\sim 500\,\mathrm{nm}$ (as shown in the photo of Fig. 4.15a). This is achieved by drop-casting $40\mu\mathrm{L}$ of IP-G and immediately starting a spin-coating ramp of $2\,\mathrm{s}$ to $300\,\mathrm{rpm}$, followed by a high speed step of $45\,\mathrm{s}$ at $9999\,\mathrm{rpm}$ (the maximum value for our instrument). Immediate start of the spin-coating recipe subsequent to the drop-casting is fundamental to avoid drop-spreading on the surface, which can result in an accumulation of filaments, as in Fig. 4.15b.

The WG overall structure was then optimized in terms of mechanical stability and

[5] Correspondent to WGs with bend losses of few percents, as discussed in the previous section.

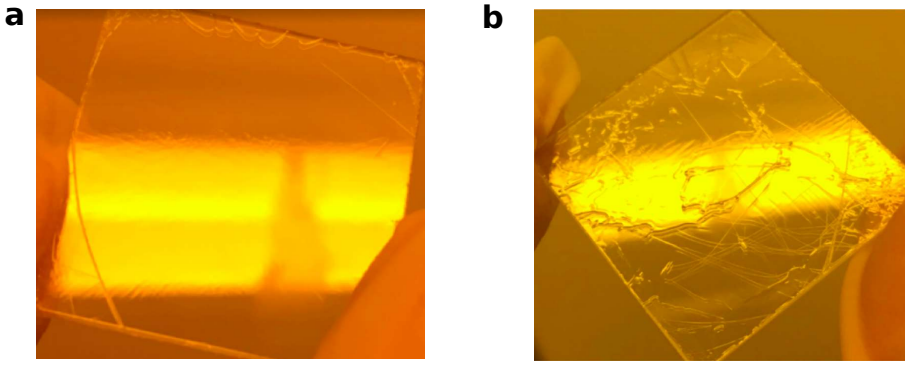

Figure 4.15: Spin-coated IP-G layers: optimized (**a**) and non-optimized (**b**) recipe.

photonic performance. The DLW trajectories consist in adjacent arch-lines in the 3D space which take into account the fitting of the voxel dimensions to the target geometry. In particular, to maximize adhesion to the substrate and lateral symmetry, every line is written starting from $0.1\,\mu$m below the interface. The total length of the WG is kept below $40\,\mu$m not to exceed half of the field of view of our imaging system ($\sim 100\,\mu$m), since excitation and collection during optical measurements are performed through the same confocal objective and imaging camera. For NCX positions $h_{NCX} < 9\,\mu$m, the WGs length is set to $20\,\mu$m by adding to the two outcouplers a completing straight top section, as shown in the rendering in Fig. 4.16a. For $h_{NCX} \geq 9\,\mu$m the total length is determined by the sum of the two outcouplers only (Fig. 4.16b).

Following this protocol, several sets of waveguides of height ranging within $3 - 20\,\mu$m

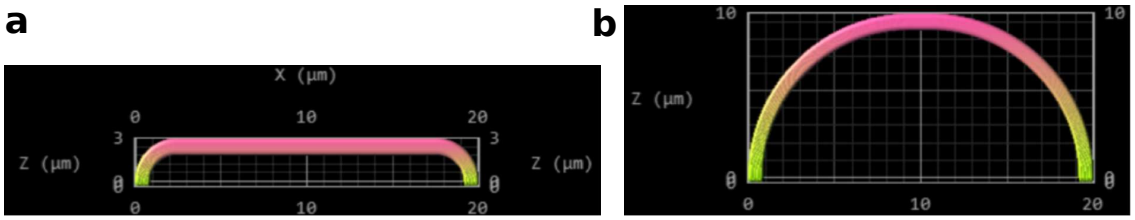

Figure 4.16: Rendering of suspended WGs with height of $3\,\mu$m (**a**) and $10\,\mu$m (**b**).

and with increasing line-trajectory density (respectively 7,12,16,20 line-density for each waveguide 3D axis) are fabricated at different powers, using IP-DIP as photoresist for sake of simplicity. We observe from SEM images that a laser power within $15 - 20\,$mW is the best compromise in terms of stiffness and mechanical stability of the waveguides, which are stable up to a height $h_{WG} \approx 13\,\mu$m. After that, on average, they deform and collapse (as shown e.g. in the SEM image in Fig. 4.17a). For higher powers, micro-explosions appear for higher line-densities, or also induced by one-

photon absorption from a local impurity on the substrate (Fig. 4.17b).
For the final selection of the writing parameters in terms of photonic performances

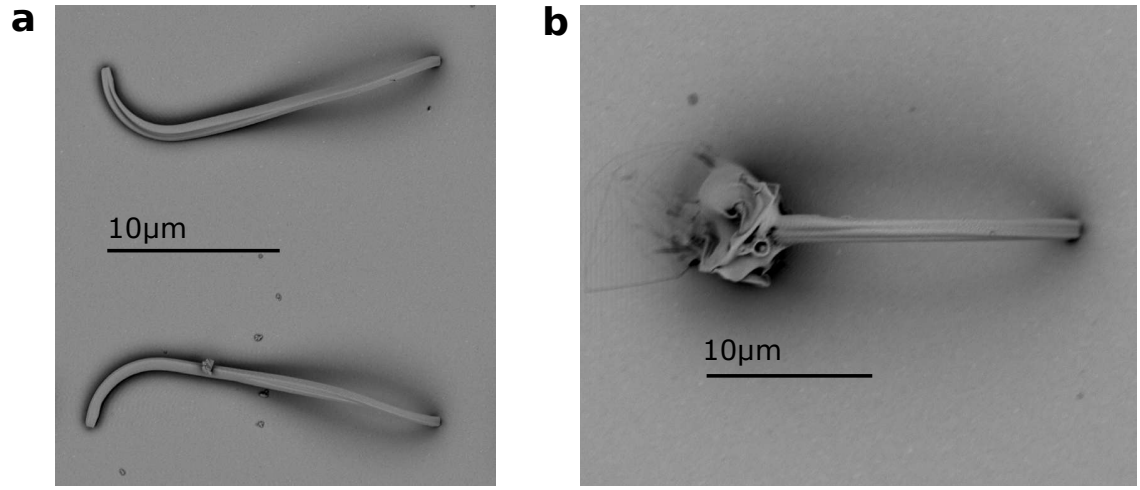

Figure 4.17: SEM images of non-optimized fabricated WGs. **a** - Collapsed WGs due e.g. to excessive height or low rigidity. **b** - Micro-explosion due to excessive DLW power.

of the structure, we analyze the waveguide transmission. For this purpose, we fabricate a set of $10\,\mu$m-high waveguides with different line-density and written at $15\,$mW, which is the lowest power in the range of interest for mechanical stability. The waveguide transmission can be evaluated by measuring the normalized laser throughput. For each structure, through the substrate, the confocal laser spot is focused onto one coupler, and the signal at the opposite coupler is measured (the longpass filter in detection is here removed), upon optimization of the incidence angle and position. The transmission, after background subtraction, is hence normalized by the laser reflection onto a mirror, also background subtracted. Finally, because of a non-optimized spatial mode-matching between the laser and the waveguide, the result is corrected for the overlap integral of the two modes [6] (as summarized in Fig. 4.18a,b). The results are presented as black dots in Fig. 4.18c as a function of the line-density ($\mathrm{D_{l,WG}}$). The highest measured value of WG transmission for these data is obtained for $\mathrm{D_{l,WG}} = 20$ and yields $21 \pm 3\,\%$. As predictable, lower values of $\mathrm{D_{l,WG}}$ result in a less efficient transmission. It is worth noticing that the black-dot data were collected from WGs initially written with the laser beginning to write each successive line from the same position (from the same outcoupler). This implies that the laser switching on at the same outcoupler for each line written, causing a considerable asymmetry of the overall structure owing to the initial power gradient, and therefore reducing

[6] Despite the multi-mode propagation, here we approximate it to a single-mode, corresponding to the measured output intensity distribution on the CCD camera.

coupling efficiency. Taking this into consideration, we repeat the transmission measurements for symmetrically written WGs: with the laser beginning to write each successive line from the previous final position. In particular, we employ a line density $\mathrm{D_{l,WG}} = 16$, since we deduce from plot 4.18c that this is a good compromise between transmission efficiency (which does not significantly change between $\mathrm{D_{l,WG}} = 12$ and $\mathrm{D_{l,WG}} = 20$, as suggested by the black dots data) and writing time. Therefore, by averaging on 10 fabricated structures, we obtain a transmission efficiency up to $40 \pm 2\,\%$ (star-point in the figure). In particular, this value includes both coupling and scattering losses owing to structure imperfections. We have tried to evaluate the two factors independently by measuring the transmission efficiency as a function of the WG's length, in order to retrieve the scattering contribution, but the measurements were not successful because of the structures' instability over $\sim 25\,\mu$m. The test can be implemented at the cost of renouncing to the simplicity of the design, e.g. by introducing some suitable supports. However, since this would reduce the overall transmission efficiency we decided not to pursue this option. In chapter 4, an estimation of the scattering contribution due to the nanocrystal presence, which is crucial for integrated devices, is given through a comparison with empty WGs.
In general, the optimized WG structures (star-point in Fig. 4.18c) exhibit a better geometric symmetry and surface smoothness (analysis by means of SEM imaging; see Fig. 4.22c)), and the probability of generating micro-explosions during fabrication is relevantly lower. Non-perfect adhesion to the substrate, effective multi-mode propagation and any fabrication imperfection, are all concurrent effects which contribute to the overall final measured transmission. However, considering that this simple structure is the result of a preliminary optimization, which does not include any structuring of the couplers nor detailed optimization of the bend radius/geometry, $40 \pm 2\,\%$ of transmission is a more than sufficient and promising outcome to test the performances of the 3D-integrated polymeric platform.

4.4.3 Micro-dome lenses optimization

In the micro-dome design the NCX are directly deposited on the substrate, either transparent silica or reflective gold. They are then covered with a spin-coated layer of PVA, which protects the NCX and also allows to begin the writing process from a laser focus position at $\sim 200\,\mathrm{nm}$ above the interface. This reduces the impact of the writing-laser strong intensity anti-node at the gold-interface, both on the NCX and on the polymerization process. In particular, we employ here a high molecular weight ($\mathrm{MW} = 85.000 - 125.000$) PVA, which we have verified to be proof against the organic solvents used in the developing step of DLW. In Fig. 4.19, we compare the fluorescence spacial map of NCX embedded in IP-DIP layers, which were covered with

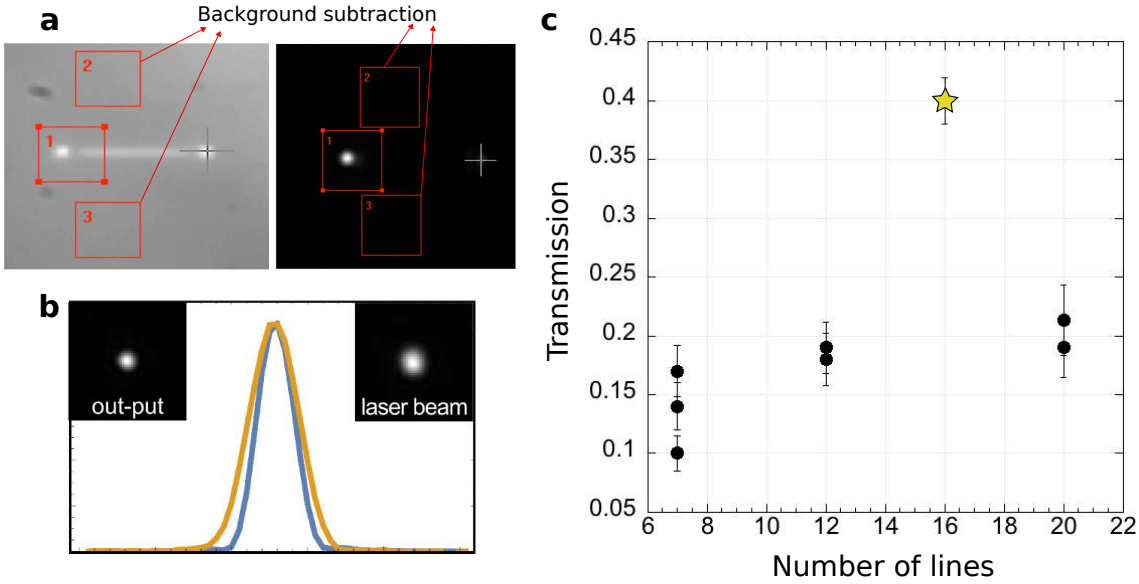

Figure 4.18: **a** - Procedure for the measurement of the transmission efficiency of a WG: the structure is identified in WL illumination and the off-resonant laser is focused onto one of the couplers (grey cross). The intensity counts at the opposite coupler (square 1) correspond to the guided light. Hence, transmission efficiency is extracted by integrating this signal (background-corrected by evaluation of the noise signal within the reference squares 2 and 3, in the figure) and normalizing to the total signal of the input laser reflection on a mirror (also background corrected). **b** - Laser spot profile at the output coupler of a WG, compared with the laser spot profile on a silver mirror (both shown in the insets). Line-cuts from the two profiles suggest a good mode-matching, as confirmed by numerical evaluation of the overlap integral that yields a value of 0.87. **c** - Black dots: Transmission efficiency measured for triplets of nominally identical asymmetrically-written WGs with height $h = 10\,\mu$m as a function of number of writing line density. As predictable, transmission and its reproducibility increase with increasing writing resolution and the highest throughput measured is $\sim 20\%$. The star-point, corresponds to the result obtained by averaging on three symmetrically-written WGs, which yields 40% transmission efficiency. This latter writing procedure has been employed for the fabrication of the final sample.

low (4.19a,b) and high (4.19c,d) MW PVA, respectively (at fixed excitation/detection parameters and initial NCX average fluorescence intensity). The reduction in fluorescence signal is evident for the NCX covered with lower MW PVA ($\mathrm{MW} = 13.000 - 23.000$), which is probably permeable to infiltration of the organic solvents to the embedded NCX. On the other hand, for NCX protected with the higher MW PVA, no evident decrease in fluorescence counts is observed within all the explored range of laser writing powers ($6 - 25\,\mathrm{mW}$).

In order to obtain a PVA layer thickness of $\sim 200\,\mathrm{nm}$, as it was designed for the simulations in Sec. 4.3.2, we use a two-step spin-coating recipe: $5\,s$-ramp to $1500\,\mathrm{rpm}$, and $120\,\mathrm{s}$ at $3500\,\mathrm{rpm}$.

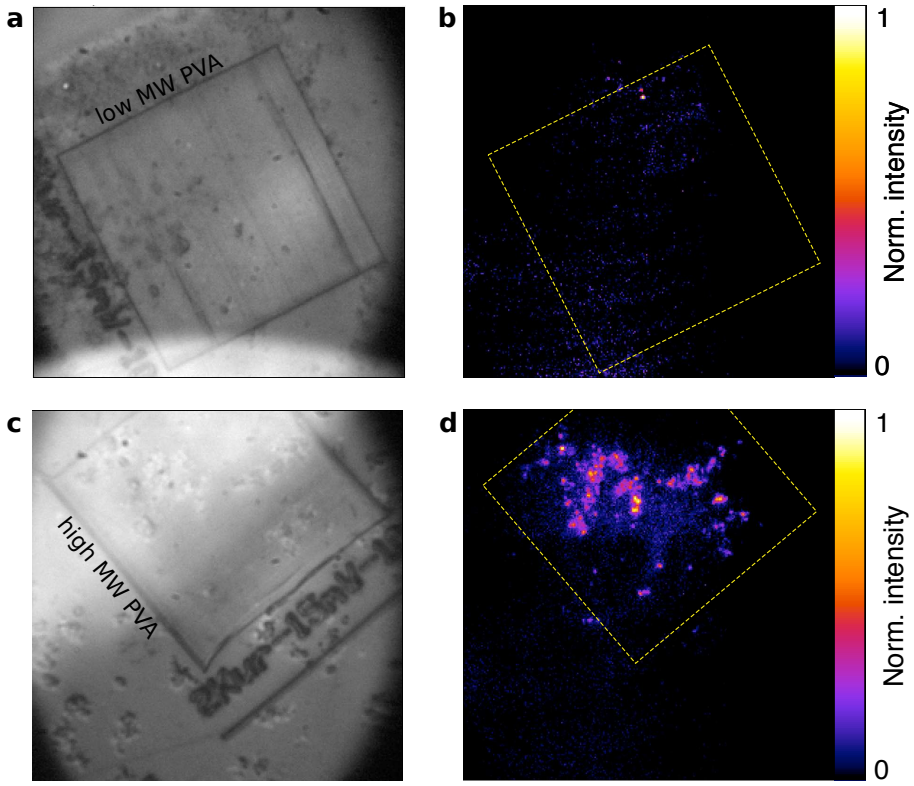

Figure 4.19: WL images and corresponding wide-field fluorescence maps, at room temperature, of IP-DIP square-layers (highlighted by the dashed yellow contour, on the right) written on densely doped DBT:Ac NCX. **a,b** - NCX were previously deposited and covered with a layer of *low* molecular weight PVA: fluorescence signal is barely visible, suggesting a damage of the NCX e.g. during the development bath. **c,d** - NCX were previously deposited and covered with a layer of *high* molecular weight PVA: fluorescence signal persists after fabrication, suggesting that in this case the embedded NCX are not compromised during the DWL-fabrication process.

The optimization of the fabrication process of the micro-dome structure is focused on the accurate reproduction of the planned dimensions, and on the smoothness of the surface. The photonic characterization is performed in Sec. 4.5.2, directly on the emitted fluorescence from the embedded NCX. Indeed, because of our current setup based on a confocal objective, a preliminary characterization of the empty structure with the laser beam in transmission could not be performed.
The DLW-trajectories for the micro-dome architecture consist in xy-layers of concentric circumferences, with the radially external circumferences fitting the voxel dimensions to the target surface coordinates. The laser power used is $7.5\,\mathrm{mW}$, which is the lowest power not exhibiting evident shrinkage of the final structure, and the writing speed is $200\,\mu\mathrm{m/s}$. Indeed, with respect to the suspended waveguide, here the bulk structure is intrinsically more stable and assures rigidity for lower powers and higher

velocities. Specifically, the incremental radius difference of the concentric circumferences is $50\,\mathrm{nm}$, while the z-increment between xy-layers decreases towards the dome pole, going from $160\,\mathrm{nm}$ to $15\,\mathrm{nm}$. The voxel overlap (considering the characterization in section. 4.4.1) is above 85% , and assures a good degree of surface smoothness in a relatively short time ($\sim 15\,\mathrm{min}$) for both the silica and gold substrates[7]. In Fig. 4.20a,b, SEM images of the micro-dome on silica and on gold respectively confirm an accurate reproduction of the structures in both cases. On gold, the interference periods are still visible. However, since the structure is non-resonant and these imperfections are of the order of few tens of nanometers, the overall photonic performances are not compromised.

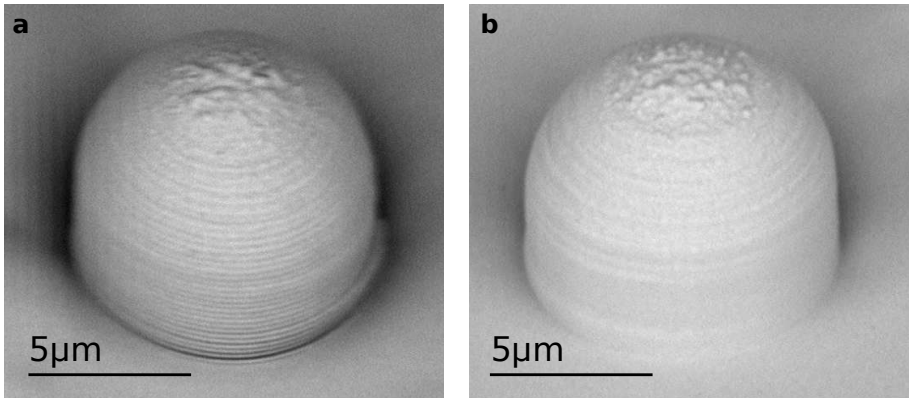

Figure 4.20: **a,b** - SEM images of micro-dome structures fabricated on gold and on silica, respectively. In **a**, dense interference patterns are visible in the vicinity of the substrate due to the reflective substrate.

4.5 3D Integration of Nanocrystals: Experimental Results

In order to explore and test the compatibility between organic molecules and polymers within the hybrid platform, we employ highly doped DBT:Ac NCX. This allows to investigate the effect of fabrication on the photonic performances of a large statics of individual molecules, which can be selectively addressed at cryogenic temperatures by means of resonant excitation.

[7]The writing parameters are kept the same for both substrates. Indeed, since the PVA layer allows to write from $\sim 200\,\mathrm{nm}$-distance from the gold interface, the structure base is not exposed to the very first anti-nodes, at which intensity is enhanced compared to the silica substrate case. Furthermore, the rest of the structure is sufficiently far from the interface (μm-distance), and the voxel dimensions are affected by gold in a negligible way, as confirmed by the second method of voxel characterization for suspended lines (sec. 4.4.1).

The fabrication of suspended WGs hosting single NCX follows the protocol described in Section. 4.4.2, desiccating NCX on the spin-coated IP-G layer and then covering them with an IP-Dip drop. Due to the high viscosity of the bottom photoresist and the platelet-like shape of the NCX, the vast majority of the crystals do not dip into the resist. Furthermore, IP-Dip drop-casting does not perturb the NCX position. The low refractive index contrast between Ac and the IP-photoresists, enables to visualize the NCX once embedded within the two layers of material, on the CCD camera of the DLW workstation. This consents the selection of isolated NCX, which can be individually integrated into a WG. The local thickness of the IP-G layer, is evaluated through the z-piezo feedback coordinates while scanning the camera focus from the silica-IP-G interface, which is identified by the high index contrast, to the NCX position. If this value is within the stability range, the corresponding trajectory coordinates are generated with a Matlab code and implemented in the GWL-file, together with the optimal writing parameters.

The fabrication of micro-domes follows the protocol illustrated in Section. 4.4.3,

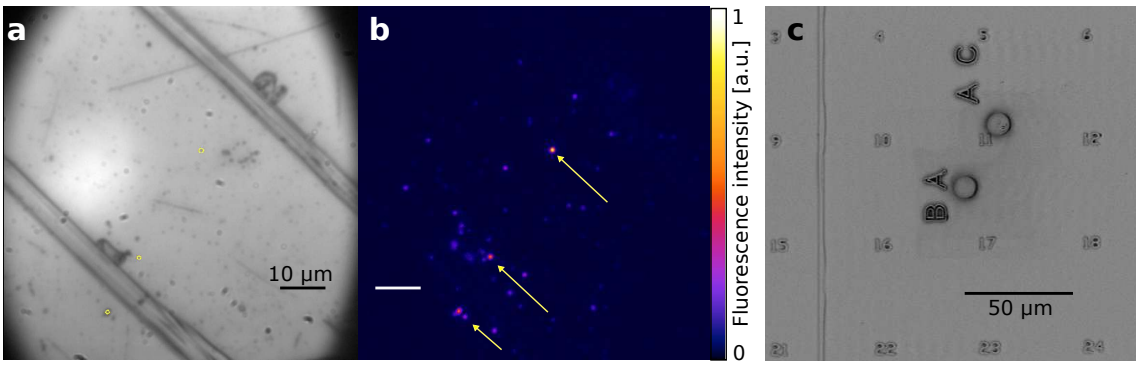

Figure 4.21: **a,b** - WL image and corresponding wide-field fluorescence map of a region of the sample. Thank to a referenced grid previously written in IP-DIP on the substrate, the brightest NCX can be selected and successively identified during the DLW of the micro-dome structures. **c** - SEM image of the final sample, where two examples of fabricated micro-domes are shown, respectively centered at the positions of previously selected NCX.

depositing the NCX on a silica or gold substrate, covering them with a spin-coated layer of PVA, drop-casting IP-Dip and writing each device on the top of a single NCX. In this case, prior to the NCX deposition, cross-numbered grids on the substrate are fabricated with IP-Dip (a WL-image is shown in Fig. 4.21a, where the grid labels are clearly visible, whereas some grid-lines had detached from the substrate during the development process). They enable identification of individual NCX on the sample after deposition (see the correspondence between the yellow cyrcles in 4.21a and the brightest NCX in the fluorescence map in Fig 4.21b), and allow selective writing upon preliminary characterization of the fluorescence intensity at room temperature. In-

deed, thanks to the index contrast between IP-Dip and PVA, both NCX and the numbered grids can be clearly distinguished after IP-Dip drop-casting. After DLW, all the fabricated devices are developed for $3-5\,\mathrm{min}$ in PGMEA (Propylene glycol methyl ether acetate), rinsed in 2-Propanol and gently dried with a controlled clean air flux. In Fig. 4.21c we show a SEM image of a final sample, where micro-domes have been written in the locations corresponding to the brightest NCX.

The accurate reproduction of the three designs can be appreciated in the SEM im-

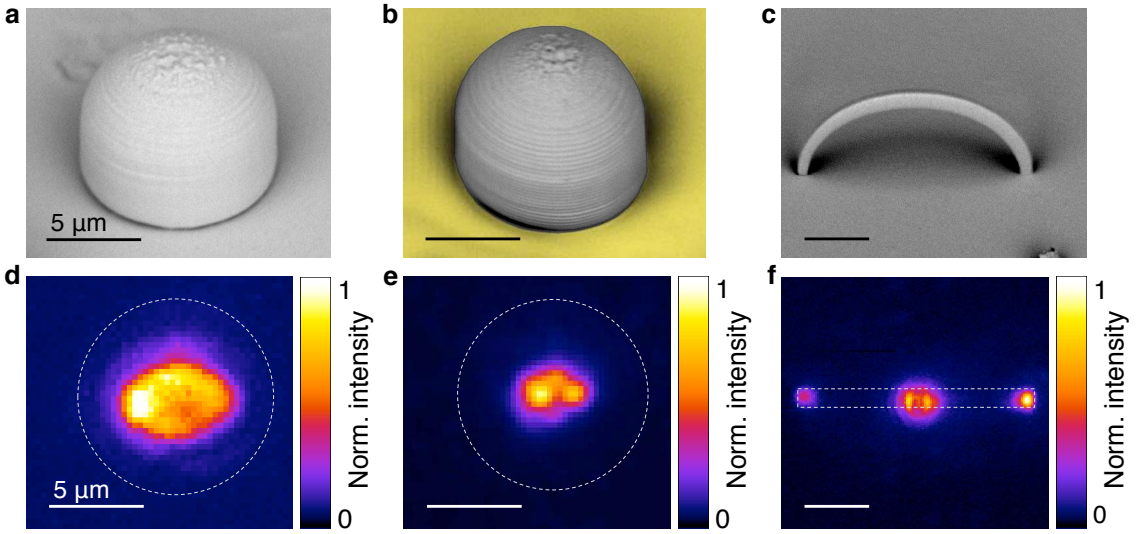

Figure 4.22: **a,b,c** - SEM images of the micro-dome on silica, micro-dome on gold and suspended WG, respectively, each embedding a DBT:Ac NCX. **d,e,f** - Corresponding fluorescence maps attesting the persistence of molecular emission after fabrication, acquired at room temperature and collected from the top in the micro-dome designs **d,e** and through the substrate in the WG geometry **f**. The dashed line in the maps denotes the contour of the respective structure.

ages reported in Figs. 4.22. For each structure, fluorescence imaging has been acquired to evaluate the persistence of molecular emission. Figures. 4.22d,e,f represent the fluorescence maps obtained at room temperature, and collected from the top in the first two cases and through the substrate in the WG geometry. The presence of fluorescence in all the devices, is a first evidence for the compatibility of the organic molecular emitters with the whole fabrication process, both on dielectric and metallic surfaces and even in the suspended architecture. Notably, upon optimization of the writing parameters, all the investigated micro-domes showed molecule emission. The integration success rate is also enhanced by defining and anchoring the coordinate system of the writing laser beam to the location of selected NCX within the optical microscope image. Deterministic positioning with such a simple and cost-effective fabrication method is a key tool for scaling up the process to more complex chips, involving e.g. multiple emitters.

The bright spots in Fig. 4.22d and Fig. 4.22e correspond to emission from the NCX at the bases of the micro-domes. Comparing the two, a first indication is obtained of the higher directivity achievable in the presence of a reflective substrate underneath the SIL-like structure. In Fig. 4.22f instead, fluorescence is observed both in correspondence with the nanocrystal position at the centre of the WG, and at the lateral output ports, where the guided emission is outcoupled. From the relative intensities, a lower bound for the molecule-to-WG coupling efficiency can be hence estimated, yielding a value of about 10%. The estimation consists in normalizing the total counts at the two outputs (background corrected) to the overall emission which is lost from the emitter position. The latter, is calculated by making the approximation of spherical emission, and by normalizing the fluorescence detected from the molecule at the middle-point of the WG (background corrected) to the acceptance angle of the objective ($\mathrm{NA} = 0.7$). This is obtained by dividing the detected fluorescence by $2\pi(1-\cos(\mathrm{NA}))/4\pi$, i.e. the collection solid angle over the total 4π. Notably, this is an under-estimation of the coupling efficiency, since is the result of the integrated signal from all the emitters in the NCX, each with different orientation and position with respect to the guided mode, hence with varying coupling efficiency. Furthermore, the additional propagation losses due to the emitter inclusion can be evaluated by comparing the normalized laser throughput ($\eta_{\mathrm{WG+NCX}} = 36 \pm 1\,\%$), with the case of empty WGs ($\eta_{\mathrm{WG}} = 40 \pm 2\,\%$), as described in Sec. 4.4.2. This measured value for the additional scattering losses of 10% can be further minimized upon selection of smaller NCX, e.g. by integrating fluorescence imaging capability in the DLW workstation, as done e.g. in Ref. [41].
In the following, single-molecule spectroscopy at cryogenic temperature is performed, using the micro-dome on gold as test bed.

4.5.1 Optical characterization at cryogenic temperatures

As reminded by the pumping scheme in the simplified Jablonski diagram in the inset of Fig. 4.23a, the Stoke-shifted fluorescence from the integrated NCX is collected through the longpass filter and analyzed in different aspects.
A typical result of the $\mathrm{g}^{(2)}(\Delta\mathrm{t})$-function for the micro-dome on gold structure is displayed in Fig. 4.23a, obtained at saturation. The best fit to the experimental data yields $\mathrm{g}^{(2)}(0) = 0.00 + 0.03$, which clearly verifies single molecule emission and proves the high purity of the single photon stream emitted in the integrated-molecule geometry.
A characteristic excitation spectrum is shown in Fig. 4.23b with a near to the life-time limited linewidth $\gamma_{\mathrm{exp}} = 70 \pm 1\,\mathrm{MHz}$. Considering that γ_{exp} is within the experimental statistics collected for the non integrated DBT:Ac NCX (Chapter 2), and that it is close to the theoretical Fourier-limited value of $40 \pm 1\,\mathrm{MHz}$ for DBT molecules, we can de-

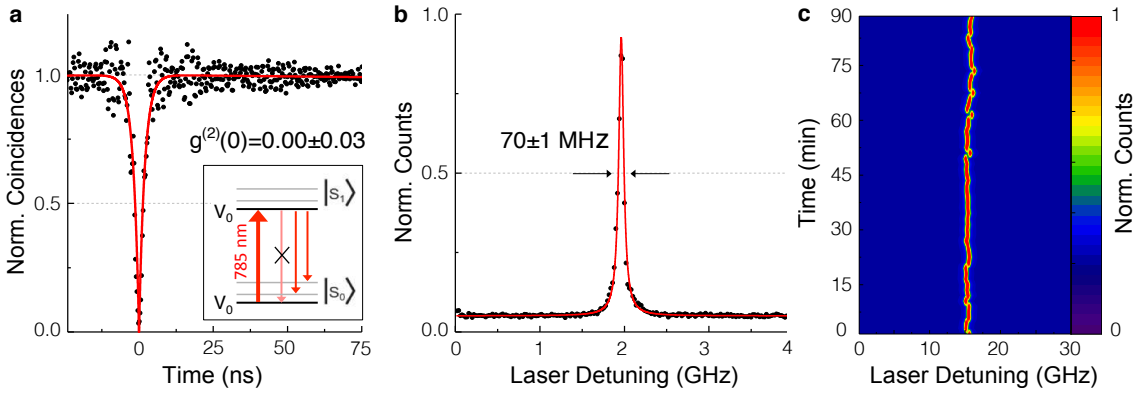

Figure 4.23: Cryogenic characterization performed on the micro-dome on gold. Inset: Simplified Jablonski diagram of the pumping scheme. **a** - Histogram of photon coincidences measured in a HBT configuration. The fit to the data yields a single-photon purity $g^{(2)}(0) = 0.00 + 0.03$. **b** - Excitation spectrum. The Lorentian fit to the experimental data yields a near to the life-time limited linewidth of (70 ± 1) MHz. **c** - Photostability of the integrated molecule emission shown by repeated linewidth measurements over time for 1.5 h, with fluctuations of the excitation central frequency within the range of few line-widths.

duce that this fabrication process does not alter significantly the NCX properties and that quantum coherence is not compromised.
Finally, spectral diffusion is investigated for 1.5 h. Fig. 4.23c, displays a good photostability of the integrated molecule emission, whose excitation central frequency fluctuates within the range of few line-widths. Being spectral diffusion a sensitive tool to appreciate the environmental disturbance on quantum emitters, these results are a relevant indication that the proposed polymeric platform is a reliable technique to embed single molecules in a photonic circuit.
We remark that in the sample of suspended WGs we could not recover narrow emission linewidths at cryogenic temperatures. These are preliminary results, and certainly there is an issue of worse thermal conduction for suspended structures with our cryostation, which would cause a frequency broadening. [8] However, we suppose that another reason is that NCX are not protected by any PVA layer, like in the case of SILs, and consequently might have been damaged during the development bath. This issue might be solved by optimizing the fabrication method in order to select smaller NCX, and by completely embedding them within the WG polymer structure, which could shield them from the permeation of development solvents.

[8] Indeed, the suspended WG design, which is measured through the substrate, is glued upside down on the cryostat cold finger through a copper mask that prevents from crushing the structure. This approach probably suffers from thermal losses which cause the WG to be at higher temperature.

4.5.2 Record photon flux from a single molecule at low temperatures

In the following, we investigate the performances of the micro-dome design in terms of light extraction from single molecules.
A typical AFM image is displayed in Fig. 4.24a. In particular, a strip-scan of the structure passing through the dome pole is shown together with a high resolved AFM map of the top $4 \times 4\mu\mathrm{m}^2$ surface area. From the dome profile we estimate the experimental dimensions of the structure, with a total height $\mathrm{h} = 9.1 \pm 0.1\mu\mathrm{m}$ and a radius $\mathrm{r} = 5.0 \pm 0.1\mu\mathrm{m}$, in good agreement with the nominal values set by the numerical optimization ($\mathrm{h_{th}} = 8.7\mu\mathrm{m}$ and $\mathrm{r_{th}} = 5.3\mu\mathrm{m}$). From the AFM map, the average surface roughness is estimated to be $\Delta\mathrm{r} = 41 \pm 4\,\mathrm{nm}$. This is evaluated by extracting two orthogonal profiles passing through the dome center, and by averaging the differences between peaks height and vallays depth. Finally, Fig. 4.24b shows one of the main results of the chapter, that is the collected photon flux as a function of pump power at low temperatures, emitted from a single molecule embedded in the polymeric micro-dome device. The measurements are compared to the case of a bare NCX and of a molecule in the micro-dome device on silica. The photon flux is shown without correction for the detector internal efficiency, $\eta_{\mathrm{det}} \simeq 50\%$. Here, the detected counts are obtained by measuring the excitation spectrum and recording the Stokes-shifted band at resonance. The fits to the detected counts yield a maximum measured photon flux at the detector equal to $R_{\infty_{NC}} = (0.18\pm0.01)$ Mcps, $R_{\infty_{dome}} = (0.66\pm0.02)$ Mcps and $R_{\infty_{Au-dome}} = (2.38 \pm 0.11)$ Mcps, respectively. However, in case indistinguishable photons from the ZPL are required, non-resonant excitation on low-density NCXs can be employed [72] and a similar count rate would be estimated, based on the expected branching ratio for DBT:Ac ($30\% - 50\%$ [51]). For each configuration, the variability in the emitter position within the crystal results in some statistical fluctuations in the measured count rate within nominally identical structures. The stronger effect is to be found for the dome-on gold, as follows from the previous discussion on Fig. 4.3.2 of Sec. 4.3.2. The direct comparison reported in Fig. 4.23b is however representative of the typical observed trend. The detected count rate from a single cold molecule in the optimized micro-dome design is to our knowledge the highest reported to date and appears particularly significant when associated with the long excited state lifetime of DBT molecules ($\simeq 4.5$ ns). With respect to the nude nanocrystal, we measure a factor 3.7 ± 0.2 improvement in the collected photon flux for the micro-dome on silica, and a factor 13 ± 1 in the case of the optimal configuration for the micro-dome on gold, which are similar to the expected factors discussed in Sec. 4.3.2. Moreover a reduction in the saturation power by about two orders of magnitude is observed, passing from a value of $(56 \pm 10)\,\mathrm{W/cm^2}$ to $(0.10 \pm 0.02)\,\mathrm{W/cm^2}$. Indeed, the presence of the modified SIL has the primary effect of increasing the effective nu-

merical aperture of the optical system, hence improving its focusing efficiency. The underneath reflective layer further increases the intensity at the emitter position for a given input power.

In Figures. 4.24c,d,e we compare the normalized BFP maps for the nude nanocrystal on silica, the micro-dome device on silica, and the micro-dome on gold. The white dashed circumferences in the plots identify the experimental maximum collection angle of $\sim 42°$, whereas the centre of the circumference corresponds to the objective optical axis. Fig. 4.24c shows a homogeneously bright map, as expected from a dipole emission (here collected from above the substrate) and consistently with the typical on-plane orientation of the DBT:Ac system [46, 63]. Conversely, Fig. 4.24d and 4.24e confirm an effective redirection into small angles achieved in the micro-devices, competitive with what is shown in much more complex structures [264]. In the last cases, the slight misalignment of the bright spots is evidence of the not perfectly centred emitter, owing both to the DLW process and to the uncertainty in the fluorophore position within the Ac nanocrystal. Consistent with the results of the numerical simulations presented in Fig. 4.3.2, the pattern of a micro-dome on gold hosting a horizontally oriented molecule at an appropriate distance from the gold surface ($\simeq 100nm$) features most of its emission within the first $30°$ (as shown in Fig. 4.3.2 of Sec. 4.3.2). It is worth noticing that this configuration is not the one exhibiting the highest directivity. Narrower emission lobes can indeed be observed, corresponding though to a lower collection efficiency, as clearly evident from the central polar plot of Fig. 4.3.2. This scenario is also described by some representative experimental results reported in Fig. 4.25. In Fig. 4.25a,b two example of BFP measurements of micro-dome on gold structures are shown, exhibiting remarkably narrow emission lobes. For each structure, the collected photon flux at low temperatures from a single embedded molecule are reported in Fig. 4.25c as a function of the pump power. Fits to the data (solid lines) give respective maximum detected count rates of $\mathrm{R_a} = 1.20 \pm 0.03\,\mathrm{Mcps}$ and $\mathrm{R_b} = 0.81 \pm 0.03\,\mathrm{Mcps}$. As expected from simulations, these values are well below the record detected photon flux reported in Fig. 4.23b ($\mathrm{R}_\infty 2.38 \pm 0.11\mathrm{Mcps}$) for the optimal configuration.

4.5.3 Efficient coupling into a fiber

The effective redirection at narrow angles combined with the high detected count rate achieved with the micro-dome device are particularly suitable for the efficient coupling into a fiber, within the perspective of a compact fiber-coupled single photon source. With the experimental setup schematically shown in Fig. 4.26b, consisting in a telescope and a tunable-distance fiber-collimator, a coupling efficiency up to $(51 \pm 1)\%$ into a single mode fiber is achieved. The target value can be estimated in

terms of mode matching by comparing the measured fluorescence spatial distribution in the micro-dome on gold with a Gaussian mode, typical of a single-mode optical fiber (Fig. 4.26a). In particular, we estimate the best overlap integral to be of the order of $\simeq 80\%$. Considering the flexibility offered by a polymeric photonic platform [265], a monolitic fiber coupler can be integrated onto the metal-coated micro-dome in order to realize an alignment-free and ultra compact fiber-coupled single-photon source.

In conclusion, the developed approach to integration, based on the combination of the remarkable photophysical properties of the DBT:Ac nanocrystal system with the versatility of polymer materials, appears promising. We have indeed demonstrated deterministic integration of individual DBT:Ac NCX in different photonic structures, all realized in-loco and with a fast and inexpensive fabrication procedure. The implemented technique enables deterministic positioning of the emitter within the target 3D-geometry, as well as a high success rate in terms of optical properties after integration, thanks to a pre-selection of the optimal nanocrystals. Indeed, the photophysical features of the bare source are recovered even after the fabrication process. Furthermore, the photonic performances of the micro-dome lenses are demonstrated by the remarkable collected photon counts, the highest ever reported from a single-molecule at $3\,\mathrm{K}$, and by the coupling efficiency to a single-mode fiber. While the measurements at cryogenic temperatures were not successful for the integrated WGs, because of a current technical limit on thermal conduction due to the suspended design, the future employment of a cryostation setup based on Helium-3 injection can possibly solve the issue and enable the analysis of more complex 3D designs.
In general, the limited photonic performances of polymers in terms of propagation losses, which arise in the integrated WGs, can be overcome by the realization of hybrid polymer-semiconductor devices which leverage the advantages of both material platforms. In this sense, the next chapter is focused on the possibility of exploiting lithographic patterning of PVA films to achieve deterministic integration of DBT:Ac NCX on silicon nitride waveguides.

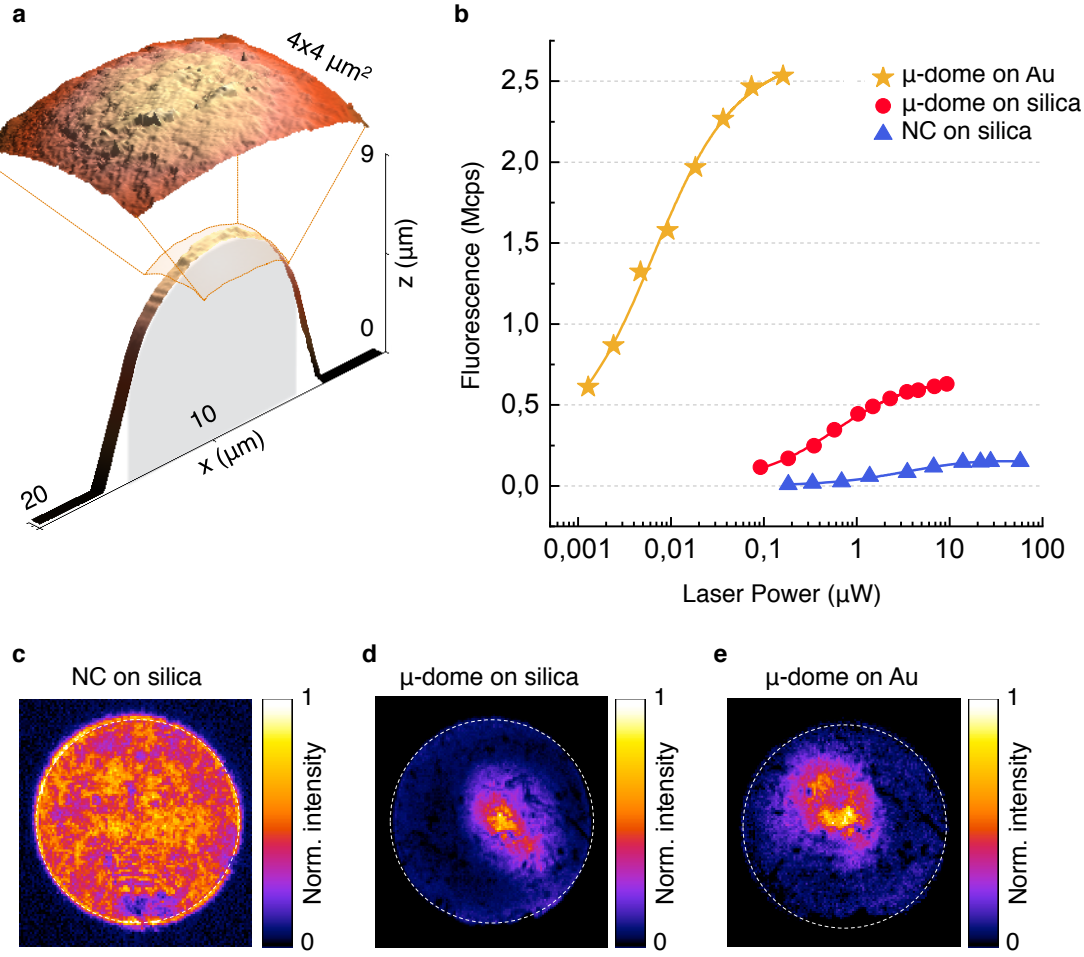

Figure 4.24: **a** - Atomic Force Microscopy (AFM) characterization of the fabricated micro-dome on gold. The strip-scan ($20 \times 1\mu m^2$) of the structure passing through the dome pole gives an estimation of the experimental dimensions, with a total height $h = 9.1 \pm 0.1\,\mu$m and a radius $r = 5.0 \pm 0.1\,\mu$m, in good agreement with the optimal values based on simulations, $h_{th} = 8.7\,\mu$m and $r_{th} = 5.3\,\mu$m, and displayed in the grey silhouette. From the AFM map of the top $4 \times 4\mu m^2$ surface area, the surface roughness is estimated to be $\Delta r = 41 \pm 4$ nm. **b** - Experimental collected photon flux at low temperature from a single molecule embedded in the fabricated micro-dome structure on gold (yellow stars), compared to the case of the micro-dome on silica (red dots) and of the bare nanocrystal (blue triangles). Saturation curves are obtained by plotting the maximum counts of the measured excitation spectrum as a function of pump power. Fits to the data (solid lines) yield corresponding maximum detected photon fluxes at the detector $R_{\infty_{Au-dome}} = (2.38 \pm 0.11)$ Mcps, $R_{\infty_{dome}} = (0.66 \pm 0.02)$ Mcps and $R_{\infty_{NC}} = (0.18 \pm 0.01)$ Mcps, respectively. **c,d,e** - Back focal plane (BFP) measurements of the emitted fluorescence showing the emission pattern for the micro-dome on gold, the micro-dome on silica and the bare nanocrystal, respectively. Detected counts are plotted in momentum space and normalized to the maximum for all plots, whereas the white dashed circumferences identify the experimental maximum collection angle of $\sim 42°$.

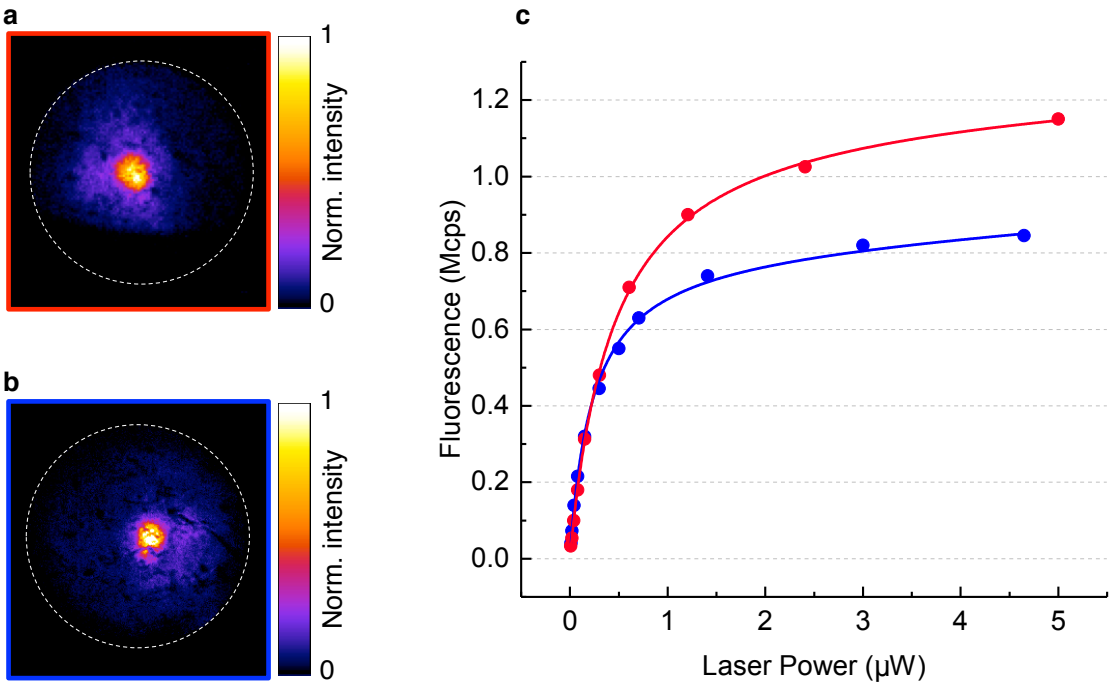

Figure 4.25: **a,b** - Back focal plane measurements of micro-dome on gold structures exhibiting narrow emission lobes. The count rates detected on a EMCCD camera are normalized and plotted in the momentum space, where the dashed white circumference indicates the maximum collection angle of our setup $\sim 42^\circ$ and the centre of the circumference corresponds to the objective optical axis. **c** - Corresponding collected photon flux at low temperatures from a single embedded molecule as a function of the pump power. Fits to the data respectively yield a maximum measured photon flux at the detector equal to $R_a = 1.20 \pm 0.3$ Mcps and $R_b = 0.81 \pm 0.3$ Mcps.

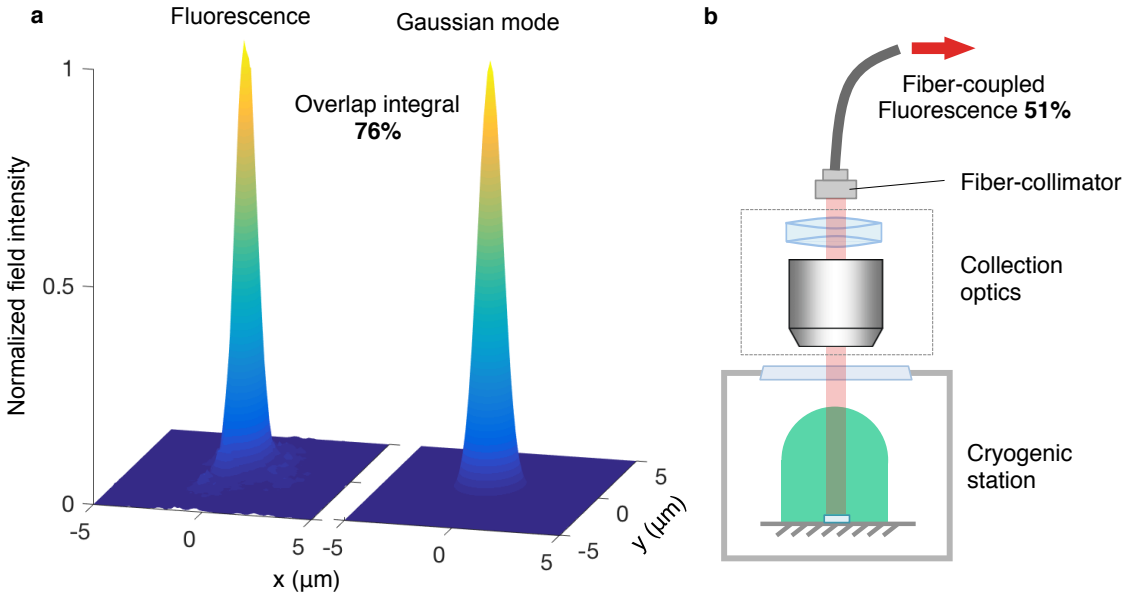

Figure 4.26: **a** - Estimation of the expected coupling efficiency for the micro-dome on gold. The target value is evaluated in terms of mode matching by comparison of the measured fluorescence spatial distribution of the integrated structure with a Gaussian mode, typical of a single mode optical fiber. The estimation gives the best overlap integral of $\sim 80\%$. **b** - Schematic of the experimental setup and measured performance of up to 51% coupling efficiency, which is normalized to the detected counts on a SPAD. In particular, the setup consists in the objective, a telescope and a tunable-distance fiber-collimator.

5

Deterministic Positioning on SiN Chips

In this last chapter, we present a strategy for deterministic positioning of molecular quantum emitters on silicon nitride (SiN) chips, based on the demonstration of 2D patterning of polyvinyl alcohol (PVA) via electron-beam lithography. In particular, micro-infiltration of DBT:Ac nanocrystals is employed for a localized deposition of the source, and a-posterior selection is enabled by subsequent coating with a PVA layer and electron-irradiation. We describe here the characterization of the lithographic process and its optimization, aimed to preserve the photo-physical properties of the embedded emitter after fabrication.

Polyvinyl alcohol (PVA) is a synthetic water-soluble polymer, employed worldwide since the beginning of the 20th century. For its excellent properties, e.g. thermal and chemical stability, strain resistance, biodegradability and non-toxicity [266, 267], it has been extensively applied in the industrial, commercial, bio-medical, and food sectors. Owing to its good transparency and hydrophilic nature, it is especially suitable as host matrix for any hydrophobic material, and in particular for DBT:Ac NCX. Indeed, once NCX are embedded in PVA, the thermal stability of the polymer assures an efficient protection from the external environment and reduces the sublimation rate of Ac, as already mentioned. For instance, as reported in the PhD thesis by Dr. Sofia Pazzagli [268], NCX covered with a spin-coated layer of PVA did not exhibit reduction of fluorescence intensity after two weeks they were left at room temperature conditions. On the contrary, a substantial reduction is found in NCX without PVA on a time scale of one day at room temperature.
In the following sections, we demonstrate for the first time in literature the possibility to pattern PVA thin films via electron-beam lithography with high spatial resolution and without the addition of any cross-linker agent. In particular, PVA is used as a negative-tone resist and is then developed in a water bath in order to wash away the unexposed parts. Finally, we identify a region of parameters for which the lithography on NCX-doped PVA does not compromise the photophyisical properties of the embedded emitters.
This technique suggests possible options for the controlled deposition of single-photon emitters on SiN , combining the optimal properties of single photon emission from fluorescent molecules and the low propagation losses of SiN chips.

The fundamental results in this chapter, achieved within a collaboration with the group of Prof. Frank Koppens, Institute of Photonic Sciences (ICFO), are reported in *Narrow linewidth quantum emitters in electron-beam shaped polymer* by C. Ciancico, et al., *Under submission*, and in S. Pazzagli, et al., *In preparation*.

5.1 DBT:Ac Nanocrystals in PVA

PVA is synthetically obtained from polyvinyl acetate through hydrolysis, with a large number of hydroxyl groups forming inter and intra chain H-bonds (Fig. 5.1a). PVA exhibits superior features as an oxygen barrier, and in general, upon protection from moisture (because of its solubility in water), its gas permeability is remarkably stable [269]. Therefore, taking also advantage of its film-forming features [270], and of its insolubility in most polar organic solvents used in nanofabrication [271], PVA is especially suitable for the DBT:Ac system as protective layer, both from the natural sublimation of Ac at room temperature conditions and also from additional fabri-

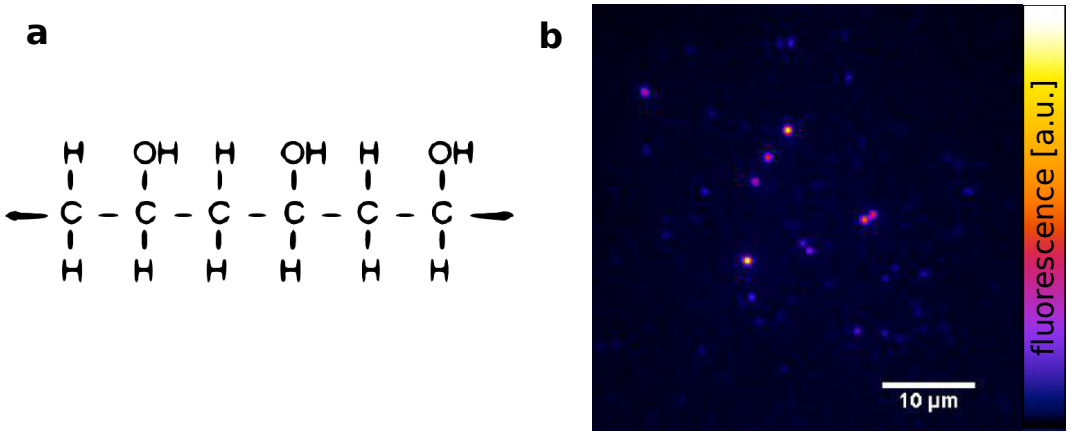

Figure 5.1: **a** - Chemical structure of polyvinyl alcohol (PVA). **b** - Example of wide-field fluorescence image of a spin-coated layer of PVA containing DBT:Ac NCX.

cation processes. For these reasons, PVA is extensively employed in our fabrication protocols, as e.g. in planar optical antenna configurations, where is used both as a spacer layer and to protect DBT:Ac from gold sputter-coating [57]. More in general, once DBT:Ac NCX are covered with a layer of PVA, their thermal stability is largely improved, resulting in stable intensity of the fluorescence emission at room temperature, within a period of weeks [268]. In practice, a standard sample is typically realized by depositing the NCX on the desired substrate (following what discussed in Chapter 2) and by subsequent deposition of a thin film of PVA (Sigma Aldrich, 5% in milliQ water solution) via spin-coating [1].
Alternatively, DBT:Ac NCX can be grown directly in a sonicating aqueous solution of PVA, following the same protocol presented in Appendix B, and obtaining a suspension of NCX in PVA. In this case, PVA has the further effect of stabilizing the suspension with consequent absence of reprecipitated particles for several month. This observation suggests that the polymer viscosity inhibits the NCX clusterization [2]. Also, viscosity affects the NCX size, which can be controlled to a certain extent by adjusting the PVA concentration in water. Fluorescence characterization (wide-field map in Fig. 5.1b) is in this case performed after spin-coating a NCX-PVA suspension on a coverglass of a resulting film-thickness of ~ 300 nm.

[1] The standard recipe yields a film thickness of $\sim 150 - 200$ nm and consists in a two-step spinning, with an initial 5 s-ramp to 1500 rpm, and 120 s at 3500 rpm.

[2] This was confirmed also by DLS measurements yielding a mono-disperse size distribution on the same suspension after one year time [268].

5.2 2D Patterning of PVA

The chemical and physical properties of PVA depend on the polymerization conditions of polyvinyl acetate and on the percentage of hydrolysis [272], which for example determine the PVA final molecular weight $(20,000 - 400,000)$. However, PVA requires a-posterior crosslinking formations in order to reduce its solubility in water and broaden its applicability, making it suitable for use e.g. in biomedical applications [273], drug delivery [274] and pervaporation systems [275]. Crosslinking consists in chemical bonding of the polymer chains with each other, with consequent modification of the macroscopic properties of the material. This process can be performed with chemical reagents, which carry multi-functional groups having good reactivity to the functional groups of the polymer, or via heat-treatment methods which induce physical crosslinking based on crystallization. Typically, heat treatment methods require the addition of acidic catalysts or cross-linker agents for efficient results.
Here, we investigate the possibility to induce cross-linking of PVA by localized heating with focused high energy radiation, without the further addition of chemical compounds. Indeed, within our perspective of patterning PVA-covered organic NCX, a purely physical treatment would avoid chemical contamination and minimize undesired effects on the emission optical properties. In this context, highly localized energy exposure of the sample can be obtained via electron-beam lithography, which is already demonstrated to effectively pattern PVA upon doping with metal nanoparticles as reactive centers [276]. In this specific case, e-beam exposure involves chemical reduction of the metallic particles with consequent release of H^+, which induces PVA crosslinking. As a result the PVA molecular weight increases and the solubility in water of the exposed area is reduced. H^+-induced cross-linking of PVA has also been observed upon adding of a photoacid generator [277].

5.2.1 Electron-Beam Lithography

Electron-beam lithography (EBL) enables the realization of extremely fine patterns with few nanometers spatial resolution [278] and on a broad variety of materials. The fabrication technique consists in scanning a focused beam of electrons across custom shapes on a surface covered with an electron-sensitive resist film. Analogously to any lithographic technique, the deposited energy changes the solubility of the material (typically a polymer) so that the exposed (unexposed) regions can be dissolved on suitable development baths (positive (negative) lithography), leaving only the desired patterns on the substrate (as summarized in Fig. 5.2a). The writing system is composed by an electron-source, a focusing optics set, a blanker for switching the

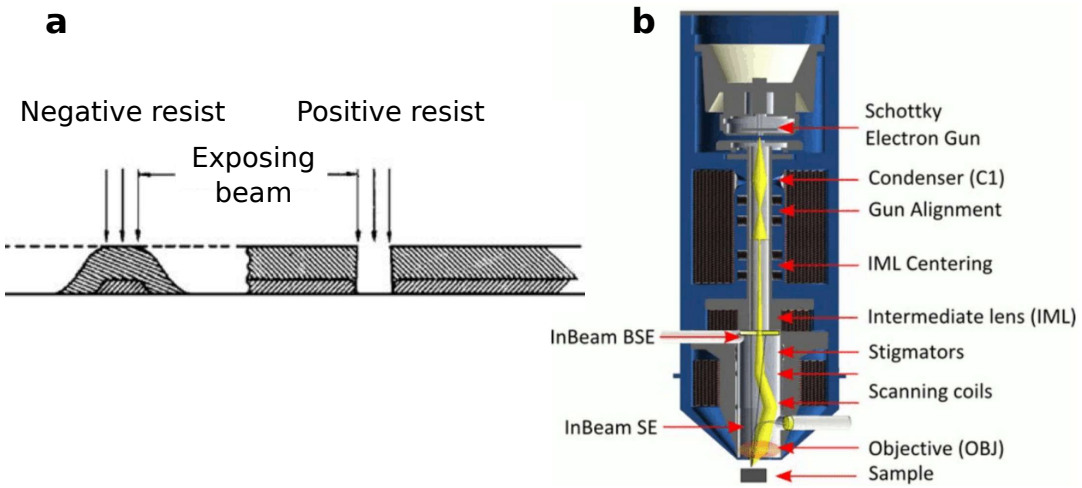

Figure 5.2: **a** - Sketches of electron-beam lithography on negative (positive) resists. The unexposed (exposed) regions can be dissolved in suitable development baths, leaving only the desired patterns on the substrate. **b** - Cross section of the column of the dual-beam facility employed in this thesis-work (Gaia3 FIB/SEM Tescan). In summary, the writing system is composed by an electron-gun, a focusing optics set for the alignment, a blanker for switching the beam on and off, a deflection system for the control of the beam direction, and a holding-stage for the substrate.

beam on and off, a deflection system for the control of the beam direction, and a holding-stage for the substrate (Fig. 5.2b). Upon proper optimization of the parameters (e.g. electron dose, exposure time, spot size), the finely focused electron-beam is therefore scanned on the sample in order to expose one pixel at a time. The correct exposure time, as well as the development time, is strongly related to the type of resist and developer used. In negative resist, the edge profile of a line exposed is bell-shaped, caused by the electron scattering. [3].

Looking more deeply at the electron trajectories in the resist and at the energy deposition in matter, fundamental contributions to the overall lithographic process are given both by primary and secondary electrons. In forward scattering, an electron can collide with an electron from one of the atoms in the substrate/resist. The incident electron will change its direction, within a typically small angle, and transfer part of its energy to the atom (Fig. 5.4a). Consequently, the atom will become exited or ionized. When the target atom is part of a resist molecule, the molecular chain may break due to this excitation or ionization. In backscattering, an electron collides with the much heavier nucleus, resulting in an elastic scattering event. The electron

[3] In positive resist, on the other hand, the exposed part is etched away and more control over the profile is possible. By using a higher dose and/or a short development time, the edge profile is dominated by the energy deposition profile, and has a shape as in figure 5.3a. A low dose and long development time yields a shape as in Fig. 5.3c. With medium dose and development, steep vertical edges can be obtained (Fig. 5.3b) [279, 280, 281].

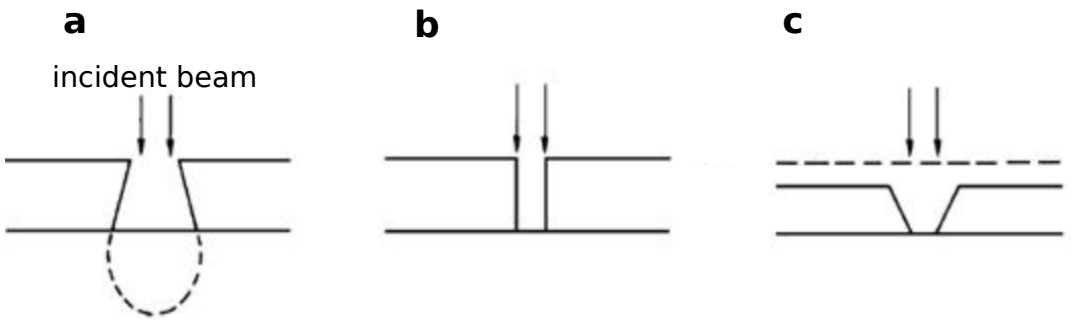

Figure 5.3: **a** - In positive resists, by using a higher dose and/or a short development time, the edge profile is dominated by the energy deposition profile. With low dose and long development time the profile is like in (**c**). With medium dose and develop, steep vertical edges can be obtained (**b**).

retains most of its energy, but changes its direction, this time within a possibly large angle (Fig. 5.4b). Therefore, electrons may also return back through the resist at a

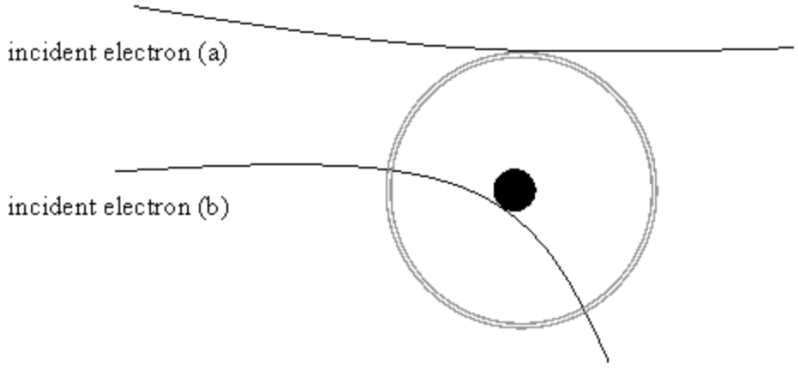

Figure 5.4: Electron-atom collisions typically take place both in the substrate and in the resist material. Consequently, the electron direction can either change within small angles, with transfer of energy to the atom which is excited/ionized, or can change within large angles in elastic scattering processes.

significant distance from the incident beam causing additional resist exposure. As the primary incident electrons loose energy via inelastic scattering, secondary electrons are produced. The efficiency of this process strongly depends on the electrons kinetic energy, therefore on their velocity. The generated secondary electrons, are then responsible of breaking of the chemical bonds within a certain distance from the original collision. Additionally, they can also generate further, lower energy electrons, resulting in an electron cascade. Together with the forward scattering, these events cause a widening of the exposure region. Also, due to the many small angle scattering events, forward scattering increases the effective beam diameter, which is

empirically given by the following formula [279]:

$$d_b = 0.9(t_f V_b)^{1.5} \tag{5.1}$$

with d_b the effective beam diameter, t_f the resist thickness and V_b the beam voltage. Hence, it is worth noticing that the initial film thickness also affects the effective lateral resolution of the lithographic process. These effects contribute to the main limit in resolution of e-beam lithography machines. The distance a typical electron travels before losing all its energy depends on both the energy of the primary electrons and the type of material it is traveling in. The fraction of electrons that are backscattered is roughly independent of beam energy. It does, however, have a strong relation to the substrate material. Substrates with a low atomic number give less backscattering than substrates with high atomic number.
In general, in order not to accumulate incident electric charges which can also deflect the electron-beam, the employed underneath substrate must be conductive. The most extensively used substrate is silicon with a thin insulating layer of silicon dioxide on top. Otherwise, other typical substrates are glass plates coated with metal (ITO [282], or chrome on glass [283]).
Besides the high set-up costs and typical low fabrication speeds (due to the pixel by pixel exposure process), owing to its resolution capabilities both on metallic and dielectric materials, e-beam lithography is employed for a huge variety of applications. Originally developed for manufacturing classical integrated circuits, it is now at the base of nanotechnology fabrication, from quantum nano-photonics circuits and photonic crystal slabs [284, 285], to plasmonic [286, 287] and metamaterials [288, 289]. Of course, the resulting patterned geometries are 2D-limited in this case.

5.2.2 Using PVA as Negative-Tone Resist

We rely on a dual-beam facility (Dual beam Gaia3 FIB/SEM Tescan, Triglav electron column equipped with beam blanker for electron lithography) to perform a detailed study and characterization on patterning of PVA via electron-exposure. In particular, we show that PVA is patternable upon e-beam exposure as single-component negative-tone resist, which to the best of our knowledge has not been previously reported.
The experimental protocol consists in spin-coating a thin film of PVA on silicon substrates, exposing it to e-beam irradiation, and developing the sample in milliQ water until the unexposed portions are dissolved (few seconds). We characterize the topology of the patterned features by means of AFM measurements. The final goal is to obtain the best compromise between high spatial resolution of the written features and low electron doses, for a minimum impact on DBT:Ac NCX once they are embed-

ded within the polymer for photonic applications. In this context, we explored the impact of the different parameters, such as the PVA molecular weight, and the beam energy. We also studied the fabrication process on different substrates, namely Au-coated glass and silicon nitride on silicon chips, in order to test the potential application in photonics. Additionally, we also analyzed the effect of adding a water-soluble photoacid (PAG, (4-fluorophenyl)diphenylsulfonium triflate), potentially compatible with the organic NCX, to increase the efficiency of the interaction with electrons.
In the following table we summarize the main features of the commercial types of PVA employed, of different molecular weight:

resist	PVA1	PVA2	PVA3	PVA4
Sigma Aldrich code	363170	363081	363065	PVA1 +PAG 527025
mol. weight	13.000-23.000	85.000-124.000	146.000-186.000	–
hydrolysis deg.	$87-89\,\%$	$87-89\,\%$	$>99\%$	–

Different molecular weights entail different viscosities and therefore spin-coater recipes must be consequently tailored, for each desired final film thickness. For our purposes, also taking into consideration the average NCX thickness of about $150\,$nm, a reasonable target PVA film thickness is $150-200\,$nm, such to efficiently protect the embedded emitters without reducing lateral resolution (according to the relation in Eq. 5.1). In Fig. 5.5a we report a collection of average thickness values of the different PVA film, based on profilometric measurements, and depending on the spin-coater velocity. For all cases, the spinning recipe consists in a first common step, which goes up to a velocity of $1500\,$rpm within a $5\,$s ramp, and in a final step of $120\,$s at the velocity reported in the x-axis. Finally, the sample is soft-baked at 60° for $90\,$s, to stabilize thickness via further evaporation of residual water. The exposed data do not show a general regular behaviour, due also to the sensitivity of the spin-coater technique to the ambient conditions, but are sufficient to obtain a reliable and reproducible result within the thickness range of interest.
The following study is based on the primary two characterization factors of EBL on any resist, namely contrast and sensitivity. While contrast is the difference in thickness between exposed and unexposed areas in the resist, sensitivity defines the extent of thickness change with respect to the electron beam dose. The dose is usually expressed in $\mu\mathrm{C}/\mathrm{cm}^2$, being the number of electric charge per unit area [290]. These two parameters can be extracted by the contrast curve, which is obtained by plotting the remaining resist thickness as a function of the dose. In Fig. 5.5b the contrast curve is shown for positive and negative resists. Specifically, the sensitivity is the dose D_{100} at which the resist is completely developed (for a positive resist) or reaches the full initial resist thickness (for a negative resist), and contrast is the slope of the curve.

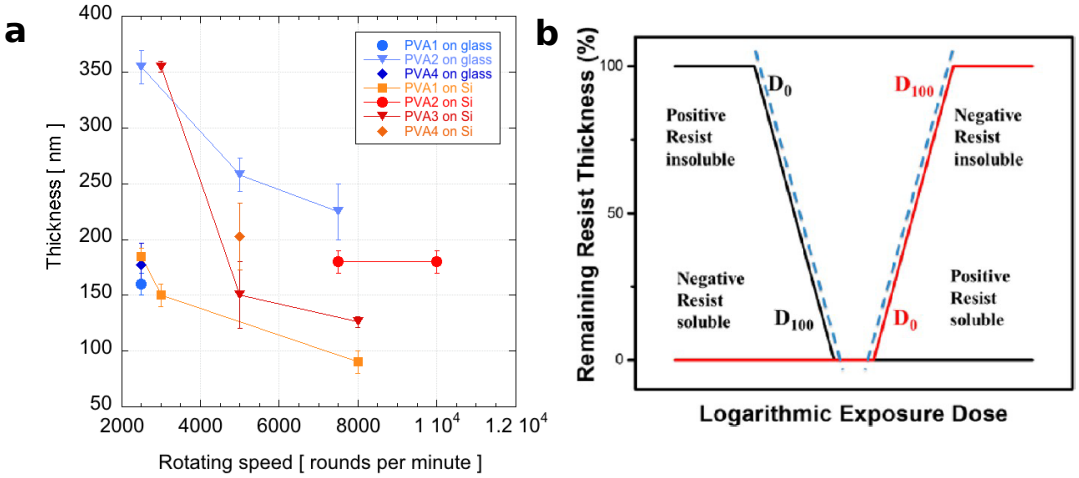

Figure 5.5: **a** - Resulting film thickness for different PVA and on different substrates, as a function of the spin-coating velocity. Error bars are associated to the average on repeated measurements. **b** - Definition of D_0 and D_{100} for positive (black) and negative resists (red). They are, respectively, the highest dose at which the resist is not yet affected by the irradiation, and the minimum dose at which the resist has undergone a complete change of its chemical structure.

The following equations expresses the interdependence of the two parameters [291]:

$$\gamma = \frac{1}{\log \frac{D_{100}}{D_0}} \tag{5.2}$$

where γ is the contrast, D_0 is the highest dose at which the resist is not yet affected by the irradiation and D_{100} is the minimum dose at which the resist has undergone a complete change of its chemical structure. Usually, the ideal condition is having high sensitivity and contrast. In our case, we rather want an efficient patterning, with high spatial resolution, with low enough doses not to compromise the ultimately embedded emitters.

In Fig. 5.6a we show an example of series of square patterns, each written with a different dose, from which we obtain the contrast curves for different types of PVA (table 5.2.2) [4]. For each square, the resist thickness is extrapolated from an AFM map and plotted as a function of the employed dose. In the AFM map of Fig. 5.6a, we can clearly distinguish the increase of the features thickness with the electron dose until a maximum value, beyond which the chemical change expands also outside the area of exposure (which is a $5 \times 5\,\mu\mathrm{m}^2$). The corresponding contrast curves for the different PVA, displayed in Fig. 5.6b, show a very similar behaviour for the not chem-

[4]For all the lithographic processes displayed in this manuscript, EBL was performed in Analysis mode (without proximity effect correction), with beam energy of 30 KeV (unless differently mentioned).

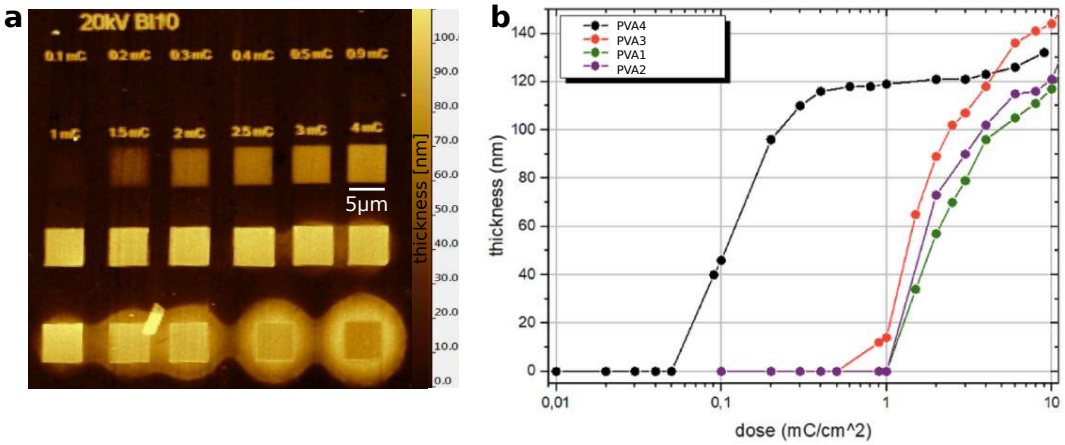

Figure 5.6: **a** - AFM map of PVA squares written with increasing dose. By measuring the squares thickness we obtain the corresponding contrast curve as a function of the dose. **b** - Contrast curves for different PVA on silicon substrate.

ically amplified polymers, with slightly increasing contrast for increasing molecular weight of PVA ($\mathrm{MW_{PVA3}} > \mathrm{MW_{PVA2}} > \mathrm{MW_{PVA1}}$) and with a similar sensitivity of about $10\,\mathrm{mC/cm^2}$. In particular, the highest molecular weight PVA3 also exhibits a lower $\mathrm{D_0}$, half of the value for PVA1 and PVA2, suggesting that the chemical change is indeed more efficient. The sensitivity of the proccess is remarkably enhanced for the case of the PVA4, with a reduction both of $\mathrm{D_0}$ and $\mathrm{D_{100}}$ of more than one order of magnitude, while keeping the contrast essentially unchanged. These results point out the relevant impact of photoacids in the sensitivity of EBL on PVA, but most importantly, they highlight the possibility of patterning the water-soluble photoresist also without any chemical addition.

In Fig. 5.7 we report the contrast curves for two different electron energies, investigated on PVA4, and for different substrate types, investigated on PVA1 and PVA4. From Fig. 5.7a we observe a negligible difference on sensitivity and a slightly higher contrast for the lower intensity of the electron beam. The comparison on the use of different substrates (Fig. 5.7b) indicates that the use of gold leads to higher sensitivities (of $\sim 20\%$) and lower contrasts (with $\mathrm{D_0}$ decreasing to half with respect to the other cases), with no significant difference between the case of PVA1 and the amplified PVA4. Furthermore, silicon nitride induces a higher contrast, whereas silicon gives a smaller $\mathrm{D_0}$. In conclusions, besides some differences, mainly concerning the lower effective dose achievable with a gold substrate, the lithographic technique on PVA can be successfully applied to all the explored substrates, typically employed in the circuitry for quantum photonics applications.

Finally, we use the chemically amplified PVA4 on silicon substrate to explore the maximum achievable resolution (minimum feasible feature) by fabricating series of

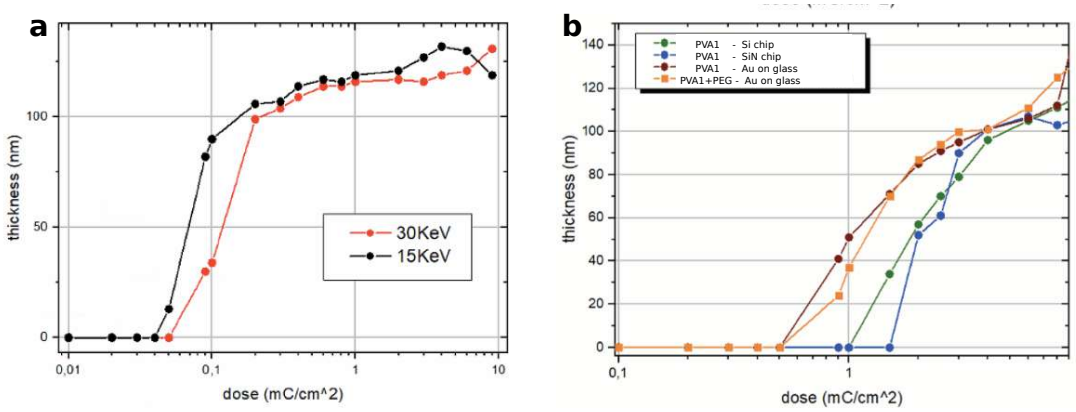

Figure 5.7: **a** - Contrast curve for PVA4 on silicon, for two different electron energies. **b** - Contrast curves for PVA1 and PVA4, on different substrates and at fixed electron energy.

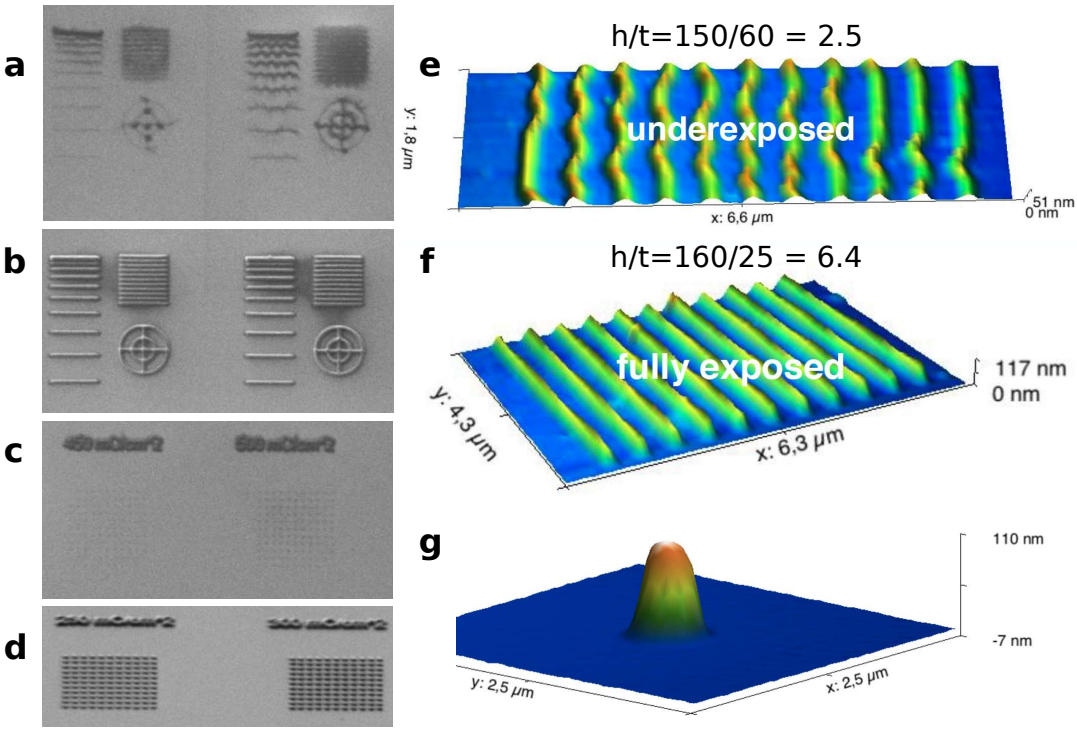

Figure 5.8: Investigation of maximum achievable resolution. **a,b,c,d** - SEM images of 1-pixel lines and 1-pixel dots fabricated with PVA4 with different doses. **e,f** - AFM map of underexposed and fully exposed lines, respectively. **g** - Example of AFM map of 1-pixel dot.

1-pixel lines and 1-pixel dots at different electron beam doses (at fixed sample preparation and development). Some significant examples of SEM images of the realized patterns are shown in Fig. 5.8, where the results for low doses (Fig. 5.8a,c) and high

doses (Fig. 5.8b,d) are compared for the 1-pixel lines and 1-pixel dots, respectively. On the right, Fig. 5.8e,f display the AFM characterization of underexposed and fully exposed lines. While the first ones appear irregular and soft, probably agitated during the development step, the second ones are completely cross-linked and robust. The aspect ratios of the lines, namely the height (h) over the thickness (t) of the single line, are $150\,\mathrm{nm}/60\,\mathrm{nm} = 2.5$ and $160\,\mathrm{nm}/25\,\mathrm{nm} = 6.4$, respectively. In Fig. 5.8g an example of the AFM map of a 1-pixel dot shows a typical cylindrical shape with bell-shaped edges. The minimum features obtained from the AFM measurements on the 1-pixel dots as a function of the beam dose are summarized in the plot in Fig. 5.9a, where they are expressed in terms of the percentage residual thickness (starting from a film thickness of 150 nm). On the right, two examples of AFM profiles from which the plot was retrieved are shown, for the $6\,\mathrm{mC/cm^2}$ (Fig. 5.9b) and $2\,\mathrm{mC/cm^2}$ (Fig. 5.9c) electron beam dose.

These findings show that the developed fabrication based on EBL exposure of PVA al-

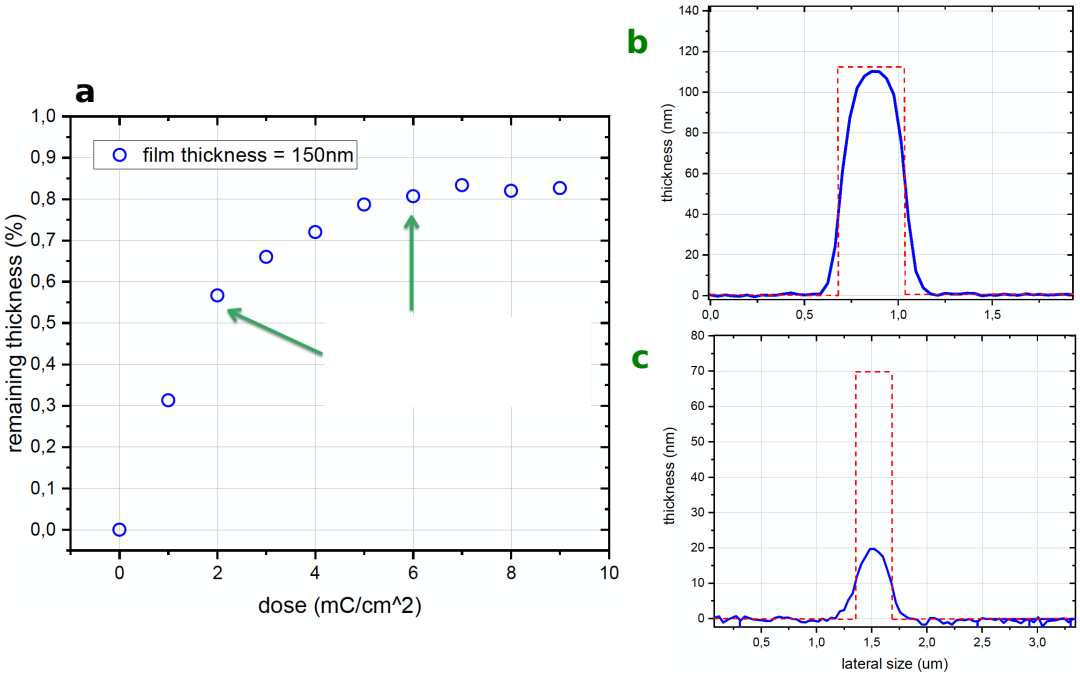

Figure 5.9: **a** - Minimum features as a function of the e-beam dose. These values are extracted from the profiles of the AFM maps of the 1-pixel dots (see Fig. 5.8g). **b,c** - Examples of 1-pixel dots profiles, for $6\,\mathrm{mC/cm^2}$ and $2\,\mathrm{mC/cm^2}$ e-beam dose, respectively.

lows the realization of 2D patterns with high spatial resolution and using low electron beam doses. We showed indeed that the minimum feature size can be tuned down to 10% of the initial film thickness (150 nm), corresponding to few tens of nanometers in our specific case. Furthermore, if we compare the sensitivity of the process (Fig.

5.6b) with the state of the art (Fig. 5.10 [292]), for the pure PVA this is of the same order of magnitude of the values reported for other water-soluble resists, while it becomes lower of one order of magnitude when using the chemically amplified PVA. Therefore, our results prove an overall competitive method for water-soluble resists, which is compatible with the employment of low doses and is thus promising for the patterning of NCX-PVA.

number	name	family	tone	developer	sensitivity ($\mu C/cm^2$)	contrast (γ)	EBL voltage (kV)	etching gases	etch rate (nm/min)	CD (nm)	dense patterns pitch/CD (nm)
1	poly(GMA-*co*-MMA-*co*-TPSMA)[32]	CARs	N	7:3 IPA:DI water	125	-	100	CF_4	40	15	20/19
2	40XT/PEDOT–PSS[35]	CARs	P	AZ7 26MIF	7	7	20	-	-	80	70/90
3	MAPDST-MMA[39]	n-CARs	N	TMAH	2	1.8	20	CHF_3/O_2	~9[a]	20	40/20
4	P(HEMA-*co*-MAAEMA)[42]	n-CARs	N	methanol	0.89	1.2	50	SF_6, wet HNA	225, 15	125	200/125
5	C_{60}-(P(CMS_{14}-HS))[47]	fullerene derivative	N	acetone	40	-	100	-	-	50	50/50
6	IM-MFP_{12-8}[49]	fullerene derivative	N	1:1 monocholoro-benzene:IPA	43	1.3	20	SF_6/C_4F_8	58	18	50/18
7	CSAR 62[56]	methacrylate	P	amyl-acetate	172	5.2	100	CF_4/O_2	100	10	150/75
8	SML[10]	methacrylate	P	7:3 IPA:DI water	60	9.2	10	SF_6/C4F_8	17	15	30/15
9	Mr-Pos EBR (Copolymer 5)[59]	methacrylate	P	amyl-acetate	74	3.0	30	SF_6/CF_4	200	29	100/29
10	$HafSO_x$[64]	inorganic	N	TMAH	21	2.5	30	CHF_3	2.2	9[67]	21/9[67]
11	$ZircSO_x$[64]	inorganic	N	TMAH	8	2.6	30	CHF_3	2.9	16	100/28
12	PSS[72]	water-soluble	N	DI water	2800	0.8	20	O_2	~17[b]	50	-
13	silk[74]	water-soluble	P, N	DI water	2250 (P); 25000 (N)	-	100	C_4F_B/O_2	546	30 (dot)	-

Figure 5.10: **Table**. Comparison of EBL processes on different materials (as reported in Ref. [292]).

5.3 Inclusion of Quantum Emitters

In this section we demonstrate the compatibility of the electron-beam lithography on PVA with the DBT-AC NCX, embedded inside. By decreasing the electron beam dose used, we show that the effect of the fabrication process on the photo-physical properties of the embedded NCX can be reduced and made negligible. This is crucial for the employment of this technique in quantum nano-photonic applications. In particular, we envisage to use 2D patterning of NCX-PVA to place the source at the point of maximum coupling efficiency on a SiN chip. In this context, we report preliminary results on micro-infiltration of NCX as efficient method for ultra-localized deposition of the sources in the area of interest of a photon circuit and consequent patterning of PVA. By combining these two experties, deterministic positioning is readily achieved by fixing the emitter via confined electron exposure, and by subsequent washing away of the other NCX during the development step (with further rinsing in acetone after development, in the case of dessicated NCX) (Fig. 5.11).

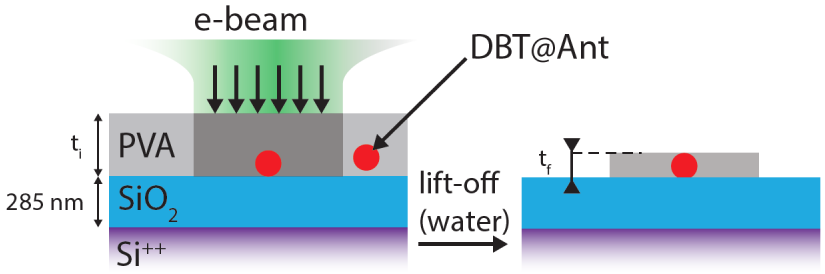

Figure 5.11: Lift-off scheme. DBT:Ac NCX (red dots) are embedded in PVA layers and deposited over a standard SiO_2 substrate. After e-beam irradiation the non-exposed zones are washed away in water and only the exposed area is left.

5.3.1 2D Patterning on NCX-PVA

For the investigation of the compatibility of DBT:Ac NCX photo-physical properties with EBL on PVA, we prepare the samples using both the protocols described in 5.1: dessication of the NCX on the substrate and subsequent deposition of PVA via spin-coating, or direct drop-casting and spin-coating of the NCX suspension in PVA. For all cases we use dense DBT-doped Ac NCX on silicon substrates, and we perform a soft post-baking prior to the lithographic process. Next, the sample is exposed with different electron doses, each applied to different areas. After development, the emission properties of the embedded emitters within the patterned regions are observed.

An example of the resulting sample is shown in Fig. 5.12a, where multiple sets of squares written at different doses are clearly distinguishable for their different colour, each corresponding to a different residual thickness. On the right, a zoom-in of the square written at $4\mathrm{mC/cm^2}$ is displayed together with the respective fluorescence map (Fig. 5.12b), collected at cryogenic temperature. It is possible to define a one-to-one correspondence between the NCX appearing as black spots in the white light image, and the bright spots in the fluorescence map, which demonstrate persistence of fluorescence after fabrication. As an opposite scenario, when the dose is too high (Fig. 5.12c), the emitters are irreversibly damaged and no fluorescence is detected in the patterned area (delimited by the red dashed line). In clear contrast, the NCX which did not undergo irradiation do exhibit fluorescence as expected.

A better understanding of the impact of EBL on the embedded emitter properties is given by Fig. 5.13 [64], where the linewidth and photostability of the fluorescence emission is compared for different doses. With gradually increasing dose, larger emission linewidths are observed, and correspondingly the linewidth distribution extracted from about 800 molecules is broadened and shifted to higher values (Fig. 5.13a). The results also show that low doses ($1\mathrm{mC/cm^2}$) have a minimum impact and that the reference distribution (from unexposed NCX) can be recovered with only a slight

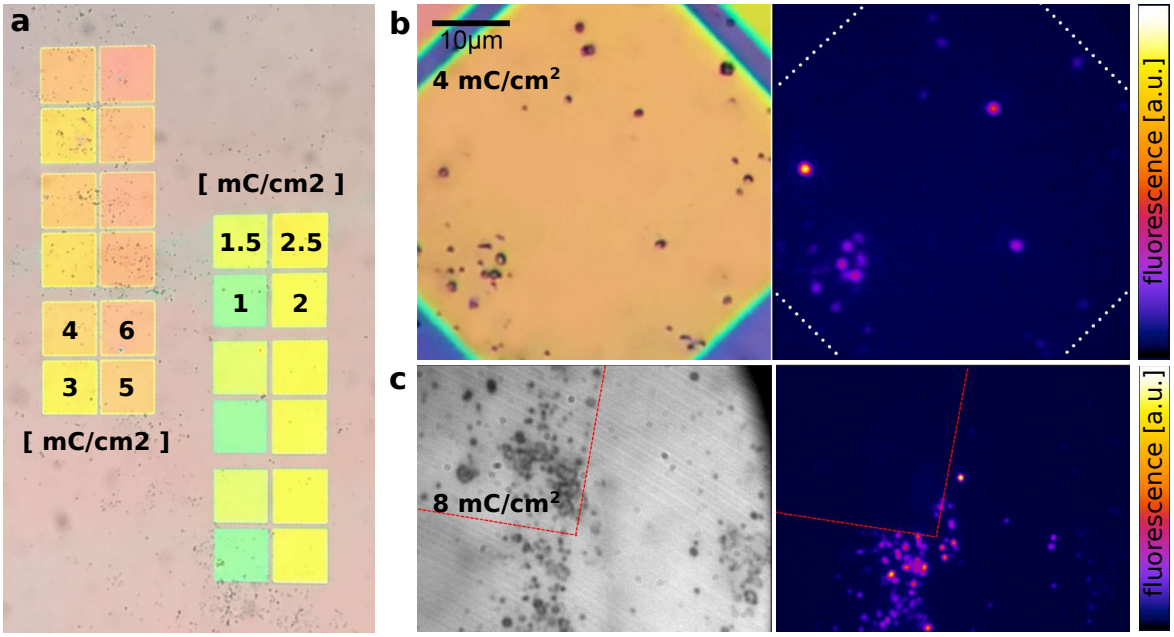

Figure 5.12: DBT:Ac NCX are here deposited on a Si substrate and covered with a layer of spin-coated PVA. **a** - WL image of the sample with different squares written over the embedded NCX with increasing doses. WL image and corresponding wide-field fluorescence map of the square written with **b** - $4\,\mathrm{mC/cm^2}$: fluorescence signal persists after fabrication. **c** - $8\,\mathrm{mC/cm^2}$: fluorescence signal is absent within the written area (dashed line), whereas is clearly visible in the unexposed zones.

broadening and leaving the peak unchanged. We correspondingly display the inhomogeneous distribution of the ZPLs of the organic molecules in a NCX of the $1\mathrm{mC/cm^2}$-exposed area, and a detailed excitation spectrum which exhibits a linewidth of 134 MHZ (5.13b). We attribute the linewidth broadening arising at higher doses to a modification of the molecule environment due to detrimental effects of the electron radiation such as electrostatic charging and deterioration of the anthracene matrix [293, 294]. Interestingly, a fraction of narrow linewidth ($< 200\,\mathrm{MHz}$) peaks remain for each e-beam dose studied. This suggests a dominant surface effect of the e-beam on the nanocrystal which can be understood assuming a random distribution of molecules within its volume: molecules closer to the surface are strongly affected by any surface reconstruction [295], electrostatic puddles [296] or amorphous carbon contaminants [297], which can lead to a broadening of emission lines. Conversely, molecules closer to the centre of the nanocrystal are less perturbed and exhibit narrower linewidths.

Finally, we monitored the behaviour of single molecule emission spectra as a function of the dose (Fig. 5.13c) to determine the influence of electron beam irradiation on the molecules spectral stability. Confirming the deductions from the previ-

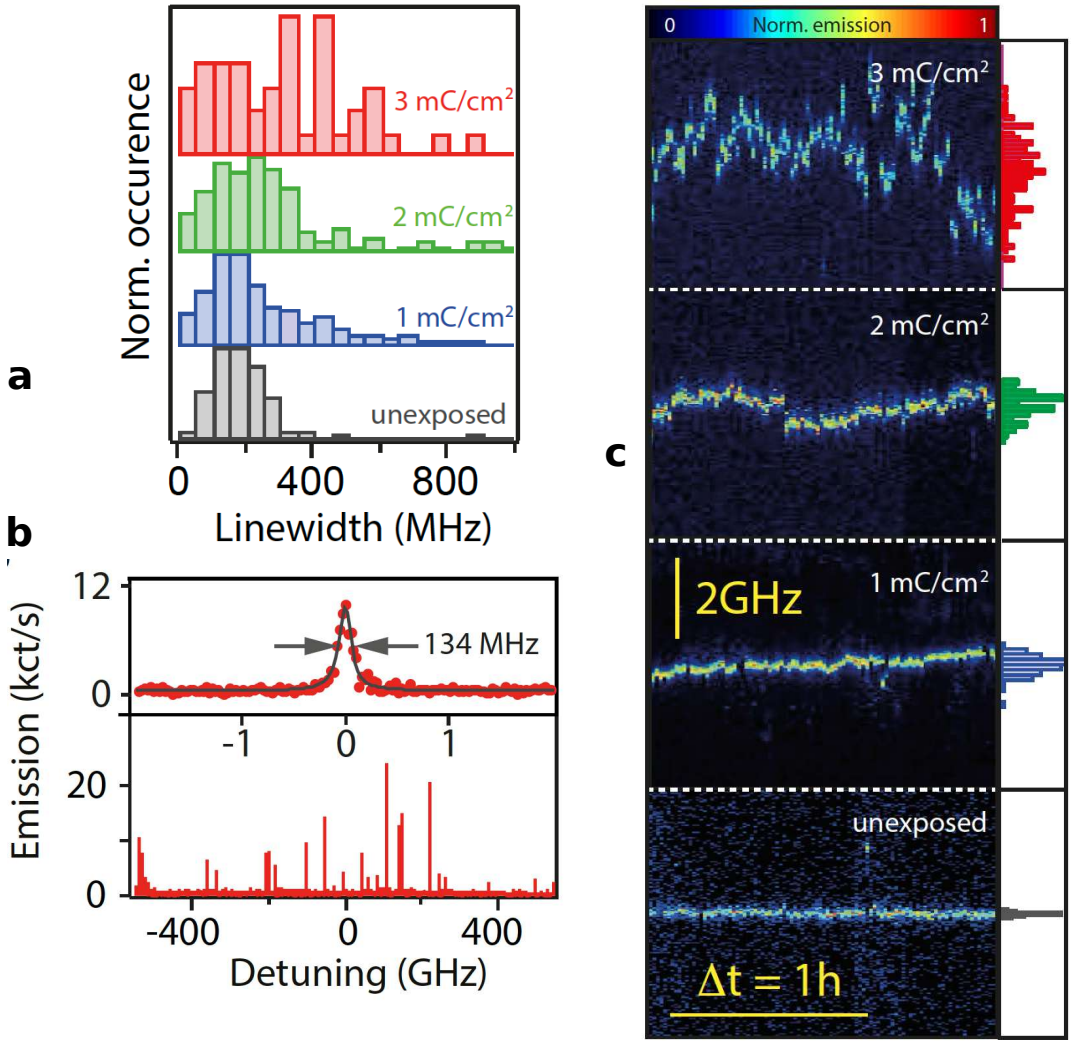

Figure 5.13: *Measurements performed at ICFO - group of Prof. Frank Koppens.* **a** - Emission peak-linewidth distribution for DBT (in Ac NCX embedded in PVA) subjected to different e-beam doses. **b** - Fluorescence excitation spectra of an ensemble (bottom) of single molecules (top: zoomed spectrum) which have been exposed with 1 mC/cm^2. **c** - Time traces of single DBT-molecules emission for unexposed, 1, 2 and 3 mC/cm^2 e-beam doses, respectively. Normalized histograms of central peak positions quantify the emitter stability in time.

ous measurements, at lower dose we observe stable lines over a time scale of hours, similar to the unexposed control sample, whereas at larger doses emission jittering arises, which can be due to the presence of fluctuating charges puddles created by e-beam exposure. It is noteworthy that emission blinking is not observed even for larger doses.

These observations demonstrate the detrimental impact of high electron-beam doses

but also show below $150\,\mathrm{MHz}$ linewidth single-photon emission for low dose values. This study is hence crucial to identify the best lithographic parameters to employ, with the lower possible dose, for the efficient 2D-integration of organic NCX with good photonic properties.

5.3.2 Preliminary Results

We present here preliminary results on deterministic positioning of DBT:Ac NCX on SiN chips. Densely DBT-doped Ac NCX are first deposited on the SiN circuit (Fig. 5.14c) [5] via micro-infiltration. Specifically, the set-up (Fig. 5.14a) (Eppendorf Femtojet) consists of a micropipette (Eppendorf Femtotips) with external diameter of about $2\,\mu$m and inner diameter of 0.5μm (Fig. 5.14b), held on a 3D micrometric stage for fine movement. The aqueous suspension of NCX is injected in the micropipette, upon filtering with a $450\,\mu$m pore-size filter (Sartorius Minisart) to get rid of eventual clusters and avoid obstruction. By monitoring the process with an optical microscope, the pipette tip is approached to the region of interest until a micro-drop of suspension is deposited via surface adhesion. Consequently to water evaporation, NCX are positioned with high precision. In particular, we aim to locate an individual NCX within the central hole of a cross-WG, shown in Fig. 5.14d, where also the four output grating outcouplers are visible (on the working principles of these couplers see Ref. [60]). Their structure is optimized to efficiently redirect the guided fluorescence of a coupled emitter towards useful collection angles. The cross-design instead, is envisioned for a cross-polarization excitation scheme. Cross-WGs allow in principle to partially avoid spectral filtering of the laser. The central hole of the WG is meant to leave place to the NCX, which can there couple to a more intense guided mode as compared to a simple evanescent-based coupling (according to a similar working principle as that of trench-WGs) [60].

In Fig. 5.15, a representative example of the final hybrid device is sketched. In average, NCX are positioned with high precision and good success rate ($\sim 1/3$ of deposited NCX are in the center of the WG structure). After the localized deposition, PVA squares are patterned by electron-beam lithography (using $2\,\mathrm{C/cm^2}$ dose). As a result, EBL shaping allows to both prevent crystal sublimation at ambient condition and provide a clean surface state (after further development in an acetone bath; in Fig. 5.15 a WL-image is shown, where the NCX position is highlited by a circle) which is crucial to achieve good emitter-WG coupling with minimized background from nearby NCX. As evident from Fig. 5.15a, the square side is $\sim 10\,\mu$m. Indeed, in this experiment a high writing resolution is not required since the photonic effect of the additional layer of PVA, which is above the layer of HSQ material, is neglegible (HSQ

[5] Designed and fabricated by P. Lombardi and A. Ovvyan, at University of Münster, in the group of Prof. Wolfram Pernice.

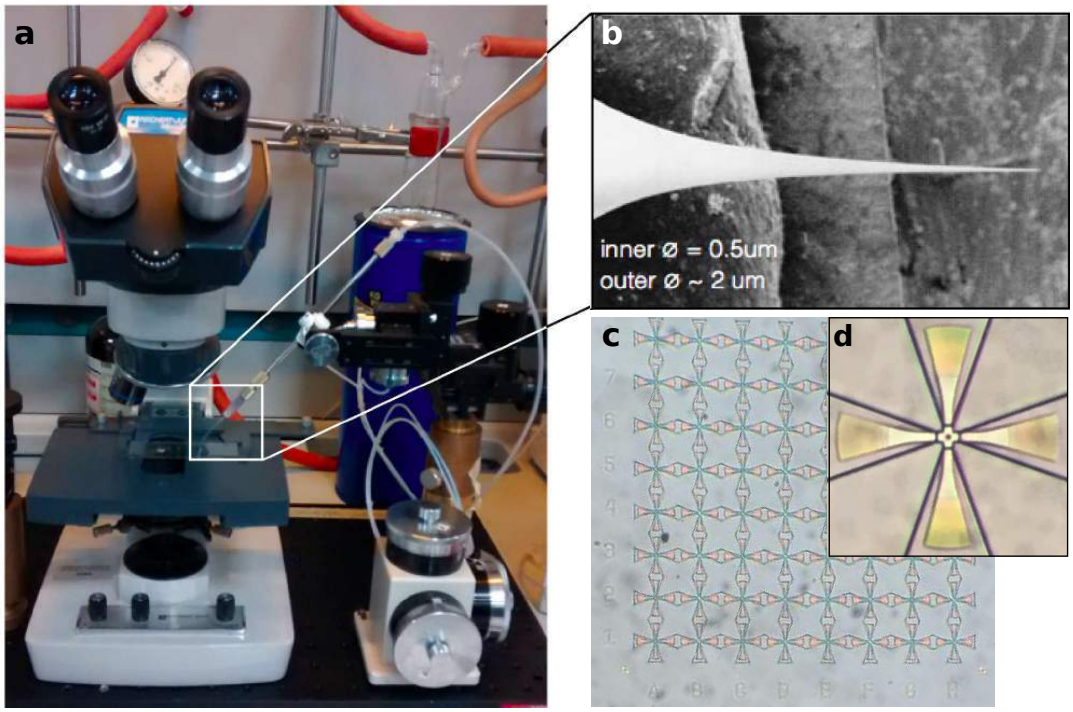

Figure 5.14: **a** - Photo of the micro-infiltration setup. **b** - SEM image of the syringe micro-tip. **c** - WL image of the SiN chip of cross-WGs. **d** - Zoom on one WG.

is applied in order to avoid the NCX to go over the grating couplers, which would otherwise compromise the fluorescence signal collection.).
Off-resonant excitation in confocal mode and at the NCX position triggers emission from the molecules which partially couples into the WG and is guided throughout the four grating outcouplers (Fig. 5.15b), proving the successful insertion of the NCX at the centre of the WG. Coupling of the molecule to the structure is estimated to be $> 10\%$. This value is the result of the integration of many molecules in the nanocrystal, each with unequal coupling efficiency owing to the different position and orientation, and is therefore an underestimation. However, this preliminary result is encouraging and can be further enhanced upon reduction of the NCX size, which is at the moment the primary limit which prevents the NCX to really enter the $1\,\mu$m-size hole.

Upon optimization, the developed technique is promising for deterministic positioning of the molecule-base QE on semiconductur photonic structures in general, which have the advantage of low propagation losses and well-established fabrication technology. Thus, an effective coupling between an individual molecule and e.g. an integrated cavity can be envisaged, foreseeing on-chip single-photon processing as for

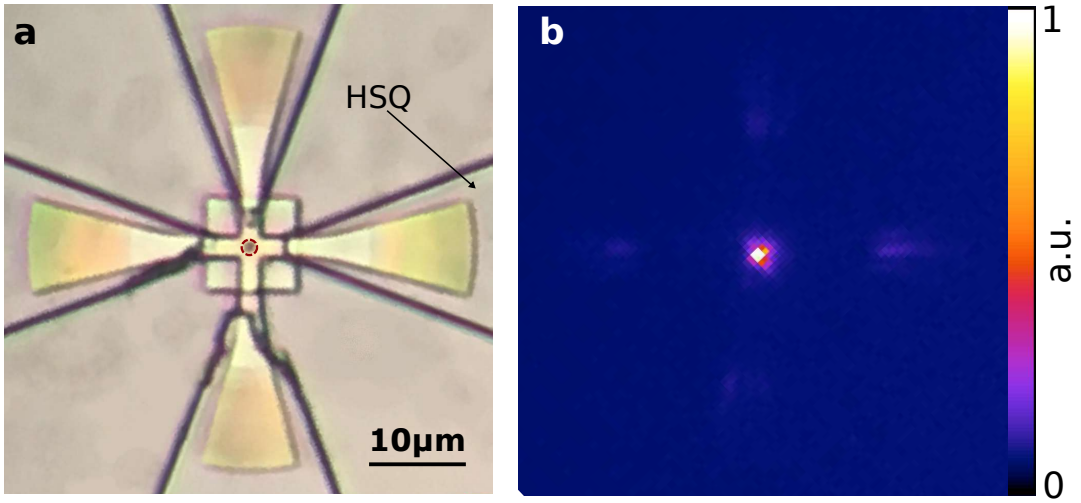

Figure 5.15: Deterministic positioning of a DBT:Ac NCX on SiN WGs. **a** - WL image: micro-infiltration was employed to position a DBT:Ac NCX in the central hole of the cross-WG in order to achieve optimal coupling efficiency. Then, e-beam lithography on PVA enabled to write a square and fix the selected NCX, whereas other NCX are washed away after development in water and washing in acetone. **b** - Corresponding wide-field fluorescence map, displaying a bright spot at the NCX central position and also guided light throughout the four outcouplers (estimated to be $\sim 10\%$ of the overall emission).

instance frequency conversion to telecom wavelenghts for efficient fiber quantum communication [298].

6

Conclusions and Outlook

The fundamentals of quantum mechanics have been extensively explored through research on atomic and molecular systems, as well as in quantum-optics and nuclear physics experiments. Already, quantum physics has proved successful in predicting antimatter, in understanding radioactivity but also electron transport in solids, including anomalous behaviours such as superconductivity in graphene superlattices [299, 300]. It offers a correct description of the interaction between light and matter, encompassing phenomena such as magnetic resonance imaging or laser radiation [301]. Now, besides fascinating fundamental questions, there is an opportunity to leverage quantum mechanics for a new generation of devices, working in concert with their classical counterparts, but outperforming them on specific tasks (see the superconductive quantum processor from Google [17]). Optics will certainly play a major role in this adventure, but still single quanta of light are not available in a scalable way.
Indeed, besides major progress has been achieved in the optimization of solid-state systems, still an ideal single-photon source is lacking.

In this thesis work we addressed this challenge by demonstrating fast and efficient integration of single-molecule quantum emitters in different photonic structures. In order to render molecular single-photon sources flexible in the coupling with nanophotonic and nanoelectronic devices (which e.g. integrate graphene-based components [55, 52]), we have to identify a suitable emitter. The simple and cost-effective

reprecipitation protocol developed in our group [63], specifically enables fast fabrication of nanostructured Ac crystals with controllable concentration of DBT molecules and exhibiting the remarkable photophysical properties of the DBT:Ac bulk system. With a photostable and life-time limited single-photon emission (at 3 K) in a nanocrystalline environment, this source is naturally suitable to deterministic positioning and integration into photonic structures.
In particular, featuring an appropriate combination of emission properties, this molecular single-photon source is demonstrated to find practical application in quantum radiometry as metrology standard for photon fluxes at the low light level, for the calibration of silicon single-photon avalanche detectors [72].

Moreover, we investigated the possibility of handling and manipulating DBT:Ac nanocrystals for achieving deterministic positioning on SiN photonic circuits. In this context, the patternability of PVA water-based polymer was demonstrated by locally heating the material with focused high energy irradiation [64]. Electron-beam irradiation is found to be an efficient method for PVA patterning even without addition of cross-linker agents. Combined to a localized deposition of DBT:Ac nanocrystals via micro-infiltration, selective patterning of PVA is hence proved successful to fix an individual quantum emitter in the region of optimal coupling to a SiN WG [64].

We finally present our recent efforts for the realization in a single-fabrication step of a multi-functional and versatile 3D polymeric platform for quantum applications. The type of emitter as well as the approach towards integration appear promising especially with respect to the scalability and to the performances in a nanophotonic environment. The experimental results entail deterministic positioning of the source, fabrication on different substrates (dielectric, metallic) as well as integration in suspended designs. Typical degradation affecting the photophysical properties of emitters after nano-fabrication is here avoided, and photostable close-to Fourier-limited emission from a single embedded dibenzoterrylene molecule at 3 K is demonstrated. As a first example of the performances attainable by our platform, we show a micro-dome lens displaying unequalled collection efficiency for single organic emitters at low temperatures, reaching photon fluxes above 2.3 Mcps (> 10 Mcps correcting for the overall setup efficiency). This value approximately doubles the state of the art for the detected count rate from a single molecule, with the improvement rising to a factor 5 considering the specific case of DBT [271, 170]. The effective fluorescence redirection displayed in back-focal-plane measurements makes this device suitable for fiber-coupling, with an expected efficiency of $\sim 80\%$ and a measured value up to 50%.

By leveraging the versatile properties of polymer materials, the use of single-molecule

emitters in nanocrystals offers appealing possibilities as outlooks of this work.
In general, single-molecules, being intrinsically identical, can convey indistinguishable photons from different remote sources [45], a key feature towards scalability. The micro-dome design demonstrated in this thesis can in this sense be extended to an array of multiple emitters. Considering the flexibility offered by laser-lithograpy on polymers [265], a monolitic fiber coupler can be integrated onto the metal-coated micro-dome in order to realize alignment-free, ultra compact and scalable fiber-coupled indistinguishable single-photon sources. In this same context, hybrid circuits [65] can be envisioned to exploit the low propagation losses of SiN circuits by using selective 3D-writing. As sketched in Fig. 6.1a, the best emitters in terms of fluorescence intensity could be connected to SiN WGs through polymeric wire-bondings, hence enabling efficient processing of the single-photon stream also to higher level of complexity. In particular, by exploiting the interference pattern originated by writing polymeric structures on gold (as observed in chapter 4; see also Fig 6.1b), a weak cavity effect (see Sec. 1.2.3) could be used to enhance collection efficiency into the bonding up to $\sim 90\%$, as shown by preliminary numerical simulations (Fig. 6.1c).

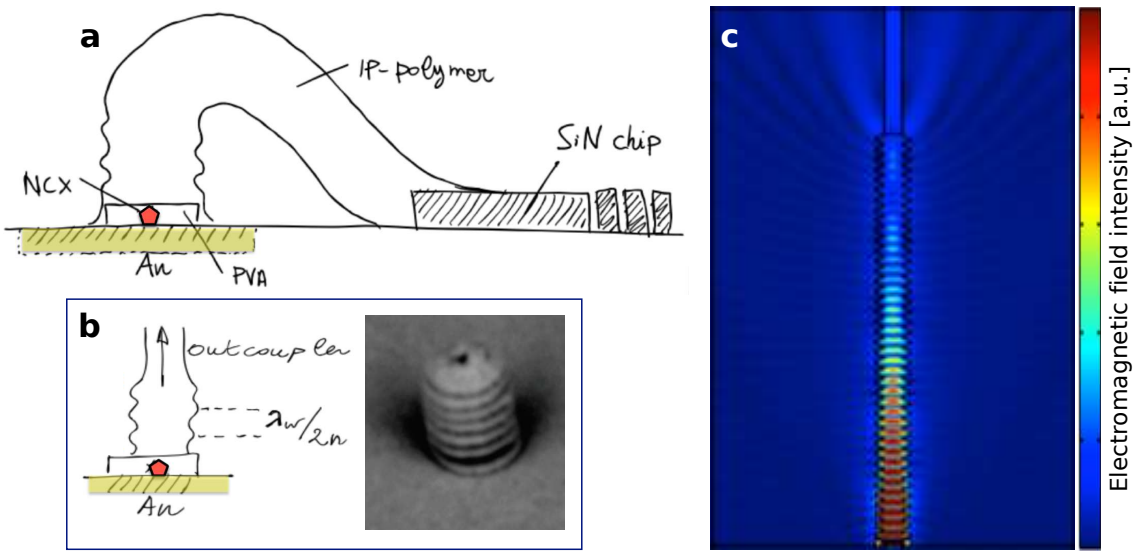

Figure 6.1: **a** - Sketch of a polymer wire-bonding for effective coupling between a DBT:Ac NCX and a SiN WG. In particular, a PVA layer is deposited for NCX-protection and a localized gold substrate is used to enhance collection efficiency. **b** - By exploiting the combined action of gold and of the interference pattern arising from DLW on gold (as reminded in the SEM image of the micropillar in the inset), a weak-cavity effect can lead to a considerable collection enhancement. **c** - 2D simulation of the dipole-emitter coupled to the micropillar weak cavity and displaying the norm of the electromagnetic field: collection enhancement up to 90% can be achieved.

Additionally, few-photon non-linearities can be also envisaged, based on such quan-

tum emitters interacting with confined optical modes [51]. The proposed approach for polymer integration can be potentially extended also to operational chips incorporating monolithic cavities, WGs and directional couplers [65, 302, 303]. For example, a complex quantum effect such as the interference among more than two particles can be observed, using on-demand single photons generated by individual molecules embedded in 3DL-written polymeric tritters [254]. Furthermore, the possibility to engineer photo-functional materials as photoresists [67] enables full customization, from the optimization of spatial resolution and mechanical stability, to the employment of photo-reactive [68] or electro-optical features for tunable resonances.

Bibliography

[1] M. Jammer, “The philosophy of quantum mechanics,” 1974.

[2] J. von Neumann, “Mathematische grundlagen der quantenmechanik,” 1932.

[3] P. A. M. Dirac, *The Principles of Quantum Mechanics*. Oxford: Clarendon Press, 1930.

[4] A. Einstein, B. Podolsky, and N. Rosen, “Can quantum-mechanical description of physical reality be considered complete?,” *Phys. Rev.*, vol. 47, pp. 777–780, 1935.

[5] L. Werner, J. Fischer, U. Johannsen, and J. Hartmann, “Accurate determination of the spectral responsivity of silicon trap detectors between 238 nm and 1015 nm using a laser-based cryogenic radiometer,” *Metrologia*, vol. 37, no. 4, pp. 279–284, 2000.

[6] E. M. L. L. D. Landau, *Quantum Mechanics*. London: Pergamon Press, 1959.

[7] W. Zurek, “Decoherence and the transition from quantum to classical,” *Physics Today*, vol. 44, pp. 36–44, 1991.

[8] H. Everett, “"relative state" formulation of quantum mechanics,” *Rev. Mod. Phys.*, vol. 29, pp. 454–462, 1957.

[9] M. Bunge, “Philosophy of science and technology,” *Dordrecht: D. Reidel Publishing Company*, 1985.

[10] T. Juffmann, A. Milic, M. Müllneritsch, P. Asenbaum, A. Tsukernik, J. Tüxen, M. Mayor, O. Cheshnovsky, and M. Arndt, “Real-time single-molecule imaging of quantum interference,” *Nature Nanotechnology*, vol. 7, no. 5, pp. 297–300, 2012.

[11] E. Collini, C. Y. Wong, K. E. Wilk, P. M. G. Curmi, P. Brumer, and G. D. Scholes, "Coherently wired light-harvesting in photosynthetic marine algae at ambient temperature," *Nature*, vol. 463, no. 7281, pp. 644–647, 2010.

[12] M. Mohseni, P. Rebentrost, S. Lloyd, and A. Aspuru-Guzik, "Environment-assisted quantum walks in photosynthetic energy transfer," *The Journal of Chemical Physics*, vol. 129, no. 17, p. 174106, 2008.

[13] N. Gisin, G. Ribordy, W. Tittel, and H. Zbinden, "Quantum cryptography," *Rev. Mod. Phys.*, vol. 74, pp. 145–195, 2002.

[14] T. D. Ladd, F. Jelezko, R. Laflamme, Y. Nakamura, C. Monroe, and J. L. O'Brien, "Quantum computers," *Nature*, vol. 464, no. 7285, pp. 45–53, 2010.

[15] A. Aspuru-Guzik and P. Walther, "Photonic quantum simulators," *Nature Physics*, vol. 8, no. 4, pp. 285–291, 2012.

[16] C. L. Degen, F. Reinhard, and P. Cappellaro, "Quantum sensing," *Rev. Mod. Phys.*, vol. 89, p. 035002, 2017.

[17] F. Arute, K. Arya, R. Babbush, D. Bacon, J. C. Bardin, R. Barends, R. Biswas, S. Boixo, F. G. S. L. Brandao, D. A. Buell, B. Burkett, Y. Chen, Z. Chen, B. Chiaro, R. Collins, W. Courtney, A. Dunsworth, E. Farhi, B. Foxen, A. Fowler, C. Gidney, M. Giustina, R. Graff, K. Guerin, S. Habegger, M. P. Harrigan, M. J. Hartmann, A. Ho, M. Hoffmann, T. Huang, T. S. Humble, S. V. Isakov, E. Jeffrey, Z. Jiang, D. Kafri, K. Kechedzhi, J. Kelly, P. V. Klimov, S. Knysh, A. Korotkov, F. Kostritsa, D. Landhuis, M. Lindmark, E. Lucero, D. Lyakh, S. Mandrà, J. R. McClean, M. McEwen, A. Megrant, X. Mi, K. Michielsen, M. Mohseni, J. Mutus, O. Naaman, M. Neeley, C. Neill, M. Y. Niu, E. Ostby, A. Petukhov, J. C. Platt, C. Quintana, E. G. Rieffel, P. Roushan, N. C. Rubin, D. Sank, K. J. Satzinger, V. Smelyanskiy, K. J. Sung, M. D. Trevithick, A. Vainsencher, B. Villalonga, T. White, Z. J. Yao, P. Yeh, A. Zalcman, H. Neven, and J. M. Martinis, "Quantum supremacy using a programmable superconducting processor," *Nature*, vol. 574, no. 7779, pp. 505–510, 2019.

[18] *https://www.ibm.com/blogs/research/2019/10/on-quantum-supremacy/*.

[19] S. Aaronson and A. Arkhipov, "The computational complexity of linear optics," in *Proceedings of the Forty-third Annual ACM Symposium on Theory of Computing*, STOC '11, (New York, NY, USA), pp. 333–342, ACM, 2011.

[20] H. Wang, J. Qin, X. Ding, M.-C. Chen, S. Chen, X. You, Y.-M. He, X. Jiang, Z. Wang, L. You, J. J. Renema, S. Hoefling, C.-Y. Lu, and J.-W. Pan, "Boson sampling with 20 input photons in 60-mode interferometers at 10^{14} state spaces," *arXiv 1910.09930*, 2019.

[21] M. Avesani, D. G. Marangon, G. Vallone, and P. Villoresi, "Source-device-independent heterodyne-based quantum random number generator at 17 gbps," *Nature Communications*, vol. 9, no. 1, p. 5365, 2018.

[22] B. Fröhlich, M. Lucamarini, J. F. Dynes, L. C. Comandar, W. W.-S. Tam, A. Plews, A. W. Sharpe, Z. Yuan, and A. J. Shields, "Long-distance quantum key distribution secure against coherent attacks," *Optica*, vol. 4, no. 1, pp. 163–167, 2017.

[23] S.-K. Liao, W.-Q. Cai, W.-Y. Liu, L. Zhang, Y. Li, J.-G. Ren, J. Yin, Q. Shen, Y. Cao, Z.-P. Li, F.-Z. Li, X.-W. Chen, L.-H. Sun, J.-J. Jia, J.-C. Wu, X.-J. Jiang, J.-F. Wang, Y.-M. Huang, Q. Wang, Y.-L. Zhou, L. Deng, T. Xi, L. Ma, T. Hu, Q. Zhang, Y.-A. Chen, N.-L. Liu, X.-B. Wang, Z.-C. Zhu, C.-Y. Lu, R. Shu, C.-Z. Peng, J.-Y. Wang, and J.-W. Pan, "Satellite-to-ground quantum key distribution," *Nature*, vol. 549, pp. 43 EP –, 2017. Article.

[24] T. Kupko, M. v. Helversen, L. Rickert, J.-H. Schulze, A. Strittmatter, M. Gschrey, S. Rodt, S. Reitzenstein, and T. Heindel, "Performance optimization and real-time security monitoring for single-photon quantum key distribution," 2019.

[25] J. Wang, S. Paesani, Y. Ding, R. Santagati, P. Skrzypczyk, A. Salavrakos, J. Tura, R. Augusiak, L. Mančinska, D. Bacco, D. Bonneau, J. W. Silverstone, Q. Gong, A. Acín, K. Rottwitt, L. K. Oxenløwe, J. L. O'Brien, A. Laing, and M. G. Thompson, "Multidimensional quantum entanglement with large-scale integrated optics," *Science*, vol. 360, no. 6386, pp. 285–291, 2018.

[26] J. C. Howell, R. S. Bennink, S. J. Bentley, and R. W. Boyd, "Realization of the einstein-podolsky-rosen paradox using momentum- and position-entangled photons from spontaneous parametric down conversion," *Phys. Rev. Lett.*, vol. 92, p. 210403, 2004.

[27] D. M. Greenberger, M. A. Horne, and A. Zeilinger, "Multiparticle interferometry and the superposition principle," *Physics Today*, vol. 46, pp. 22–22, 1993.

[28] B. Lounis and W. E. Moerner, "Single photons on demand from a single molecule at room temperature," *Nature*, vol. 407, no. 6803, pp. 491–493, 2000.

[29] B. Lounis and M. Orrit, "Single-photon sources," *Reports On Progress In Physics*, vol. 68, no. 5, pp. 1129–1179, 2005.

[30] E. Neu, M. Agio, and C. Becher, "Photophysics of single silicon vacancy centers in diamond: implications for single photon emission," *Opt. Express*, vol. 20, no. 18, pp. 19956–19971, 2012.

[31] M. W. Doherty, N. B. Manson, P. Delaney, F. Jelezko, J. Wrachtrup, and L. C. Hollenberg, "The nitrogen-vacancy colour centre in diamond," *Physics Reports*, vol. 528, no. 1, pp. 1 – 45, 2013.

[32] S. Buckley, K. Rivoire, and J. Vučković, "Engineered quantum dot single-photon sources," *Reports on Progress in Physics*, vol. 75, no. 12, p. 126503, 2012.

[33] W. E. Moerner, "Single-photon sources based on single molecules in solids," *New Journal of Physics*, vol. 6, pp. 88–88, 2004.

[34] M. Davanco, J. Liu, L. Sapienza, C.-Z. Zhang, J. V. De Miranda Cardoso, V. Verma, R. Mirin, S. W. Nam, L. Liu, and K. Srinivasan, "Heterogeneous integration for on-chip quantum photonic circuits with single quantum dot devices," *Nature Communications*, vol. 8, no. 1, p. 889, 2017.

[35] S. Aghaeimeibodi, B. Desiatov, J.-H. Kim, C.-M. Lee, M. A. Buyukkaya, A. Karasahin, C. J. K. Richardson, R. P. Leavitt, M. Lončar, and E. Waks, "Integration of quantum dots with lithium niobate photonics," *Applied Physics Letters*, vol. 113, no. 22, p. 221102, 2018.

[36] P. Schnauber, J. Schall, S. Bounouar, T. Höhne, S.-I. Park, G.-H. Ryu, T. Heindel, S. Burger, J.-D. Song, S. Rodt, and S. Reitzenstein, "Deterministic integration of quantum dots into on-chip multi-mode interference couplers via in-situ electron beam lithography," *Conference on Lasers and Electro-Optics Europe and European Quantum Electronics Conference*, p. eb2 2, 2019.

[37] U. Jantzen, A. B. Kurz, D. S. Rudnicki, C. Schäfermeier, K. D. Jahnke, U. L. Andersen, V. A. Davydov, V. N. Agafonov, A. Kubanek, L. J. Rogers, and F. Jelezko, "Nanodiamonds carrying silicon-vacancy quantum emitters with almost lifetime-limited linewidths," *New Journal of Physics*, vol. 18, no. 7, p. 073036, 2016.

[38] J. Liu, K. Konthasinghe, M. Davanço, J. Lawall, V. Anant, V. Verma, R. Mirin, S. W. Nam, J. D. Song, B. Ma, Z. S. Chen, H. Q. Ni, Z. C. Niu, and K. Srinivasan, "Single self-assembled InAs/

$$\mathrm{GaAs}$$

quantum dots in photonic nanostructures: The role of nanofabrication," *Phys. Rev. Applied*, vol. 9, p. 064019, 2018.

[39] A. Sipahigil, R. E. Evans, D. D. Sukachev, M. J. Burek, J. Borregaard, M. K. Bhaskar, C. T. Nguyen, J. L. Pacheco, H. A. Atikian, C. Meuwly, R. M. Camacho, F. Jelezko, E. Bielejec, H. Park, M. Lončar, and M. D. Lukin, "An integrated diamond nanophotonics platform for quantum-optical networks," *Science*, vol. 354, no. 6314, pp. 847–850, 2016.

[40] H. Thyrrestrup, G. Kirsanske, H. Le Jeannic, T. Pregnolato, L. Zhai, L. Raahauge, L. Midolo, N. Rotenberg, A. Javadi, R. Schott, A. D. Wieck, A. Ludwig, M. C. Löbl, I. Söllner, R. J. Warburton, and P. Lodahl, "Quantum optics with near-lifetime-limited quantum-dot transitions in a nanophotonic waveguide," *Nano Letters*, vol. 18, pp. 1801–1806, Mar 2018.

[41] Q. Shi, B. Sontheimer, N. Nikolay, A. W. Schell, J. Fischer, A. Naber, O. Benson, and M. Wegener, "Wiring up pre-characterized single-photon emitters by laser lithography," *Scientific Reports*, vol. 6, p. 31135, 2016.

[42] S. Morozov, M. Gaio, S. A. Maier, and R. Sapienza, "Metal-dielectric parabolic antenna for directing single photons," *Nano Letters*, vol. 18, no. 5, pp. 3060–3065, 2018.

[43] M. Sartison, S. L. Portalupi, T. Gissibl, M. Jetter, H. Giessen, and P. Michler, "Combining in-situ lithography with 3D printed solid immersion lenses for single quantum dot spectroscopy," *Scientific Reports*, vol. 7, p. 39916, 2017.

[44] P. Frantsuzov, M. Kuno, B. Janko, and R. A. Marcus, "Universal emission intermittency in quantum dots, nanorods and nanowires," *Nature Physics*, vol. 4, pp. 519–, 2008.

[45] R. Lettow, Y. L. A. Rezus, A. Renn, G. Zumofen, E. Ikonen, S. Götzinger, and V. Sandoghdar, "Quantum interference of tunably indistinguishable photons from remote organic molecules," *Phys. Rev. Lett.*, vol. 104, p. 123605, 2010.

[46] C. Toninelli, K. Early, J. Bremi, A. Renn, S. Götzinger, and V. Sandoghdar, "Near-infrared single-photons from aligned molecules in ultrathin crystalline films at room temperature," *Opt. Express*, vol. 18, no. 7, pp. 6577–6582, 2010.

[47] M. Rezai, J. Wrachtrup, and I. Gerhardt, "Polarization-entangled photon pairs from a single molecule," *Optica*, vol. 6, no. 1, pp. 34–40, 2019.

[48] A. A. L. Nicolet, P. Bordat, C. Hofmann, M. A. Kol'chenko, B. Kozankiewicz, R. Brown, and M. Orrit, "Single dibenzoterrylene molecules in an anthracene crystal: Main insertion sites," *Chemphyschem*, vol. 8, pp. 1929–1936, 2007.

[49] J. Hwang, M. Pototschnig, R. Lettow, G. Zumofen, A. Renn, S. Götzinger, and V. Sandoghdar, "A single-molecule optical transistor," *Nature*, vol. 460, p. 76, 2009.

[50] A. Maser, B. Gmeiner, T. Utikal, S. Gøtzinger, and V. Sandoghdar, "Few-photon coherent nonlinear optics with a single molecule," *Nat Photon*, vol. 10, no. 7, pp. 450–453, 2016.

[51] D. Wang, H. Kelkar, D. Martin-Cano, D. Rattenbacher, A. Shkarin, T. Utikal, S. Götzinger, and V. Sandoghdar, "Turning a molecule into a coherent two-level quantum system," *Nature Physics*, vol. 15, no. 5, pp. 483–489, 2019.

[52] K. Schádler, C. Ciancico, S. Pazzagli, P. Lombardi, A. Bachtold, C. Toninelli, A. Reserbat-Plantey, and F. H. L. Koppens, "Electrical control of lifetime-limited quantum emitters using 2D materials," *Nano Lett.*, vol. 19, no. 6, pp. 3789–3795, 2019.

[53] F. Troiani, A. Ghirri, M. Paris, C. Bonizzoni, and M. Affronte, "Towards quantum sensing with molecular spins," *Journal of Magnetism and Magnetic Materials*, p. 165534, 2019.

[54] Y. Tian, P. Navarro, and M. Orrit, "Single molecule as a local acoustic detector for mechanical oscillators," *Phys. Rev. Lett.*, vol. 113, p. 135505, 2014.

[55] G. Mazzamuto, A. Tabani, S. Pazzagli, S. Rizvi, A. Reserbat-Plantey, K. Schädler, G. Navickaite, L. Gaudreau, F. S. Cataliotti, F. Koppens, and C. Toninelli, "Single-molecule study for a graphene-based nano-position sensor," *New Journal of Physics*, vol. 16, no. 11, p. 113007, 2014.

[56] C. Toninelli, Y. Delley, T. Stoferle, A. Renn, S. Gotzinger, and V. Sandoghdar, "A scanning microcavity for in situ control of single-molecule emission," *Applied Physics Letters*, vol. 97, no. 2, p. 021107, 2010.

[57] S. Checcucci, P. Lombardi, S. Rizvi, F. Sgrignuoli, N. Gruhler, F. B. Dieleman, F. S. Cataliotti, W. H. Pernice, M. Agio, and C. Toninelli, "Beaming light from a quantum emitter with a planar optical antenna," *Light: Science & Applications*, vol. 6, no. 4, p. e16245, 2016.

[58] S. M. Skoff, D. Papencordt, H. Schauffert, B. C. Bayer, and A. Rauschenbeutel, "Optical-nanofiber-based interface for single molecules," *Phys. Rev. A*, vol. 97, p. 043839, 2018.

[59] S. Faez, P. Türschmann, H. R. Haakh, S. Götzinger, and V. Sandoghdar, "Coherent interaction of light and single molecules in a dielectric nanoguide," *Phys. Rev. Lett.*, vol. 113, p. 213601, 2014.

[60] P. Lombardi, A. Ovvyan, S. Pazzagli, G. Mazzamuto, G. Kewes, O. Neitzke, N. Gruhler, O. Benson, W. Pernice, F. Cataliotti, *et al.*, "Photostable molecules on chip: integrated single photon sources for quantum technologies," in *European Quantum Electronics Conference*, p. EB_P_16, Optical Society of America, 2017.

[61] S. Grandi, M. P. Nielsen, J. Cambiasso, S. Boissier, K. D. Major, C. Reardon, T. F. Krauss, R. F. Oulton, E. A. Hinds, and A. S. Clark, "Hybrid plasmonic waveguide coupling of photons from a single molecule," *arXiv:1905.06321*, 2019.

[62] P. Türschmann, N. Rotenberg, J. Renger, I. Harder, O. Lohse, T. Utikal, S. Götzinger, and V. Sandoghdar, "Chip-based all-optical control of single molecules coherently coupled to a nanoguide," *Nano Letters*, vol. 17, pp. 4941–4945, Aug 2017.

[63] S. Pazzagli, P. Lombardi, D. Martella, M. Colautti, B. Tiribilli, F. S. Cataliotti, and C. Toninelli, "Self-assembled nanocrystals of polycyclic aromatic hydrocarbons show photostable single-photon emission," *ACS Nano*, vol. 12, no. 5, pp. 4295–4303, 2018.

[64] C. Ciancico, K. Schádler, S. Pazzagli, M. Colautti, P. Lombardi, C. Toninelli, F. Koppens, and A. Reserbat-Plantey, "Narrow linewidth quantum emitters in electron-beam shaped polymer," *Under submission*.

[65] M. Schumann, T. Bückmann, N. Gruhler, M. Wegener, and W. Pernice, "Hybrid 2D-3D optical devices for integrated optics by direct laser writing," *Light: Science & Applications*, vol. 3, p. e175, 2014.

[66] N. Lindenmann, G. Balthasar, D. Hillerkuss, R. Schmogrow, M. Jordan, J. Leuthold, W. Freude, and C. Koos, "Photonic wire bonding: a novel concept for chip-scale interconnects," *Opt. Express*, vol. 20, no. 16, pp. 17667–17677, 2012.

[67] H. Kudo and T. Nishikubo, "Development of novel photo-functional materials based on cyclic oligomers," *Polymer Journal*, vol. 41, p. 569, 2009.

[68] S. Nocentini, F. Riboli, M. Burresi, D. Martella, C. Parmeggiani, and D. S. Wiersma, "Three-dimensional photonic circuits in rigid and soft polymers tunable by light," *ACS Photonics*, vol. 5, no. 8, pp. 3222–3230, 2018.

[69] Y. Liao, C. A. Anderson, P. A. Sullivan, A. J. P. Akelaitis, B. H. Robinson, and L. R. Dalton, "Electro-optical properties of polymers containing alternating nonlinear optical chromophores and bulky spacers," *Chemistry of Materials*, vol. 18, no. 4, pp. 1062–1067, 2006.

[70] C. Paquet and E. Kumacheva, "Nanostructured polymers for photonics," *Materials Today*, vol. 11, no. 4, pp. 48 – 56, 2008.

[71] M. Colautti, P. E. Lombardi, M. Trapuzzano, F. S. Piccioli, S. Pazzagli, B. Tiribilli, S. Nocentini, F. S. Cataliotti, D. Wiersma, and C. Toninelli, "Quantum optics with single molecules in a three-dimensional polymeric platform," *arXiv:1909.07334*, 2019.

[72] P. Lombardi, M. Trapuzzano, M. Colautti, G. Margheri, I. P. Degiovanni, M. López, S. Kück, and C. Toninelli, "A molecule-based single-photon source applied in quantum radiometry," *Advanced Quantum Technologies*, p. 1900083.

[73] P. A., "'subtle in the lord ...' the science and the life of albert einstein," p. 382, 1982.

[74] M. O. Scully and M. S. Zubairy, *Quantum optics*. 1997.

[75] J. D.-R. Cohen-Tannoudji and G. Grynberg, "Photons and atoms: Introduction to quantum electrodynamics," 1997.

[76] P. J. Mosley, J. S. Lundeen, B. J. Smith, P. Wasylczyk, A. B. U'Ren, C. Silberhorn, and I. A. Walmsley, "Heralded generation of ultrafast single photons in pure quantum states," *Phys. Rev. Lett.*, vol. 100, p. 133601, Apr 2008.

[77] C. Joshi, A. Farsi, S. Clemmen, S. Ramelow, and A. L. Gaeta, "Frequency multiplexing for quasi-deterministic heralded single-photon sources," *Nature Communications*, vol. 9, no. 1, p. 847, 2018.

[78] V. Ansari, E. Roccia, M. Santandrea, M. Doostdar, C. Eigner, L. Padberg, I. Gianani, M. Sbroscia, J. M. Donohue, L. Mancino, M. Barbieri, and C. Silberhorn, "Heralded generation of high-purity ultrashort single photons in programmable temporal shapes," *Opt. Express*, vol. 26, pp. 2764–2774, Feb 2018.

[79] S. Paesani, Y. Ding, R. Santagati, L. Chakhmakhchyan, C. Vigliar, K. Rottwitt, L. K. Oxenløwe, J. Wang, M. G. Thompson, and A. Laing, "Generation and sampling of quantum states of light in a silicon chip," *Nature Physics*, vol. 15, no. 9, pp. 925–929, 2019.

[80] D. Llewellyn, Y. Ding, I. I. Faruque, S. Paesani, D. Bacco, R. Santagati, Y.-J. Qian, Y. Li, Y.-F. Xiao, M. Huber, M. Malik, G. F. Sinclair, X. Zhou, K. Rottwitt, J. L. O'Brien, J. G. Rarity, Q. Gong, L. K. Oxenlowe, J. Wang, and M. G. Thompson, "Chip-to-chip quantum teleportation and multi-photon entanglement in silicon," *Nature Physics*, vol. 16, no. 2, pp. 148–153, 2020.

[81] T. Pierre, L. J. Hanna, S. S. F., H. H. R., G. Stephan, S. Vahid, L. Peter, and R. Nir, *nanoph*, vol. 8, ch. Coherent nonlinear optics of quantum emitters in nanophotonic waveguides, p. 1641. 2019 2019. 10.

[82] W. D.-G. Vogel W, "Quantum optics," 2006.

[83] G. Loudon, *Quantum theory of light*. 2000.

[84] M. S. P. Meystre, *Elements of quantum optics*. 2007.

[85] H. T. Dung, L. Knöll, and D.-G. Welsch, "Resonant dipole-dipole interaction in the presence of dispersing and absorbing surroundings," *Phys. Rev. A*, vol. 66, p. 063810, 2002.

[86] Z. Ficek and R. Tanaś, "Entangled states and collective nonclassical effects in two-atom systems," *Physics Reports*, vol. 372, no. 5, pp. 369–443, 2002.

[87] J. W. Goodman, *Statistical optics*. 1985.

[88] J. D.-R. Cohen-Tannoudji and G. Grynberg, *Atom-photon interactions: basic processes and applications*. 2007.

[89] J. R. Lakowicz, *Principles of fluorescence spectroscopy*. 1998.

[90] C. Brunel, B. Lounis, P. Tamarat, and M. Orrit, "Triggered source of single photons based on controlled single molecule fluorescence," *Phys. Rev. Lett.*, vol. 83, pp. 2722–2725, 1999.

[91] J.-B. Trebbia, H. Ruf, P. Tamarat, and B. Lounis, "Efficient generation of near infra-red single photons from the zero-phonon line of a single molecule," *Opt. Express*, vol. 17, no. 26, pp. 23986–23991, 2009.

[92] R. Verberk and M. Orrit, "Photon statistics in the fluorescence of single molecules and nanocrystals: Correlation functions versus distributions of on- and off-times," *The Journal of Chemical Physics*, vol. 119, no. 4, pp. 2214–2222, 2003.

[93] Reynaud, Serge, "La fluorescence de résonance : Etude par la méthode de l´atome habillé," *Ann. Phys.*, vol. 8, pp. 315–370, 1983.

[94] C. Zinoni, B. Alloing, L. H. Li, F. Marsili, A. Fiore, L. Lunghi, A. Gerardino, Y. B. Vakhtomin, K. V. Smirnov, and G. N. Gol'tsman, "Single-photon experiments at telecommunication wavelengths using nanowire superconducting detectors," *Applied Physics Letters*, vol. 91, no. 3, p. 031106, 2007.

[95] R. Brouri, A. Beveratos, J.-P. Poizat, and P. Grangier, "Photon antibunching in the fluorescence of individual color centers in diamond," *Opt. Lett.*, vol. 25, no. 17, pp. 1294–1296, 2000.

[96] M. Rezai, J. Wrachtrup, and I. Gerhardt, "Coherence properties of molecular single photons for quantum networks," *Phys. Rev. X*, vol. 8, p. 031026, 2018.

[97] M. Oxborrow and A. G. Sinclair, "Single-photon sources," *Contemporary Physics*, vol. 46, no. 3, pp. 173–206, 2005.

[98] C. U. P. R. A. Diaspro, G. Chirico and J. Dobrucki, "Photobleaching," *Handbook of biological confocal microscopy. Springer*, 2006.

[99] W. Göhde, U. C. Fischer, H. Fuchs, J. Tittel, T. Basché, C. Bräuchle, A. Hermann, and K. Müllen, "Fluorescence blinking and photobleaching of single terrylenediimide molecules studied with a confocal microscope," *The Journal of Physical Chemistry A*, vol. 102, no. 46, pp. 9109–9116, 1998.

[100] M. Nirmal, B. O. Dabbousi, M. G. Bawendi, J. J. Macklin, J. K. Trautman, T. D. Harris, and L. E. Brus, "Fluorescence intermittency in single cadmium selenide nanocrystals," *Nature*, vol. 383, no. 6603, pp. 802–804, 1996.

[101] J. Bernard, L. Fleury, H. Talon, and M. Orrit, "Photon bunching in the fluorescence from single molecules: A probe for intersystem crossing," *The Journal of Chemical Physics*, vol. 98, no. 2, pp. 850–859, 1993.

[102] W. E. Moerner and D. P. Fromm, "Methods of single-molecule fluorescence spectroscopy and microscopy," *Review of Scientific Instruments*, vol. 74, no. 8, pp. 3597–3619, 2003.

[103] D. Leibfried, R. Blatt, C. Monroe, and D. Wineland, "Quantum dynamics of single trapped ions," *Rev. Mod. Phys.*, vol. 75, pp. 281–324, Mar 2003.

[104] D. Press, T. D. Ladd, B. Zhang, and Y. Yamamoto, "Complete quantum control of a single quantum dot spin using ultrafast optical pulses," *Nature*, vol. 456, no. 7219, pp. 218–221, 2008.

[105] J. Clarke and F. K. Wilhelm, "Superconducting quantum bits," *Nature*, vol. 453, no. 7198, pp. 1031–1042, 2008.

[106] N. Somaschi, V. Giesz, L. De Santis, J. C. Loredo, M. P. Almeida, G. Hornecker, S. L. Portalupi, T. Grange, C. Antón, J. Demory, C. Gómez, I. Sagnes, N. D. Lanzillotti-Kimura, A. Lemaítre, A. Auffeves, A. G. White, L. Lanco, and P. Senellart, "Near-optimal single-photon sources in the solid state," *Nature Photonics*, vol. 10, p. 340, 2016.

[107] H. Wang, Z.-C. Duan, Y.-H. Li, S. Chen, J.-P. Li, Y.-M. He, M.-C. Chen, Y. He, X. Ding, C.-Z. Peng, C. Schneider, M. Kamp, S. Höfling, C.-Y. Lu, and J.-W. Pan, "Near-transform-limited single photons from an efficient solid-state quantum emitter," *Phys. Rev. Lett.*, vol. 116, p. 213601, 2016.

[108] Y.-M. He, H. Wang, C. Wang, M.-C. Chen, X. Ding, J. Qin, Z.-C. Duan, S. Chen, J.-P. Li, R.-Z. Liu, C. Schneider, M. Atatüre, S. Höfling, C.-Y. Lu, and J.-W. Pan, "Coherently driving a single quantum two-level system with dichromatic laser pulses," *Nature Physics*, vol. 15, no. 9, pp. 941–946, 2019.

[109] C. K. Hong, Z. Y. Ou, and L. Mandel, "Measurement of subpicosecond time intervals between two photons by interference," *Phys. Rev. Lett.*, vol. 59, pp. 2044–2046, 1987.

[110] A. A. . F. C. Grynberg, G., "Introduction to quantum optics: From the semi-classical approach to quantized light," 2010.

[111] A. Kiraz, M. Atatüre, and A. Imamoğlu, "Quantum-dot single-photon sources: Prospects for applications in linear optics quantum-information processing," *Phys. Rev. A*, vol. 69, p. 032305, Mar 2004.

[112] T. Grange, G. Hornecker, D. Hunger, J.-P. Poizat, J.-M. Gérard, P. Senellart, and A. Auffèves, "Cavity-funneled generation of indistinguishable single photons from strongly dissipative quantum emitters," *Phys. Rev. Lett.*, vol. 114, p. 193601, May 2015.

[113] C. Santori, D. Fattal, J. Vuckovic, G. S. Solomon, and Y. Yamamoto, "Indistinguishable photons from a single-photon device," *Nature*, vol. 419, no. 6907, pp. 594–597, 2002.

[114] I. Aharonovich, D. Englund, and M. Toth, "Solid-state single-photon emitters," *Nature Photonics*, vol. 10, p. 631, 2016.

[115] Y. R. Shen, "The principles of nonlinear optics," *New York: Wiley*, 1984.

[116] M. D. Eisaman, J. Fan, A. Migdall, and S. V. Polyakov, "Invited review article: Single-photon sources and detectors," *Review of Scientific Instruments*, vol. 82, no. 7, p. 071101, 2011.

[117] S. Wengerowsky, S. K. Joshi, F. Steinlechner, J. R. Zichi, S. M. Dobrovolskiy, R. van der Molen, J. W. N. Los, V. Zwiller, M. A. M. Versteegh, A. Mura, D. Calonico, M. Inguscio, H. Hübel, L. Bo, T. Scheidl, A. Zeilinger, A. Xuereb, and R. Ursin, "Entanglement distribution over a 96-km-long submarine optical fiber," *Proceedings of the National Academy of Sciences*, vol. 116, no. 14, pp. 6684–6688, 2019.

[118] J. Yin, Y. Cao, Y.-H. Li, S.-K. Liao, L. Zhang, J.-G. Ren, W.-Q. Cai, W.-Y. Liu, B. Li, H. Dai, G.-B. Li, Q.-M. Lu, Y.-H. Gong, Y. Xu, S.-L. Li, F.-Z. Li, Y.-Y. Yin, Z.-Q. Jiang, M. Li, J.-J. Jia, G. Ren, D. He, Y.-L. Zhou, X.-X. Zhang, N. Wang, X. Chang, Z.-C. Zhu, N.-L. Liu, Y.-A. Chen, C.-Y. Lu, R. Shu, C.-Z. Peng, J.-Y. Wang, and J.-W. Pan, "Satellite-based entanglement distribution over 1200 kilometers," *Science*, vol. 356, no. 6343, pp. 1140–1144, 2017.

[119] A. S. Parkins, P. Marte, P. Zoller, and H. J. Kimble, "Synthesis of arbitrary quantum states via adiabatic transfer of zeeman coherence," *Phys. Rev. Lett.*, vol. 71, pp. 3095–3098, 1993.

[120] A. Kuhn, M. Hennrich, and G. Rempe, "Deterministic single-photon source for distributed quantum networking," *Phys. Rev. Lett.*, vol. 89, p. 067901, 2002.

[121] J. McKeever, A. Boca, A. D. Boozer, R. Miller, J. R. Buck, A. Kuzmich, and H. J. Kimble, "Deterministic generation of single photons from one atom trapped in a cavity," *Science*, vol. 303, no. 5666, pp. 1992–1994, 2004.

[122] C. Abeywardana, V. Stepanov, F. H. Cho, and S. Takahashi, "Magnetic resonance spectroscopy using a single nitrogen-vacancy center in diamond ," in *Quantum and Nonlinear Optics III* (Q. Gong, G.-C. Guo, and B. S. Ham, eds.), vol. 9269, pp. 27 – 33, International Society for Optics and Photonics, SPIE, 2014.

[123] T. Basché, W. E. Moerner, M. Orrit, and H. Talon, "Photon antibunching in the fluorescence of a single dye molecule trapped in a solid," *Phys. Rev. Lett.*, vol. 69, pp. 1516–1519, 1992.

[124] M. Orrit, J. Bernard, R. Brown, and B. Lounis, "Ii optical spectroscopy of single molecules in solids," vol. 35 of *Progress in Optics*, pp. 61 – 144, Elsevier, 1996.

[125] P. Tamarat, A. Maali, B. Lounis, and M. Orrit, "Ten years of single-molecule spectroscopy," *The Journal of Physical Chemistry A*, vol. 104, no. 1, pp. 1–16, 2000.

[126] Y.-M. He, Y. He, Y.-J. Wei, D. Wu, M. Atatüre, C. Schneider, S. Höfling, M. Kamp, C.-Y. Lu, and J.-W. Pan, "On-demand semiconductor single-photon source with

near-unity indistinguishability," *Nature Nanotechnology*, vol. 8, pp. 213 EP –, Feb 2013. Article.

[127] Y.-J. Wei, Y.-M. He, M.-C. Chen, Y.-N. Hu, Y. He, D. Wu, C. Schneider, M. Kamp, S. Höfling, C.-Y. Lu, and J.-W. Pan, "Deterministic and robust generation of single photons from a single quantum dot with 99.5% indistinguishability using adiabatic rapid passage," *Nano Letters*, vol. 14, pp. 6515–6519, Nov 2014.

[128] A. V. Kuhlmann, J. H. Prechtel, J. Houel, A. Ludwig, D. Reuter, A. D. Wieck, and R. J. Warburton, "Transform-limited single photons from a single quantum dot," *Nature Communications*, vol. 6, no. 1, p. 8204, 2015.

[129] J. C. Loredo, N. A. Zakaria, N. Somaschi, C. Anton, L. de Santis, V. Giesz, T. Grange, M. A. Broome, O. Gazzano, G. Coppola, I. Sagnes, A. Lemaitre, A. Auffeves, P. Senellart, M. P. Almeida, and A. G. White, "Scalable performance in solid-state single-photon sources," *Optica*, vol. 3, pp. 433–440, Apr 2016.

[130] M. Abbarchi, F. Troiani, C. Mastrandrea, G. Goldoni, T. Kuroda, T. Mano, K. Sakoda, N. Koguchi, S. Sanguinetti, A. Vinattieri, and M. Gurioli, "Spectral diffusion and line broadening in single self-assembled gaasalgaas quantum dot photoluminescence," *Applied Physics Letters*, vol. 93, no. 16, p. 162101, 2008.

[131] M. Orrit and T. Basché, "Steady light from quantum dots, at last. but how?," *ChemPhysChem*, vol. 10, no. 14, pp. 2383–2385, 2009.

[132] M. J. Fernée, T. Plakhotnik, Y. Louyer, B. N. Littleton, C. Potzner, P. Tamarat, P. Mulvaney, and B. Lounis, "Spontaneous spectral diffusion in cdse quantum dots," *The Journal of Physical Chemistry Letters*, vol. 3, pp. 1716–1720, Jun 2012.

[133] M. Davanço, C. S. Hellberg, S. Ates, A. Badolato, and K. Srinivasan, "Multiple time scale blinking in inas quantum dot single-photon sources," *Phys. Rev. B*, vol. 89, p. 161303, Apr 2014.

[134] X. Y. Wang, W. Q. Ma, J. Y. Zhang, G. J. Salamo, M. Xiao, and C. K. Shih, "Photoluminescence intermittency of ingaas/gaas quantum dots confined in a planar microcavity," *Nano Letters*, vol. 5, pp. 1873–1877, Oct 2005.

[135] O. Benson, C. Santori, M. Pelton, and Y. Yamamoto, "Regulated and entangled photons from a single quantum dot," *Phys. Rev. Lett.*, vol. 84, pp. 2513–2516, Mar 2000.

[136] M. Müller, S. Bounouar, K. D. Jöns, M. Glässl, and P. Michler, "On-demand generation of indistinguishable polarization-entangled photon pairs," *Nature Photonics*, vol. 8, no. 3, pp. 224–228, 2014.

[137] T. H. Chung, G. Juska, S. T. Moroni, A. Pescaglini, A. Gocalinska, and E. Pelucchi, "Selective carrier injection into patterned arrays of pyramidal quantum dots for entangled photon light-emitting diodes," *Nature Photonics*, vol. 10, no. 12, pp. 782–787, 2016.

[138] J. Liu, R. Su, Y. Wei, B. Yao, S. F. C. d. Silva, Y. Yu, J. Iles-Smith, K. Srinivasan, A. Rastelli, J. Li, and X. Wang, "A solid-state source of strongly entangled photon pairs with high brightness and indistinguishability," *Nature Nanotechnology*, vol. 14, no. 6, pp. 586–593, 2019.

[139] J. Q. Grim, A. S. Bracker, M. Zalalutdinov, S. G. Carter, A. C. Kozen, M. Kim, C. S. Kim, J. T. Mlack, M. Yakes, B. Lee, and D. Gammon, "Scalable in operando strain tuning in nanophotonic waveguides enabling three-quantum-dot superradiance," *Nature Materials*, vol. 18, no. 9, pp. 963–969, 2019.

[140] B. Lounis, H. Bechtel, D. Gerion, P. Alivisatos, and W. Moerner, "Photon antibunching in single cdse/zns quantum dot fluorescence," *Chemical Physics Letters*, vol. 329, no. 5, pp. 399 – 404, 2000.

[141] P. Michler, A. Imamoglu, M. D. Mason, P. J. Carson, G. F. Strouse, and S. K. Buratto, "Quantum correlation among photons from a single quantum dot at room temperature," *Nature*, vol. 406, no. 6799, pp. 968–970, 2000.

[142] P. Senellart, G. Solomon, and A. White, "High-performance semiconductor quantum-dot single-photon sources," *Nature Nanotechnology*, vol. 12, pp. 1026–, 2017.

[143] A. Gruber, A. Dräbenstedt, C. Tietz, L. Fleury, J. Wrachtrup, and C. v. Borczyskowski, "Scanning confocal optical microscopy and magnetic resonance on single defect centers," *Science*, vol. 276, no. 5321, pp. 2012–2014, 1997.

[144] C. Kurtsiefer, S. Mayer, P. Zarda, and H. Weinfurter, "Stable solid-state source of single photons," *Phys. Rev. Lett.*, vol. 85, pp. 290–293, 2000.

[145] F. Jelezko, C. Tietz, A. Gruber, I. Popa, A. Nizovtsev, S. Kilin, and J. Wrachtrup, "Spectroscopy of single n-v centers in diamond," *Single Molecules*, vol. 2, no. 4, pp. 255–260, 2001.

[146] Gaebel, "Room-temperature coherent coupling of single spins in diamond," *Nature Physics*, 2006.

[147] E. Togan, Y. Chu, A. S. Trifonov, L. Jiang, J. Maze, L. Childress, M. V. G. Dutt, A. S. Sørensen, P. R. Hemmer, A. S. Zibrov, and M. D. Lukin, "Quantum entanglement between an optical photon and a solid-state spin qubit," *Nature*, vol. 466, no. 7307, pp. 730–734, 2010.

[148] E. Neu, D. Steinmetz, J. Riedrich-Möller, S. Gsell, M. Fischer, M. Schreck, and C. Becher, "Single photon emission from silicon-vacancy colour centres in chemical vapour deposition nano-diamonds on iridium," *New Journal of Physics*, vol. 13, no. 2, p. 025012, 2011.

[149] C. Wang, C. Kurtsiefer, H. Weinfurter, and B. Burchard, "Single photon emission from SiV centres in diamond produced by ion implantation," *Journal of Physics B: Atomic, Molecular and Optical Physics*, vol. 39, no. 1, pp. 37–41, 2005.

[150] M. E. Trusheim, B. Pingault, N. H. Wan, M. Gündoğan, L. D. Santis, K. Chen, M. Atatüre, and D. Englund, "Quantum optics with tin-vacancy emitters in diamond," in *Conference on Lasers and Electro-Optics*, p. FM4A.1, Optical Society of America, 2019.

[151] T. Iwasaki, Y. Miyamoto, T. Taniguchi, P. Siyushev, M. H. Metsch, F. Jelezko, and M. Hatano, "Tin-vacancy quantum emitters in diamond," *Phys. Rev. Lett.*, vol. 119, p. 253601, Dec 2017.

[152] A. Sipahigil, K. D. Jahnke, L. J. Rogers, T. Teraji, J. Isoya, A. S. Zibrov, F. Jelezko, and M. D. Lukin, "Indistinguishable photons from separated silicon-vacancy centers in diamond," *Phys. Rev. Lett.*, vol. 113, p. 113602, Sep 2014.

[153] T. T. Tran, M. Kianinia, K. Bray, S. Kim, Z.-Q. Xu, A. Gentle, B. Sontheimer, C. Bradac, and I. Aharonovich, "Nanodiamonds with photostable, sub-gigahertz linewidth quantum emitters," *APL Photonics*, vol. 2, no. 11, p. 116103, 2017.

[154] M. Arcari, I. Söllner, A. Javadi, S. Lindskov Hansen, S. Mahmoodian, J. Liu, H. Thyrrestrup, E. H. Lee, J. D. Song, S. Stobbe, and P. Lodahl, "Near-unity coupling efficiency of a quantum emitter to a photonic crystal waveguide," *Phys. Rev. Lett.*, vol. 113, p. 093603, 2014.

[155] G. Kiršanskė, H. Thyrrestrup, R. S. Daveau, C. L. Dreeßen, T. Pregnolato, L. Midolo, P. Tighineanu, A. Javadi, S. Stobbe, R. Schott, A. Ludwig, A. D. Wieck, S. I. Park, J. D. Song, A. V. Kuhlmann, I. Söllner, M. C. Löbl, R. J. Warburton, and P. Lodahl, "Indistinguishable and efficient single photons from a quantum dot in a planar nanobeam waveguide," *Phys. Rev. B*, vol. 96, p. 165306, 2017.

[156] K. Debnath, A. Z. Khokhar, S. A. Boden, H. Arimoto, S. Z. Oo, H. M. H. Chong, G. T. Reed, and S. Saito, "Low-loss slot waveguides with silicon (111) surfaces realized using anisotropic wet etching," *Frontiers in Materials*, vol. 3, p. 51, 2016.

[157] T. G. Tiecke, K. P. Nayak, J. D. Thompson, T. Peyronel, N. P. de Leon, V. Vuletić, and M. D. Lukin, "Efficient fiber-optical interface for nanophotonic devices," *Optica*, vol. 2, no. 2, pp. 70–75, 2015.

[158] A. W. Snyder and J. Love, "Optical waveguide theory," *Springer Science & Business Media*, 2012.

[159] R. G. Hunsperger and J. R. Meyer-Arendt, "Integrated optics: theory and technology," *Applied Optics*, vol. 31, p. 298, 1992.

[160] M. Davanço and K. Srinivasan, "Efficient spectroscopy of single embedded emitters using optical fiber taper waveguides," *Opt. Express*, vol. 17, no. 13, pp. 10542–10563, 2009.

[161] J. Volz, M. Scheucher, C. Junge, and A. Rauschenbeutel, "Nonlinear pi phase shift for single fiber-guided photons interacting with a resonator-enhanced atom," in *Nonlinear Optics*, p. NW2A.2, Optical Society of America, 2015.

[162] L. Novotny and B. Hecht, "Principles of nano-optics," *Cambridge University Press*, 2012.

[163] S. M. Mansfield and G. S. Kino, "Solid immersion microscope," *Applied Physics Letters*, vol. 57, no. 24, pp. 2615–2616, 1990.

[164] P. Siyushev, F. Kaiser, V. Jacques, I. Gerhardt, S. Bischof, H. Fedder, J. Dodson, M. Markham, D. Twitchen, F. Jelezko, and J. Wrachtrup, "Monolithic diamond optics for single photon detection," *Applied Physics Letters*, vol. 97, no. 24, p. 241902, 2010.

[165] V. Zwiller and G. Björk, "Improved light extraction from emitters in high refractive index materials using solid immersion lenses," *Journal of Applied Physics*, vol. 92, no. 2, pp. 660–665, 2002.

[166] W. Barnes, G. Björk, J. Gérard, P. Jonsson, J. Wasey, P. Worthing, and V. Zwiller, "Solid-state single photon sources: light collection strategies," *The European Physical Journal D - Atomic, Molecular, Optical and Plasma Physics*, vol. 18, no. 2, pp. 197–210, 2002.

[167] A. W. Schell, T. Neumer, and O. Benson, "Numerical analysis of efficient light extraction with an elliptical solid immersion lens," *Opt. Lett.*, vol. 39, no. 16, pp. 4639–4642, 2014.

[168] T. Schröder, F. Gädeke, M. J. Banholzer, and O. Benson, "Ultrabright and efficient single-photon generation based on nitrogen-vacancy centres in nanodiamonds on a solid immersion lens," *New Journal of Physics*, vol. 13, no. 5, p. 055017.

[169] S. Castelletto, J. P. Harrison, L. Marseglia, A. C. Stanley-Clarke, B. C. Gibson, B. A. Fairchild, J. P. Hadden, Y.-L. D. Ho, M. P. Hiscocks, K. Ganesan, S. T. Huntington, F. Ladouceur, A. D. Greentree, S. Prawer, J. L. O. Brien, and J. G. Rarity, "Diamond-based structures to collect and guide light," *New Journal of Physics*, vol. 13, no. 2, p. 025020, 2011.

[170] G. Wrigge, I. Gerhardt, J. Hwang, G. Zumofen, and V. Sandoghdar, "Efficient coupling of photons to a single molecule and the observation of its resonance fluorescence," *Nat. Phys.*, vol. 4, no. 1, pp. 60–66, 2008.

[171] E. Fermi, "Quantum theory of radiation," *Rev. Mod. Phys.*, vol. 4, pp. 87–132, 1932.

[172] S. M. Barnett, B. Huttner, and R. Loudon, "Spontaneous emission in absorbing dielectric media," *Phys. Rev. Lett.*, vol. 68, pp. 3698–3701, 1992.

[173] K. H. Drexhage, "Iv interaction of light with monomolecular dye layers," vol. 12 of *Progress in Optics*, pp. 163 – 232, Elsevier, 1974.

[174] P. Goy, J. M. Raimond, M. Gross, and S. Haroche, "Observation of cavity-enhanced single-atom spontaneous emission," *Phys. Rev. Lett.*, vol. 50, pp. 1903–1906, 1983.

[175] A. Kamli and M. Babiker, "Dielectric cavity qed between photonic crystals: An effective uniaxial medium approach," *Phys. Rev. A*, vol. 62, p. 043804, 2000.

[176] F. L. Kien, N. H. Quang, and K. Hakuta, "Spontaneous emission from an atom inside a dielectric sphere," *Optics Communications*, vol. 178, no. 1, pp. 151–164, 2000.

[177] S. Bozhevolnyi and F. García-Vidal, "Focus on plasmonics," *New Journal of Physics*, vol. 10, no. 10, p. 105001, 2008.

[178] E. T. Jaynes and F. W. Cummings, "Comparison of quantum and semiclassical radiation theories with application to the beam maser," *Proceedings of the IEEE*, vol. 51, pp. 89–109, Jan 1963.

[179] M. Brune, F. Schmidt-Kaler, A. Maali, J. Dreyer, E. Hagley, J. M. Raimond, and S. Haroche, "Quantum rabi oscillation: A direct test of field quantization in a cavity," *Phys. Rev. Lett.*, vol. 76, pp. 1800–1803, Mar 1996.

[180] J. Vučković, M. Pelton, A. Scherer, and Y. Yamamoto, "Optimization of three-dimensional micropost microcavities for cavity quantum electrodynamics," *Phys. Rev. A*, vol. 66, p. 023808, Aug 2002.

[181] M. Pelton, C. Santori, J. Vuc˘ković, B. Zhang, G. S. Solomon, J. Plant, and Y. Yamamoto, "Efficient source of single photons: A single quantum dot in a micropost microcavity," *Phys. Rev. Lett.*, vol. 89, p. 233602, Nov 2002.

[182] J. Vučković, D. Fattal, C. Santori, G. S. Solomon, and Y. Yamamoto, "Enhanced single-photon emission from a quantum dot in a micropost microcavity," *Applied Physics Letters*, vol. 82, no. 21, pp. 3596–3598, 2003.

[183] V. Giesz, S. L. Portalupi, T. Grange, C. Antón, L. De Santis, J. Demory, N. Somaschi, I. Sagnes, A. Lemaître, L. Lanco, A. Auffèves, and P. Senellart, "Cavity-enhanced two-photon interference using remote quantum dot sources," *Phys. Rev. B*, vol. 92, p. 161302, Oct 2015.

[184] M. Lermer, N. Gregersen, F. Dunzer, S. Reitzenstein, S. Höfling, J. Mørk, L. Worschech, M. Kamp, and A. Forchel, "Bloch-wave engineering of quantum dot micropillars for cavity quantum electrodynamics experiments," *Phys. Rev. Lett.*, vol. 108, p. 057402, Jan 2012.

[185] R. Albrecht, A. Bommer, C. Deutsch, J. Reichel, and C. Becher, "Coupling of a single nitrogen-vacancy center in diamond to a fiber-based microcavity," *Phys. Rev. Lett.*, vol. 110, p. 243602, Jun 2013.

[186] D. Press, S. Götzinger, S. Reitzenstein, C. Hofmann, A. Löffler, M. Kamp, A. Forchel, and Y. Yamamoto, "Photon antibunching from a single quantum-dot-microcavity system in the strong coupling regime," *Phys. Rev. Lett.*, vol. 98, p. 117402, Mar 2007.

[187] D. Englund, D. Fattal, E. Waks, G. Solomon, B. Zhang, T. Nakaoka, Y. Arakawa, Y. Yamamoto, and J. Vučković, "Controlling the spontaneous emission rate of single quantum dots in a two-dimensional photonic crystal," *Phys. Rev. Lett.*, vol. 95, p. 013904, Jul 2005.

[188] T. Yoshie, A. Scherer, J. Hendrickson, G. Khitrova, H. M. Gibbs, G. Rupper, C. Ell, O. B. Shchekin, and D. G. Deppe, "Vacuum rabi splitting with a single quantum dot in a photonic crystal nanocavity," *Nature*, vol. 432, no. 7014, pp. 200–203, 2004.

[189] A. Tandaechanurat, S. Ishida, D. Guimard, M. Nomura, S. Iwamoto, and Y. Arakawa, "Lasing oscillation in a three-dimensional photonic crystal nanocavity with a complete bandgap," *Nature Photonics*, vol. 5, no. 2, pp. 91–94, 2011.

[190] J. Vuckovic, M. Loncar, and A. Scherer, "Surface plasmon enhanced light-emitting diode," *IEEE Journal of Quantum Electronics*, vol. 36, pp. 1131–1144, Oct 2000.

[191] W. Barnes and P. Worthing, "Spontaneous emission and metal-clad microcavities," *Optics Communications*, vol. 162, no. 1, pp. 16 – 20, 1999.

[192] A. V. Akimov, A. Mukherjee, C. L. Yu, D. E. Chang, A. S. Zibrov, P. R. Hemmer, H. Park, and M. D. Lukin, "Generation of single optical plasmons in metallic nanowires coupled to quantum dots," *Nature*, vol. 450, no. 7168, pp. 402–406, 2007.

[193] N. P. de Leon, B. J. Shields, C. L. Yu, D. E. Englund, A. V. Akimov, M. D. Lukin, and H. Park, "Tailoring light-matter interaction with a nanoscale plasmon resonator," *Phys. Rev. Lett.*, vol. 108, p. 226803, May 2012.

[194] X.-W. Chen, M. Agio, and V. Sandoghdar, "Metallodielectric hybrid antennas for ultrastrong enhancement of spontaneous emission," *Phys. Rev. Lett.*, vol. 108, p. 233001, Jun 2012.

[195] K. J. Russell, T.-L. Liu, S. Cui, and E. L. Hu, "Large spontaneous emission enhancement in plasmonic nanocavities," *Nature Photonics*, vol. 6, pp. 459 EP –, May 2012.

[196] D. Wang, H. Kelkar, D. Martin-Cano, D. Rattenbacher, A. Shkarin, T. Utikal, S. Götzinger, and V. Sandoghdar, "Turning a molecule into a coherent two-level quantum system," *Nature Physics*, vol. 15, no. 5, pp. 483–489, 2019.

[197] D. Rattenbacher, A. Shkarin, J. Renger, T. Utikal, S. Götzinger, and V. Sandoghdar, "Coherent coupling of single molecules to on-chip ring resonators," *New Journal of Physics*, vol. 21, p. 062002, jun 2019.

[198] P. E. Barclay, C. Santori, K.-M. Fu, R. G. Beausoleil, and O. Painter, "Coherent interference effects in a nano-assembled diamond nv center cavity-qed system," *Opt. Express*, vol. 17, pp. 8081–8197, May 2009.

[199] J. Wolters, A. W. Schell, G. Kewes, N. Nüsse, M. Schoengen, H. Döscher, T. Hannappel, B. Löchel, M. Barth, and O. Benson, "Enhancement of the zero phonon line emission from a single nitrogen vacancy center in a nanodiamond via coupling to a photonic crystal cavity," *Applied Physics Letters*, vol. 97, no. 14, p. 141108, 2010.

[200] T. van der Sar, J. Hagemeier, W. Pfaff, E. C. Heeres, S. M. Thon, H. Kim, P. M. Petroff, T. H. Oosterkamp, D. Bouwmeester, and R. Hanson, "Deterministic nanoassembly of a coupled quantum emitter–photonic crystal cavity system," *Applied Physics Letters*, vol. 98, no. 19, p. 193103, 2011.

[201] D. Englund, B. Shields, K. Rivoire, F. Hatami, J. Vuckovic, H. Park, and M. D. Lukin, "Deterministic coupling of a single nitrogen vacancy center to a photonic crystal cavity," *Nano Letters*, vol. 10, pp. 3922–3926, Oct 2010.

[202] Y. Chen, A. Ryou, M. R. Friedfeld, T. Fryett, J. Whitehead, B. M. Cossairt, and A. Majumdar, "Deterministic positioning of colloidal quantum dots on silicon nitride nanobeam cavities," *Nano Letters*, vol. 18, pp. 6404–6410, Oct 2018.

[203] B. L. M. O. Ph. Tamarat, F. Jelezko, *Shpolskii Spectroscopy and Other Site-Selection Methods.* 2000.

[204]

[205] A. Zumbusch, L. Fleury, R. Brown, J. Bernard, and M. Orrit, "Probing individual two-level systems in a polymer by correlation of single molecule fluorescence," *Phys. Rev. Lett.*, vol. 70, pp. 3584–3587, 1993.

[206] T. Basché and W. E. Moerner, "Optical modification of a single impurity molecule in a solid," *Nature*, vol. 355, no. 6358, pp. 335–337, 1992.

[207] S. Kummer, T. Basché, and C. Bräuchle, "Terrylene in p-terphenyl: a novel single crystalline system for single molecule spectroscopy at low temperatures," *Chemical Physics Letters*, vol. 229, no. 3, pp. 309 – 316, 1994.

[208] A. Boiron, B. Lounis, and M. Orrit, "Single molecules of dibenzanthanthrene in n-hexadecane," *The Journal of Chemical Physics*, vol. 105, no. 10, pp. 3969–3974, 1996.

[209] A. A. L. Nicolet, C. Hofmann, M. A. Kol'chenko, B. Kozankiewicz, and M. Orrit, "Single dibenzoterrylene molecules in an anthracene crystal: Spectroscopy and photophysics," *ChemPhysChem*, vol. 8, no. 8, pp. 1215–1220, 2007.

[210] P. Bordat and R. Brown, "Elucidation of optical switching of single guest molecules in terrylene/p-terphenyl mixed crystals," *Chemical Physics Letters*, vol. 331, no. 5, pp. 439 – 445, 2000.

[211] P. Bordat and R. Brown, "Correspondence between electronic origins and substitution sites in pentacene/p-terphenyl mixed crystals by molecular modelling," *Chemical Physics Letters*, vol. 291, no. 1, pp. 153 – 160, 1998.

[212] C. P. Brock and J. D. Dunitz, "Temperature dependence of thermal motion in crystalline anthracene," *Acta Crystallographica Section B*, vol. 46, no. 6, pp. 795–806, 1990.

[213] P. Siyushev, G. Stein, J. Wrachtrup, and I. Gerhardt, "Molecular photons interfaced with alkali atoms," *Nature*, vol. 509, p. 66, 2014.

[214] C. Hofmann, A. Nicolet, M. A. Kol'chenko, and M. Orrit, "Towards nanoprobes for conduction in molecular crystals: Dibenzoterrylene in anthracene crystals," *Chemical Physics*, vol. 318, no. 1, pp. 1 – 6, 2005. Molecular Nanoscience.

[215] F. Jelezko, P. Tamarat, B. Lounis, and M. Orrit, "Dibenzoterrylene in naphthalene: A new crystalline system for single molecule spectroscopy in the near infrared," *The Journal of Physical Chemistry*, vol. 100, pp. 13892–13894, Jan 1996.

[216] N. R. Verhart, M. Müller, and M. Orrit, "Spectroscopy of single dibenzoterrylene molecules in para-dichlorobenzene," *ChemPhysChem*, vol. 17, no. 10, pp. 1524–1529, 2016.

[217] S. Faez, N. R. Verhart, M. Markoulides, F. Buda, A. Gourdon, and M. Orrit, "Design and synthesis of aromatic molecules for probing electric fields at the nanoscale," *Faraday Discuss.*, vol. 184, pp. 251–262, 2015.

[218] R. Kubo, *Fluctuation, Relaxation, and Resonance in Magnetic Systems*. 1965.

[219] W. H. Hesselink and D. A. Wiersma, "Optical dephasing and vibronic relaxation in molecular mixed crystals: A picosecond photon echo and optical study of pentacene in naphthalene and p-terphenyl," *The Journal of Chemical Physics*, vol. 73, no. 2, pp. 648–663, 1980.

[220] D. Walser, G. Zumofen, A. Renn, and T. Plakhotnik, "Line broadening and line shifts in one- and two-photon single-molecule spectra," *The Journal of Physical Chemistry A*, vol. 105, pp. 3022–3028, Apr 2001.

[221] W. P. Ambrose, T. Basché, and W. E. Moerner, "Detection and spectroscopy of single pentacene molecules in a p-terphenyl crystal by means of fluorescence excitation," *The Journal of Chemical Physics*, vol. 95, no. 10, pp. 7150–7163, 1991.

[222] M. O. U. P. W. T. Basché, W. E. Moerner, *Single-Molecule Optical Detection, Imaging and Spectroscopy*. John Wiley & Sons, 1996.

[223] K. K. Rebane and I. Rebane, "Peak value of the cross-section of zero-phonon line's absorption," *Journal of Luminescence*, vol. 56, no. 1, pp. 39 – 45, 1993.

[224] W. E. Moerner, T. Plakhotnik, T. Irngartinger, M. Croci, V. Palm, and U. P. Wild, "Optical probing of single molecules of terrylene in a shpol'kii matrix: A two-state single-molecule switch," *The Journal of Physical Chemistry*, vol. 98, no. 30, pp. 7382–7389, 1994.

[225] C.-H. Su, A. D. Greentree, and L. C. L. Hollenberg, "Towards a picosecond transform-limited nitrogen-vacancy based single photon source," *Opt. Express*, vol. 16, pp. 6240–6250, Apr 2008.

[226] I. Aharonovich, S. Castelletto, D. A. Simpson, C.-H. Su, A. D. Greentree, and S. Prawer, "Diamond-based single-photon emitters," *Reports on Progress in Physics*, vol. 74, p. 076501, jun 2011.

[227] L. Li, E. H. Chen, J. Zheng, S. L. Mouradian, F. Dolde, T. Schröder, S. Karaveli, M. L. Markham, D. J. Twitchen, and D. Englund, "Efficient photon collection from a nitrogen vacancy center in a circular bullseye grating," *Nano Letters*, vol. 15, no. 3, pp. 1493–1497, 2015.

[228] A. M. Stoneham, "Shapes of inhomogeneously broadened resonance lines in solids," *Rev. Mod. Phys.*, vol. 41, pp. 82–108, 1969.

[229] K. K. Rebane, *Impurity Spectra of Solids: Elementary Theory of Vibrational Structure*. Springer Science & Business Media, 2012.

[230] D. A. Wiersma, *Coherent Optical Transient Studies of Dephasing and Relaxation in Electronic Transitions of Large Molecules in the Condensed Phase*, ch. 47, pp. 421–485. John Wiley & Sons, Ltd, 1981.

[231] J. B. Spring, P. L. Mennea, B. J. Metcalf, P. C. Humphreys, J. C. Gates, H. L. Rogers, C. Söller, B. J. Smith, W. S. Kolthammer, P. G. R. Smith, and I. A. Walmsley, "Chip-based array of near-identical, pure, heralded single-photon sources," *Optica*, vol. 4, pp. 90–96, Jan 2017.

[232] G. Noh, D. Choi, J.-H. Kim, D.-G. Im, Y.-H. Kim, H. Seo, and J. Lee, "Stark tuning of single-photon emitters in hexagonal boron nitride," *Nano Letters*, vol. 18, pp. 4710–4715, Aug 2018.

[233] M. Bauer and L. Kador, "Microscopic heterogeneities in the electrical properties of sic as studied with single-molecule spectroscopy," *The Journal of Physical Chemistry B*, vol. 107, pp. 14301–14305, Dec 2003.

[234] C. Brunel, P. Tamarat, B. Lounis, J. C. Woehl, and M. Orrit, "Stark effect on single molecules of dibenzanthanthrene in a naphthalene crystal and in a n-hexadecane shpol'skii matrix," *The Journal of Physical Chemistry A*, vol. 103, pp. 2429–2434, Apr 1999.

[235] T. Y. Latychevskaia, A. Renn, and U. P. Wild, "Higher-order stark effect on single-molecules," *Chemical Physics*, vol. 282, no. 1, pp. 109 – 119, 2002.

[236] T. Plakhotnik, E. A. Donley, and U. P. Wild, "Single-molecule spectroscopy," *Annual Review of Physical Chemistry*, vol. 48, no. 1, pp. 181–212, 1997.

[237] I. Gerhardt, G. Wrigge, P. Bushev, G. Zumofen, M. Agio, R. Pfab, and V. Sandoghdar, "Strong extinction of a laser beam by a single molecule," *Phys. Rev. Lett.*, vol. 98, p. 033601, Jan 2007.

[238] W. E. Moerner and L. Kador, "Finding a single molecule in a haystack," *Analytical Chemistry*, vol. 61, pp. 1217A–1223A, Nov 1989.

[239] G. Mazzamuto, "Single organic molecules and light transport in thin film," *Ph.D. Thesis, University of Florence*, 2016.

[240] M. A. Lieb, J. M. Zavislan, and L. Novotny, "Single-molecule orientations determined by direct emission pattern imaging," *J. Opt. Soc. Am. B*, vol. 21, no. 6, pp. 1210–1215, 2004.

[241] P. Kang, C. Chen, L. Hao, C. Zhu, Y. Hu, and Z. Chen, "A novel sonication route to prepare anthracene nanoparticles," *Materials Research Bulletin*, vol. 39, no. 4, pp. 545 – 551, 2004.

[242] J. D. Jackson, "Classical electrodynamics," 1999.

[243] H. F. Arnoldus and J. T. Foley, "Transmission of dipole radiation through interfaces and the phenomenon of anti-critical angles," *J. Opt. Soc. Am. A*, vol. 21, no. 6, pp. 1109–1117, 2004.

[244] B. Kozankiewicz, J. Bernard, and M. Orrit, "Single molecule lines and spectral hole burning of terrylene in different matrices," *The Journal of Chemical Physics*, vol. 101, no. 11, pp. 9377–9383, 1994.

[245] J. L. O'Brien, A. Furusawa, and J. Vuckovic, "Photonic quantum technologies," *Nature Photonics*, vol. 3, no. 12, pp. 687–695, 2009.

[246] C. J. Chunnilall, I. P. Degiovanni, S. Kück, I. Müller, and A. G. Sinclair, "Metrology of single-photon sources and detectors: a review," *Optical Engineering*, vol. 53, no. 8, pp. 1 – 17, 2014.

[247] J. Zwinkels, A. Sperling, T. Goodman, J. C. Acosta, Y. Ohno, M. L. Rastello, M. Stock, and E. Woolliams, "Mise en pratiquefor the definition of the candela and associated derived units for photometric and radiometric quantities in the international system of units (SI)," *Metrologia*, vol. 53, no. 3, pp. G1–G1, 2016.

[248] W. Schmunk, M. Rodenberger, S. Peters, H. Hofer, and S. Kück, "Radiometric calibration of single photon detectors by a single photon source based on nv-centers in diamond," *Journal of Modern Optics*, vol. 58, no. 14, pp. 1252–1259, 2011.

[249] M. López, H. Hofer, and S. Kück, "Detection efficiency calibration of single-photon silicon avalanche photodiodes traceable using double attenuator technique," *Journal of Modern Optics*, vol. 62, no. 20, pp. 1732–1738, 2015.

[250] C. A. Balanis, *Antenna Theory: Analysis and Design*. 2005.

[251] G. Porrovecchio, M. Šmid, M. López, H. Hofer, B. Rodiek, and S. Kück, "Comparison at the sub-100 fW optical power level of calibrating a single-photon detector using a high-sensitive, low-noise silicon photodiode and the double attenuator technique," *Metrologia*, vol. 53, no. 4, pp. 1115–1122, 2016.

[252] B. Kozankiewicz and M. Orrit, "Single-molecule photophysics, from cryogenic to ambient conditions," *Chem. Soc. Rev.*, vol. 43, pp. 1029–1043, 2014.

[253] *In preparation*.

[254] N. Spagnolo, C. Vitelli, L. Aparo, P. Mataloni, F. Sciarrino, A. Crespi, R. Ramponi, and R. Osellame, "Three-photon bosonic coalescence in an integrated tritter," *Nature Communications*, vol. 4, p. 1606, 2013.

[255] Y. Xie, Z. Lu, F. Li, J. Zhao, and Z. Weng, "Lithographic fabrication of large diffractive optical elements on a concave lens surface," *Opt. Express*, vol. 10, pp. 1043–1047, Oct 2002.

[256] S. Y. Lin, J. G. Fleming, D. L. Hetherington, B. K. Smith, R. Biswas, K. M. Ho, M. M. Sigalas, W. Zubrzycki, S. R. Kurtz, and J. Bur, "A three-dimensional photonic crystal operating at infrared wavelengths," *Nature*, vol. 394, no. 6690, pp. 251–253, 1998.

[257] J. Roels, I. De Vlaminck, L. Lagae, B. Maes, D. Van Thourhout, and R. Baets, "Tunable optical forces between nanophotonic waveguides," *Nature Nanotechnology*, vol. 4, no. 8, pp. 510–513, 2009.

[258] J. B. Mueller, J. Fischer, F. Mayer, M. Kadic, and M. Wegener, "Polymerization kinetics in three-dimensional direct laser writing," *Advanced Materials*, vol. 26, no. 38, pp. 6566–6571, 2014.

[259] L. J. Jiang, Y. S. Zhou, W. Xiong, Y. Gao, X. Huang, L. Jiang, T. Baldacchini, J.-F. Silvain, and Y. F. Lu, "Two-photon polymerization: investigation of chemical and mechanical properties of resins using Raman microspectroscopy," *Opt. Lett.*, vol. 39, no. 10, pp. 3034–3037, 2014.

[260] M. H. Olsen, "Two-photon polymerization of immune cell scaffolds.," pp. PhD dissertation, Technical University of Denmark, 2013.

[261] M. G. Guney and G. K. Fedder, "Estimation of line dimensions in 3d direct laser writing lithography," *Journal of Micromechanics and Microengineering*, vol. 26, no. 10, p. 105011, 2016.

[262] C. Reinhardt, S. Passinger, B. N. Chichkov, C. Marquart, I. P. Radko, and S. I. Bozhevolnyi, "Laser-fabricated dielectric optical components for surface plasmon polaritons," *Opt. Lett.*, vol. 31, no. 9, pp. 1307–1309, 2006.

[263] S. Rekštytė, T. Jonavičius, and M. Malinauskas, "Direct laser writing of microstructures on optically opaque and reflective surfaces," *Optics and Lasers in Engineering*, vol. 53, pp. 90 – 97, 2014.

[264] E. Johlin, S. A. Mann, S. Kasture, A. F. Koenderink, and E. C. Garnett, "Broadband highly directive 3d nanophotonic lenses," *Nature Communications*, vol. 9, no. 1, p. 4742, 2018.

[265] T. Gissibl, S. Thiele, A. Herkommer, and H. Giessen, "Two-photon direct laser writing of ultracompact multi-lens objectives," *Nature Photonics*, vol. 10, p. 554, 2016.

[266] C. DeMerlis and D. Schoneker, "Review of the oral toxicity of polyvinyl alcohol (pva)," *Food and Chemical Toxicology*, vol. 41, no. 3, pp. 319 – 326, 2003.

[267] T. M. Maria, R. A. de Carvalho, P. J. Sobral, A. M. B. Habitante, and J. Solorza-Feria, "The effect of the degree of hydrolysis of the pva and the plasticizer concentration on the color, opacity, and thermal and mechanical properties of films based on pva and gelatin blends," *Journal of Food Engineering*, vol. 87, no. 2, pp. 191 – 199, 2008.

[268] S. Pazzagli, "Organic nanocrystals and polymeric waveguides: a novel path towards integrated quantum nanophotonics," *PhD Thesis, University of Florence*, 2018.

[269] Y. Xianda, W. Anlai, and C. Suqin, "Water-vapor permeability of polyvinyl alcohol films," *Desalination*, vol. 62, pp. 293–297, 1987.

[270] F. Horii, S. Hu, T. Ito, H. Odani, R. Kitamaru, S. Matsuzawa, and K. Yamaura, "Cross polarization/magic angle spinning 13c n.m.r. study of solid structure and hydrogen bonding of poly(vinyl alcohol) films with different tacticities," *Polymer*, vol. 33, no. 11, pp. 2299 – 2306, 1992.

[271] C. Polisseni, K. D. Major, S. Boissier, S. Grandi, A. S. Clark, and E. A. Hinds, "Stable, single-photon emitter in a thin organic crystal for application to quantum-photonic devices," *Opt. Express*, vol. 24, no. 5, pp. 5615–5627, 2016.

[272] N. Limpan, T. Prodpran, S. Benjakul, and S. Prasarpran, "Influences of degree of hydrolysis and molecular weight of poly(vinyl alcohol) (pva) on properties of fish myofibrillar protein/pva blend films," *Food Hydrocolloids*, vol. 29, no. 1, pp. 226 – 233, 2012.

[273] S. V. Caro JR., C. S. P. Sung, and E. W. Merrill, "Reaction of hexamethylene diisocyanate with poly(vinyl alcohol) films for biomedical applications," *Journal of Applied Polymer Science*, vol. 20, no. 12, pp. 3241–3246, 1976.

[274] F. Arranz, E. M. Bejarano, and M. Sanchez-Chaves, "Poly(vinyl alcohol) functionalized by chloroacetate groups. coupling of bioactive carboxylic acids," *Macromolecular Chemistry and Physics*, vol. 195, no. 12, pp. 3789–3798, 1994.

[275] M. Heydari, A. Moheb, M. Ghiaci, and M. Masoomi, "Effect of cross-linking time on the thermal and mechanical properties and pervaporation performance of poly(vinyl alcohol) membrane cross-linked with fumaric acid used for dehydration of isopropanol," *Journal of Applied Polymer Science*, vol. 128, no. 3, pp. 1640–1651, 2013.

[276] J. Marqués-Hueso, R. Abargues, J. Canet-Ferrer, S. Agouram, J. L. Valdés, and J. P. Martínez-Pastor, "Au-pva nanocomposite negative resist for one-step three-dimensional e-beam lithography," *Langmuir*, vol. 26, no. 4, pp. 2825–2830, 2010.

[277] J. M. Havard, S.-Y. Shim, J. M. J. Fréchet, Q. Lin, D. R. Medeiros, C. G. Willson, and J. D. Byers, "Design of photoresists with reduced environmental impact. 1. water-soluble resists based on photo-cross-linking of poly(vinyl alcohol)," *Chemistry of Materials*, vol. 11, no. 3, pp. 719–725, 1999.

[278] V. R. Manfrinato, A. Stein, L. Zhang, C.-Y. Nam, K. G. Yager, E. A. Stach, and C. T. Black, "Aberration-corrected electron beam lithography at the one nanometer length scale," *Nano Letters*, vol. 17, no. 8, pp. 4562–4567, 2017.

[279] P. Rai-Choudhury, *Handbook of microlithography, micromachining, and microfabrication: microlithography*, vol. 1. Iet, 1997.

[280] D. R. Medeiros, A. Aviram, C. R. Guarnieri, W. . Huang, R. Kwong, C. K. Magg, A. P. Mahorowala, W. M. Moreau, K. E. Petrillo, and M. Angelopoulos, "Recent progress in electron-beam resists for advanced mask-making," *IBM Journal of Research and Development*, vol. 45, no. 5, pp. 639–650, 2001.

[281] I. Raptis, B. Nowotny, N. Glezos, M. Gentili, and G. Meneghini, "Electron beam lithography simulation on homogeneous and multilayer substrates," *Japanese Journal of Applied Physics*, vol. 39, no. Part 1, No. 2A, pp. 635–644, 2000.

[282] J. W. Lussi, C. Tang, P.-A. Kuenzi, U. Staufer, G. Csucs, J. Vörös, G. Danuser, J. A. Hubbell, and M. Textor, "Selective molecular assembly patterning at the nanoscale: a novel platform for producing protein patterns by electron-beam lithography on SiO2/indium tin oxide-coated glass substrates," *Nanotechnology*, vol. 16, no. 9, pp. 1781–1786, 2005.

[283] A. A. Tseng, Kuan Chen, C. D. Chen, and K. J. Ma, "Electron beam lithography in nanoscale fabrication: recent development," *IEEE Transactions on Electronics Packaging Manufacturing*, vol. 26, pp. 141–149, April 2003.

[284] B.-S. Song, S. Noda, T. Asano, and Y. Akahane, "Ultra-high-q photonic double-heterostructure nanocavity," *Nature Materials*, vol. 4, no. 3, pp. 207–210, 2005.

[285] S. Fan, P. R. Villeneuve, J. D. Joannopoulos, and E. F. Schubert, "High extraction efficiency of spontaneous emission from slabs of photonic crystals," *Phys. Rev. Lett.*, vol. 78, pp. 3294–3297, 1997.

[286] S. I. Bozhevolnyi, V. S. Volkov, E. Devaux, J.-Y. Laluet, and T. W. Ebbesen, "Channel plasmon subwavelength waveguide components including interferometers and ring resonators," *Nature*, vol. 440, no. 7083, pp. 508–511, 2006.

[287] L. Novotny and N. van Hulst, "Antennas for light," *Nature Photonics*, vol. 5, p. 83, 2011. Review Article.

[288] D. Lin, P. Fan, E. Hasman, and M. L. Brongersma, "Dielectric gradient metasurface optical elements," *Science*, vol. 345, no. 6194, pp. 298–302, 2014.

[289] N. Engheta, "Circuits with light at nanoscales: Optical nanocircuits inspired by metamaterials," *Science*, vol. 317, no. 5845, pp. 1698–1702, 2007.

[290] A. E. Grigorescu and C. W. Hagen, "Resists for sub-20-nm electron beam lithography with a focus on HSQ: state of the art," *Nanotechnology*, vol. 20, no. 29, p. 292001, 2009.

[291] Z. Cui, "Nanofabrication," *Course notes, ECE*, vol. 730, 2008.

[292] A. S. Gangnaik, Y. M. Georgiev, and J. D. Holmes, "New generation electron beam resists: A review," *Chemistry of Materials*, vol. 29, no. 5, pp. 1898–1917, 2017.

[293] R. Egerton, P. Li, and M. Malac, "Radiation damage in the tem and sem," *Micron*, vol. 35, no. 6, pp. 399 – 409, 2004. International Wuhan Symposium on Advanced Electron Microscopy.

[294] T. Susi, J. Kotakoski, R. Arenal, S. Kurasch, H. Jiang, V. Skakalova, O. Stephan, A. V. Krasheninnikov, E. I. Kauppinen, U. Kaiser, and J. C. Meyer, "Atomistic description of electron beam damage in nitrogen-doped graphene and single-walled carbon nanotubes," *ACS Nano*, vol. 6, no. 10, pp. 8837–8846, 2012.

[295] F. Banhart, "Irradiation effects in carbon nanostructures," *Reports on Progress in Physics*, vol. 62, no. 8, pp. 1181–1221, 1999.

[296] G. B., *Radiation-induced charge storage and polarization effects*, vol. 33. 1980.

[297] J. H. L. Watson, "An effect of electron bombardment upon carbon black," *Journal of Applied Physics*, vol. 18, no. 2, pp. 153–161, 1947.

[298] A. Singh, Q. Li, S. Liu, Y. Yu, X. Lu, C. Schneider, S. Höfling, J. Lawall, V. Verma, R. Mirin, S. W. Nam, J. Liu, and K. Srinivasan, "Quantum frequency conversion of a quantum dot single-photon source on a nanophotonic chip," *Optica*, vol. 6, pp. 563–569, May 2019.

[299] Y. Cao, V. Fatemi, A. Demir, S. Fang, S. L. Tomarken, J. Y. Luo, J. D. Sanchez-Yamagishi, K. Watanabe, T. Taniguchi, E. Kaxiras, R. C. Ashoori, and P. Jarillo-Herrero, "Correlated insulator behaviour at half-filling in magic-angle graphene superlattices," *Nature*, vol. 556, p. 80, Mar 2018.

[300] Y. Cao, V. Fatemi, S. Fang, K. Watanabe, T. Taniguchi, E. Kaxiras, and P. Jarillo-Herrero, "Unconventional superconductivity in magic-angle graphene superlattices," *Nature*, vol. 556, pp. 43 EP –, Mar 2018. Article.

[301] M. Tegmark and J. A. Wheeler, "100 years of the quantum," 2001.

[302] H. Gehring, A. Eich, C. Schuck, and W. H. P. Pernice, "Broadband out-of-plane coupling at visible wavelengths," *Opt. Lett.*, vol. 44, pp. 5089–5092, Oct 2019.

[303] T. Wienhold, S. Kraemmer, S. F. Wondimu, T. Siegle, U. Bog, U. Weinzierl, S. Schmidt, H. Becker, H. Kalt, T. Mappes, S. Koeber, and C. Koos, "All-polymer photonic sensing platform based on whispering-gallery mode microgoblet lasers," *Lab Chip*, vol. 15, pp. 3800–3806, 2015.

[304] H. Kasai, H. S. Nalwa, H. Oikawa, S. Okada, H. Matsuda, N. Minami, A. Kakuta, K. Ono, A. Mukoh, and H. Nakanishi, "A novel preparation method of organic microcrystals," *Japanese Journal of Applied Physics*, vol. 31, no. Part 2, No. 8A, pp. L1132–L1134, 1992.

[305] H. Kasai, H. Kamatani, S. Okada, H. Oikawa, H. Matsuda, and H. Nakanishi, "Size-dependent colors and luminescences of organic microcrystals," *Japanese Journal of Applied Physics*, vol. 35, no. Part 2, No. 2B, pp. L221–L223, 1996.

[306] H. Katagi, H. Kasai, S. Okada, H. Oikawa, K. Komatsu, H. Matsuda, Z. Liu, and H. Nakanishi, "Size control of polydiacetylene microcrystals," *Japanese Journal of Applied Physics*, vol. 35, no. Part 2, No. 10B, pp. L1364–L1366, 1996.

[307] H.-B. Fu and J.-N. Yao, "Size effects on the optical properties of organic nanoparticles," *Journal of the American Chemical Society*, vol. 123, no. 7, pp. 1434–1439, 2001.

[308] H.-R. Chung, E. Kwon, H. Oikawa, H. Kasai, and H. Nakanishi, "Effect of solvent on organic nanocrystal growth using the reprecipitation method," *Journal of Crystal Growth*, vol. 294, no. 2, pp. 459 – 463, 2006.

[309] K. D. Major, Y.-H. Lien, C. Polisseni, S. Grandi, K. W. Kho, A. S. Clark, J. Hwang, and E. A. Hinds, "Growth of optical-quality anthracene crystals doped with dibenzoterrylene for controlled single photon production," *Review of Scientific Instruments*, vol. 86, no. 8, p. 083106, 2015.

[310] S. Jo, H. Yoshikawa, A. Fujii, and M. Takenaga, "Epitaxial growth of anthracene single crystals on graphite (0001) substrate with physical vapor growth technique," *Surface Science*, vol. 592, no. 1, pp. 37 – 41, 2005.

Appendix

A

Computational Modelings

In this thesis we have employed the commercial software COMSOL Multiphysics (Radio Frequency and Wave Optics modules), which implements the finite-element method (FEM), to model light propagation in optical WGs and into SILs devices. We here recall the general steps of the FEM [268].
The choice of the simulation domain is critical with respect to artefacts, such as spurious reflections. In particular, Perfectly matched layers (PMLs) are introduced to simulate total absorption of any incident electromagnetic mode. The PML thickness is chosen by performing convergence tests. In other words, the total simulation space is correctly truncated imposing the perfect electric conductor boundary conditions (PEC), i.e. $\mathbf{n} \times \mathbf{E} = 0$, where $\mathbf{n}$ is the vector normal to the interface. Hence, subdomains characterized by the dielectric constant of the associated material define the geometry of the problem. Consequently, at the dielectric interfaces the continuity condition on the tangential components of the fields $\mathbf{n} \times (\mathbf{E}_1 - \mathbf{E}_2)$ and $\mathbf{n} \times (\mathbf{B}_1 - \mathbf{B}_2)$ are fulfilled, with the subscript referring to the two adjacent materials.
Finally, the total simulation domain is discretized into a mesh grid of finite elements. To accurately describe the regions with strong field gradients, a finer mesh ($d << \lambda$, with d the average size of the finite elements) is used in the near-field of the dipole source or at the interface between different materials, whereas a coarser mesh ($d \sim \lambda/2$) can be employed in the regions where the fields are expected to change slowly.
We briefly explain the method used for the optimization of the WG structure described in Chapter 4, whereas details concerning the SIL structure are directly given

in the main text, within the same chapter.

The WG treated in this thesis is at first considered as z-translational invariant, since the nominal transverse section is constant. Therefore, 2D-domain simulations of the WG cross-section are used for the analysis of the guided modes. For a defined operating waevelength, the mode solver finds numerical solutions of the Maxwell equation in the absence of sources, yielding the field distributions of the supported modes and their effective refractive indices $n_{eff,m}$.
Coupling efficiency β and emission enhancement α are then determined by simulating the emission of a dipole coupled to the photonic structure. In this case a 3D domain is used, and the software computes the electromagnetic field excited by the dipole. Despite a more correct calculation of the figures of merit would entail the separate evaluation for each excited mode, normalized to the overlap integral between the field at the output and the modal field profile, here we have considered excitation of the fundamental mode only. In particular, the emitter is modeled as a linear harmonic electric current of length l oriented along $\hat{\mathbf{d}}$ on the transverse plane and parallel to the substrate, which is a suitable approximation for a dipole emission in the considered transverse plane. The β-factor can hence be calculated according to equation $\Gamma_{WG}/\Gamma_{tot} = P_{WG}/P_{tot}$, from Sec. 1.2.1. The power in the waveguide mode is well described (since we assume excitation of the fundamental mode only) by integrating the Poynting vector flux through the two end faces of the waveguide before the PML, while the total radiated power is given by the power flow through the surface of a volume containing the emitter. In order to estimate α, the same simulation domain is converted into a homogeneous medium by simply setting the refractive indices of all subdomains equal to that of vacuum or to the dielectric medium embedding the source. The parameter is then given by the ratio between the total radiated power calculated in the presence and in the absence of the waveguide. Owing to the symmetry of the system, the simulation domain can be divided in half with respect to a vertical plane containing the emitter and orthogonal to the direction of propagation. Boundary condition corresponding to a perfect magnetic conductor (PMC) $\mathbf{n} \times \mathbf{B}$ are then applied to this cutting plane, imposing a null value of the magnetic field tangential component on the plane, i.e. a non null tangential electric field, thus ensuring the dipole emission. The PMC plane acts in practice as a mirror for the dipole, doubling its dipole moment. Consequently, the computed electromagnetic field in the truncated simulation domain is divided by two.

B

Fabrication of DBT:Ac Nanocrystals

The reprecipitation method was developed by Nakanishi and co-workers [304] and allowed the production of a series of nanoparticles - including perylene [305], polydiacetylene [306], pyrazolines [307] and anthracene [308] - which were found to possess size-dependent properties below a threshold size of 100 nm. Such a method relies on the insolubility of organic materials in water. It consists in dissolving the organic compound in a water-soluble solvent and disperse this solution drop-wise into vigorously stirred water at room temperature. After few minutes of stirring, the compound is reprecipitated in the form of NCX dispersed in water, with size and shape determined by several conditions such as water temperature, droplet size, injected solution concentration or presence of surfactants [308]. In particular, the protocol we present here is adapted from the procedure developed by Kang and colleagues, who demonstrated the advantages of using sonication, rather than magnetic stirring, in terms of monodispersity in size and, with an average of hundreds nanometers.
The procedure starts with preparing a 1 mM solution of DBT in toluene and a 5 mM solution of anthracene in acetone, that are then mixed together in different proportions. In this work, we use two main optimal recipes:

- for individual Ac NCX with single molecule concentration the DBT:toluene solution with the Ac:acetone mixture is diluted by a factor of 10^8. Such NCX assure single-photon emission even at room temperature under non-resonant excitation.

- for densely DBT-doped NCX, a dilution ratio of 10^2 gives a sufficiently low DBT concentration within the single Ac NCX to enable efficeint spectral selection of individual molecules under resonant excitation at cryogenic temperatures.

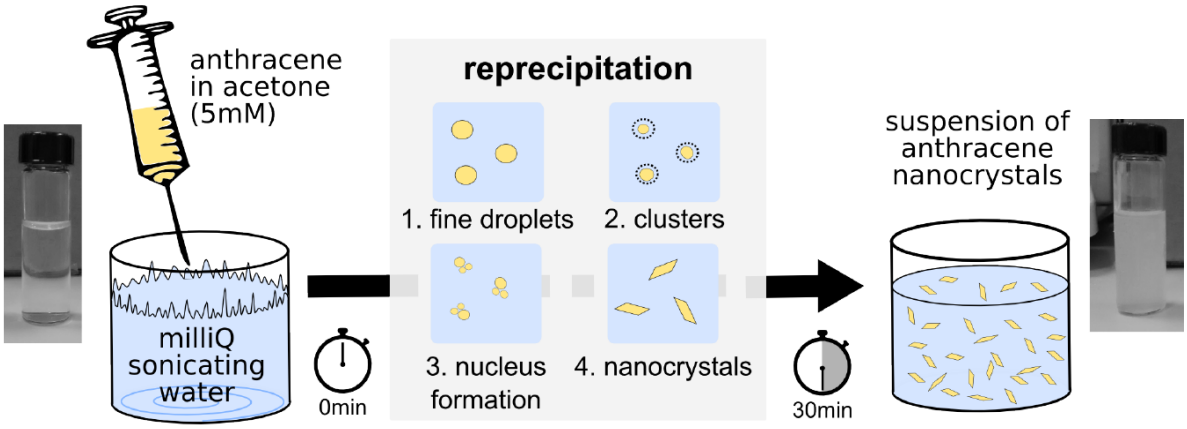

Figure 2.1: Scheme of the reprecipitation protocol and of the DBT-doped Ac NCX formation process.

As sketched in Fig. 2.1, $250\,\mu$L of the mixture are injected into 5 mL sonicating water (deionized by a Milli-Q Advantage A10 System, $18.2\,\mathrm{m\Omega cm}$ at $25°$C) at room temperature. The mixture separates into small droplets and acetone gradually dissolves in water and, correspondingly, the concentration in the micro-droplets becomes supersaturated until the compound is reprecipitated in the form of NCX. We continuously sonicate for 30 min time, untill a turbid-white suspension is obtained. In order to obtain a reproducible reprecipitation, it is fundamental to minimize the presence of impurities both in the water and in the tools used.

Morphology and Crystallinity

Evaluation of the NCX size is done by scanning electron microscopy (SEM, Phenom Pro, PhenomWorld) and atomic force microscopy (AFM, Pico SPM from Molecular Imaging in AC mode equipped with a silicon probe NSG01 (NT-MDT) with 210 KHz resonant frequency). In Fig. 2.2a,b, we can recognize some NCX exhibiting peculiar features of crystalline Ac, as the hexagonal shape, whereas others have a more round-like geometry. The results from the AFM analysis on a statistic of more than 90 different NCX, are reported in Fig. 2.2c. In average, NCX exhibit a thickness $\mathrm{t} = (65 \pm 13)$nm and an equivalent diameter $\mathrm{d_{eq}} = (113 \pm 64)$ nm, with a resulting aspect ratio $\mathrm{t/d_{eq}} = (0.6 \pm 0.2)$.

The crystalline nature of NCX is studied by mean of X-ray diffraction (XRD Bruker New D8 instrumemt). According to the Bragg's law $\mathrm{n}\lambda = 2\mathrm{d}\sin(\theta)$, the incident X-ray

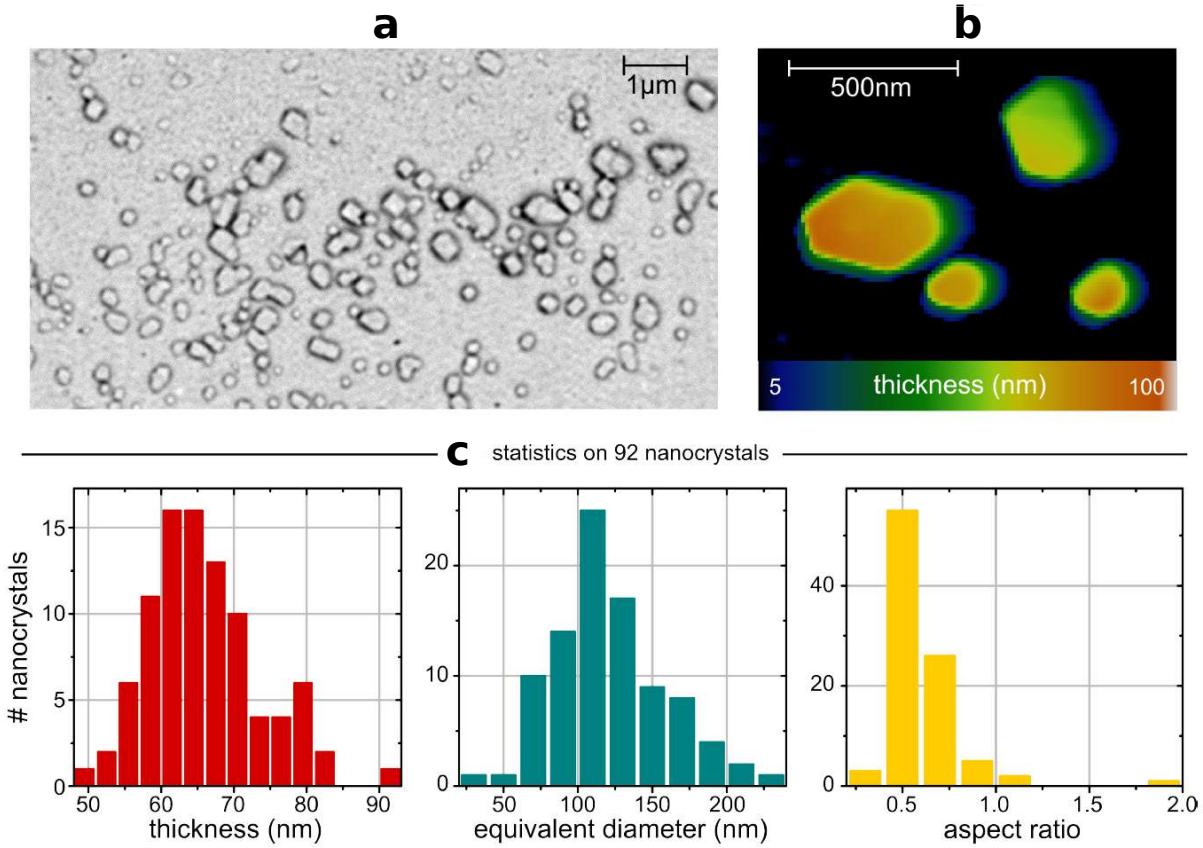

Figure 2.2: Typical SEM (**a**) and AFM (**b**) images of DBT:Ac NCX, once drop-casted and desiccated on a bare coverglass. **c** - Statistical analysis on AFM images yields the following average values: NCX thickness (65 ± 13) nm, NCX equivalent diameter (113 ± 64) nm, and aspect ratio (0.6 ± 0.2).

radiation interacts with the crystalline sample producing a constructive interference pattern, from which the lattice d-spacings can be inferred. Given the incidence angle θ (between the radiation direction and the sample surface) and the radiation wavelength λ, the peaks appearing in the diffraction pattern enable the identification of the crystal material by comparison with reference patterns. In Fig. 2.3a, the result for DBT:Ac NCX is compared to the bulk systems, respectively fabricated via spin-coating [46] and co-sublimation [214, 309]. In all cases, we observe a strong diffracted peak at $9.17°$, corresponding to the (001) plane, and other equivalent periodic peaks corresponding to (002), (003), and (004) planes (see Fig. 3.1b for an illustration of the crystal edges of an Ac single crystal, fabricated via vapor growth by Jo and colleagues [310]), matching the crystallographic data of an anthracene monoclinic system [212]. Fig. 3.1c reports the XRD pattern measured from the solely DBT powder. We observe that DBT peaks are not resolved in any of the XRD patterns in Figure 4.6a, as DBT

molecules are just impurities within the Ac matrix.

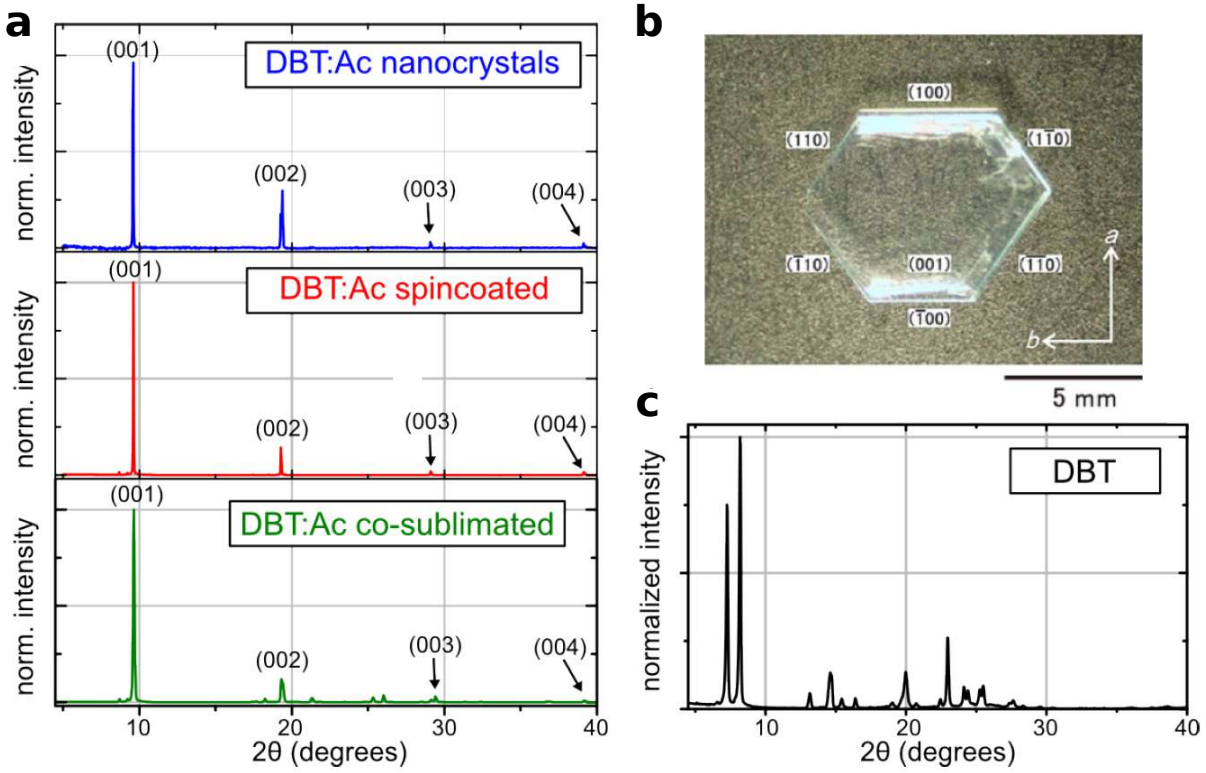

Figure 2.3: **a** - Comparison of the normalized XRD patterns measured for DBT:Ac NCX, spincoated DBT:Ac and co-sublimated DBT:Ac crystals, in which only the (001) and its higher order reflection are well resolved. This means that, once deposited on the substrate, Ac crystals and NCX tend to be iso-oriented with c-axis perpendicular to the substrate, due to their natural platelet-like morphology. **b** - Figure adapted from Ref. [310], showing a 10 mm-sized Ac single crystal obtained by physical vapor growth, reported here for convenience to illustrate how the crystal's edges reflect its fundamental structure. **c** - XRD pattern measured for the solely DBT powder.

C

Photon-Loss Considerations

With reference to the setup employed in Chapter 3, Sec. 3.1, the following table summarizes the single elements efficiencies. We ascribe to these values the experimental losses that are taken into accounts for the calibration of the silicon SPAD in Chapter 3. The note d) here refers to the results of simulations in Ref. [57].

Element	Efficiency	Symbol
Cryostat windows	0.85	
Objective transmission	0.7	
Beam splitter	0.9	
Spectral filters[a]	0.85	
Mirrors and lenses[b]	0.54	
Fiber coupling[c]	0.75	
Overall optical setup	**0.18**	β_{opt}
Photon flux detector	**0.6**	β_{det}
HBT detectors	0.65	
Collection (N.A.=0.67)[d]	**0.35**	β_{col}

a) residual losses due to close proximity of filters' edges;
b) 9x metallic mirrors; 5x spherical lenses;
c) Objective lens transmission @785nm = 0.8; coupling to fiber ~ 0.94
d) Collection obtained with N.A.=0.67 objective lens according to simulations

Figure 3.1: **Table**. Single optical elements efficiency.